Sede Amministrativa: Università degli Studi di Padova

Centro di Ateneo di Studi e Attività Spaziali "Giuseppe Colombo" C.I.S.A.S.

DOTTORATO DI RICERCA IN SCIENZE TECNOLOGIE E MISURE SPAZIALI

CURRICOLO: MISURE MECCANICHE PER L'INGEGNERIA E LO SPAZIO (MMIS)

35° CICLO

DEVELOPMENT OF NON-CONTACT MEASUREMENT TECHNIQUES FOR 3D SHAPE ANALYSIS

Coordinatore: Ch.mo Prof. Francesco Picano

Supervisore: Ch.mo Prof. Gianluca Rossi

Dottorando: Iva Xhimitiku

Declaration

I, Iva Xhimitiku, hereby declare that the contents and organization of this dissertation "Development of non-contact techniques for 3D shape analysis" constitute my own original work and does not compromise in any way the rights of third parties, including those relating to the security of personal data.

I confirm that:

• This work was done wholly or mainly while in candidature for a research degree at this University.

• Where any part of this thesis has previously been submitted for a degree or any other qualification at this University or any other institution, this has been clearly stated.

• Where I have consulted the published work of others, this is always clearly attributed.

• Where I have quoted from the work of others, the source is always given. With the exception of such quotations, this thesis is entirely my own work.

• I have acknowledged all main sources of help.

• Where the thesis is based on work done by myself jointly with others, I have made clear exactly what was done by others and what I have contributed my-self.

Iva Xhimitiku

2023

"I often say that when you can measure what you are speaking about, and express it in numbers, you know something about it; but when you cannot measure it when you cannot express it in numbers, your knowledge is of a meagre and unsatisfactory kind; it may be the beginning of knowledge, but you have scarcely, in your thoughts, advanced to the stage of "science", whatever the matter may be."

(William Thomson - Lord Kelvin)

"Measure what is measurable and make measurable what is not so."

(Galileo Galilei)

I would like to dedicate this thesis to my loving family, friends and my Love.

Acknowledgement

Abstract

This work is aimed towards the defining procedure and models to quantify the uncertainty of volume measurements with and without references. The major contributions of this thesis work are in the possibility of use low-cost 3D scanning techniques approach of complex scene for shape analysis and volume estimation.

Index

List of Figures

List of Tables

Introduction

Over the past few decades, vision-based three-dimensional (3D) shape measurement techniques have found developments and extensive applications in various fields due to their precision, very high measurement speed in many points, efficiency, and non-contact nature. The rapid advancements in 3D software and hardware have revolutionised the acquisition and reconstruction of complex surfaces, expanding their usability across different disciplines [1]. Accurately understanding the shape of a 3D object remains a critical challenge in many manufacturing processes [2], [3]. The integration of 3D scan data with design and manufacturing software enables the generation of highly accurate data for constructing intricate organic shapes, surpassing the capabilities of traditional 3D surface modelling software. These techniques offer numerous advantages, such as rapid data acquisition, non-contact nature, compatibility with available hardware, and notable measurement precision, making them highly suitable for industries, e.g., reverse engineering, prototyping, 3D printing, manufacturing, medical sciences, agriculture, and cultural heritage preservation. With the increasing adoption of 3D measurement techniques across diverse applications, new and more complex challenges emerge. No single 3D sensing technology can provide a universal solution to all these challenges. Various fields require efficient and precise data processing to extract geometric features, including distances, areas, and volume estimations [4], [5]. Volume estimation of complex geometry is a particularly challenging issue that has received significant attention in the literature, leading to the exploration of different approaches and methodologies [6], [7], [8]. In this study, some of these issues have been analysed to develop a procedure for evaluating the uncertainty.

The research activity focuses on developing measurement methods for inspecting complex geometric structures. The potential of combining different scanning techniques with Alpha Shape, Alpha Critical, Alpha Optimal, and Convex Hull algorithms for various applications and shape complexity has been developed for invariant shapes (e.g., 3D printed object), slow variant shapes (e.g., plants),

moving objects (e.g., human body). Thus, the work aims to define procedures and models to quantify the uncertainty of volume measurements with and without references. Additionally, measurement methods have been developed to be valid for low-cost 3D scanning techniques. The significant contributions of this thesis work are the possibility of using a low-cost 3D scanning approach of complex geometry for shape measurement and volume estimation. The following items are discussed in this thesis: The advantage of Structured Light scanning system on different applications (Cultural heritage, biomedicine, sports training, design); deep learning algorithms for detecting anomalies in lettuce plants growing in a controlled greenhouse (agriculture); the relationship between leaf area and volume of artificial apple tree (agriculture, controlled environment); 3D shape measurement techniques for human body reconstruction (biomedicine): multi-scanning approach with low and high-cost instrument. The leading 3D scanning techniques with different cost ranges and resolutions were used, compared, and often integrated into all these applications. Besides improving the model's geometry, the integration aims to support the quality of surface measurements and improve interpretation and detail in complex objects.

Chapter One: This chapter illustrates a theoretical background and literature covering the different measurement technologies in integrating scanner technologies and feature extraction, texture mapping and image segmentation.

Chapter Two summarises data acquisition and pre-processing methods to generate the 3D models using different scanner techniques for complex shape geometry. Here, several 3D measurement techniques and volume evaluation algorithms are shown.

Chapter Three: This chapter aims to understand the uncertainty of volume evaluation algorithms: Alpha Shape, a developed algorithm Alpha Critical (AC), Alpha Optimal and Convex Hull. The algorithms were tested on simple and complex shapes objects.

Chapter Four: In this chapter, the evaluation of uncertainty surface measurement reconstruction and volume evaluation by different algorithms will be applied to static geometry in various fields and scenarios.

Chapter Five presents a methodology for 3D reconstruction and volume estimation by the algorithms on artificial trees.

Chapter Six: A Deep Learning Algorithm for detecting anomalies in lettuce plant growing, 2D and 3D data comparison is presented.

Chapter Seven presents a methodology for reconstructing a complex shape and movement.

The research focuses on 3D measurement using non-contact and low-cost techniques for data extraction on complex geometries, specifically complex shapes such as 3D printed objects (no movement), plants (slow), and the human body caracterised by variations in subject position (high movement). The primary objective of the research is to evaluate the uncertainty reconstruction and volume evaluation of complex geometries using different algorithms, such as alpha shape and a developed alpha shape algorithm (based on the alpha critical, convex hull). Additionally, the aim is to consider the instrument performances, the reconstruction method of 3D scanned geometry and the application field in the evaluation process.

This study highlights the importance of low-cost 3D scanning techniques in various fields. The research aims to assess the performance and reliability of non-contact methods in capturing complex geometries and extracting uncertainty measurements from 3D scanned models. By comparing different low-cost 3D scanning technologies, such as structured light scanning and photogrammetry, this study examines their significance in applications spanning clothing design, ergonomic analysis, healthcare interventions, and other relevant fields. Factors such as ease of use, portability, and data processing requirements are considered to identify the most suitable technique for each field. The findings of this research will emphasise the crucial role of affordable and accessible 3D scanning solutions in enabling advancements and innovation across diverse disciplines.

Chapter 1

Theory Background

This chapter presents an overview of state-of-the-art of non-contact measurement techniques used in three-dimensional (3D) analysis. Traditionally, the characterisation of complex geometries relied on manual measurements or water-based methods, which were prone to limitations such as errors and incurred significant labour and time costs. To overcome these limitations, there has been a growing interest in developing automated methods that enable quick, accurate, and efficient object feature extraction. Three-dimensional modelling plays a crucial role in acquiring in-depth knowledge of geometry. Various scanning techniques, including digital photographs, have been developed to generate detailed 3D models. Furthermore, companies have started investigating the integration of 3D vision systems and evaluating multiple commercial sensors to assess their specifications for electronic object characterisation, such as range, wavelength, resolution, and price. Therefore, a comprehensive study focusing on sensors and components is necessary to facilitate advancements in this field.

1.1 Electromagnetic spectrum, Laser, Geometric optics, and Sensor

As electromagnetic waves interact with objects, its behaviour changes. Each object surface uniquely interacts with the waves, resulting in varying levels of reflection and absorption. Wave phenomena involve the propagation of energy without the transport of matter. Waves, including sound and light, exhibit oscillating quantities like the height of water in a sea wave, air pressure in a sound wave, or the intensity of the electric and magnetic fields in a light wave. Wave propagation may require a material medium, except for light waves, which can propagate in a vacuum. By studying wave motion, including types of waves,

polarisation, propagation, refraction, and diffraction, it is possible to understand the functioning of various devices such as lenses, reflectors, antennas, and lasers.

1.1.1 Waves Classification

Various waves can be classified based on their applications and propagation characteristics. The first criterion distinguishes waves into two categories: those that require a material medium to propagate (mechanical or elastic waves) and those that can travel even in a vacuum (electromagnetic waves). The second criterion divides waves into transverse and longitudinal waves. Transverse waves have vibrations perpendicular to the propagation direction, exemplified by light and sea waves. As observed in sound waves, longitudinal waves have vibrations parallel to the propagation direction. Electromagnetic waves are transverse, such as light waves and sea waves that move horizontally and vibrate vertically. Like sound waves, longitudinal waves propagate through compressions and rarefactions in the direction of motion. The wavefront represents the surface defined by points equidistant from the vibration source. The diagram in Figure 1 summarises the classification of waves and their main characteristics.
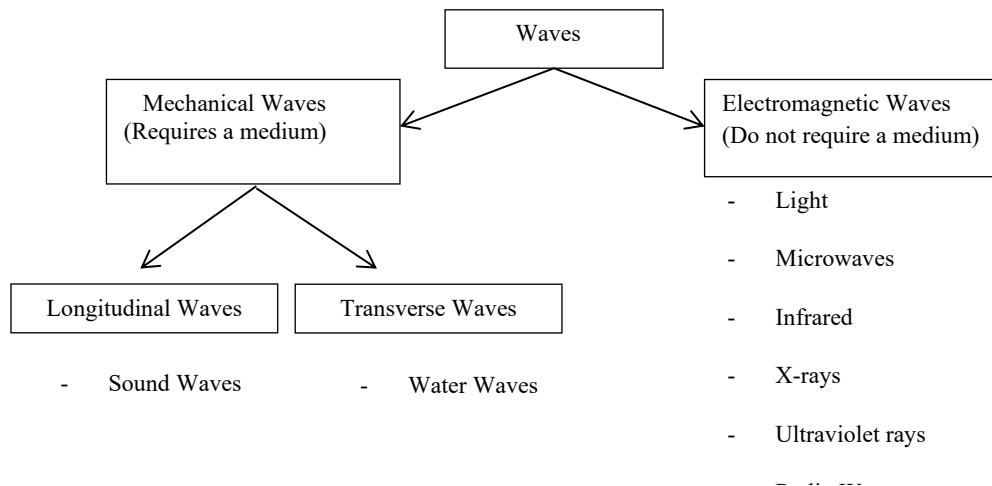
Figure 1 Classification of waves

Mechanical waves are the most readily observed; they will be used below as a useful reference to describe the behaviour and main characteristics of all waves. The wave motion, whatever the type of wave, can be described through several fundamental characteristics.

1.1.2 Electromagnetic (EM) energy, Active (microwave) vs passive (optical) sensors

Light waves oscillate electric and magnetic fields, commonly experienced as visible light. They are transverse waves, meaning the oscillation occurs perpendicular to the direction of propagation. Unlike mechanical waves, light waves do not require a medium to propagate and can travel through space. Light, or more generally, "optical radiation" (near-infrared, visible and near-ultraviolet), is a portion of a much larger radiation spectrum. The electromagnetic spectrum is defined by Maxwell wave [9]:

$$\left| \nabla^2 \vec{E} = \varepsilon_0 \mu_0 \frac{\partial^2 \vec{E}}{\partial t^2} \qquad \nabla^2 \vec{B} = \varepsilon_0 \mu_0 \frac{\partial^2 \vec{B}}{\partial t^2} \right|$$

Equation 1 Maxwell Equation

E is the wave equation for the electric and B magnetic fields. The solution of these equations is an electromagnetic field propagating in a vacuum with speed equal to $c=2.99792458 \times 10^8$ m/s. This field can be considered an overlap of electromagnetic waves (i.e., radiation). This means that radiations originated by the same physical process independently of the frequency (or wavelength). However, since the electromagnetic spectrum extends for more than 18 decades, wave-matter interaction strongly depends on wave frequency. This implies that the way the radiation is generated, transmitted and detected are different, depending on the wave frequency. Electromagnetic energy is generally measured by its wavelength or frequency unit (Figure 2). All matter generates this energy with an absolute temperature above zero. The sun, however, is the prime source of this energy and produces a full spectrum of electromagnetic radiation, known as the electromagnetic spectrum. Of this full range, the visible spectrum only encompasses one-millionth of the total capacity.
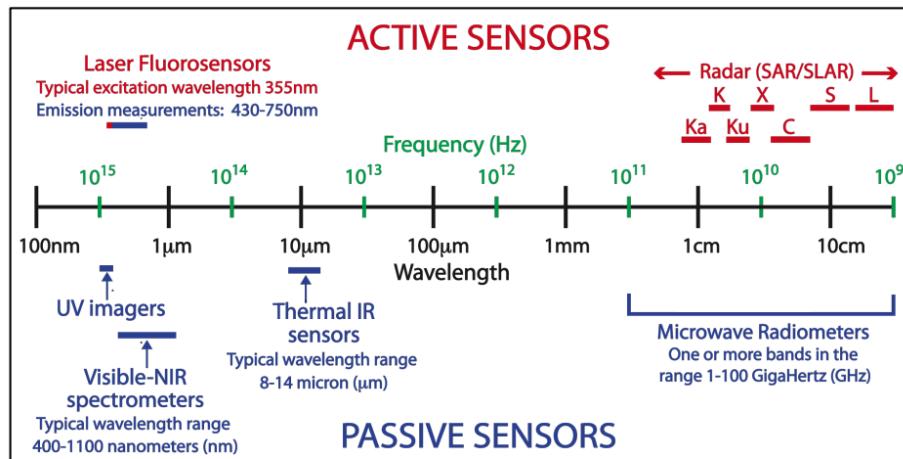
Source: SEOS (2016)

Figure 2 Electromagnetic spectrum and its relation to passive and active remote

3D measurements techniques based on in detecting electromagnetic energy, and they can be classified into active and passive sensors. Factors including atmospheric clarity, spectral characteristics of objects, sun angle and intensity, and filter selection, play a crucial role in the data capture process. Active remote sensors emit electromagnetic energy and detect the energy returned from the object or surface. Optical sensors capture the reflected or emitted electromagnetic energy and transform it into a grid array of cells, also known as pixels. Each pixel contains a raw digital number (DN) that represents the level of reflectance or emittance in a specific region of the electromagnetic spectrum, such as visible (VIS), near-infrared (NIR), or shortwave infrared (SWIR) [10]. The collective arrangement of pixels forms a raster image. Each raster image possesses distinct characteristics specific to its 3D scanner system. These characteristics encompass spatial, spectral, temporal, and radiometric resolution.

In conclusion, Specialised knowledge and expertise in image interpretation are required to extract valuable information from 3D scan data. Three levels of knowledge are necessary for image interpretation:

- Understanding the subject of interest.

- Considering the unique characteristics of the location.

- Recognising the resolution characteristics of the 3D scanning system.

A comprehensive understanding of these factors is essential to derive useful information from the imagery [11].

1.1.3 CCD and CMOS

Image sensors are of two kinds: Complementary Metal-Oxide Semiconductor (CMOS) and Charge-Coupled Devices (CCD). Both types convert light into electric charge and process it into electronic signals. CCD sensors transfer the charge of each pixel through a limited number of output nodes, resulting in high output uniformity. In contrast, CMOS sensors have individual charge-to-voltage conversion capabilities for each pixel and often incorporate additional functions like amplifiers and noise-correction mechanisms. However, these functions increase design complexity and reduce the available area for light capture. In summary, CCDs and CMOS imagers have strengths and weaknesses, making them better suited for different scenarios. CCDs demonstrate superior image quality and uniformity, whereas CMOS imagers provide added functionalities and enable high-speed parallel processing. In summary, CMOS imagers have gained traction in high-volume consumer applications and machine vision. The choice between CCDs and CMOS imagers depends on the specific requirements of the application (Figure 3).
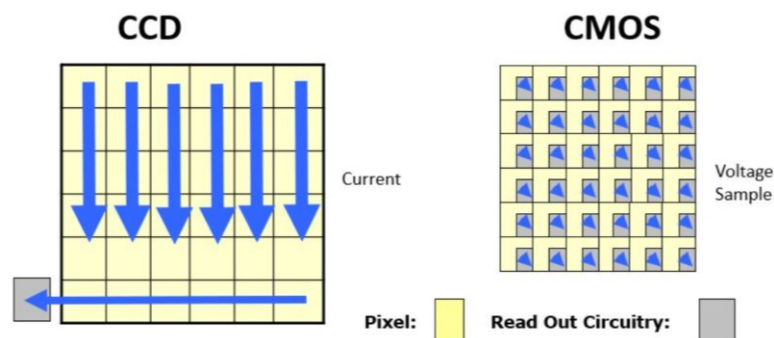
Figure 3 Scheme CCD and CMOS sensors

Uniformity is lower in CMOS imagers than in CCDs because each pixel performs its conversion. However, CMOS imagers offer high-speed performance with massively parallel processing. CMOS designers have focused on developing imagers for mobile phones, resulting in significant improvements in image quality. CMOS imagers outperform CCDs in high-volume consumer applications in almost

every performance parameter. CCDs must be updated for machine vision as CMOS imagers take the lead. However, CCDs may still be preferable for specific applications such as imaging in the NIR or UV with specific requirements like global shutters or low noise. The choice between CCD and CMOS imagers depends on leverage, volume, and supply security.

In summary, CCDs and CMOS imagers have strengths and weaknesses, making them better suited for different scenarios. CCDs demonstrate superior image quality and uniformity, whereas CMOS imagers provide added functionalities and enable high-speed parallel processing. In summary, CMOS imagers have gained traction in high-volume consumer applications and machine vision. The choice between CCDs and CMOS imagers depends on the specific requirements of the application at hand.

1.1.4 Geometric Optics

Light propagation can be described using four models. Ray optics uses rays to explain light propagation, wave optics utilizes scalar waves, electromagnetic optics employ electromagnetic waves, and quantum optics employs quantum mechanical particles (photons) described by a wave function to explain light propagation. These models provide different perspectives and approaches to understanding the behaviour of light. Figure 4 .

a)

b)
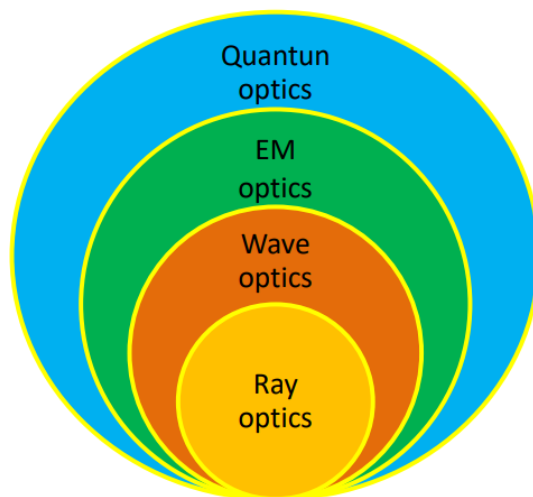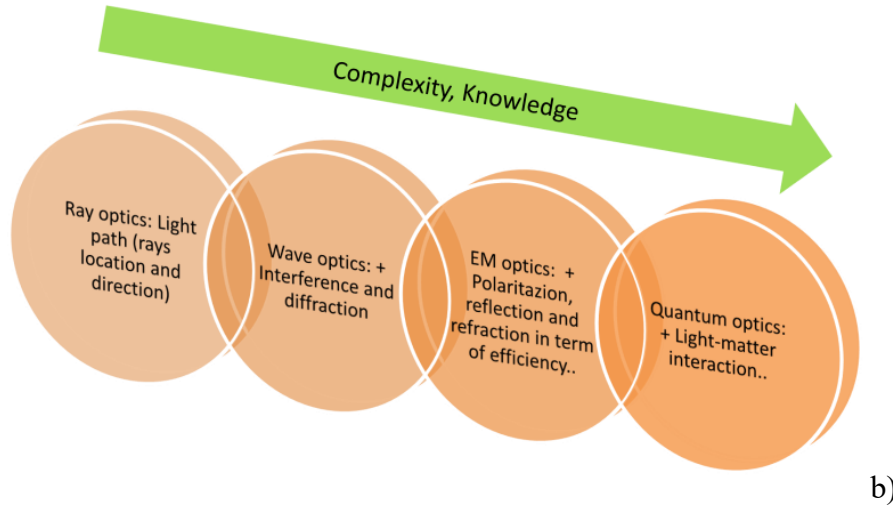
Figure 4 a) Propagation of light; b) Complexity of system

Quantum optics is a broad field that studies the interaction between light (photons) and materials, including the photoelectric effect. When light interacts with the surface of a material, it can lead to phenomena such as reflection, refraction, and polarization. Understanding the efficiency of optical systems requires knowledge of electromagnetic optics. Wave optics allows us to analyse the intensity distribution, design cameras, and determine resolution capabilities, although efficiency must be directly addressed. This analysis plays a crucial role in assessing the quality of images. On the other hand, ray optics simplifies light as rays and provides a simpler model. Geometrical optics has limitations due to diffraction effects.

Ray-optics or geometric optics: Light follows two fundamental laws of propagation: reflection and refraction. The angle of incidence is equal to the angle of reflection (Equation 2). Refraction occurs when the refracted ray lies in the plane of incidence, and Snell's law determines its angle (Figure 5).

$$\vartheta_r = \vartheta_i$$
$$n_t \sin \vartheta_t = n_i \sin \vartheta_i$$

Equation 2 Reflection, Refraction and diffraction
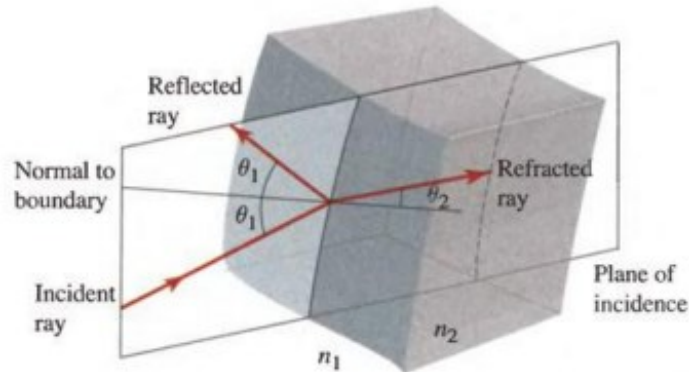
Figure 5 Snell's low

Light follows two fundamental laws of propagation: reflection and refraction. The angle of incidence is equal to the angle of reflection in the process of reflection. Refraction occurs when the refracted ray lies in the plane of incidence, and Snell's law determines its angle. It neglects the wave nature of light and assumes straight-line propagation. Factors like Root Mean Square (RMS) blur diameter, encircled energy, and RMS wavefront error determine image quality. First-order specifications include wavelength, field of view, focal length, entrance pupil diameter, and f-number (Figure 6). The f-number, also known as the focal ratio or f-stop, represents the light-gathering capability of an optical system. It is calculated by dividing the system's focal length by the diameter of the entrance pupil. A lower f-number indicates a larger aperture and allows more light to enter, while a higher f-number corresponds to a smaller aperture and reduced light intake. The f-number is crucial in determining the depth of field, diffraction, and exposure in photography.
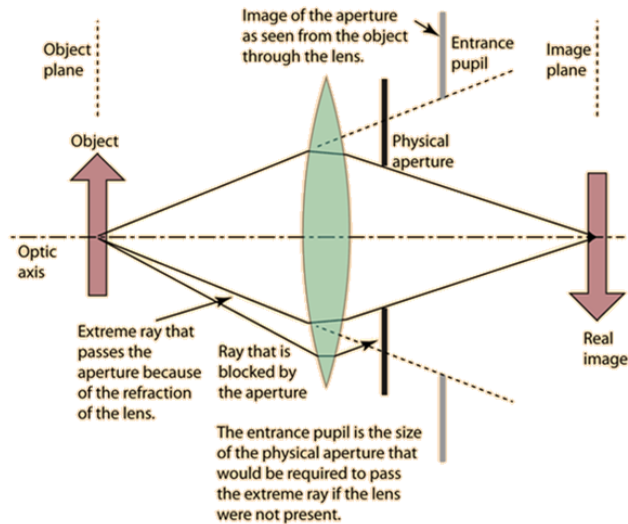
Figure 6 Lens and ray optics scheme

The field of view (FOV) refers to the observable area seen through the human eye or an optical device. It represents the maximum area captured by the device and is measured horizontally, vertically, and diagonally. The sensor size and focal length of the camera lens influence the FOV. A fixed focal length lens allows for different working distances to obtain varying sizes of FOV, while the lens's focal length determines the angular FOV (AFOV) and overall FOV (Figure 7).
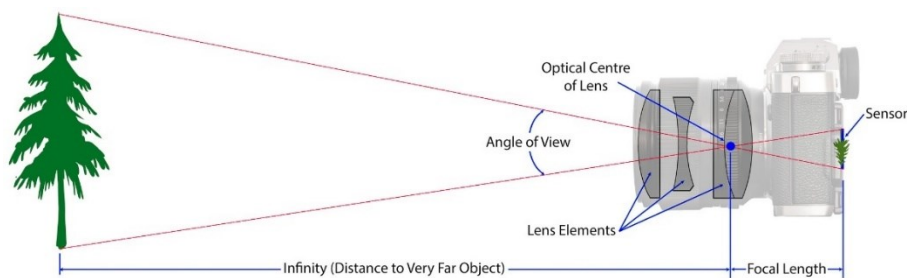
Figure 7 Field of View of camera lens

Shorter focal length lenses may exhibit higher distortion and generally perform less than longer focal length lenses. They may need to provide adequate coverage for medium to large sensor sizes. An ideal sensor should have specific characteristics, including the absence of geometric aberration and the ability to collect photons with 100% efficiency.

Depending on the specific applications, complex geometries have traditionally been characterised through manual measurements, which are susceptible to errors and involve significant labour and time costs. As a result, there has been a growing interest in developing automated methods that can efficiently and accurately extract object features. While simple techniques like using digital cameras based on CCD or complementary CMOS sensors have been employed to estimate specific properties like height or volume, they have limitations in capturing detailed geometric characteristics, especially in agricultural applications where vegetative organs may overlap. To acquire a comprehensive understanding of geometry, 3D measurements techniques are required.

1.2 3D Measurements Technique

The specific application often determines the selection of technology. Equally significant are the essential characteristics required for a successful implementation, such as execution speed, accuracy, repeatability, and integration costs. All 3D scanning techniques yield a point cloud consisting of individual points in 3D space with X, Y, and Z coordinates. The spatial resolution and accuracy of these coordinates and the inclusion of intensity or colour information depend on the measuring device used. Also, resolution refers to the minimum point-to-point distance, known as the sampling distance. At the same time, accuracy represents the difference between the measured and real (reference) objects in terms of point clouds.

Various techniques available for performing 3D scans, can be categorized into different technologies. Figure 8 provides a classification of 3D measuring techniques, highlighting two main categories: active illumination-based and passive approaches. Active illumination refers to sensors that use an active light emitter, while passive sensors utilize the environmental light conditions for measurement [12].
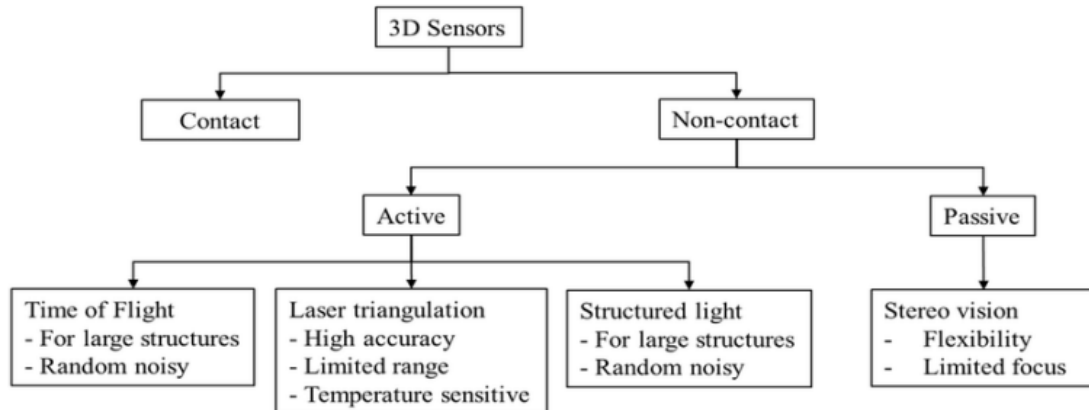
Figure 8 Scheme of 3D sensors

Active techniques may require a more complex setup and calibration, making them better suited for simultaneously conveying large amounts of information and improving their ability to capture complex shapes. These techniques rely on the emission and detection of active signals, which can be affected by ambient conditions and may have limitations in outdoor environments. On the other hand, laser triangulation and structured light techniques provide an in-depth, conceptual understanding of the measured objects. They allow for capturing colour information, stimulating critical and divergent thinking, and offering high speed, resolution, and accuracy [13]. These active techniques are suitable for capturing detailed surface information and are portable for various scanning environments.

Passive techniques, such as photogrammetry, Structure from Motion (SfM), and depth cameras, are not affected by lighting conditions and can provide accurate measurements. The amount of information captured simultaneously allows them to offer a better framework for multisensory learning experiences. Additionally, they are often low-cost and provide simultaneous colour information. However, passive techniques may not accurately capture colour information, and the resolution may be lower than active techniques e.g., Light Detection and Ranging (LiDAR) [14]. These techniques may require more computational processing for data reconstruction and may need to be improved in capturing complex surface details or measuring transparent or reflective objects [15].

These measurement methods have been extensively studied in the literature regarding performance, cost and applications. Here the main techniques used and applications are shown.

Photogrammetry (PH): Photogrammetry is a technique that identifies physical objects' and environments' shape and position by analysing and interpreting photographs.

Triangulation is a fundamental process in photogrammetry used to calculate the 3D coordinates of a point by examining its projections in multiple images. The process requires knowledge of the camera parameters and the correspondence of image points across multiple views. Each image point corresponds to a line in 3D space, and the intersection of these lines determines the 3D location of the point. However, measurement inaccuracies, noise, and other factors can lead to deviations, and the goal is to find the 3D point that best fits the measured image points. Photogrammetry often uses feature extractors, such as corners or interest points, to identify corresponding image points for triangulation [16] [17] [18].

Figure 9 show a result of a survey with aero photogrammetric techniques of Villa Capitini, Perugia, Italy. The aim of this study was to analyse and understand aero photogrammetric survey techniques in order to develop an architectural project for Villa Capitini (Figure 9).
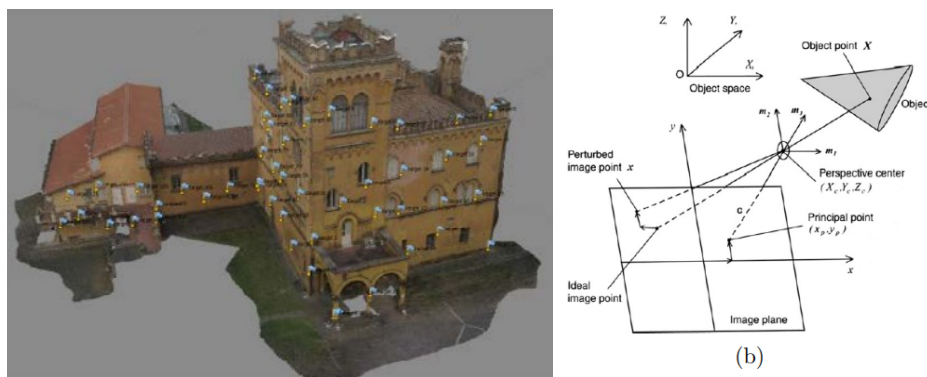
Figure 9 (a) Principle of photogrammetric measurement [18]; (b) perspective projection from the 3D object space to the 2D image plane [17].

Determining an object's shape and position in close-range 3D modelling involves reconstructing bundles of rays defined by each camera's perspective

centre. Stereo-photogrammetry uses two images, while multi-image photogrammetry can involve unlimited images. Interior orientation parameters, including the perspective centre and image distortion, describe a camera's internal geometry. Exterior orientation parameters determine the camera's position and orientation in the global coordinate system. The collinearity equations establish the relationship between 3D object coordinates, and 2D image coordinates. The close-range photogrammetric workflow includes image acquisition, camera calibration, image orientation, point measurement, point cloud generation, surface generation, and texturing [19] [20]. Reliable software packages facilitate scene modelling, but challenges remain in creating accurate and realistic 3D models. Incorrect parameter recovery can lead to distorted results [8] [21] [22] .

In Figure 10 and Figure 11, two different applications in small object (maximum length 30 mm) are showed. Two works were performed at University of Perugia.   In particular Figure 10 show a reconstruction of shape by photogrammetric techniques of a 3D printed part in order to test know the potential application in 3D printing. Figure 11 shows a mechanical application, the aim was to evaluate the curvature radius of a blade.
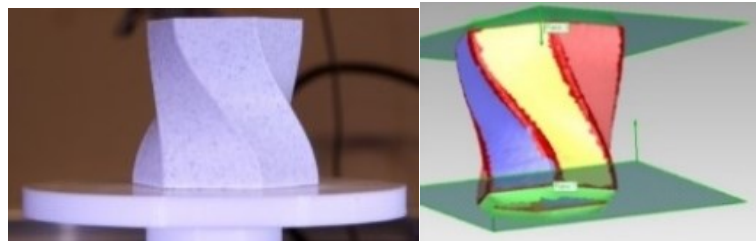
Figure 10 3D printed part reconstructed by Photogrammetry techniques
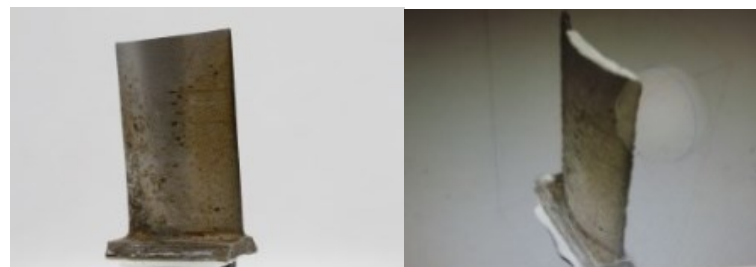
Figure 11 metal blade part reconstructed by Photogrammetry techniques

The processing time can be significantly prolonged, especially when dealing with many captured images. Consequently, photogrammetry remains a specialized field that requires extensive knowledge and substantial experience to achieve high-quality and comprehensive 3D models [23]. Moreover, it exhibits limitations in real-time applications [23].

Both photogrammetry and stereovision leverage the principle of triangulation to determine the 3D position of a point by analyzing its projections in multiple images or views. Photogrammetry typically focuses on reconstructing the 3D structure of a scene from images, while stereovision uses multiple cameras to extract depth information and create a 3D representation of the environment.

Stereo vision (SV) is a photogrammetric technique that captures 3D information about a scene or object using two monocular cameras. In stereovision, a point's depth or 3D position estimation is achieved through triangulation. Triangulation involves identifying corresponding points in two or more images acquired from distinct viewpoints. By knowing the relative positions and orientations of the cameras, the system estimates the depth of a point based on the disparities between the corresponding image points. The depth calculation involves triangulating the corresponding image points to determine their intersection in 3D space, estimating the point's depth or distance from the cameras. (Figure 12).
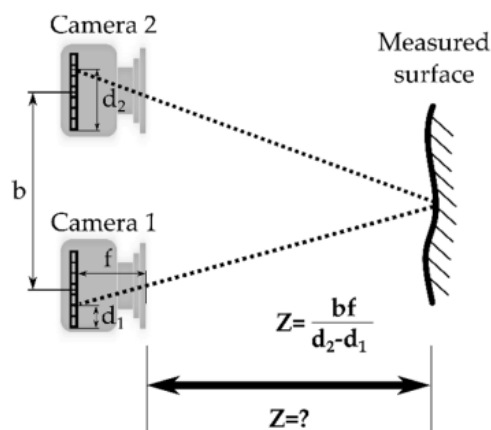
Figure 12 Schematic representation of stereo vision (right) triangulation. "Z", depth; "b", baseline length; "d", position of the incoming light beam on the image sensor; and "f", focal length.

The process includes camera calibration, stereo rectification, stereo matching, and point cloud reconstruction. SV generates high-resolution 3D point clouds and is beneficial for real-time applications. However, it requires prior calibration and is influenced by the robustness of stereo-matching algorithms and lighting conditions. The use of SV in real-time applications has been made possible by the development of faster processors and the introduction of affordable stereo cameras in recent years [24]. Stereovision and Structure from Motion (SfM) measurements are unaffected by lighting conditions, but they do not capture color information.

Structure from Motion (SfM): The combination of Structure from Motion (SfM) and multi-view stereo (MVS) techniques enables the creation of 3D point clouds using a series of images taken from different perspectives. Unlike Stereo Vision (SV), which uses a single RGB camera, SfM and MVS require moving the camera and capturing multiple images with significant overlap. Using algorithms like SIFT and SURF, the SfM process identifies invariant feature points across multiple images. This results in a sparse 3D point cloud, determination of camera parameters, and estimation of position and orientation. MVS utilizes projective matrices from SfM to generate a dense 3D point cloud with a higher point count. SfM-MVS is a cost-effective method that provides accurate and realistic 3D representations without prior calibration or knowledge of camera position. However, real-time applications face challenges in image acquisition and processing. Large-scale field applications of SfM-MVS struggle with automatic image systems and addressing variations in object position between images (e.g., in the case of 3D plant reconstructions where the position can vary from two images because of wind).

Computed Tomography (CT): High-resolution X-ray computed tomography (HRCT) and nuclear magnetic resonance imaging (MRI) offer alternative perspectives on spatial resolution compared to techniques used in medicine and industry. HRCT and MRI allow non-invasive visualization of various complex structures, such as plant, human, and mechanical parts, e.g., trabecular structures, for aerospace applications. MRI relies on water content to determine pixel intensity, while HRCT is more suitable for objects with low moisture content. Both techniques provide digital output for 3D visualizations and precise measurements. The tomograph is made up of a radiogen tube that generates the X-rays that hit the sample and are absorbed by it, the beam that is able to pass through the body is impressed on the detector (Figure 13 a).
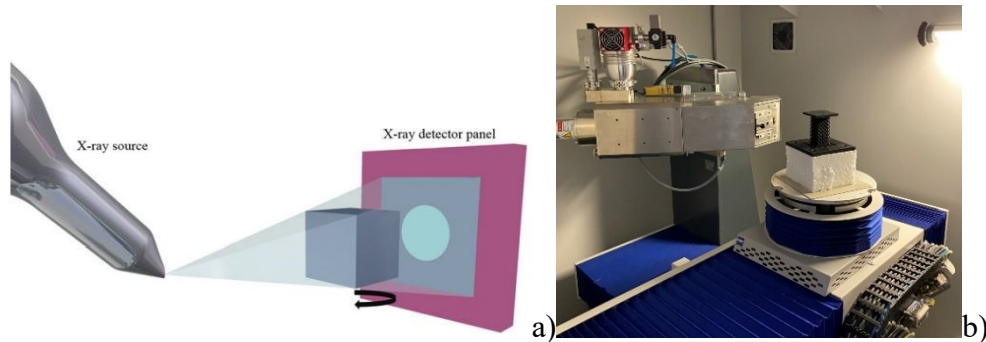
Figure 13 a) CT scan scheme b) Zeiss Metromom 1500 CT scanner.

Figure 13 shows an example of CT scanning Zeiss Metromom 1500 used to analyse trabecular structures for aerospace applications performed in a study with the University of Perugia, Italy. The objective was to evaluate the displacement measurements by tomographic analysis on trabecular structures made in additive manufacturing (AM) used in aerospace (Figure 14). In this case, the scanning times were very long, especially for the scanning of metal parts, where it can take up to 12 hours. In order to check the displacements, the specimen had to be loaded with weight. Since a high load is needed to load a titanium specimen, and the machine has a weight limitation, the specimen's geometry was printed in polylactic acid (PLA).
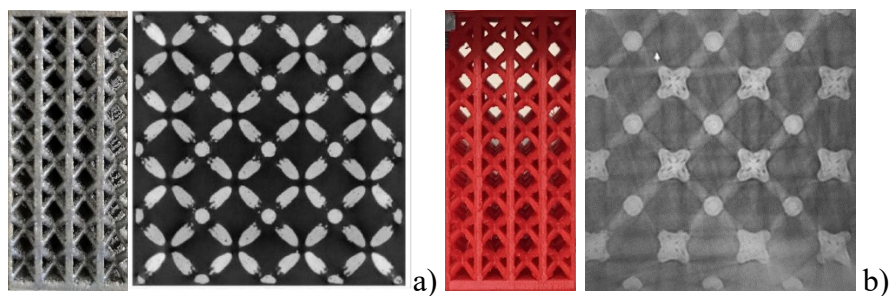
Figure 14 Trabecular structure 3D printed a) in AlSi10Mg and section b) Trabecular structure 3D printed in PLA and section.

However, HRCT poses health risks and cannot be used in vivo. Limitations of these techniques include size restrictions, cost, acquisition time, challenges in field applications, and potential health risks. HRCT and MRI have applications beyond agriculture, such as in medicine for diagnosing and treating various conditions.

Laser Imaging Detection and Ranging (LiDAR): The advancement of commercial devices like smartphones and tablets has facilitated rapid scanning capabilities with LiDAR technology [25]. LiDAR technology, known for its complexity, is widely recognized for its ability to extract valuable and relevant information from the environment. This technology measures light travel time to extract valuable information from the environment. In LiDAR, light signals are emitted, the returning wavefront is measured, and distance is estimated by analysing the speed at which the signal propagates. LiDAR sensors can be classified as 1-D, 2-D, or 3-D [26], depending on their scan dimensions. These sensors employ infrared lasers to measure distances and can be solid-state or incorporate moving components such as rotating mirrors [27]. The unprocessed data acquired from the sensors are initially stored in a polar format and can be transformed into Cartesian coordinates later. Precise positioning systems like Simultaneous Localization and Mapping (SLAM), Inertial Measurement Unit (IMU), and Global Navigation Satellite System (GNSS) are used to record scans and determine the sensor's position [28] [29]. SLAM algorithms and IMU sensors are essential in estimating movement and generating accurate 3D point clouds [30]. Integrating with GNSS systems enhances the overall accuracy of the measurements. It is crucial to consider accuracy and performance since laser beam interception can affect distance measurements [31]. A comprehensive understanding of laser beam dimensions and carefully selecting the appropriate sensors are vital in addressing these challenges [32] [33] [34].

In general, the distance to the object and the angular movement of the sensor are crucial to obtain accurate volume estimates. All procedures for volume estimation should incorporate additional devices to control or estimate and correct the measurements.

Terrestrial laser Scanner (TLS): Directly comparing these systems is challenging due to differences in technical specifications and measurement principles. Laser scanning systems often use mechanical deflection mechanisms and one-dimensional measurement techniques to scan in various directions. Terrestrial laser scanners have diverse applications, categorised based on measurement principles and technical specifications [35], [36]. Different measurement principles include the Time of Flight, Phase Difference, and Optical Triangulation, each with specific ranges and accuracies. Technical specifications such as scanning speed, field of view, and spatial resolution are crucial for system

selection. Comprehensive investigation procedures are yet to be developed, but individual tests provide insights into system performance [37]. Categorising laser scanners based on measurement principles or technical properties aid users in finding the suitable system for their needs. The integration of additional devices like cameras and Global Positioning System (GPS) enhances system capabilities.

An Example of TLS based scanner is showed in Figure 15. This study was performed with National Research Committee (CNR), Q.f.P. Quality for Passion S.R.L. company and University of Perugia, Italy. Critical analysis of instruments and measurement techniques of the shape of trees was performed of: Terrestrial Laser scanner and Structured Light scanner [38].
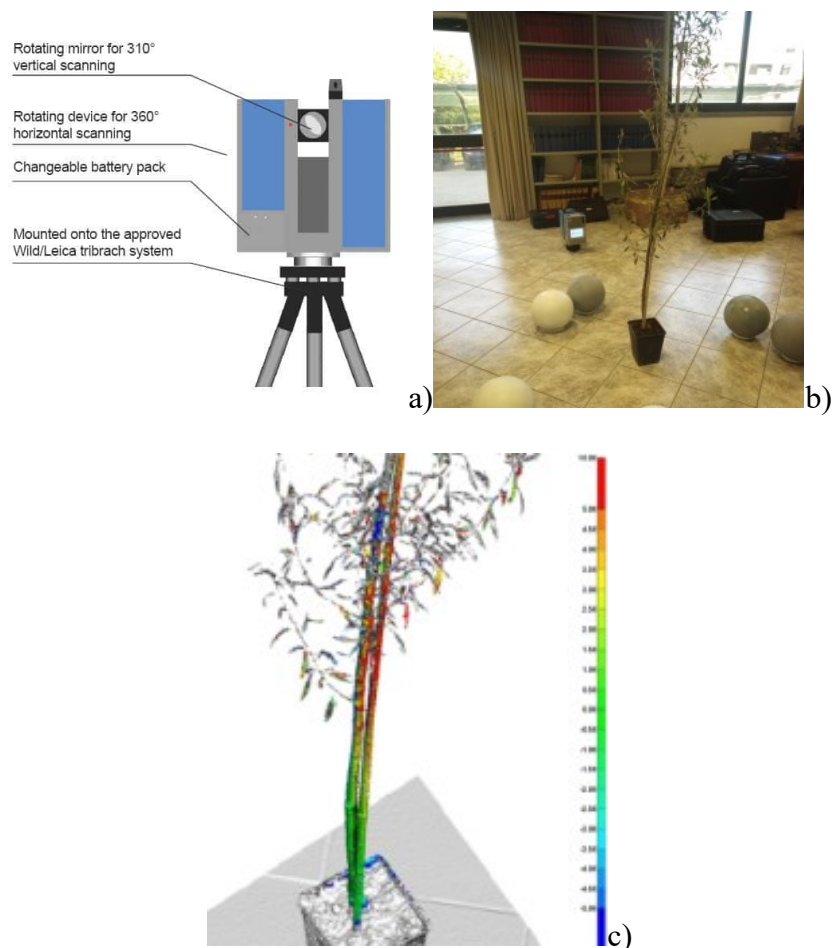
Figure 15 a) Z + F IMAGER 5010X, Zoller + Fröhlich, Germany b) Scanning c) Comparison between Structured Light and TSL scan [38].

The time-of-flight scanner measures the time interval between the emission of the laser pulse and its return to the sensor. The distance to the object is obtained by multiplying the speed of light by half of this time interval Figure 16. One benefit of these systems is their capability to employ high-energy pulses within a brief time interval, mitigating the impact of background noise. However, to obtain accurate measurements, short pulses must be used, which can only carry a small amount of energy. However, distance accuracy usually is higher in phase difference.
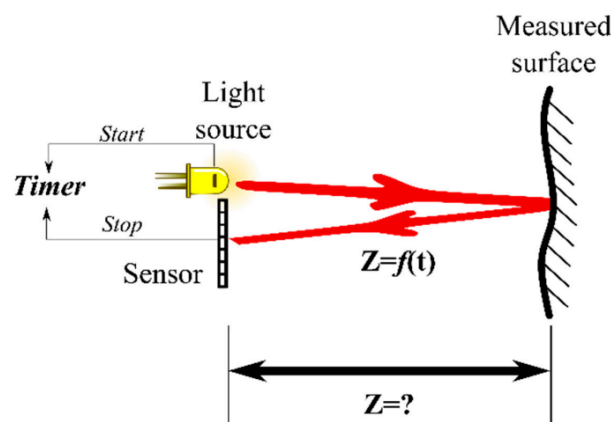
Figure 16 Schematic representation of the basic principle of time-of-flight measurement, where distance "Z" is dependent on the time "t" that takes a light pulse to travel.

In this case, a Phase Difference scanner was used. These scanners, which utilize a modulated laser beam with a harmonic wave reflected from the object's surface, have advantages and disadvantages. On the pro side, these scanners accurately determine the phase difference between emitted and received light, enabling precise distance measurements. The scanners utilize mirrors that rotate horizontally and vertically, enabling scanning in various directions. The scanners obtain coordinates transformed into Cartesian coordinates by measuring polar angles and distances. However, there are limitations. The range can be constrained by the power of the reflected light, potentially affecting long-distance measurements. Additionally, the scanners require mechanical components for rotation, which may introduce complexity and potential mechanical failures [39].

Laser Sheet: A variant of laser triangulation is the projection of a laser sheet obtained with a light plane. The intersection of the light plane with the object's surface generates a profile that allows for the simultaneous calculation of depth

values for a large set of points from a single image, speeding up the acquisition process. By creating multiple profiles, the shape of a surface can be measured. The laser sheet consists of aligned points forming a segment. This can be generated by pointing a laser beam at a rotating or oscillating mirror or through a cylindrical lens that produces a continuous laser sheet. Mechanical movement in the x-y plane is required to acquire an area or surface of a target using laser sheet sensors, with the camera making measurements along the y-axis by observing the laser emitter's projection on the target along the x-axis. This procedure enables the determination of multiple points on the measurement surface, and triangulation is used to calculate distances. By scanning the sheet in various directions, multiple profiles are obtained, allowing for the digitisation of a surface and measurement of coordinates in three dimensions.

Figure 17 3D printed leaf scanned with SCANTECH (HANGZHOU) CO., LTD. show a 3D printed leafe with 3D system, mjp 250 plus and scanned with SIMSCAN 3D scanner by SCANTECH (HANGZHOU) CO., LTD.
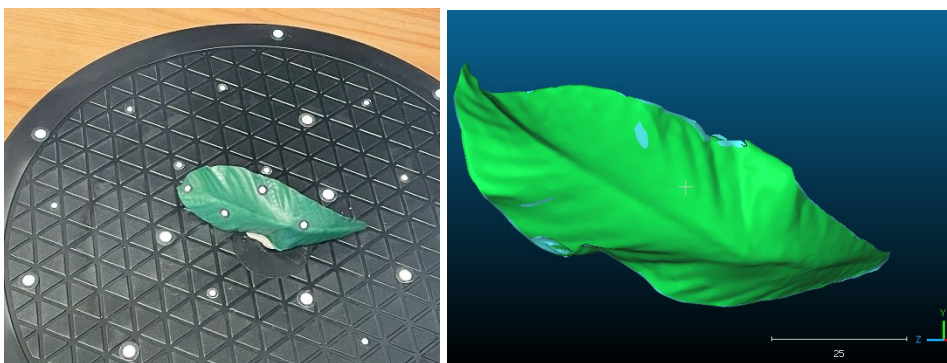
Figure 17 3D printed leaf scanned with SCANTECH (HANGZHOU) CO., LTD.

These scanners offer fast and straightforward operation and instant generation of point clouds. They can measure objects, making them suitable for reverse engineering and small object reproduction applications. However, limitations exist, including occlusion and reflection or absorption of light, which can affect performance. The range of measurement and resolution depends on the angle between the camera and the laser and is limited. Laser sheets have advantages such as adaptability to small targets, high precision, and the ability to measure various materials, including in dark or illuminated environments. However, potential risks

to the human eye, performance dependence on the illuminated material, and the need for object and laser-camera movement can be disadvantages.

Structured Light Sensors (SL): An accurate technique developed in recent years based on these measurements techniques is Structured Light (SL) is also one of the most reliable [39].Structured Light scanners are recognised for their accuracy, reliability, and advantages. SL utilises a projector to emit a known light pattern that distorts upon hitting the object. This distortion generates a disparity map captured by a camera, enabling distance determination. Similar to stereo vision, SL calculates distances using baseline separation. It is an active stereo vision technique based on the emission of a known light pattern by a projector that is distorted when hitting a target, generating a disparity map that is captured by a camera. The distance is determined by applying the same procedure as in stereo vision except that, in this case, the baseline is equal to the separation between the projector and the camera (Figure 18 Schematic representation of light beam triangulation. "Z", depth; "b", baseline length; "d", position of the incoming light beam on the image sensor; and "f", focal length.
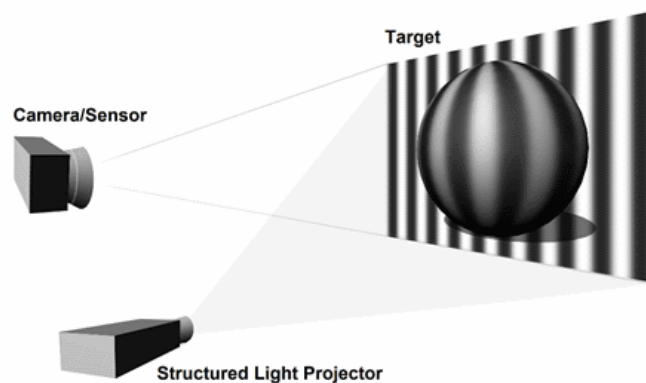
Figure 18 Schematic representation of light beam triangulation. "Z", depth; "b", baseline length; "d", position of the incoming light beam on the image sensor; and "f", focal length.

Unlike laser triangulation, SL projects fringe patterns onto the surface, capturing the entire area in one scan. SL scanners offer fast scanning and low power consumption. However, SL scanners have limitations. They have a shorter range, typically 0.8 to 4 meters, making them suitable for short-range applications. SL technology is primarily designed for indoor conditions and may lose depth data

under direct sunlight. Nevertheless, SL scanners perform well in low-light conditions. Nighttime scanning can provide deep images, but colour information may degrade.

An application performed in collaboration with Illinois University, in aero spatial filed is showed in Figure 19. The scans were performed in a tunnel wind "Raffaele belli" in University of Perugia. The aim was to compare the deformation of the shape of a NASA's new parachute with different wind speed. Another application in wind tunnel is showed in Figure 20. In this case the aim was to reconstruct the scape of helmet for wind analysis with. In Figure 21 a body part was scanned with structured light systems in order to reconstruct a prothesis. This work was conducted with University of Torino (PoliTo), University of Brescia Measurements group (MMTBis) and with Semidoro Orthopaedic Clinic, in Perugia.

Figure 19 Parachute scanned with Structured Light system
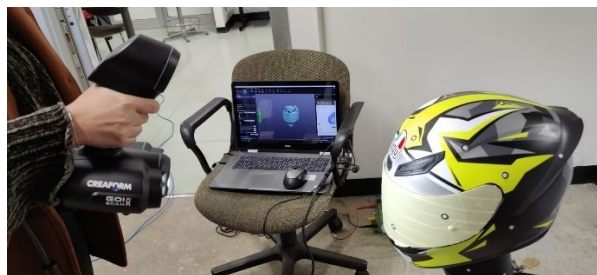
Figure 20 Helmet scanned with Structured Light system
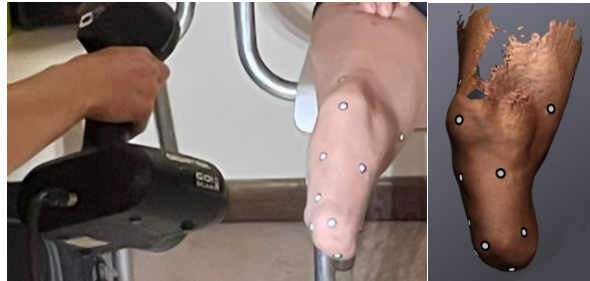
Figure 21 Body part scanned with Structured Light system

Comparing structured light to laser scanners, each has its advantages and limitations. Laser scanners based on triangulation offer high resolution and accuracy by projecting laser lines or dots. They are versatile and widely used in various fields. However, laser scanners face challenges with surface properties and require precise positioning. Ambient light levels can affect scanning quality.

In summary, Structured Light scanners provide accurate and reliable scanning with fast capture times and colour information. They require minimal positioning targets and have power consumption advantages. However, they have a shorter range, are sensitive to lighting conditions, and may experience colour degradation. Project requirements and factors such as scanning range, surface properties, and environmental conditions determine the appropriate choice between Structured Light and laser scanners.

RGB-D sensors: RGB-D cameras, also known as RGB Depth cameras or depth cameras, are imaging devices that simultaneously capture colours Red, Blue and Green (RGB) and depth (D) information of a scene or object using IR laser projector, an IR CMOS sensor [40] [41]. These cameras provide depth data in addition to the traditional RGB images, enabling the creation of 3D representations and accurate measurements. The functioning of RGB-D cameras can be based on different technologies, such as Structured Light or Time of Flight (ToF). The popularity of RGB-D cameras has grown rapidly in various research fields because of their capability to capture real-time 3D colour images, compact design, and affordability. [42].

In Figure 22 a biomedical application of RGB-D camera Azure Kinect is showed. The amiss was to reconstruct the human body with low-cost sensors, compared with Structured Light System. The Image is nosily but is well reconstructed.
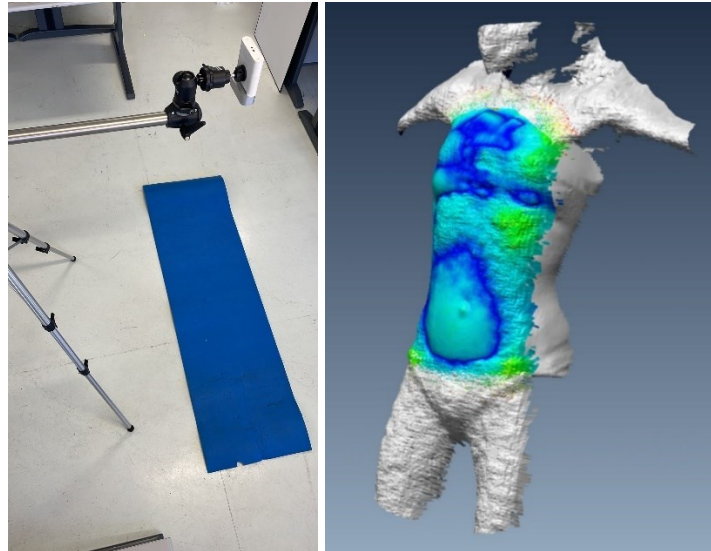
Figure 22 Scan of Body part by Azure Kinect Compared with Structured Light
Scanner GO!Scan 50

RGB-D cameras enable the capture of precise depth information, facilitating accurate 3D reconstruction and precise measurements. This technology can capture real-time depth data, enabling live applications and interactive experiences. RGB-D cameras provide both colour and depth information in a single capture, facilitating the alignment of RGB and depth data. These cameras are used in various fields, including robotics, augmented reality, virtual reality, computer vision, object recognition, 3D scanning, and human-computer interaction. The depth measurement range of RGB-D cameras is typically limited compared to other depth sensing technologies. Additionally, Changes in lighting conditions, especially infrared interference, can affect the accuracy of depth measurements. Moreover, issues related to Occlusion and reflection: Transparent or reflective surfaces can cause difficulties in capturing accurate depth information due to light interference.

In summary, RGB-D cameras simultaneously capture colour and depth information, providing accurate depth measurements and enabling 3D reconstruction. These cameras have various applications but are sensitive to lighting conditions and may have a limited range, but low cost compared to other technologies.

Active Stereo Vision In the current market, there is an emergence of affordable and compact stereo vision sensors (e.g., the Intel RealSense series). Active stereo

cameras are a type of stereo vision camera that actively employ a light source, such as a laser or structured light, to simplify the stereo matching problem and enhance depth perception. These cameras use the concept of triangulation, similar to human binocular vision, to determine depth information by analyzing the disparities between corresponding pixels in the images captured by the two sensors.

In Figure 23 an example of reconstruction of an artificial plant and noise reconstruction by RGB-D Intel Real Sense camera [43] is showed. The study was performed in University of Perugia and aims to determinate the usage of this kind of sensors with complex shape.

Figure 23 Reconstruction of artificial plant using low-cost RGB-D camera Intel Real Sense.

Active stereo cameras excel in low-light environments by employing infrared projectors or other light sources to illuminate the scene actively. This active illumination enhances visibility and enables accurate depth perception. Unlike passive stereo cameras, active stereo cameras can handle non-textured scenes or objects with textureless surfaces, as they flood the scene with structured lighting, thereby providing the necessary details for accurate depth estimation. These cameras can be used as a hybrid technology, combining time-of-flight and stereo triangulation approaches for depth perception. This technology can offer improved accuracy and flexibility in different scenarios. However, active stereo cameras also have some limitations; they can experience reduced effectiveness in direct sunlight or regions with high interference from the same external light sources used for illumination. In summary, active stereo cameras offer advantages such as improved performance in low-light conditions, suitability for non-textured scenes, and the

ability to be used as a hybrid depth-perceiving technology. However, they may be susceptible to interference and come with an additional cost compared to passive stereo cameras, but it is low compared to other technologies.

In conclusion, advancements in data acquisition technologies are anticipated to lead to cost-effective and high-speed solutions, enabling the processing of larger data volumes and delivering enhanced accuracy in results. Currently, different sensors are chosen based on specific requirements. Photogrammetric sensors have limitations due to changes in light conditions, while LiDAR systems are reliable but more expensive and lack colour information. RGB-D cameras offer a low-cost solution with colour and depth images but lower resolution. Other technologies like ToF cameras and SL sensors are still in research. Practical implementation depends on cost-benefit analysis. Photogrammetry has potential with low-resolution cameras. ToF cameras offer high sampling rates for depth data and are more cost-effective than LiDAR and structured ligh systems. ToF cameras have lower resolution and noisy in-depth images. SV provides higher resolution and robustness under sunlight but has higher computational costs. ToF cameras are suitable for measuring targets with non-uniform textures. RGB-D cameras provide colour information while the point density is lower than LiDAR. Real-time acquisition is possible with RGB-D, although the point clouds are less realistic than structure-from-motion (SfM). RGB-D cameras have become a low-cost alternative to LiDAR systems in 3D object characterization. Handling large amounts of data from scanning is challenging, requiring automated systems for processing point cloud files. On-board processing and availability of results after scanning can be improved using artificial intelligence and big data techniques. Deep learning and multi-modal data from RGB-D cameras can enhance neural network performance. However, more datasets are needed to train models for complex geometry characterization.

1.3 Volume evaluation algorithms

With the increase of technologies for the virtual reconstruction of 3D environments and objects, many devices, such as Kinect, Lidar, Real sense, make it possible to acquire a depth image with increasing accuracy and resolution. Several fields, such as mobile robotics [48], reverse prototyping, industrial automation, and land management, require accurate and efficient data processing to extract geometrical features from the real environment, such as distances, areas, and

volume estimations [26]. In particular, the estimation of the volume is an important challenge in many fields [47]. Object volume evaluation based on 3D point cloud data involves shape reconstruction using different methods [49]. The choice of algorithm depends on specific requirements and characteristics, such as the object's complexity (concave, convex shape, thin detail, holes) [52].

Point clouds or meshes are commonly used to represent the volume of a 3D object. However, accurate volume measurement poses several challenges. As explained before, one primary issue is the estimation problem due to overestimation and underestimation in existing methods. The inaccuracies arise from difficulties in boundary detection, noise tolerance, and inadequate methods to accurately fit the shape of complex objects. Some methods may fail to accurately detect the boundary points, especially when these boundaries are not sharp or have a variable density. This can lead to jagged boundaries that deviate from the object's shape. Moreover, issues related to noise tolerance are significant. Noise within a point cloud can significantly affect volume measurements, especially if the model is used in precision-demanding applications. Traditional algorithms may struggle with out-of-plane noise and fail to deliver satisfactory results if the noise exceeds a certain level.

Commercially licensed software like Geomagic Wrap Wrap 2021 Inc. and open-source options like CloudCompare are commonly used for shape reconstruction, analysis, and volume evaluation. Geomagic Wrap is known for its advanced surfacing, measurement accuracy, and automation capabilities, making it preferred in engineering and archaeology. CloudCompare excels in point cloud registration, comparison, filtering, and 2.5D volume calculation, with the advantage of being open-source, flexible, and cost-effective. However, both platforms have limitations in volume calculation for complex geometries. To address these limitations, alternative algorithms, e.g., the Slicing Method, Voxelization, Alpha Shape, and Convex Hull can be employed for shape reconstruction and volume measurements.

[51] reviewed a volume evaluation algorithm such as CH AS and their proposed algorithms. The authors shown the analysis (Figure 24 alpha shape, convex hull and voxelization method [51]..
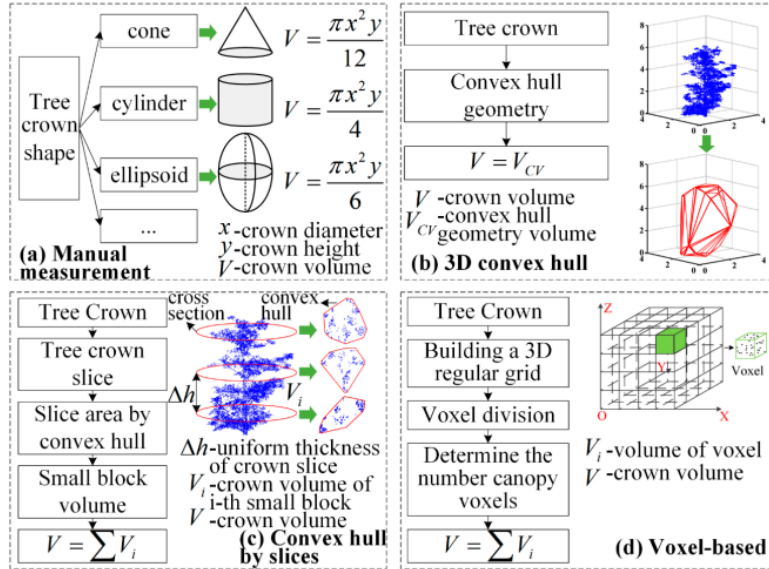
Figure 24 alpha shape, convex hull and voxelization method [51].

The Slicing Method divides a 3D object into 2D slices and estimates volume by summing individual slice volumes. Voxelization partitions the object's volume into voxels, enabling volume approximation by counting voxels. Alpha Shape accurately represents complex and irregular geometries, capturing small details and cavities. Convex Hull provides a compact representation of convex shapes but may oversimplify non-convex or complex objects. These methods offer advantages beyond volume evaluation, facilitating 3D shape reconstruction, deformation measurement, and complex structure analysis in various fields like medical image processing and structural design. While the Slicing Method and voxelization algorithms achieve high accuracy for known and homogeneous solids, they depend on the point cloud quality and are unsuitable for complex shapes. The Slicing Method estimates volume by dividing objects into cross-sections, requiring careful selection of axis, orientation, and slice thickness. Voxelization discretizes objects into a grid of voxels, balancing accuracy and computational efficiency. However, it faces challenges related to voxel resolution, memory requirements, and loss of geometric detail. The Alpha Shape (AS) algorithm reconstructs shapes based on a parameter called the "alpha value," adjusting this parameter makes obtaining a range of shapes acceptable value, from a Convex Hull (CH, for a low alpha value) to a more detailed shape, (for a higher alpha value). Alpha Shape handles complex and irregular geometries with holes and voids but determining the Optimal Alpha Value (AS Opt) can be challenging. Finally, the Convex Hull (CH) algorithm

provides a compact representation of convex shapes and can approximate volume or surface area. However, it may not accurately represent concave or complex shapes, and outliers or noise in the data can affect the results (e.g., overestimating the volume [31], [50]).

Geomagic and CloudCompare are valuable tools for 3D analysis, but they have limitations in volume evaluation for complex geometries. Therefore, exploring alternatives is necessary for more accurate and detailed shape reconstruction and volume measurement of complex geometry (e.g., Alpha Shape, Optimal Alpha Value, and Convex Hull), which is essential in various scientific and industrial applications. As an algorithm for evaluating the volume of images acquired by different scanners, the alpha shape method will be presented in the next section.

1.3.1 Alpha shape

The Alpha Shape Algorithm is a robust approach for estimating the volume of a 3D object from a point cloud. This algorithm mitigates the problem of overestimation and underestimation and addresses the limitations of boundary detection and noise tolerance. The Alpha Shape Algorithm is able to detect boundary points more accurately and naturally, even when the boundaries are not sharp, or the density of the boundary points varies. This results in smoother, more natural boundaries that better represent the object's shape [53]. Moreover, the Alpha Shape Algorithm can tolerate a greater amount of noise compared to other methods. It is particularly robust to out-of-plane noise, capable of producing satisfactory results even when the noise is substantial.

The alpha shape is a specific interpretation within the general notion of shape. In computational geometry, an alpha shape, or α-shape, refers to a family of simple linear curves in the Euclidean plane associated with the shape of a finite number of points. Given a set S of points in either 2D or 3D, it is possible to determine the shape defined by these points. An α-shape edge is drawn between two points if a circle of radius does not contain any other points from the data set, and the two points lie on the circumference of the circle [53]. It is important to note that a convex hull is a specific type of alpha shape. A convex hull is the smallest set of convex edges that can enclose all points. However, not all alpha shapes are convex hulls. The convex hull corresponds to an alpha shape with an infinite alpha valu. Several analogies have been presented in the literature to provide a more intuitive understanding of the alpha shape concept. For example, in 2D, it is possible to think

of the 'rubber' tool [51]. By entering a set of points and setting the tool to a specific size (a circle with a radius of alpha), it is possible to erase all sorts of things without deleting any points (Figure 25 Example of how the edges of the alpha shape are drawn ([53]). Image by Nataraj Akkiraju. Figure 26 Schematic of the 3D alpha shape method. For a given set of discrete points, the alpha shape extracted using the alpha value α (a) and the alpha shape extracted using the alpha value α+ (b). As the alpha value increases (α < α+), the fineness of the extracted alpha shape decreases (red dotted box in (b)). α → ∞ (c), in which the extracted alpha shape is a convex hull [51].).

Figure 25 Example of how the edges of the alpha shape are drawn ([53]). Image by Nataraj Akkiraju.
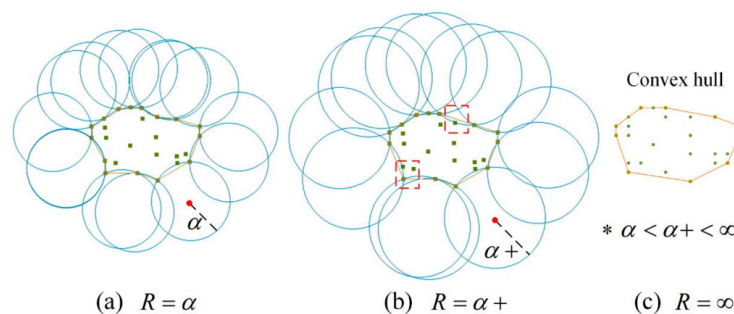
(a) $R = \alpha$ (b) $R = \alpha+$ (c) $R = \infty$

Figure 26 Schematic of the 3D alpha shape method. For a given set of discrete points, the alpha shape extracted using the alpha value α (a) and the alpha shape extracted using the alpha value α+ (b). As the alpha value increases (α < α+), the fineness of the extracted alpha shape decreases (red dotted box in (b)). α → ∞ (c), in which the extracted alpha shape is a convex hull [51].

Returning to the formal definition of the alpha shape, it is worth noting that the parameter determines the level of 'refinement'. A more significant parameter value results in a coarser joining of points, approaching the limit of the convex hull, while

a smaller value connects closer points. Figure 27 illustrates that the convex hull or larger alpha values (Figure 27 b, c, d) occupy a volume equal to or greater than the underlying object's (Figure 27 a). Conversely, very small alpha values lead to underestimating the original volume (Figure 27 f). The alpha shape and the original volumes coincide for a specific optimal value of alpha radius (Figure 27 e). This concept also applies to 3D point clouds.

Going back to the formal definition of the alpha-shape, it can be said that the parameter dictates the level of 'refinement': a very large one joins points more roughly, up to the limit of the convex hull, while a smaller one only joins points closer together. As can be seen in the Figure 27 the convex hull or however large (Figure 27 b, c, d) occupy a volume equal to or greater than that of the underlying object (Figure 27 a). On the other hand, very small alphas underestimate the original volume (Figure 27 f). For a certain optimal volume, the two volumes of the alpha shape and the original, coincide (Figure 27 e). The same concept applies to 3D point clouds.
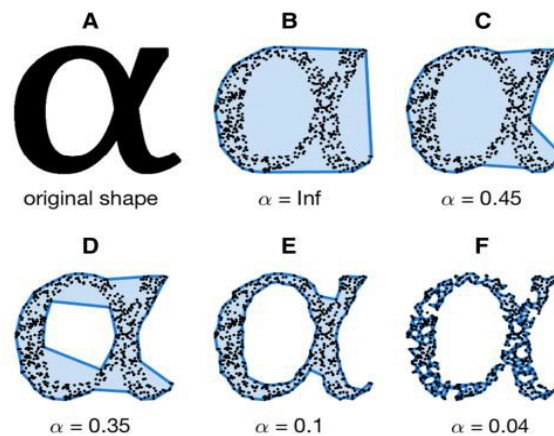
Figure 27 b) A original image, B convex hull, C-E images for decreasing alpha, F alpha too small [55].

The computational cost associated with importing and processing dense point clouds is a significant drawback of the algorithm. Particularly with high-resolution images, these point clouds can be extremely dense, containing hundreds of millions of points. An interesting paradox known as the coastline paradox has been described in the literature by [56]. This paradox highlights that the length of a continental mass's coastline needs to be more well-defined and depends on the measurement method and level of cartographic simplification. Different approximations are available when certain assumptions are made about the minimum size of coastline features. Using a few straight lines to estimate the curve's length will make the result

shorter than the actual length. However, as more lines are used, the estimated sum approaches the true length of the curve (Figure 28). In this case, both methods yield similar values, revealing how the radius Alpha Critical is influenced by the increasing number of points in the cloud. The greater the density of points, the more pronounced this influence becomes. Additionally, there is a correlation between the volume increase and the alpha radius. As alpha increases, the volume also increases.

Figure 28 An example of the coastline paradox. If the coast of Great Britain is measured using units 100 km long, the length of the coast is about 2,800 km. With units of 50 km, the total length is about 3,400 km, about 600 km longer [56].

The situation is similar to the Alpha Shape, where the reconstructed shape and volume vary with the number of points in the cloud [57]. Nonetheless, due to the optimised algorithm, the resulting volumes remain closely aligned even when images with varying numbers of points are used. However, thanks to the optimised algorithm, the resulting volumes remain closely aligned, even when images with different numbers of points are used. To illustrate this concept, the optimal alpha value is calculated using the already optimised algorithm. This is the alpha value that produces a volume that is very similar to the reference volume.

Parameters: In the context of 3D measurements, one of the challenges lies in accurately determining volumes, particularly in identifying the optimal parameters for the task. Before delving into the details of these parameters, it is crucial to establish a clear understanding of the concept of volume. In this context, volume refers to the critical alpha, which represents the alpha radius encompassing all the points forming the final object. For complex objects like trees, the critical alpha

corresponds to the radius that includes all points, resulting in a connected and unified object.

With a reference measurement, it becomes possible to evaluate the 'optimal' alpha that yields a volume closest to the reference volume. However, before illustrating these cases, the parameters used in this algorithm will be introduced:

Alpha shape (A.S.): This algorithm employs Matlab's 'alpha shape' function. It takes the point cloud matrix and the alpha parameter as inputs and returns the surface shape of the object. The volume is subsequently calculated using the 'volume' function.

Critical alpha (C.A.): This function determines the critical alpha radius that induces a noticeable transition in shape. Two types of critical alpha can be specified: 'all-points' and 'one-region'. The 'all-points' option finds the minimum radius that encloses all the points in the point cloud. In contrast, the 'one-region' option determines the minimum radius for which the reconstructed shape contains all points and forms a single region.

Alpha spectrum (A.Sp.): It refers to a vector containing sorted alpha values in descending order, where each value corresponds to a unique shape. The length of the alpha spectrum vector represents the number of distinct shapes that can be generated using different alpha values. It is possible to determine the range of alpha values that produce significant shape variations by examining the alpha spectrum. This information is valuable in selecting appropriate alpha values for reconstructing objects and calculating their respective volumes. The non-uniform distribution of alpha values in the spectrum allows for a more detailed exploration of shape variations by scrolling through the vector with different steps. In summary, the alpha spectrum provides a reference for selecting alpha values that result in distinct shapes and helps capture the complexity and diversity of objects in 3D measurements [55].

In summary, while there are several challenges to measuring volume from a point cloud or mesh, the Alpha Shape Algorithm addresses many of these issues by providing more accurate boundary detection, better noise tolerance, and a more realistic representation of the actual object. It is more accurate, robust, and reliable than many existing methods for volume measurement from point clouds.

1.4 Uncertainty analysis

Evaluation Metrics

One of the challenges encountered in non-contact 3D measurements is the need for standardised procedures for uncertainty estimatio. Standards are pivotal as they provide technical specifications for measuring equipment, typically expressed as maximum permissible error limits. Furthermore, they establish criteria for these technical specifications to determine conformity or non-conformity. In situations where the uncertainty of measurement results hinders decision-making, standards also outline the rules to be adopted. These rules carry both technical and legal-contractual implications by placing the burden of proof of conformity on the manufacturer/supplier and the burden of proof of non-conformity on the purchaser/user. A decision rule is proposed to address any ambiguity arising from uncertainty, ensuring clarity in the interpretation of test results [58]. It is worth noting that adopting different standards is often driven by commercial considerations rather than scientific ones.

In numerous studies, several parameters are employed to analyse the results of 3D measurements. Commonly utilised parameters, as outlined in [59] (Table 1 Metrics for determinate geometry errors [59].), include:

Table 1 Metrics for determinate geometry errors [59].

Term	Meaning	Equation
RMSE	The standard deviation of the prediction residuals	$RMSE = \sqrt{\frac{\sum_{i=1}^{n}(\hat{y}_i - y_i)^2}{n}}$ where $\hat{y}_i$ is the estimated value, y_i is the observed value and n is the sample size
RRMSE	RMSE relative to mean	$RRMSE = \frac{RMSE}{\bar{x}}$
MSE	The average squared errors of prediction residuals	$MSE = \frac{1}{n}\sum_{i=1}^{n}(y_i - \hat{y}_i)^2$
R^2	The proportion of the variance of one variable that can be explained by the variance of the second variable	$R^2 = 1 - \frac{\sum_{i=1}^{n}(y_i - \mu_y)^2}{\sum_{i=1}^{n}(y_i - \hat{y}_i)^2}$ where μ_y is the mean of observed values
MAE	The average of the absolute values of prediction residuals	$MAE = \frac{\sum_{i=1}^{n}|\hat{y}_i - y_i|}{n}$
MAPE	The average of the absolute values of prediction residuals divided by the actual values	$MAPE = \frac{1}{n}\sum_{i=1}^{n}\left|\frac{y_i - \hat{y}_i}{y_i}\right|$
CCC	Interpreted similarly to R^2, but used to compare two methods predictions or to measure repeatability of repeats of a single method	$CCC = \frac{2\rho\sigma_y\sigma_{\hat{y}}}{\sigma_y^2 + \sigma_{\hat{y}}^2 + (\mu_y - \mu_{\hat{y}})^2}$ where σ_y represents the variability of either the observed value or another variable and $\sigma_{\hat{y}}$ and $\mu_{\hat{y}}$ the variability and the mean of either the estimated value or another variable
RCV	The minimal significant difference between temporally different measurements	$RCV = \pm q\sqrt{2\left(\sigma_y^2 + \sigma_{\hat{y}}^2\right)}$ where q is the quantile for the desired probability from a standard normal distribution
MCC	Measures the agreement of binary classifications	$MCC = \frac{TP \times TN - FP \times FN}{\sqrt{(TP+FP)(TP+FN)(TN+FP)(TN+FN)}}$ where TP is true positives, TN is true negatives, FP is false positives and FN is false negatives of binary classification

Root Mean Square Error (RMSE) measures the average deviation between the predicted and actual values, providing an overall error estimate.

Relative RMSE (RRMSE): Similar to RMSE, but normalised by the mean of the actual values, allowing for comparison across different datasets.

Mean Squared Error (MSE): It calculates the average squared difference between predicted and actual values, giving more weight to more significant errors.

Coefficient of determination (R2): It represents the proportion of variance in the dependent variable that can be explained by the independent variable(s).

Mean Absolute Error (MAE): It measures the average absolute difference between predicted and actual values, providing a more robust measure of error.

Mean Absolute Percentage Error (MAPE): Like MAE, but expressed as a percentage of the actual values, allowing for relative comparison.

Lin's Concordance Correlation Coefficient (CCC): It assesses the agreement between two sets of measurements, accounting for accuracy and precision.

Simple Average Ensemble (SAE) combines multiple models or measurements by taking the average, enhancing overall performance and reducing variability.

Reference Change Values (RCV): It indicates the minimum detectable change between two measurements, providing a threshold for significance.

Matthews Correlation Coefficient (MCC): It measures the quality of a binary classification model by considering true positives, true negatives, false positives, and false negatives.

Coefficient of error (CE): It quantifies the relative error in the mean measurement by dividing the standard error of the mean by the mean itself.

Coefficient of variation (CV): It expresses the standard deviation as a percentage of the mean, providing a measure of relative variability within a population.

In summary, the absence of standardised procedures poses a challenge in non-contact 3D measurements. Standards provide technical specifications, criteria for conformity assessment, and guidance for decision-making in the face of uncertainty. Various parameters and metrics, such as RMSE, RRMSE, MSE, R2, MAE, MAPE, CCC, SAE, RCV, and MCC, are commonly employed to analyse the results. The coefficients of error (CE) and variation (CV) aid in characterising population variability. Correction factors like CCC are used for data rectification, while MAPE quantifies deviations from reference objects.

The uncertainty of reconstruction, assessed through the Guide to the Expression of Uncertainty (GUM) [60], aids in calibration studies relative to 3D measuring instruments.

Methodologies for identifying geometry uncertainty.

Two methodologies can be used to determine error function parameters in non-contact 3D measurements. The first is the direct detection method, which utilises dedicated instruments to identify errors. The second is the indirect method, which involves estimating errors by comparing measured values with calibration values of geometric elements from reference samples. Uncertainty analysis, encompassing measurement repeatability (Type A evaluation) and data obtained from non-statistical procedures, is performed according to the guidelines [60]. To evaluate the volume and its uncertainty, the mean value ($\bar{x}$) and standard deviation ($\sigma(x)$) of measurements are determined based on N repetitions under the same acquisition and environmental conditions defined by GUM:

$$\bar{x} = \frac{1}{N} \sum_{k=1}^{N} x_k$$

<div align="right">1. 1</div>

$$\sigma(x) = \sqrt{\frac{1}{N-1} \sum_{k=1}^{N} (x_k - \bar{x})^{\wedge}2}$$

<div align="right">1. 2</div>

The uncertainty due to measurement repeatability is:

$$u_R(\bar{x}) = \frac{\sigma(x)}{\sqrt{N}}$$

<div align="right">1. 3</div>

The difference between these quantities, normalised to the total uncertainty (Eq. 1.3), is measured by the correlation coefficient (R) and the coefficient of determination (R^2). An ideal approximation would hav $R^2 = 1$, meaning that the regression line perfectly represents the trend of the data. If, on the other hand, $R^2 = 0$, the linear approximation cannot be considered correct in terms of the interpretation of the phenomenon. The least-squares linear regression technique approximates the data trend with a straight line, assuming a linear relationship between the dependent and independent variables. However, alternative regression or data transformation techniques may be necessary for non-linear relationships. The correlation coefficient ranges between -1 and +1, indicating the degree of linear

relationship between variables. While discrete data can be analysed using regression techniques to identify trends or determine intermediate values, calibration factors derived from uncertainty analysis enhance volume measurements and provide insights into different 3D scanning methods [60].

In summary, direct detection and indirect estimation can be employed to identify error function parameters in non-contact 3D measurements. Uncertainty analysis accounts for measurement repeatability and non-statistical data, with volume evaluation benefiting from this analysis. The correlation coefficient and coefficient of determination are crucial in assessing data trends and the suitability of linear approximation. Regression techniques analyse discrete data and determine trends or intermediate values. The study compares different 3D scanning methods, utilising a reference measurement to evaluate the volume and derive calibration factors for improved measures.

1.5 Conclusions

3D scanning technology has become a standard tool in many fields. It is used in recent product development and production processes to create highly accurate 3D representations of real-world objects. Over time, 3D scanning technology has revolutionised, resulting in improved accuracy, faster scanning times, and better overall results [12], [13].

Additionally, 3D modelling software allows for precise and complete preservation of the scanned data, although it can be time-consuming for complex items. This technology has proven to be essential in various applications, bringing history back to life and enabling easy access through exact digital reproductions of diverse objects. As 3D scanning continues to advance, it is anticipated to become a requirement for ensuring proper manufacturing processes, reducing the need for physical prototypes, and facilitating accurate measurements before production. The applications of 3D scanning are extensive and diverse. It is widely used in heritage preservation, industry, design, agriculture, reverse engineering, aerospace, and more. Different types of 3D scanning technologies are available, each of them with its advantages and limitations. Contact-based scanners physically touch the object, while non-contact scanners, such as 3D scanners, collect datas without physical interaction. However, complex objects bring challenges for 3D scanning, such as dark, shiny, reflective, or transparent materials and the object's movement (such as

wind affecting outdoor agricultural applications), which may affect the accuracy of the scans.

One significant limitation of modern 3D scanners is their cost. Additional expenses include setup accessories and operator training. While outsourcing 3D scanning services may be more expensive, it can be cost-effective for frequent scanning needs. On the other hand, this has been partly solved with the advancement of new low-cost 3D scanning technologies. It is worth to acknowledge that the choice of 3D scanning technology depends on the specific application and the essential characteristics required, such as execution speed, accuracy, repeatability, and integration costs.

However, one challenge in selecting suitable scanners for different applications is the absence of standardised guidelines governing their use [58], [59], [47]. The studies concern individual applications. This investigation needed a system that could provide an overview of comparing scanners in different applications. Depending on the specific application and the complexity of the geometry that needs to be scanned, users must conduct extensive tests with the scanner to understand its functionality and the uncertainties associated with the reconstruction process [52]. However, the number of studies comparing 3D scanners across different applications is limited [49]. Various authors have evaluated scanner's performances in the existing literature, but most of them have focused on specific applications. There must be a comprehensive framework for applying these scanners in different fields. This thesis aims to explore and compare different scanners with varying performances and costs in diverse areas. It considers explicitly complex geometries and subjects in motion to provide an overview for users of these instruments.

Another challenge lies in reconstructing complex geometries and evaluating volumes. Some advanced software can accurately evaluate the volume of closed shapes, while others can measure the volume of open shapes (with holes) but may overestimate it [52]. Several algorithms have been developed to address this goal, but not all are suitable for reconstructing complex geometries and may have long computation times. Among these algorithms, the alpha shape algorithm is particularly well-suited for complex geometries. However, selecting the optimal alpha value that closely reconstructs the original geometry remains crucial. An alpha shape algorithm has been developed to determine the optimal alpha based on a reference measurement and analyse the uncertainties associated with shape

reconstruction and volume measurement to address this task. In some applications, obtaining a reference or repeating measurements is challenging, particularly when conditions change frequently, such as in a plant environment. In such cases, the developed algorithm allows for volume reconstruction with alpha values analysis and the selection of the optimal alpha. Finally, when the subject being scanned is in motion, like the human body, where no reference or trend is available, a multi-modal scanning approach that integrates different 3D measurement tools is proposed.

Overall, this thesis aims to comprehensively analyse different 3D scanners with varying performances and costs across various applications, considering complex geometries, subject movement, and uncertainties associated with shape reconstruction and volume measurement. The developed algorithms and methodologies advance the understanding and application of 3D scanning in practical scenarios.

Chapter 2

Instrument, Set-up, Digitalization process and Algorithms

This thesis work will involve analysing and utilising 3D scanning techniques and new software. Additionally, the setup employed across various chapters will be discussed to address issues related to different scanning techniques.

In this Chapter, test cases and the digitalisation process will be examined. Filtering, smoothing and methodological processes will be analysed to achieve the final shape. In the digitalisation process, potential filters and smoothing are evaluated to reconstruct the final geometry that heavily depends on the operator.

The thesis work will include a photogrammetric techniques analysis to assess the uncertainty in reconstruction, which depend on factors such as picture percentage overlapping, acquisition time, computational time, and the resolution of 3D point clouds influenced by the choice of scanners [59]. In particular, as mentioned in Chapter 1, establishing the appropriate level of precision required by users presents an intricate dilemma, as it varies depending on specific use cases and the operational costs of individual commercial enterprises [60]. Key challenges include 3D scanning sensors and systems issues, the absence of standardised methods, and geometric complexity [58]. The scanning system configuration is crucial since it directly influences the calibration, affecting the digitalisation process. Additionally, variations in light conditions can directly impact the system's performance during tests. For complex geometries, a statistical analysis will be covered in Chapter 5. Some authors discussed dividing those geometries into parts, but computational time and software acknowledgements are needed. In addition, sensors will only evaluate a few elements of complex geometries, particularly thin details, e.g., leaves [61]. The uncertainty of each scanning technique was assessed through a comprehensive literature analysis. This analysis covers cost, timing, and

point cloud resolution. For example, LiDAR is available in both high and low-cost options and produces considerable noise [62], [63]. While RGB-D cameras showed promise in overcoming occlusion issues and restoring porosity in low-cost systems [64]. Lastly, photogrammetry holds the potential for fast processing times at a low cost, although it involves longer computation times [59].

The final analysis presents the developed Alpha shape algorithm. As explained in some research [65], [66], there is a need to find the definition of reference volume in the 3D reconstructed model given by a high-cost 3D scanner [67]. In [68], the authors investigate the uncertainty sensitivity analysis and its impact on the alpha radius for achieving a reference volume (given by a high-resolution scanner). In summary, in Chapter 3, a sensitivity analysis using spectrum and alpha-critical parameters is conducted to give a threshold for choosing the optimal alpha value for shape reconstruction.

Optical, LiDAR and RGB-D camera systems were used among the measurement techniques seen before in particular the instrument used are: Structured Light scanner (SL), LiDAR scanners, photo camera with CCD and CMOS sensors for photogrammetry (Ph) and RGB-D sensors distinguishing two categories: based on high or low value of cost and resolution. These differences are related in particular on professionality of scanner. This section will present the different instruments used in this work, the digitalization process and algorithms used. Then, in Chapter 4, it will be highlighted examples of applications within the fields of different sensors are tested during experimental case studies, carried out in different field: Cultural Heritage (CH), Biomedicine (B), Design (D), Sport Training (ST) and Agriculture (A).

2.1 Instruments

(SL): The Go!SCAN 50 (15k€) is a hand-held scanner based on structured light with high speed. In total, this scanner uses three cameras positioned at various angles and depths. In the centre of the device, an RGB camera is installed surrounded by LED flashlight to capture textures without the need for special light setup. The scanner works at a rate of 550000 measurements per second, covering a scanning area of 380×380 mm with a resolution of 0.5 mm and a point accuracy up to 0.1 mm. A lamp guidance system helps to set the scanning distance between 0.3 and 3.0 m. The surface is captured while moving the hand-held scanner over the

object. Moreover, it is possible to reduce the noise arising from movement, by setting the appropriate parameters on the acquisition software (VX Element by Creaform, v. 0.9) [61]. The Go!SCAN 50 is the only certified instrument among those used for this work; for this reason, the respective reconstructed 3D geometries have been considered as the most accurate and used as reference to evaluate the uncertanty of the other techniques [62] [63].

(L1_High): BMS3D-HD Backpack mobile scanner by VIAmetris is a portable scanner for indoor, outdoor and underground scanning. Designed for fast and accurate data capture, it can be used in both pedestrian and motorized ways. The panel of applications is vast, ranging from land surveying and construction sites to facilities management or precision agriculture. The accuracy is about one centimetre relative, up to 50 km/h of continuous capture, 30 Mega pixels high-resolution 360º images. Performance: Dual LiDARs architecture 1 x 320,000 points per second, 1 x 640,000 points per second, Camera with 15 pictures per second. The bMS3D is a versatile solution, for indoor, outdoor or even underground scanning. It has been designed for fast and accurate environment data capture. The system is built around a 30Mpx panoramic camera, two 300.000 pts/sec VLP16 LiDAR, an onboard Central Unit, an IMU and a GNSS receiver. The proprietary software used for post-processing is PPiMMS. that automatically corrects drifts to compute precise and dense 3D point clouds. This system is based on SLAM algorithm, this has allowed a lot of mapping applications.

(L2_Low): The iPad Pro LiDAR scanner is a pulsed laser able to capture surroundings up to 5 m through a photon-level reading since it works at time of flight, the time required for data acquisition is strictly related to the speed of light and distance. Apple itself does not specify the accuracy of the respective technologies or hardware [25]. This tool allows scanning objects and exporting scans as 3D textured CAD models. The scanning resolution used for our applications was 0.2 mm. The scanning time for a particular subject varies from operator to operator since using each scanner is an acquired skill. In general, scanning could take about 15 min depending on the desired accuracy level of the resulting scan [14]. As a rule of thumb, the fastest technique is the LiDAR scanning and the slowest one is the SL system.

(Ph1_High): The Canon Eos 7d is equipped with a CMOS 18 Megapixel sensor (5184x3456 pixels). In this work it mounts a 24-millimeter lens. Each image is

taken manually with fixed exposure from 0.85 meters with respect to the plants, the acquisition time required 15 minutes. An overlapping of 80% is maintained between each image, resulting in a total of 60 photos per each session. The scanning time is comparable to that of the LiDAR system. The post processing time required about 2 hours.

(Ph2_Low): The automated 3D-printed scanner is based on an Arduino Uno board. The robot mounts a low-cost Aukey full HD camera, (1920x1080 pixels). The Arduino board drives two stepper motors, one dedicated to the movement of the robot along the plants row, running on a cog track, one to control the camera. In this work, the robot is programmed to proceed with steps of 0.15 meters along the plants row and take five photographs each 18 degrees, to cover a total of 90 degrees, perpendicular to the proceeding direction, allowing to have a set of 300 photos, with an overlapping of 90%. The optimal distance between the track and the plants row is 0.85 meters, while the distance of the camera from the ground is 0.15 meters. Each photo acquisition session took about 30 minutes but can be easily reduced by one third by optimizing the downtime between the various robot operations. In Chapter 6, the low-cost photogrammetric scanning system will be shown. The post processing time required about 10 minutes (Figure 30).
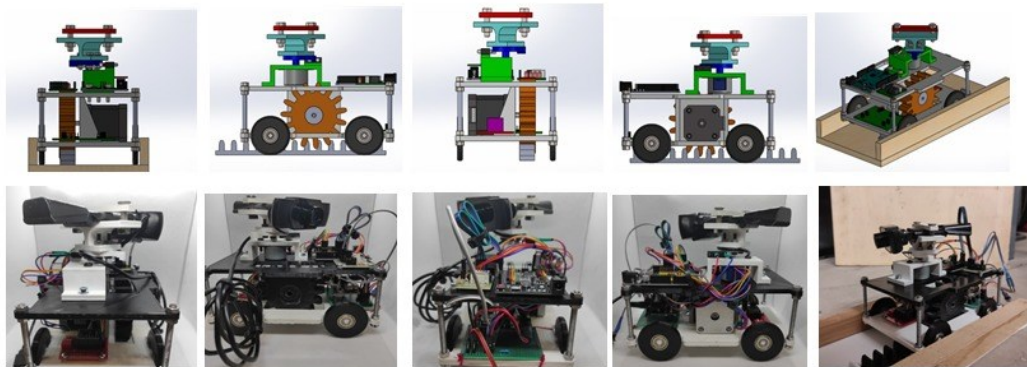
Figure 29 Automated 3D printed scanner

(Ph3_Low): For this application a commercial smartphone Redmi Note 10 with an average cost of 190 € was used. It is equipped with a duo camera system dedicated for commercial use. Its technology includes a digital stabilizer, 30 fps video speed and Video rec. 4K (2160p). This tool has been paired to Zephyr software (3D Flow, v. Aerial 3.1) in order to obtain a 3D reconstruction. This software uses Structure

from Motion (SfM) algorithms for photogrammetric processing of digital images to create 3D spatial data.
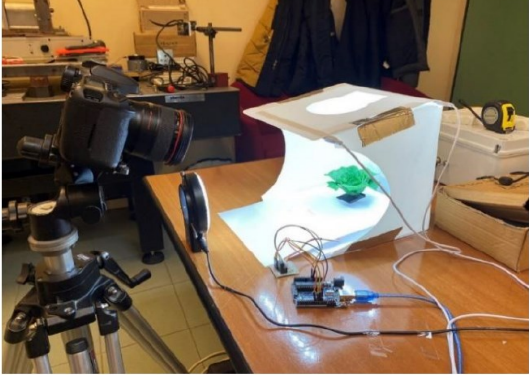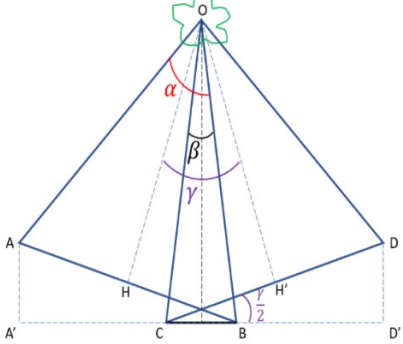
Depending on the application, the data was reconstructed with two high prestation Photogrammetric software: Agisoft Metashape 1.8.4 (3499 €) and Zephyr software 3D Flow, v. Aerial 3.1 (3900 €). The techniques and tools that were chosen from the numerous alternatives on the market in various applications.

(RGB-D Low): In a continuous-wave (CW) time-of-flight (ToF) camera, light from an amplitude modulated light source is backscattered by objects in the camera's field of view, and the phase delay of the amplitude envelope is measured between the emitted and reflected light. This phase difference is translated into a distance value for each pixel in the imaging array. The Azure Kinect (500€) is also based on a CW ToF camera; it uses the image sensor presented in [64]. Unlike Kinect v1 and v2, it supports multiple depth sensing modes and the color camera supports a resolution up to 3840 × 2160 pixels [42], [40].

2.1.1 Photogrammetric technique analysis and volume evaluation by Cloud Compare

In the case of photogrammetric techniques, the minimum ratio overlapping of the picture was analysed. This overlapping percentage of picture was used as test to apply in the real plant, as showed in Chapter 4. The tests were performed on a 3D printed lettuce plant that will be analysed in Paragraph 2.3.2 of this Chapter. The following Table 2 show the set-up of the test bench for acquisitions via Canon. The system consisting of complex geometry + Arduino stepper motor, was placed inside a light box with Light-Emitting Diode (LED) lighting. The acquisition systems were placed at the established distance from the object by supports considering the percentage overlap. Tests were conducted at the following distances: High-cost Canon = 35 cm; Low-cost Webcam = 20 cm. Using Matlab it was also possible to calculate the percentages of overlap obtained with the various acquisition systems as a function of the number of pictures and camera parameters. For the calculation of the overlapping percentage of the images and the setup, the following scheme in Table 2 was considered.

Table 2 Setup and instruments used (Left), Overlapping percentage evaluation (Right).

List of the software used in the different phases of the study:	Calculation of image overlap percentage:
-Arduino Ide: driving stepper motors;	- AB and CD represent two consecutive pixel images;
- Geomagic Wrap: volume and surface evaluation of reference geometry;	- OH and OH' represent the distances between the image and the plan;
- Python: masking process;	- Angle α represents the aperture of the camera;
- Matlab: calculation of image overlap percentage;	- Angle β represents the angle of intersection of the two images;
- Metashape: image processing;	- Angle γ represents the angular step between the two images.
- CloudCompare: point cloud processing;	

To carry out the acquisition, the model was connected to a stepper motor driven by Arduino Uno platform. By means of an Arduino Ide sketch, it was possible to control and varying the rotation angles of the stepper according to the number of acquisitions. In particular, the following parameter was varied in the algorithm: Float degrees = "rotation angle value in degrees; The following degrees of rotation were set for the acquisitions: 5°; 8°; 11°; 30°; 45°. Indicating with *n* the number of photos taken, the angle of overlap β was calculated from the following relation:

$$\beta = (n * \alpha - 360)/n$$

From the knowledge of the distance OH and the size of the image AB, the distance OB e was given, through the calculation of angle β, from geometric considerations, the segment CB was evaluated. Knowing that, according to the bench configuration adopted, the vertical overlap of the images is equal to 100%, the overlap percentage is calculated as the ratio between the segment CB and the

image projection A'B. Through the scaling factor, obtained by measuring the plan support, it is possible to convert from dimensions in pixels to millimetres. Once the set-up phase of the bench was completed, it was possible to proceed with the acquisitions. Each picture was acquired, remotely via computer, to avoid any vibrations would create problems with focusing the image. For the Canon in particular, the EOS Utility 3.11.0, Canon U.S.A., Inc. software was used, while an own developed software using Python was used for the webcam. The following acquisition sequences were carried out:

- Canon: 75 pictures, 48 pictures, 35 pictures, 10 pictures, 8 pictures;

- Webcam: 77 pictures, 48 pictures, 33 pictures, 24 pictures, 16 pictures.

For both cases the lower number of pictures filed the reconstruction, in fact the minimum pictures needed for high-cost sensor is 10. For the webcam the minimum pictures needed for reconstruct the image is 33.

So, Canon with 75, 48, 35 and 10 pictures and Webcam with 77, 48 and 33 photos was used for the analysis.

Table 3 Webcam recontruction varyn number of pictures Table 4 Canon EOS 7D present the results regarding the overlap percentage and processing times achieved by Metashape for both webcam and canon.

Table 3 Webcam recontruction varyn number of pictures

n. of pictures	Time Build Dense Cloud [min]	Points number	% Overlapping	Time [sec]
16	n.c.	n.c.	66.6	n.c.
24	n.c.	n.c.	77.9	n.c.
33	**9.95**	**781055**	**84.0**	**17**
48	18.43	831829	89.0	33
77	58.93	1551510	93.2	86

Where n.c. denotes 'not calculated' due to the unavailability of generated point cloud data. The point cloud reconstruction was achieved solely from 33 webcam-captured images, wherein the percentage of overlap among these images exceeded 80%.

Table 4 Canon EOS 7D

n. of pictures	Time Build Dense Cloud [min]	Points number	% Overlapping	Time [sec]
8	n.c.	n.c.	19.1	n.c.
10	**19.38**	**3226745**	**36.5**	**23**
35	92	4649979	82.4	94
48	161	5185781	87.2	141
75	333	5565596	91.8	249

By employing a Canon camera with its high-resolution capability, it was feasible to reduce the total number of acquired photographs to a mere 10. Correspondingly, this reduction was achieved while maintaining a 36.5% overlap percentage between consecutive images.

On the other hand, utilising a webcam, characterised by a lower resolution, significantly expedited the point cloud generation process in Metashape due to reduced computational time.

In Figure 30 the overlapping percentage in relation to number of pictures are shown.
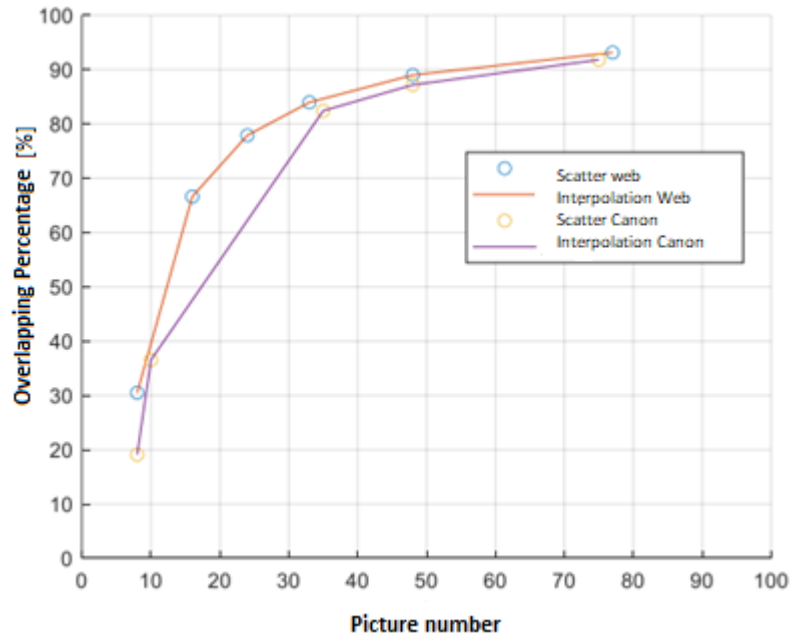
Figure 30 Overlapping Percentage Vs Number of pictures

From this it can be verified that as the number of photos increases, the number of points found in the scattered clouds, in the dense clouds and the processing time while there is an asymptotic trend, with asymptote at 100% for the overlap percentage. The difference between the two overlap curves depends on the type of optics: although the two optics are very different (24 mm for the Canon and 5 mm for the webcam) the two curves remain very close to each other. In particular, in the graphs there is an initial step due to the impossibility of reconstructing the cloud below a minimum number of photos. The exponential step allows the number of photos to be increased up to an optimal value where a good resolution is obtained with low processing times. It is possible to think of increasing the number of photos without worsening the processing times for the low-resolution sensor, while for the high-resolution sensor the increase in time is more abrupt. In Canon with 75 pictures, for example the elaborating time was 400 minutes, in webcam 77 was 100 minutes Figure 31.
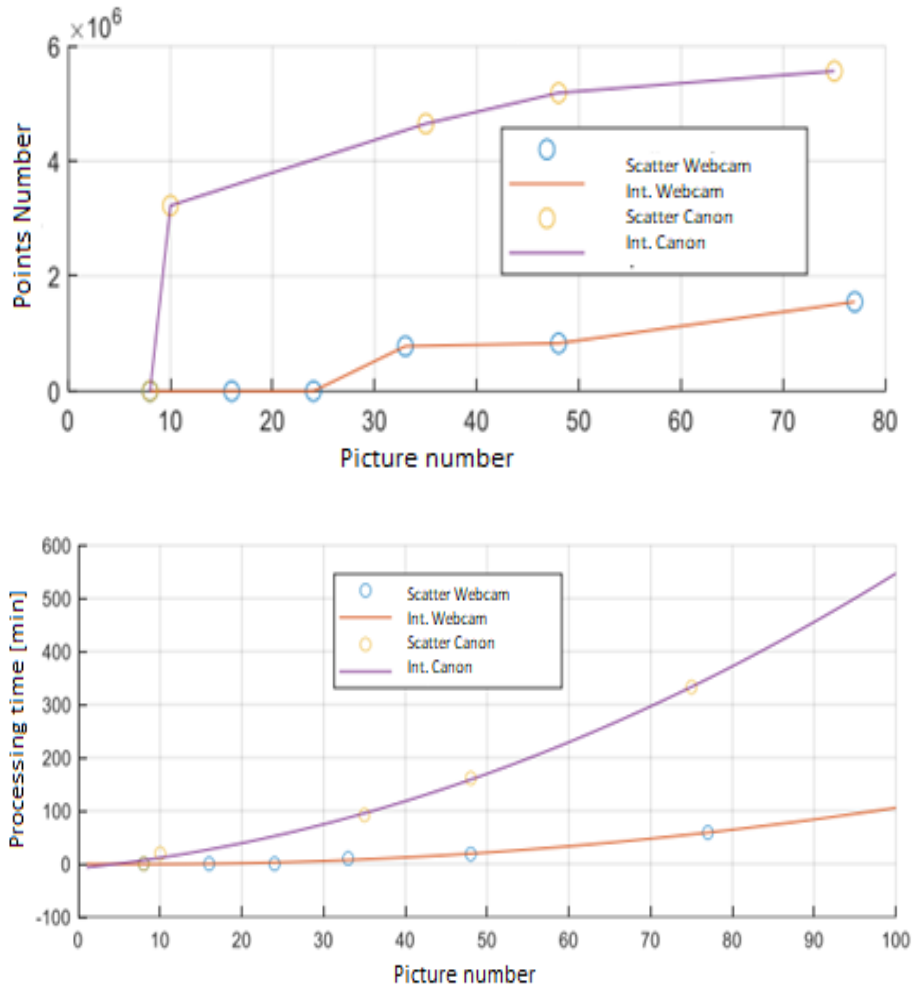
Figure 31 Number of pictures vs point number (top) and vsprocessing time (bottom) for both Canon and webcam.

To proceed with the reconstruction of the model, it was necessary to mask the sequence of photos taken in order to eliminate all background elements that could create noise during the process. Masking was carried out using a dedicated Python script which assigns the value 0 (black) to each pixel that does not fall within the range of shades of green indicated according to the RGB model. The pictures will then be imported and processed in the Metashape software Figure 32.

Figure 32 Example of Masking process in a picture of a lettuce plant: Original picture, Filtered picture and Masked picture.

Using the Metashape platform, the images were aligned by automatically detecting common points between the various acquisitions. In the first triangulation phase, a low number of points were detected points from the images (tie points that make up the sparse cloud) [65]. The model given by the instruments were aligned manually in CloudCompare. Despite the manual alignment using three points, excellent overlaps were achieved between the models. For greater repeatability of the calculation, all acquired models were segmented so as to have a distance of 0.1 mm between the points. This led to a reduction in the number of points in order to be able to process the result with the compiler at our disposal. For example, from the acquisitions made with the Canon reconstructed models with 75 pictures have over 5 million points, however our device did not have a sufficient memory depth to process the calculation. There are cases where it is difficult to close the shape or to resort to modelling techniques and methods because the starting shape is not well reconstructed by scanners. This is the case with complex geometries, especially under unfavourable scanning conditions. The CloudCompare software allows the volume calculation to be carried out by selecting the point cloud of the model and the reference plane. The plane must be rasterized and segmented to obtain a point cloud. The volume results from 2.5D processing as it is extrapolated from the elevation of the points with respect to the lower plane. The raster Image consists of a 2D image composed by a set of pixels with associated an elevation value (Δh), as shown in Figure 33. The raster image is divided in cell and the volume 2.5D is evaluated by summing up the contribution of each cell. This contribution is the volume of the elementary parallelepiped corresponding to the cell footprint, multiplied by the height difference resulting from the two clouds, as shown in Figure 33, with cell dimensions that depend on the accuracy required in the calculation of the final volume.
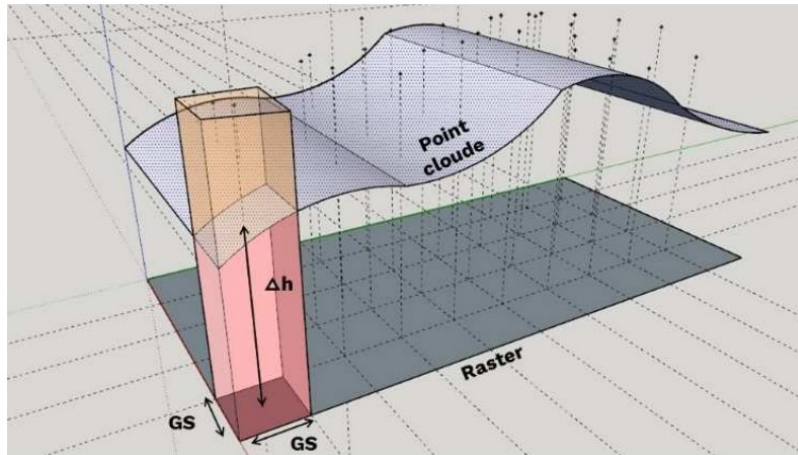
Figure 33 Generation of the 2.5D raster.

The grid step (GS) depends on the accuracy required in calculating the final volume. The objects' volume (V) is calculated through a specific algorithm 2.5D by adding the contribution of each cell with the formula:

$$V = \sum (Gs^2 \times \Delta h)$$

One of the parameters to take into account is the point clouded density that will influence the calculation of volume. In this evaluation high number of points is needed. Table 5 the value used in the example are shown. In Chapter 6, the analyses performed and the results obtained will be shown in more detail.

Table 5 Parameter volume evaluation by CC.

Volume CC	
Parameters	**Values**
Grid Step	1 mm
Matching Cells	90 %
Point Cloud density	1000 points/cm^2

In this case the volume is overestimated. Finally, the height and the volume of the six scans given by Canon and Webcam were compared with STL file (the

volume of STL file was evaluated by Geomagic Wrap). The aim is to analyse the reconstructed model. The following are views of the models processed in CloudCompare Figure 34.
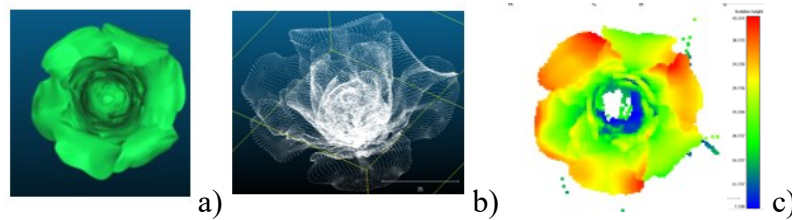
Figure 34 3D printed lettuce plant: a) STL model; b) Canon with point cloud 77 pictures c) Comparison. The colour bar represents the relative height (the colour position is expressed as a percentage). Red represent the farthest points from level 0, while blue indicate the nearest points from level 0.

The colour bar indicates the heigh (distances of points from levl 0 or reference plane), in red the height of object that measures the distance between reference plane and the farthest points (max=43 mm) and blue are representing the nearest distances between the reference plane and points (min= 7mm). The values obtained are considerably higher than the model volume calculated with Geomagic Wrap as the volume calculation via CloudCompare refers to the volume subtended by the point cloud up to the reference plane. For this reason, there are high deviations from this reference geometry. The values that come closest are also those obtained with the lower-resolution acquisitions of the Canon and the webcam, as they have more scattered points and therefore overestimate the volume value.

Upon importing the point clouds into CloudCompare, the volume values and percentage errors were documented in Table **6**, with reference given by the volume of the STL calculated using Geomagic Wrap (7018.66 mm^3).

Table 6 volume values given by different instruments and percentage errors

	Volume [$mm3$]	Error percentage [%]
Canon 75	192088.1	92.53
Canon 48	186151.8	89.57
Canon 35	191301.1	92.14
Canon 10	199024.5	96.00

webcam 77	189644.3	91.31
webcam 48	188951.3	90.97
webcam 33	199258.5	96.12
STL	187137.6	90.06
SL	208954.0	100.97

Concerning the comparisons made against STL, it can be seen that even with acquisitions with lower resolution (Canon 35, Webcam 33), a maximum percentage error of 96 % was obtained. In comparison, SL exceeded the reference volume by about 100 %. This case was tested during the PhD tutoring work at the University of Perugia. From the results obtained, it emerged that it is also possible to evaluate the volume of the plant using low-cost methodologies that also limit calculation times. Furthermore, accepting overestimated volume, it is possible to carry out the analysis through subsampled clouds. This allows calculation times to be reduced from hours few minutes. Therefore, decreasing the quality of the acquisition system does not reduce efficiency in terms of both time and values obtained. Furthermore, it emerged how, in the absence of an STL file, it is possible to refer measurements to acquisitions, considering an overestimation of the volume obtained with the latter due to the surface interpolation raster.

2.2 Digitalization process

The 3D measurement tools shown enable digital models to be obtained from a point cloud or mesh up to an accurate 3D model even for more complex geometries. For complex objects, it is usually necessary to subdivide the point cloud into portions belonging to uniform entities through the so-called segmentation phase; each entity is then modelled separately, while the overall model is generated from the union of the individual modelled entities. Once this procedure is completed, the final model can be derived. It must emphasize that the enormous amount of data that can be obtained by means of a 3D scanner represents a more complex shape of representation of the object than the classic CAD survey restitution [66], [67]. For this reason, an exhaustive representation that can be obtained from a complex real model is the corresponding three-dimensional model, which allows the object to be explored by obtaining measurements and sections from any point or position of the object. The textured provide a very detailed description of the object, from which accurate metric information can be obtained.

Before obtaining the final digitized model, operations were performed on the scans, such as filtering, cleaning and smoothing. The methodology of digitalization process is described by following steps:

1) Scanning: First, scanners' performances were evaluated in terms of times required to obtain the final geometry. The geometries were then compared through a fully automated operation, performed by dedicated software: Geomagic Wrap. It should be reminded that mesh coming from different scanning are not iso-topological [68] and this can make this operation more critical in addition to the number of points (in case of point cloud) or triangles (in case of mesh) being processed for different applications respectively.

2) Post-processing: A high pretence software tools and operator's skills are necessary. Sometimes, data acquisition results in more than one point cloud, so these point clouds or meshes have to be registered and then merged in order to obtain one single object cloud. A cleaning phase follows, where spurious points are eliminated; these points are generated by environment noise and by subject motion or by the camera scanner resolution being close to the size of geometric details. A triangulated mesh is then generated, and it is smoothed to obtain a more regular geometry. The smoothing phase must be performed carefully in order to avoid losing relevant information. Finally, the mesh is edited to avoid double vertices, discontinuities of face's normal, holes, internal faces, so obtaining a manifold geometry. At the end of editing, the mesh is optimised to reduce the number of triangles (or points number in case of point cloud).

3) Comparison smoothing algorithms: The software used may affect the 3D analysis as alignment algorithms and deviation measurements vary. However, the number of studies, which compared 3D analysis software, are limited. The authors are unaware of a study neither focusing on the reliability of the new nonmetrology-grade software nor comparing it with an ISO-12836 recommended and commonly used metrology grade inspection software. In the software Geomagic Wrap it is possible to choose the type of noise reduction according to shape: Free Form and Prismatic shape. The first smooth the curvature of the surface and is suitable for sculptural shapes. This is an aggressive noise reduction technique. The second, on the other hand, helps to preserve the shape and is more suitable for products sharp-edged; the Prismatic shape is divided into two algorithms: 'conservative', which aims to unchanged the shape feature and 'aggressive' algorithm, which tends to

clean considerably the mesh details. Varying the level of smooth and the number of iterations will produce smoothing level maps.

4) Alignment: It is very important that the alignment error is kept around the standard deviation of the instrument, verified in the test phase on a ground plane; keeping to this value for the alignment of all sockets guarantees better results. On the other hand, the average distance between the two range maps must be below the resolution of the range camera, measured at the same distance at which the object was acquired (i.e. between 40 and 50 cm for Go!SCAN 50). Exceeding the limit may result in a loss of detail and consistency on the geometry. Following this procedure, all scans are aligned.

5) Filtering number of points: The next step is entirely manual and consists of removing portions of the range map that are not part of the object. An example of this is the ground plane from the object. We have chosen to do this operation only after alignment to reduce the operation to one rather than repeating it for each individual range map if it is done together with the filtering phase. The difficulty in this part lies in finding the noise reduction that defines the contours of the scan by cleaning it of surface noise but does not take away geometric data. Noise reduction compensates for the error due to movement by, for example, removing isolated meshes. The result of this is a more uniform arrangement of point cloud or meshes that can be analysed more easily.

5) Measurements: The Volume, area, length or other object's parameters was then evaluated using Geomagic Wrap software and finally compared with algorithms.

The null hypothesis was that a recent non-metrology-grade 3D analysis software's ability to detect deviations would not be different from that of a commonly used metrology-grade software [69].

2.2.1 Test case of Digitalization Process

Once the digitalization process has been defined, it will then be tested on a real scanned geometry in order to assess the quality of the final product. Scanning was carried out using Structured Light, in particular the GO! Scan 50 with a resolution of 1 mm was used. The aim is to evaluate the goodness of alignment, reconstruction, modelling and compare the results as smoothing and filtering parameters changes.

A stone from Frasassi Caves, Genga (AN), Marche in Italy, was taken as a case study, due to the low amount of data to be processed and the richness and depth of detail on the surface, to evaluate the smoothing algorithm without the expense of computational time. Then nine parawais of deviation analyses, using SL raw point cloud as reference, were carried out by the "3D Comparison" tool to assess the right degree between shape preservation and noise reduction. The values that were considered are the three levels of smoothness: Freeform (F), Aggressive (A), and Conservative (C) and the number of iterations from 1 to 4 level. Finally, the range map obtained by applying different smoothness and iteration levels is showed; in particular, how the standard deviation between two model (reference raw point cloud and smoothed ones) varies by changing the algorithm type. The deviation map must be uniform because it must insist only on the features that constitute the 3D model, showing the noise that is distributed over all the acquisitions. The various parameters indicate the distances of the object before and after application of the algorithm. The deviation between the reference model and the aligned ones is represented by a colour spectrum where are allocated the distances in a given threshold. The blue colours of range map represent subtracted material and red colour the added material. The parameters analyzed are: Maximum distance (mm) that is the threshold of the maximum deviation represented by the colour bar. This value was set equal to the resolution of the instrument/acquisition software (in this case 0.5 mm); Distant Point (%) are the points too distant from the threshold σ are not evaluated; Mean Distance (mm) is the average distance acceptable (threshold) between the points of two acquisitions; Standard Deviation (mm) describe the variability of distances; Root mean square (RMS) value describes surface's absolute accuracy, including both random and systematic errors, while standard Deviation (Dev.std) is an index of surface's noise. Accuracy expresses the percent of points on the reconstructed model, that are within 2σ i.e., 1 mm. completeness denotes the percent of points on the reference model that are within 2 mm of the reconstructed models. The parameters and standard deviation between acquisitions distances are shown in Table 7.

Table 7 Smoothing and filtering parameters of Geomagic Wrap

Noise reduction	Smoothing level	Max dist. (mm)	Distanza media (mm)	Dev. St. (mm)	Iteration
Free form	1	1	0.12	0.16	a
Free form	2	1	0.18	0.25	b
Free form	3	1	0.26	0.33	c
Free form	4	1	0.34	**0.4**	d

Aggressive	1	1	0.03	0.04	e
Aggressive	2	1	0.04	0.06	f
Aggressive	3	1	0.06	0.1	g
Aggressive	4	1	0.12	0.17	h
Conservative	1	1	0.02	**0.02**	i
Conservative	2	1	0.03	0.04	l
Conservative	3	1	0.04	0.06	m
Conservative	4	1	0.07	0.11	n

The values show that some smooth levels, with minimum values of Dev. Std (e.g., "Free form", "Aggressive"), loss of detail. Thus, these smooth levels are optimal values that lie below the scanner's resolution (for some detail e.g., hole). Figure 35 represents the deviation spectrum that is a graphical representation of the noise reduction showing the differences between the modelled scan from the raw cloud (Indicated from "a" to "n"). Remembering that the deviation map must be uniform because it must insist only on the features that constitute the 3D model, showing the noise that is distributed over all the acquisitions (Figure 36).
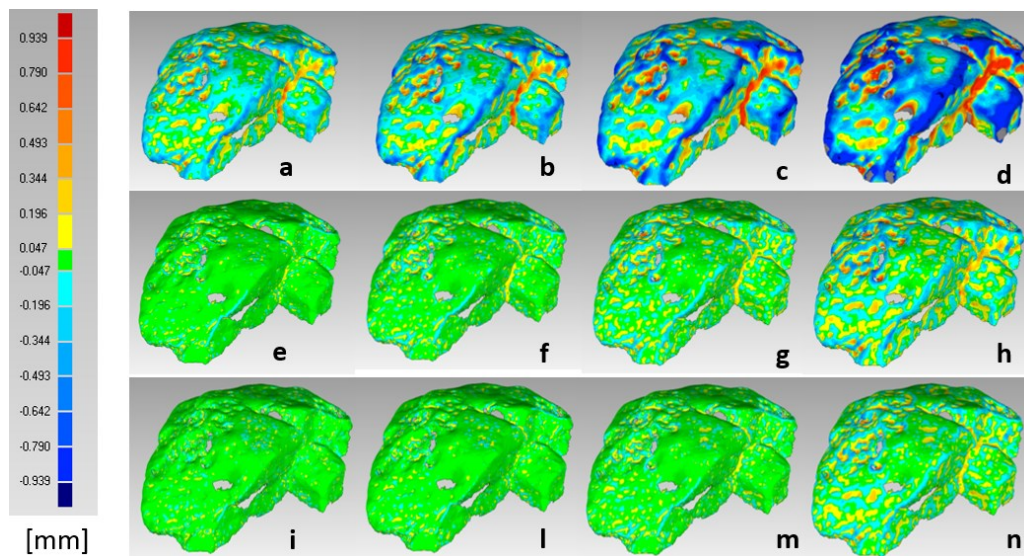
Figure 35 Scan of a stone. Deviation map between raw cloud and cloud with smoothing algorithms applied. Red areas indicate the maximum deviation, green areas the deviation established as acceptable; intermediate values occupy the colour scale between red and green. Blue indicates the points that have not changed. (The lower-case letter refers to the letters also shown in Table 4.3 which indicate the type of algorithm applied to the cloud).

This "anomaly" near the hole occurs because the algorithm for calculating the smoothing operation is different. Therefore "conservative" will be used where there are incisions or fine details, which with "free form" would be incorporated into the smoothing process. A qualitative comparison is showen in Figure 36. This comparison shows that for some values, the smoothing algorithm causes a loss of shape detail, particularly on the excessively 'deep' parts, such as near the holes. To obtain the best detail-smoothing solution, the more iterations are applied, the more noise is removed. Increasing the smoothness level means lost details (Figure 36). also shows that as the number of iterations increases, the level of cleanliness of the range map improves. It is therefore generally advisable to use a high number of iterations. A value of the notches and holes detectable by the SL scanner, tested on a stone, was assessed to be around 0.5 mm to 2 mm, approximately two times above the sigma. While in the other cases, the 'free form' algorithm was applied, particularly where a very smooth surface prevails. The 'aggressive' type was discarded, as at low levels results are very similar to conservative but with significantly higher standard deviation and mean distance values; while with maximum levels of smoothing and number of iterations, similarities with free form and a fair loss of detail are obtained. Finally, the 'conservative' algorithm with a medium-high level of smoothing and a high number of iterations was considered valid, since with such combinations it is possible to maintain good detail and obtain a scan sufficiently cleaned of background noise. In addition, the 'free form' algorithm with minimum smoothing values and number of iterations was also evaluated for objects with a sculptural shape and a smooth surface devoid of detail. Some of these combinations were discarded at a first approach as they did not solve the problem of holes or noise such as disconnected or self-intersecting meshes. Two of the three types of smoothing were chosen: "free form" and "conservative prismatic shapes (Figure 35 Scan of a stone. Deviation map between raw cloud and cloud with smoothing algorithms applied. Red areas indicate the maximum deviation, green areas the deviation established as acceptable; intermediate values occupy the colour scale between red and green. Blue indicates the points that have not changed. (The lower-case letter refers to the letters also shown in Table 4.3 which indicate the type of algorithm applied to the cloud).).
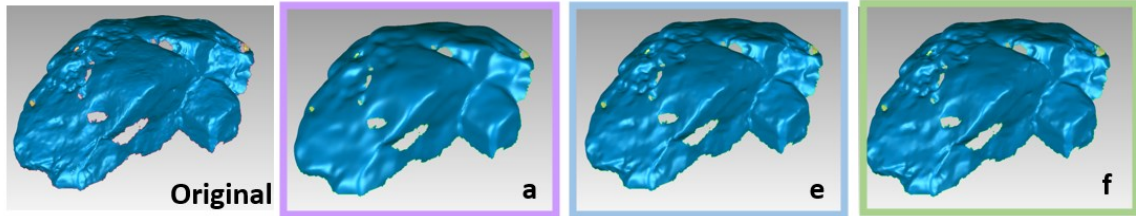
Figure 36 Stone filtering using a) Freeform with smoothing level 1; b) Aggressive with smoothing level; 1 c) Aggressive with smoothing level 2.

In conclusion, low smooth level of iterations algorithms outperforms the others in terms of accuracy and modelling quality, revealing Conservative's algorithms superiority against Freeform and convergent geometry's contribution to reconstruction quality.

2.3 Algorithms

Alpha Shape (A.S.) [55], Alpha Critical (A.C.), Alpha Optimal (A.O.) and Convex Hull (C.H.) algorithms will be used in this thesis work (Chapter 3 and 4) for the reconstruction of shape and the volume evaluation. A test case based on simple object was used for preliminary a study.

Using these algorithms, it is possible to reconstruct a shape such that the volume obtained is close to the reference volume in order to be able to perform a more accurate analysis of the object. Having a reference volume, and the scanned object undergoes deformations over time, through the implemented algorithm it is possible to detect these changes with respect to the initial value.

Alpha optimal algorithms

If exist a reference volume, the algorithm resorts to an iterative approach that leads to achieving volumes very close to the real ones.

The body of the algorithm involves determining first the alpha spectrum. The former is saved, with the intention of having meaningful alpha values to use in reconstructing the shape. However, the MATLAB 'alpha spectrum' function returns a large vector, the larger the number of points [55]. This makes it unthinkable to try to reconstruct the shape of the point cloud using all the values of the spectrum; therefore, it is necessary to find a starting point. The discriminating point around which the alpha varies is the A.C. which, as mentioned earlier, represents the

minimum value of alpha capable of creating a shape that encloses all the points in the cloud.

One of the problems with the algorithm is the computational cost linked to the time needed to import and process the point clouds. These, in fact, for point cloud acquired with high-resolution scanners can be particularly dense and may contain hundreds of millions of points. The purpose of this section is to demonstrate that through the algorithm developed to determine the volume with Alpha Spectrum, subsampled point clouds can be used without loss of generality.

Considering the properties of the values contained in the spectrum, it was decided to use this vector as a reference within which to scroll through the alpha values, evaluate the reconstructed images, and calculate the respective volumes. In this way, only significant alpha values are taken into account, avoiding neglecting alpha values that could generate significant shape variations. This non-uniformity of the vector will later be exploited for the calculation of the volumes, relative to the different alphas, by scrolling the vector in different steps to obtain a greater or lesser detail of the optimal alpha. To highlight this variation in density within the "spectrum" vector, histograms are shown, distinguished by different orders of magnitude of alpha, and equally spaced in the intervals to facilitate comparison.

In Figure 37 the spectrum of the stone presented in digitalization process is shown considering the value of alpha (a): 0<a<100 mm, 100<a<1000 mm, 1000<a<10000 mm and 10000<a<100000 mm.
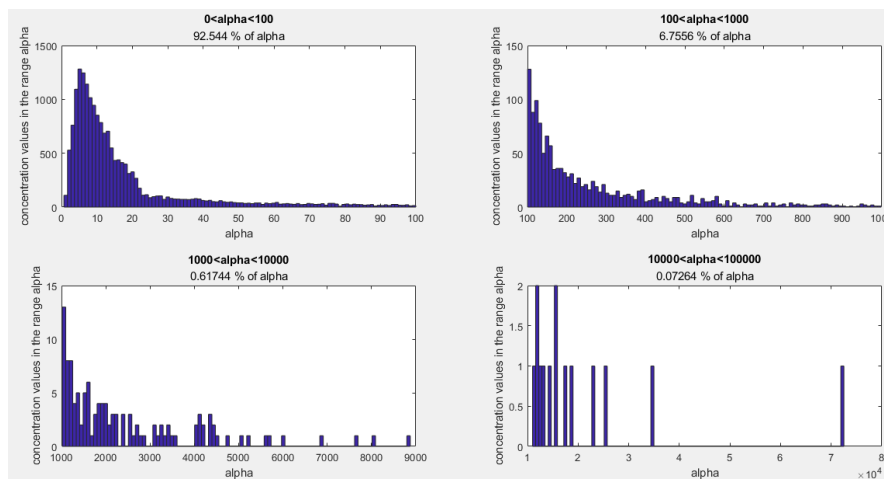
Figure 37 Alpha spectrum of stone. Top left: 0<a<100 mm; Top right: 100<a<1000 mm; Bottom left: 1000<a<10000 mm; Bottom right: 10000<a<100000 mm.

This non-uniformity of the vector will be used to calculate the volumes, relative to the different alphas, by scrolling the vector in different steps to obtain greater or lesser detail of the optimal alpha. The situation with Alpha Shape is analogous to the coastline paradox presented in the introduction, as the number of points in the cloud varies alpha, the reconstructed shape varies with it and consequently the volume. However, thanks to the optimised algorithm, the resulting volumes are close to each other despite using images with different numbers of points. To demonstrate this concept, the Alpha Optimal (A opt) is calculated with the already optimised algorithm, i.e., the alpha value for which A.S. leads to a volume very close to the reference volume. It has been calculated that both optimal alpha and optimal volume variation is depending on the points used to subsample the points cloud. Although it would be preferable for the optimal volume to remain the same, when looking at the relative percentage error of the volumes compared to the reference volume, the results are nevertheless encouraging. In fact, the relative errors remain very small and within a very narrow range of around 0.02 %. This is why it was decided to use sub-sampling of the points clouds upstream of the algorithm, in order to reduce calculation times for object with particularly dense point clouds. This study was conducted during the PhD tutoring work.

In the case of object with a reference volume, the algorithm uses an iterative procedure. In the first phase of the programme, as mentioned above, the alpha spectrum, the C.A., i.e., of the shape reconstructed with the C.A., are obtained and the critical volumes are evaluated. First, the programme then compares the critical volume with the reference volume and divides the case where the former is overestimated or underestimated with respect to the latter. For simplicity, it goes on to explain the underestimated case, because the overestimated one is mirrored. The fact that the critical volume underestimates the reference volume implies that alpha must be increased to get closer to the real volume. In order not to reconstruct shapes with insignificant alpha, the alpha values contained in the spectrum are scrolled, obtained with the "alpha spectrum" function discussed in the previous paragraphs. The first step is then to identify the position of the C.A. in the spectrum, from which we proceed by increasing alpha with step 100, in order to speed up the calculation; in fact, for each alpha the algorithm calculates the volume of the corresponding shape and the relative error with respect to the reference volume: $e = |Vi\,(alpha)$ - $Vrif|\,Vrif,$ where Vi(alpha) stands for the volume calculated with a certain alpha at the i-step of the cycle and reference volume (V.rif.) for reference volume. The error is evaluated within a first while loop, from which it is exited as soon as a minimum point in the relative error is found. Below is an example of the relative

error calculated on a point cloud of a stone in Figure 38 a show the relative error (for the 100 alpha values) evaluated within a first while loop, from which it is exited as soon as a minimum point in the relative error. In Figure 38 b) the relative error calculated for the 200 alpha values is shown.
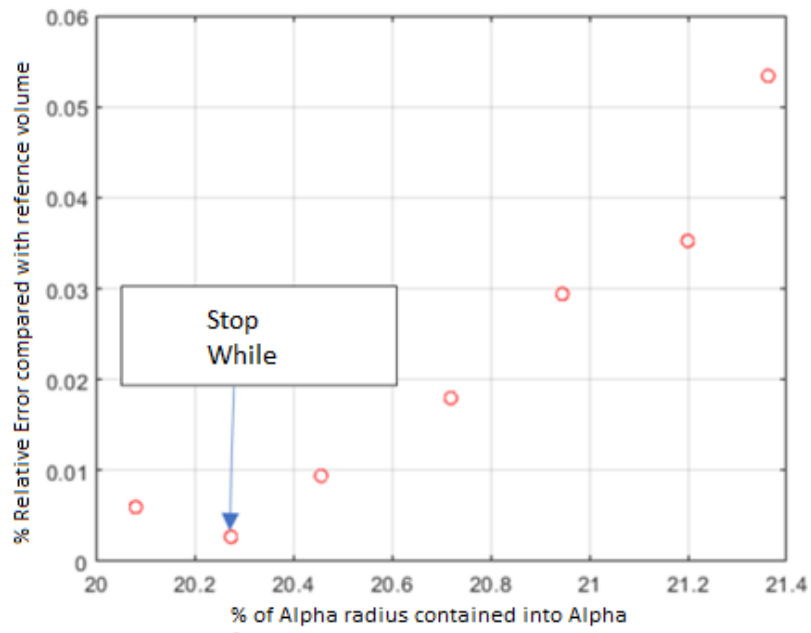
a)
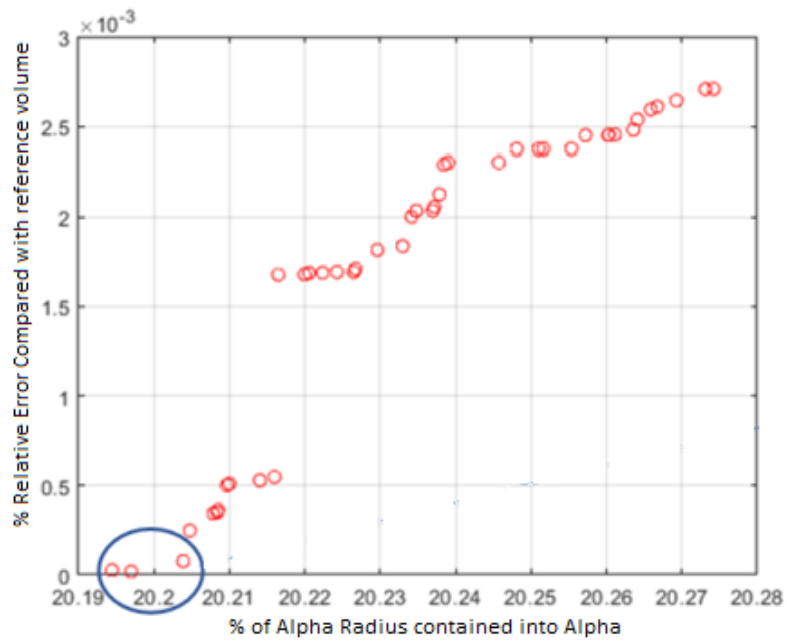
b)

Figure 38 a) Relative error evaluated for 100 values of alpha; b) Relative error evaluated for 200 values of alpha

However, the alpha value thus obtained may not be the optimal one; in fact, the 200 values straddling it were not evaluated. Therefore, a second while loop is used that analyses the range of alpha values that were not evaluated, calculating the error as done previously. The optimal alpha is the one for which the error is minimal. If the critical volume is overestimated, the procedure is essentially the same, but the alpha spectrum is scrolled for decreasing alpha values. As mentioned earlier, the optimal volume and alpha thus obtained are finally exported to a .dat file.

1.4 Conclusions

The uncertainty of different measurement techniques was studied in the literature (Structured Light scanner) [78], [79], (Photogrammetry) [59], (RGB-D) [80], [81], (LiDAR) [82], [83]. The overlap percentage and the volume were evaluated by CloudCompare [59]. This analysis corroborates existing literature, suggesting that processing times exhibit exponential growth as the number of photographs increases [59]. Additionally, the overestimation of the volume, as calculated through integration, remains almost constant across all acquisition methods at approximately 90%, in contrast to the 300% observed in the Convex Hull algorithm [66]. The level of smoothing in the digitalisation process (paper smoothing comparison) was evaluated among the smoothing processes. The best result is the "conservative" with smoothing level 1 with a standard deviation of 0.02 mm. This value is higher than the scanner uncertainty, which is 0.01 mm [79]. The spectrum [55], the reference volume threshold and the optimal alpha were evaluated [66], and an algorithm was developed to find the optimal alpha for volume calculation close to the reference volume.

The results obtained was in a relative percentage error of less than $0,5 \times 10^{-3}$, while in paper [66], the error results in $1 \, e^{-4}$.

Chapter 3

Algorithms tests on simple and complex geometry

3.1 Introduction

Alpha shapes are a family of piecewise linear simple curves in the Euclidean plane that define the shape of a finite set of points. The parameter α controls the resulting shape, with $\alpha = 0$ yielding convex hulls and $\alpha > 0$ producing more complex shapes capturing local geometry. Every convex hull has an alpha shape, but not every alpha shape is convex. Alpha shapes are formed from a subcomplex of the Delaunay triangulation of the points, and their edges are drawn between two points when a generalised disk of radius $1/\alpha$ contains none of the point set, with the two points lying on its boundary. They are closely related to alpha complexes, which consist of edges and triangles with radii at most $1/\alpha$. Alpha shapes find applications in shape analysis and quantifying complex structures of irregular-shaped objects, and they can handle points with weights in dimensions beyond two. The choice of α determines the level of detail in the resulting shape, where larger values yield simpler shapes and smaller values capture finer geometric details. The optimal α value is chosen based on the specific application and desired level of detail. Overall, alpha shapes are a versatile tool for defining point sets' shapes and find use in various applications, including biological shape analysis and surface reconstruction from unorganised data points, along with generating surface meshes for functional analyses [84], [85].

Alpha shapes, also known as α-shapes, are primarily used for reconstructing objects based on point samples, particularly for surfaces captured by 3D scanners. The goal is to connect these points, forming triangles or lines to create a comprehensive surface reconstruction of the object. However, using α-shapes for surface reconstruction comes with challenges that need addressing: Determining

the Optimal α: Selecting the α parameter is crucial as it controls the size of the α-shape radius used to connect points. Too small α values can result in gaps, leaving some regions disconnected, while overly large values may merge separate objects or lose fine details. Finding the optimal α often involves a trial-and-error approach using interactive methods like sliders to achieve satisfactory results. Handling Non-Uniform Point Sets: Dealing with point sets of varying densities across the surface poses challenges for α-shapes. Regions with higher point density require smaller α values for accurate detail capture, while regions with lower density may need larger α values for proper connections. However, this can lead to undesirable relationships between separate objects or loss of sharp features. Researchers have proposed techniques like density scaling to address these issues, allowing finer detail in denser regions and aiding in detecting and separating neighbouring objects with different densities. In conclusion, α-shapes offer a versatile method for surface reconstruction from point samples. Accurate and visually satisfactory results depend on selecting the appropriate α parameter and addressing non-uniform point set challenges. The effectiveness of various techniques in overcoming these challenges depends on specific point cloud data and the requirements of the surface reconstruction task. [86].

Alpha shapes offer advantages in handling highly detailed point clouds, but practical considerations such as scanning techniques can affect point cloud density. Ensuring equal points in comparative studies is crucial to avoid biased results. Optimal alpha refinement coefficients are introduced as a metric for shape complexity, with sensitivity analysis showing that denser point clouds require finer refinement coefficients. Alpha shape complexity appears more sensitive to concave features than surface rugosity. Downsampling point clouds may lead to losing finer features and coarser refinement coefficients. A feature should have at least 3 or 4 data points within the point cloud for inclusion in alpha shapes analysis. The optimal refinement coefficients depend on point cloud density, which is manageable for comparative analyses. Finding a compromise between required detail and computational processing time is essential. Implementing alpha shapes is straightforward, automated, and efficient for large datasets, showing promise in various applications. However, alpha shapes may not equally capture certain aspects of complexity related to convex and concave topology, and they tend to overestimate the object. Attributing between-subject variation in alpha volume to specific geometric features may be challenging. Careful metric selection is crucial for specific applications [68].

The paper [87] presents an alpha-shape method for reconstructing object shapes from unorganised point sets. Critical factors in the process include normal and density estimation. Density estimation is vital for capturing high-density regions in the point set and achieving automatic shape construction. The alpha-shape method proves powerful for surface reconstruction, allowing adjustment of alpha values for different shapes from the point set to the convex hull. To address non-uniform point distribution challenges, the algorithm scales the alpha radius based on point density using a new adaptive bandwidth estimator. However, assessing density estimation quality remains challenging, especially in extreme variations of point density. Selecting an optimal bandwidth for multivariate density estimation, particularly in 3D space, requires further investigation.

In [61], the issue of reconstructing thin geometry like plant leaves from 3D point clouds is discussed. Existing methods need help balancing accuracy and robustness against noise and missing points. The study evaluates different geometric models for leaf area estimation based on synthetic and real data, considering leaf shape and acquisition process criteria. Alpha-Shape and four other techniques are compared, showing that it tends to underestimate leaf area. Real data experiments reveal additional factors like noise near leaf borders or holes in point clouds that significantly affect estimated leaf areas. Highly curved leaves may also lead to underestimation. The authors propose using a geometric model that considers expected boundary shapes as prior knowledge to enhance robustness. Parameter sensitivity analysis recommends using Moving Least Squares (MLS) and Statistical Outlier Removal (SOR) filters for most cases. However, complex phenomena like leaf torsion and occlusions need further consideration. Real-world scenarios may introduce additional challenges requiring refinement of the reconstruction process. Parameters may need tuning for different plant species, which could be limited by data availability for parameter optimisation.

In [88] a surface reconstruction method using α-shapes is discussed. The technique approximates an unknown surface with a simplicial surface based on 3D α-shapes, accommodating surfaces with various topologies and data types. α-shapes are generalised polytopes derived from Delaunay triangulation, defining the outer shells of surfaces. The challenge lies in generating a 3D manifold simplicial surface from an α-shape for accurate reconstruction. The method selects an appropriate α-shape to expose details implied by data points and reconstruct the geometry effectively. The α value determines the level of detail in the surface representation.

The paper explains the steps for exterior face enumeration to construct the final simplicial surface, especially when the surface has a boundary. The method is tested on various data sets, including sparse and anisotropic data, dense and noisy data, and surfaces with boundaries. It is flexible and practical for surface reconstruction from unorganised data points, accommodating different data types and anisotropic data. However, it may have limitations with non-orientable surfaces, and severe noise levels can impact accuracy. The method's effectiveness depends on the input data's characteristics and desired level of detail in the reconstructed surface.

Paper [89] explores the concept of conformal alpha shapes and their benefits over traditional alpha shapes in surface reconstruction. Conformal alpha shapes adapt to the local geometry of a point set using a local scale parameter $\alpha^{\wedge}$, making them more effective for handling non-uniformly sampled surfaces. The paper compares the behaviour of ordinary and conformal alpha shapes on the Stanford Bunny model. It highlights how conformal alpha shapes better preserve the shape's features even with varying point densities. Conformal alpha shapes are precious for provable surface reconstruction algorithms that filter candidate sets, and for surface reconstruction approaches examining critical simplices. They significantly advance surface reconstruction techniques, enabling multi-scale topological analysis of point clouds. However, implementing and computing conformal alpha shapes may require more computational resources and time than traditional alpha shapes. The choice of the local scale parameter $\alpha^{\wedge}$ is critical and may impact the quality of the resulting reconstruction, requiring careful consideration and expertise. While conformal alpha shapes excel with non-uniformly sampled surfaces, they may not provide significant advantages over traditional alpha shapes for uniformly distributed data.

As told before, the alpha value is a crucial threshold parameter to establish connections among points within a tumour to form a single object.

In [67], researchers investigated the impact of different alpha values on tumour volume estimation using the α-shape method. When alpha was set to 0 mm, the tumour volume was reported as 0 mm, as expected since all points were disconnected. The tumour volume grew proportionally as alpha increased from 0.0 mm to 3.0 mm. At an alpha of 0.9 mm, significant and rapid growth in tumour volume was observed, indicating that the α-shape method successfully connected all tumour points, forming a single object with a non-zero volume. The authors

concluded that a minimum alpha value of 0.9 mm was needed to represent a complete single tumour object with all details. Beyond this threshold, the tumour volume reached saturation with minimal growth, suggesting all tumour points were already connected. The α-shape method exhibited minor uncertainty in volume estimation (6%) compared to other methods used in the study and provided volume estimations closest to the gold-standard volume. It also showed a lower deviation (overestimation) from the gold standard for volumes of large geometries, indicating its accuracy and precision. The α-shape method effectively connected tumour points and offered accurate volume estimations. However, careful consideration and validation of the threshold parameter (alpha) based on tumour characteristics are essential, as some shapes may exhibit varying responses to the α-shape method.

Paper [90] introduces the "Locally density-adaptive-a-shapes" (LDA-a-shapes) method for reconstructing shapes from unorganised sample points in two (R2) or three (R3) dimensions. LDA-a-shapes utilise a family of "LDA-a-hulls," parameterised by "a," to represent flexible shapes with varying levels of detail. Two fundamental concepts derived from LDA-a-hulls are the "LDA-a-shape," meaning shape boundaries with differing densities, and the "LDA-a-complex," capturing surface and internal structure. The method efficiently computes using a simple algorithm based on Delaunay triangulation, making it scalable for real-world applications. LDA-a-shapes handle non-uniform point distributions and outliers, ensuring accurate shape reconstruction. However, selecting the appropriate parameter "a" and managing the trade-off between detail and complexity are essential considerations when using LDA-a-shapes.

The paper [91] highlights the limitations of traditional α-shapes in handling complex surface structures due to their inability to detect certain surface discontinuities and arrangements adequately. To address this, anisotropic α-shapes are proposed as a promising method for reconstructing triangulated surfaces from point sets with non-uniform distributions, especially in areas with higher point densities. Anisotropic α-shapes offer improved handling of challenging point sets but may require user input for parameter settings. The paper also introduces an anisotropic adaptive method for triangular mesh smoothing to reduce noise and improve the quality of 3D scanned objects. However, user input introduces subjectivity and potential biases, and determining optimal settings can be challenging. Additionally, the complexity of anisotropic shapes may lead to increased computational overhead compared to straightforward approaches.

Overall, the papers discuss various methods for reconstructing geometries from 3D point clouds and the challenges of handling non-uniform point distributions and noise. The articles discuss the use of 3D point clouds for reconstructing the geometries of various objects, including plants, and the associated challenges. The authors describe different methods for reconstructing geometries from 3D point clouds, such as Alpha-Shape, and evaluate their performance on synthetic and real data. They also discuss the use of refinement coefficients and density to improve the quality of reconstructions. The papers include a detailed analysis of alpha behaviour with changing density and comparing geometries with nearly uniform points and those scanned to understand point cloud filtering from scans.

In conclusion, the problems associated with alpha shape algorithms include challenges in determining the optimal α parameter, which may lead to gaps or unwanted connections in the surface. The trial-and-error process for finding the optimal α value can be time-consuming. Handling non-uniform point sets is problematic, as different regions may require different α values, leading to potential inaccuracies. While alpha shapes can take noisy data, they may struggle with severely noisy or heavily distorted point clouds. Additionally, the computational complexity of alpha shapes can be an issue, especially for large point clouds, impacting real-time or interactive applications. The study explores how different refinement coefficients in alpha shapes affect volume estimation for simple and complex shapes. It involves testing various dimensions, densities, and geometries using STL as a reference volume. The research includes uniform and non-uniform point sets, observing alpha behaviour with changing density. The primary focus is to analyse and understand trends and uncertainties in reconstruction concerning refinement coefficients. The study aims to determine the minimum, maximum, and optimal alpha values and introduces the concept of critical alpha to focus on relevant intervals efficiently.

The spectrum allows the algorithm's adaptability to different shapes, dimensions, and point densities, enabling the selection of the most appropriate α-shape with the highest level of detail allowed by the data.

The aim of this paragraph is to understand how the volume evaluation of the Alpha Shape (AS) algorithm varies by varying the radius parameters. After this, the other three algorithms Alpha Critical (AC), Alpha Optimal (AO) and Convex Hull (CH) were analysed.

Alpha Shape (AS)

Study of the uncertainty of reconstruction varying alpha radius. Alpha shape volume given by changing alpha radius from 5 mm to 105 mm with a step of 10 mm (for a total of eleven value of alpha radius), was evaluated. Then the corresponding volume was estimated. For well know the alpha shape algorithms radius parameter effect, two analysis was performed:

Test A: The total uncertainty of each eleven alpha radius was evaluated in order to analyse the effect of the alpha radius changing on volume evaluation.

Test B: The maximum, minimum, averages and standard deviations (Box Plot) in order to analyse the effect of the alpha algorithm's reconstruction on static object.

MAPE was also evaluated in both test, which indicates, for each alpha radius, how far the model given by alpha shape algorithm is from the reference.

Alpha Critical (AC), Alpha Optimal (AO) and Convex Hull (CH)

The uncertainty of reconstruction of underestimated geometry enclosing all points. Since the alpha critical is a fixed function (has not changing parameters) and the object studied are closed, "all-point" and "one region" coincide. In this case the alpha radius needed for enclose all point is evaluated. Thanx the reference is also possible to evaluate the optimal alpha that gives the expected volume (reference). Finally, the volume gives by Convex Hull algorithms was evaluated and compared with the previous ones. Again, MAPE was evaluated in order to know how far the measurements are from references the reconstructed model by those algorithms and volume evaluation.

These two analyses show the procedure that characterises the tests that will be carried out. First two tests were performed: Test case on simple "virtual" object (Pyramid, Cube and Sphere) drown in CAD; Test case on real object with a complex shape (3D printed lettuce plant). In Chapter 3 The same analysis will be applied on scans of static object (never scanned) before. Finally in Chapter 5 this analysis will be applied on acquisitions of more complex object: an artificial tree.

3.2 Materials and Methods

3.2.1 Simple virtual object Test case

First objects were drawn with SolidWork 2022 three pyramid P and three cubes C by varying the side length; Finally, three Spheres S were drawn by varying the diameter. The dimensions analysed are side length 10, 20 and 50 mm. For the sphere we refer to the diameter and the same measures were used. We called this samples as Sample group 1. Another group of the same geometry but with different size 100, 300, 500 mm were analysed called Sample group 2. Those objects were exported in STL format, then the mesh was subsampled in point cloud by CloudCompare for analyse the effect of size variation on volume evaluation with the same number of points (np) for all geometry. Was decided to use the subsampling by using 9000 points for each acquisition, that mean that the density of point (np/area [mm^2]) decrease with the increasing of object size. The total of samples tested is 18. The objective is to identify the influence of point density and object size on volume reconstruction uncertainty in a quantitative way. For this case, the same number of points (equal to 9000) where fixed, varying the sample's size for analyse the effect of density and dimensions on reconstructions algorithms. In Figure 39 show the total of samples analysed.
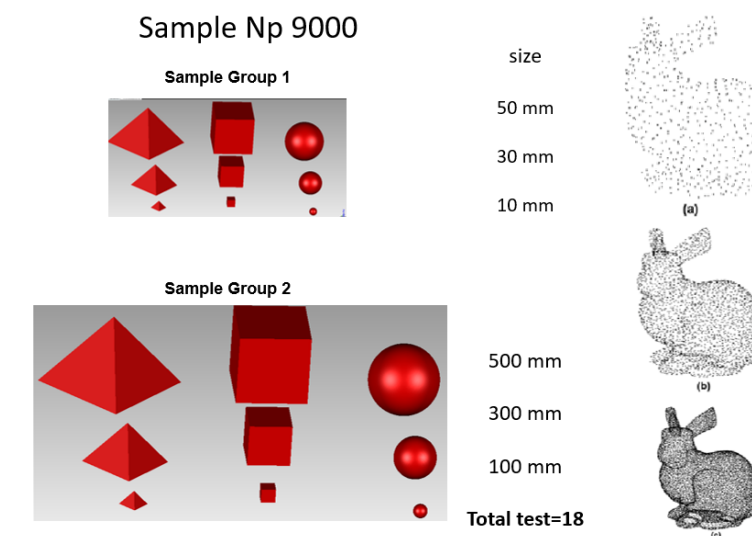
Figure 39 Simple Object with different size and same number of points. Effect of density values, ρ, on the simplified 3D point set. (a) ρ = 2.5 (b) ρ = 5 (c) ρ =10. [A new point cloud simplification algorithm, Carsten Moenning, N. Dodgson, 2003].

In the previous Figure, the rabbit represents the effect of density (same number of points) on size of the subsampled point clouds. In Table 1 it is possible to notice the correspondence between shape, volume, density and size between the two group. The volume and the area were evaluated using Geomagic Wrap 2022. In order to estimate the performance of this software, the density was also evaluated going to divide the area by points number.

Table 8 Area, Volume and density of Sample group 1(Top): Np 9000, size 10 mm, 30 mm, 50 mm; Sample group 2 (Bottom): Np 9000, size 100 mm, 300 mm, 500 mm.

np=9000	Area [mm^2]	Volume [mm^3]	Density np/[mm^2]
P_10	546.41	666.67	16.47
P_30	4917.69	18000.00	1.83
P_50	18577.95	101333.30	0.48
Q_10	600.00	1000.00	15.00
Q_30	5400.00	27000.00	1.67
Q_50	15000.00	125000.00	0.60
S_10	314.12	523.47	28.65
S_30	2827.08	14133.59	3.18
S_50	7852.80	65433.28	1.15

np=9000	Area [mm^2]	Volume [mm^3]	Density np/[mm^2]
P_100	54641.02	666666.67	0.17
P_300	491769.16	18000000	0.02
P_500	1857794.71	101333346	0.01
Q_100	60000	1000000	0.15
Q_300	540000.01	27000001	0.02
Q_500	1500000.00	125000000	0.01
S_100	31411.95	523466.23	0.29
S_300	282707.55	14133588	0.03
S_500	785298.75	65433279	0.01

The Table show the correlation between the size and density of the two samples group: the density of Sample group 1 is one hundred time the value of Sample 2, this relationship is constant for all geometries, so the volume evaluation is reliable. The littlest objects have a high density except for pyramid and cube with 50 mm of size where the density is < 1 np/mm^2 while Sample 2 has a density always less than 1 np/mm^2.

3.2.2 Complex Geometry Test case

A more complex object, lettuce plant, is scanned using 4 different methods, each one with different resolution and cost: Structured Light scanner SL (5 scans), Photogrammetry with high-cost Canon EOS 7D PH (3 scans with 35, 48 and 75 pictures), Photogrammetry with low-cost Webcam Ph (3 scans with 33, 48 and 77 pictures) and blue laser sheet high resolution scan CONTROL 3000 (1 scan) [70]. The reference was the STL model of the 3D printed lettuce plant with a number of points equal to 3000 np. Also, the STL was subsampled as did for simple geometry for a total of 13 measurements. Also, STL file was subsampled in order to know the effect of subsampling on final volume. The aim is to identify the best relationship between tool and resolution in order to reduce data, optimise calculation time and reduce the economic resources required, while maintaining meaningful data. The same analysis showed before, in a virtual object, was applied into a scanned object with complex shape: a 3D printed lettuce plant. Since it is difficult to have a reference and the algorithms would go to overestimate the volume (paragraph 2.1.1), in this case reference was the STL file. Table 9 the reference and the original number of points of different scans is shown with the reference or Ground Truth (GT) (Table 9 Instruments and Number of points of original point clous.

Table 9 Instruments and Number of points of original point clous

GT=7018,66 [mm^3]	N.points [adm]
Laser	151461
PH1 35	4497795
PH2 48	5029720
PH3 75	5564132
Ph 33	715685
Ph 48	830748
Ph 77	1550464
STL	76442
SL 1	54798
SL 2	733010
SL 3	45826
SL 4	56346
SL 5	57899

The table show the increasing of points number with the resolution and performance of instruments.

Alpha Spectrum

First, an analysis of alpha spectrum was carried out aimed to understand what the best investigation range is for varying the alpha ray. Through the spectrum, it was possible to understand which are the best investigation ranges, i.e., where the density of alpha ray values is concentrated. This analysis was carried out on all geometries. Shown in Figure 40 are the spectra of spheres with radius 30 mm and (Figure 41) 300 mm and the 3D printed lettuce scanned with photogrammetric techniques in Figure 42 by Ph 75 (Canon) and PH 77 (Webcam) in Figure 43 and 44.
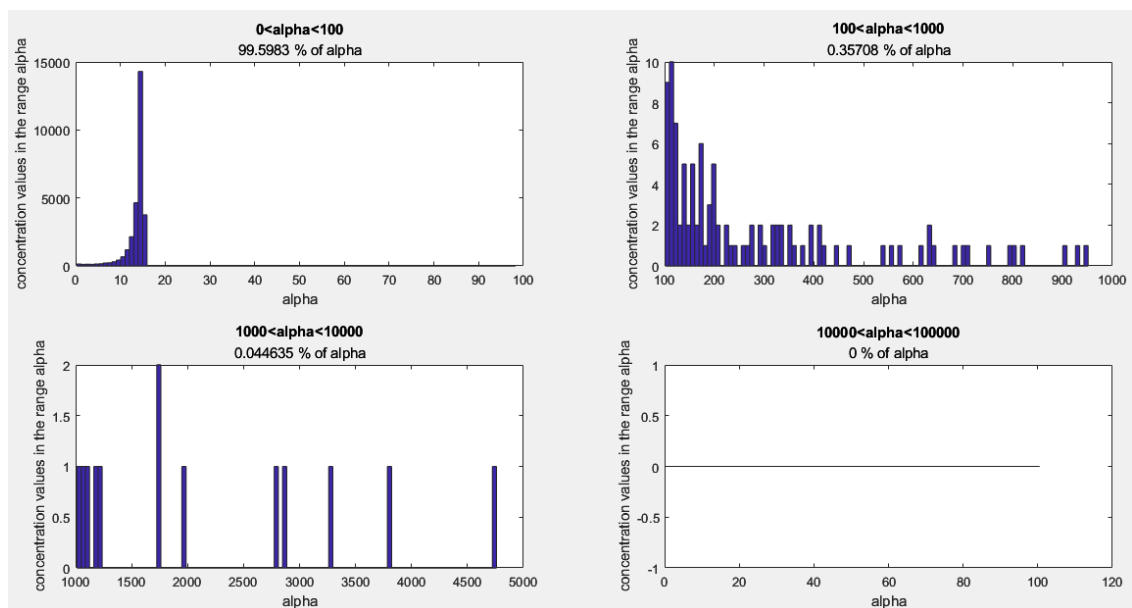
Figure 40 Spectrum alpha Sphere with diameter 30 mm 900 pn
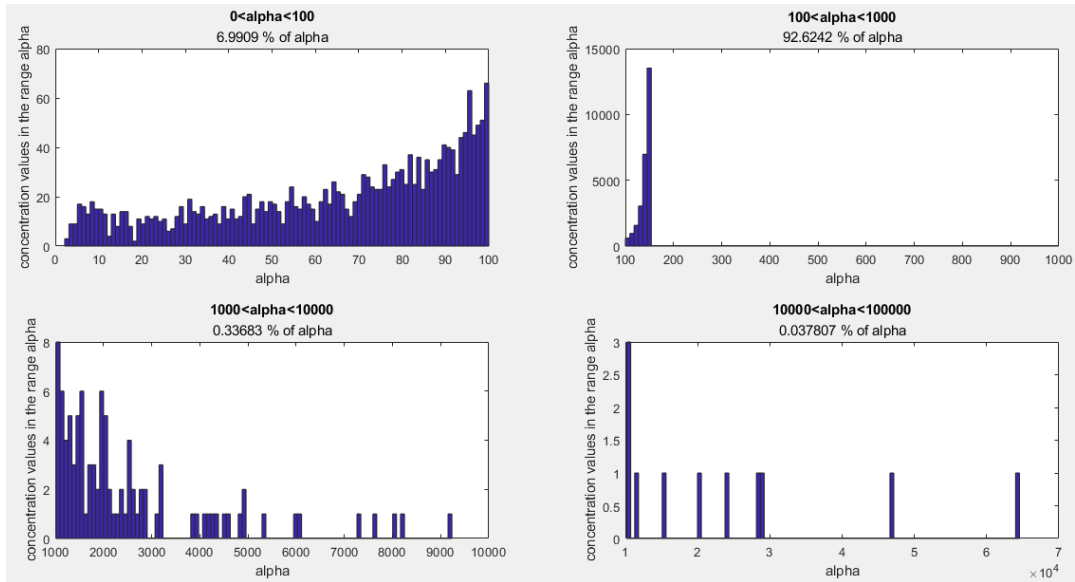
Figure 41 Spectrum of Alpha radius of Sphere with diameter 300 mm 900 points.
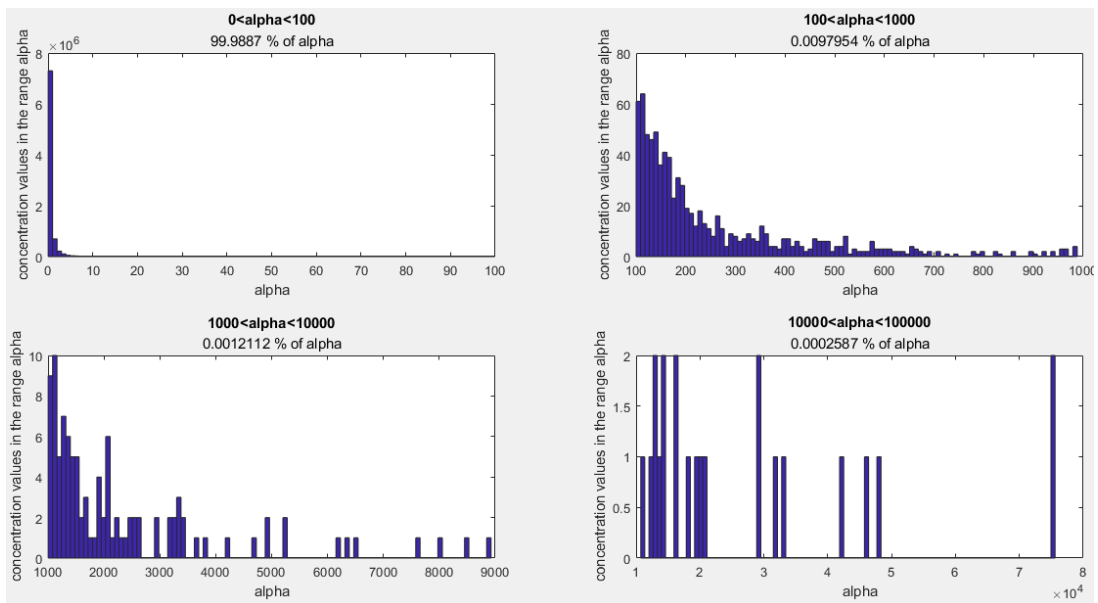
Figure 42 Spectrum of Alpha radius of Lettuce Canon 77 Original 3000 points.
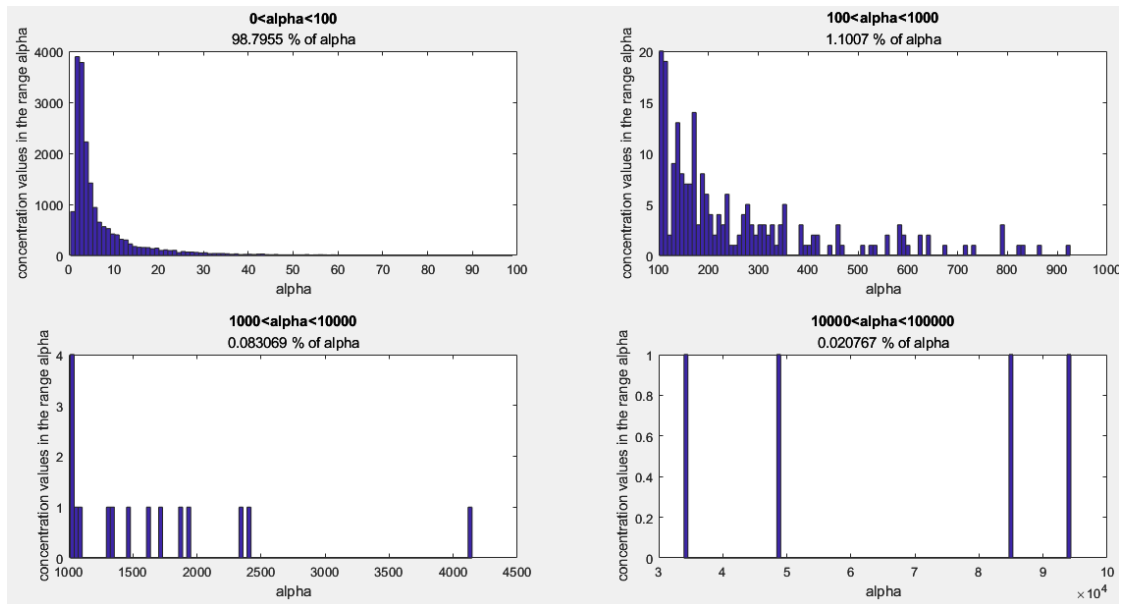
Figure 43 Spectrum of Alpha radius of Lettuce Canon 77 Subsampled 3000 points

As can be seen from previous Figure, as the size of the sphere increases, the spectrum tends to shift towards alpha values > 100 mm, where the density of alpha rays is 92.62 %, while only 6.99 % of alpha is between 0 and 10 mm. Furthermore, for spheres with a diameter of 30 mm there are no alphas between $10000 < a < 100000$. For all other cases, more than 95 % of the alpha rays are concentrated within this value. For these reasons the range of alpha radius variation was selected between 5 mm and 105 mm.

3.3 Results

3.3.1 Alpha Shape (AS) on Simple virtual objects

For each alpha radius the volume was evaluated by Alpha Shape algorithms of both Sample group 1 and 2. Figure 44 and Figure 45 show the result of the volume varying alpha radius for the different geometries (Pyramid, Cube and Sphere) and size.
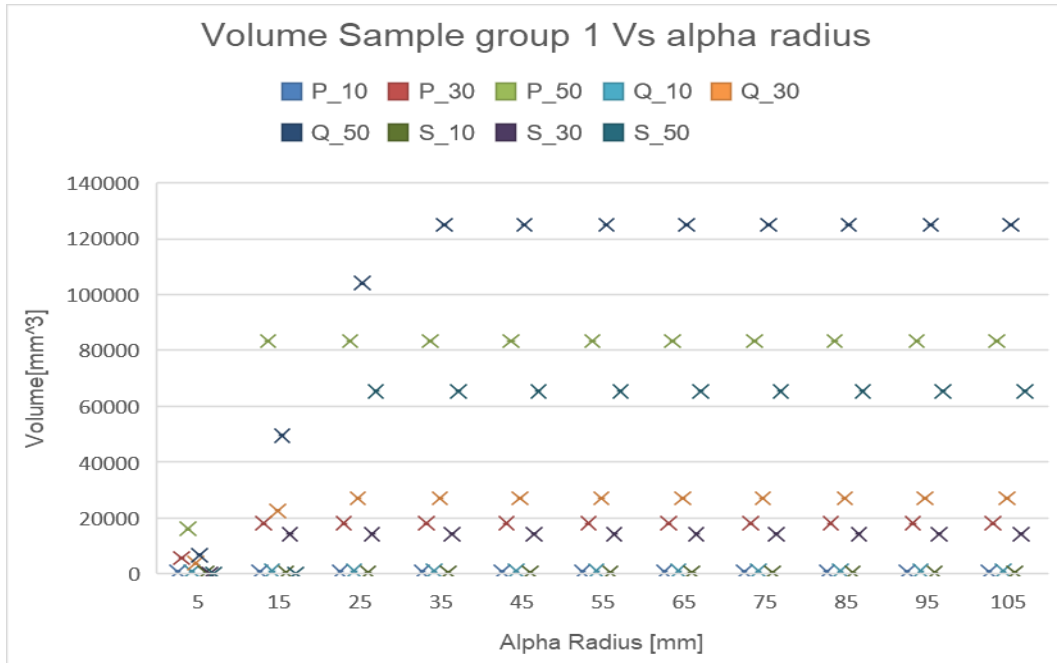
Figure 44 Box Plot Volume Vs Alpha Sample Group 1
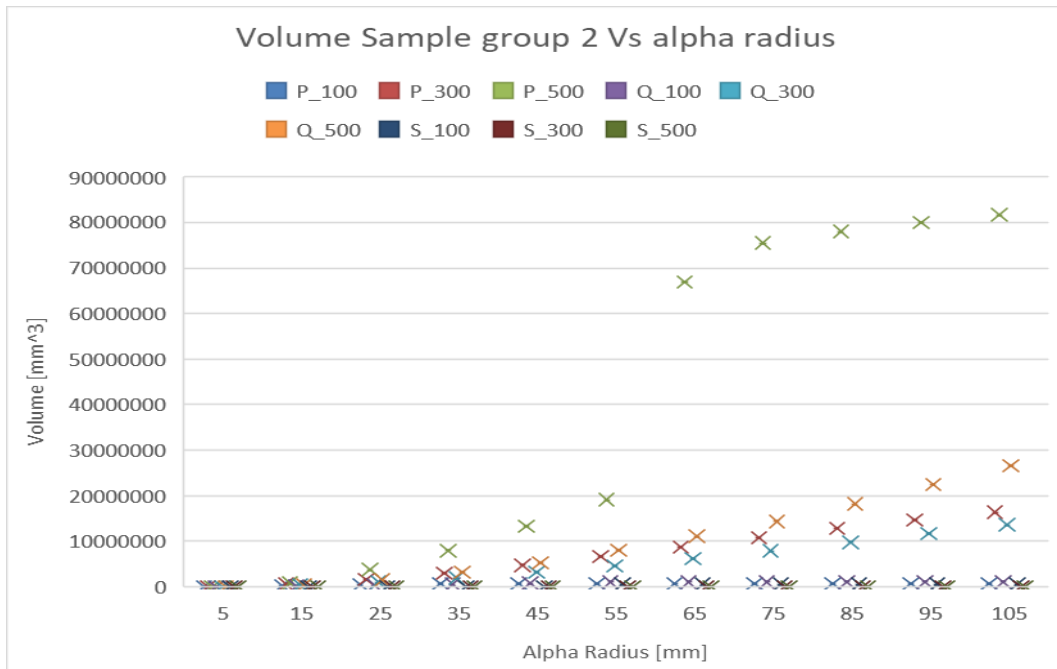
Figure 45 Box Plot Volume Vs Alpha Sample Group 2

In Sample 1 the volume increases for all objects. For radius equal to 5 mm the shape is not reconstructed, and the volume is not evaluated. In Sample group 2, after alpha= 55 mm the algorithms overestimate the pyramid volume. In both cases the volume increase with alpha radius. In most cases the alpha radius equal to 5 mm failed the reconstruction. Following an example of alpha shape reconstruction of Pyramid Figure 46, Cube Figure 47 and Sphere Figure 48 with side/diameters equal to 30 mm and 300 mm is shown.
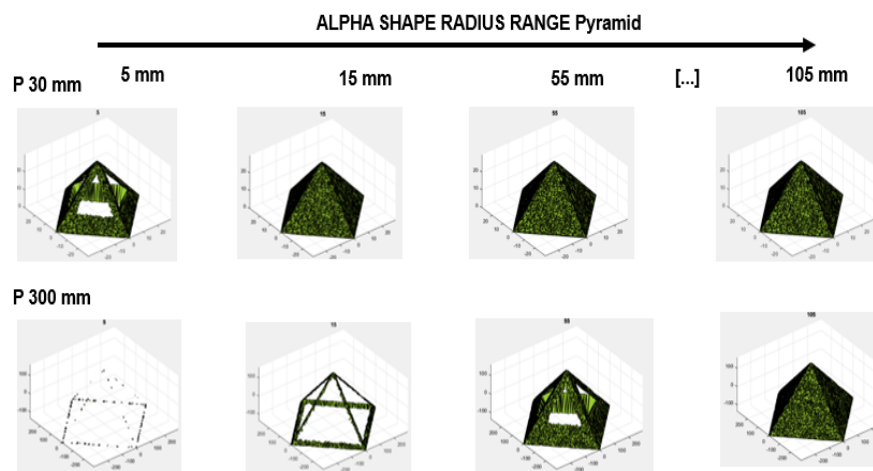
Figure 46 Alpha shape reconstruction of Pyramid varying the side length of the two group: 30 mm (Sample group 1) and 300 mm (Sample group 2).
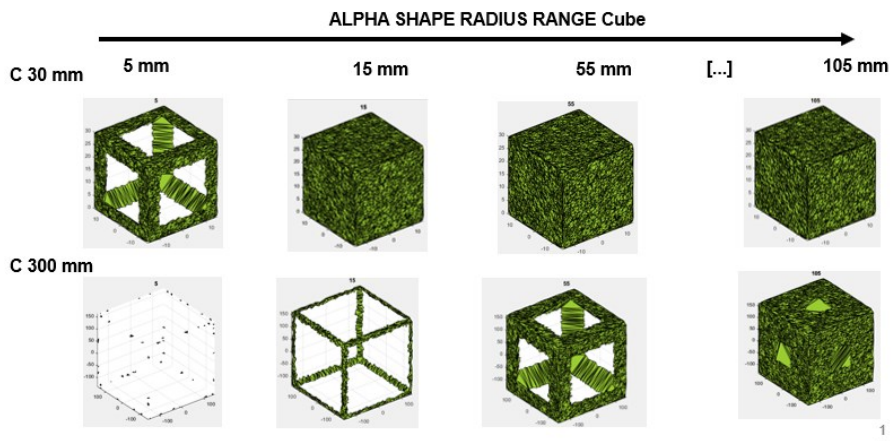
Figure 47 Alpha shape reconstruction of Cube varying the side length of the two group: 30 mm (Sample group 1) and 300 mm (Sample group 2).

Figure 48 Alpha shape reconstruction of Sphere varying the side length of the two group: 30 mm (Sample group 1) and 300 mm (Sample group 2).

For some values of alpha, the shapes of the objects are not reconstructed. In particular the sphere of Sample group 2 is never reconstructed in fact the volume is zero.

Test A: Effect of reconstruction on model. In Table 10 are shows the Maximum (Max), Minimum (Min), Mean, Standard deviation (Dev.Std), the Uncertainty (Unc) and the Uncertainty Percentage (Unc %) of the alpha radius (A.R.) changing from 5 to 105 mm of Sample Group 1.

Table 11 and Table 11 Max, Min, Mean, Dev.Std, Unc and the Unc % of the A.R. reconstruction changing from 5 to 105 mm of Sample Group 2.those metrics 2 are shown.

Table 10 Max, Min, Mean, Dev.Std, Unc and the Unc % of the A.R. reconstruction changing from 5 to 105 mm of Sample Group 1.

[mm]	5	15	25	35	45	55	65	75	85	95	105
Max	100.00	100.00	17.80	17.80	17.80	17.79	17.79	17.79	17.79	17.79	17.79
Min	0.03	0.02	0.01	0.01	0.01	0.01	0.01	0.01	0.01	0.01	0.01
Mean	61.18	21.70	3.88	2.03	2.03	2.03	2.03	2.03	2.03	2.03	2.03
Dev.Std	40.53	33.36	7.15	5.58	5.58	5.57	5.57	5.57	5.57	5.57	5.57
Unc	13.51	11.12	2.38	1.86	1.86	1.86	1.86	1.86	1.86	1.86	1.86

Unc%	22.08	51.24	61.38	91.56	91.60	91.61	91.63	91.65	91.67	91.68	91.69

Table 11 Max, Min, Mean, Dev.Std, Unc and the Unc % of the A.R. reconstruction changing from 5 to 105 mm of Sample Group 2.

A.R. [mm]	5	15	25	35	45	55	65	75	85	95	105
Max	19363.39	738314.1	3703995	7925037	13205699	19091311	66950190	75452144	78011929	79983256	81662915
Min	0.05	1.08	2.75	8.8	29.85	42.88	57.67	77.86	109.06	158.71	249.55
Mean	4112.69	235987.9	930072	1897562	3066527	4487252	10548549	12278668	13430508	14540075	15590921
Devstd	6473.2	241890.5	1137184	2437302	4073989	5894007	20321181	22898203	23691651	24377213	25032024
Unc	2157.73	80630.16	379061.2	812433.9	1357996	1964669	6773727	7632734	7897217	8125738	8344008
Unc%	52.47	34.17	40.76	42.81	44.28	43.78	64.21	62.16	58.8	55.89	53.52

Investigation range is correct after some alpha vale. The problematic alphas are located in: Sample 1: 5mm< alpha < 35mm and Sample 2: 5mm< alpha < 55mm.

For Sample group 2 the uncertainty has a minimum of 34 % in alpha= 15mm. After decrease form 52.5% in alpha = 5 mm to 43,7 % in alpha= 55 mm. From alpha 65 mm to alpha 105 mm the uncertainty is varying linearly from 64% to 53.5%. In these ranges, for the same number of points and geometries with different sizes, the uncertainty of the reconstruction is higer on small geometries (Sample 1). Alpha=5mm filed. For a large variation in alpha, the uncertainty decreases with until it becomes constant.

Looking at uncertain reconstruction of the different geometry, Table 12 shows the uncertainty (Unc), the uncertainty percentage (Unc %), the Correction factor (CC factor) and the uncertainty percentage corrected (Unc corr. %) eliminating the alpha radius equal to 5 mm that failed in all the acquisitions The minimum (Min), the maximum (Max) and the standard deviation (Dev.Std) are shown.

Table 12 uncertain reconstruction of the different geometry of Sg1 and Sg2

Sg1	Max	Min	Mean	Devstd	Corr fact	Unc	Unc %	Unc corr.
P_10	666.60	666.47	666.58	0.04	1.00	0.01	0.00	0.00
P_30	17996.89	5586.11	16868.05	3741.80	0.94	1128.19	6.69	0.00
P_50	83309.74	16072.81	77189.45	20270.10	0.76	6111.66	7.92	0.00
Q_10	999.88	833.06	984.70	50.29	0.99	15.16	1.54	0.00
Q_30	26996.17	3788.65	24476.04	6993.07	0.91	2108.49	8.62	1.70

Q_50	124971.31	6618.85	105445.89	39944.90	0.84	12043.84	11.42	6.60
S_10	522.82	522.82	522.82	0.00	1.00	0.00	0.00	0.00
S_30	14116.17	0.04	12832.89	4256.18	0.91	1283.29	10.00	0.00
S_50	65353.54	0.08	53471.14	26436.67	0.82	7970.96	14.91	11.11

Sg2	**Max**	**Min**	**Mean**	**Dev Std**	**Corr fact**	**Un unc**	**Unc %**	**Un corr.**
P_100	666504.52	19363.39	532721.00	221778.84	0.80	66868.84	12.55	8.58
P_300	16354339.58	4884.81	7223201.24	5540225.38	0.40	1670440.80	23.13	21.07
P_500	81662914.88	390.28	38793198.08	34888488.54	0.38	10519275.09	27.12	25.38
Q_100	999766.93	11380.46	695761.31	376705.95	0.70	113581.12	16.32	13.38
Q_300	13550583.78	935.71	5433385.60	4506420.61	0.20	1358736.94	25.01	23.12
Q_500	26560872.77	58.67	10044748.57	8822129.29	0.08	2659972.06	26.48	24.71
S_100	522808.07	0.28	285176.92	260311.84	0.54	78486.97	27.52	25.82
S_300	249.55	0.57	70.07	72.75	0.00	21.94	31.31	29.86
S_500	250.98	0.05	110.20	75.76	0.00	22.84	20.73	18.41

Indicating with s1 Unc % the percentage uncertainty of alpha shape reconstruction of the different geometry of Sample group 1, and with s2 Unc % the uncertainty reconstruction of group 2, the ratio between the shapes of the two group is evacuated. This relationship is shown as well as the density s1 in Table 13 (of group 1) and Density s2 (of group 2).

Table 13 Uncertainty ratio of different Samples group.

Objects	s1 Unc %	s2 Unc %	Us2/Us1 %	Density s1 np/[mm^2]	Density s2 np/[mm^2]
P_1	0.002	8.58	0.02	16.47	0.17
P_3	6.68	21.07	31.70	1.83	0.02
P_5	7.92	25.38	31.21	0.48	0.01
Q_1	1.54	13.38	11.51	15.00	0.15
Q_3	8.62	23.12	37.28	1.67	0.02
Q_5	11.42	24.71	46.22	0.60	0.01
S_1	0	25.82	-	28.65	0.29
S_3	10	29.86	33.49	3.18	0.03
S_5	14.90	18.41	80.93	1.15	0.01

The maximum uncertainty ratio between two samples is located in sphere with diameter =500 mm (80%). For some geometry e.g., Pyramid (side length = 10 mm), the density ($15 np/mm^3$) and size are influencing the final reconstruction, in fact the uncertainty of reconstruction is low. But is different for cube with the same length a similar density, in this case the uncertainty relationship is 11.51%.

Test B: A Box Plot of influence of alpha radius changing on volume evaluated for all geometries is shown in Figure 49 (Sg1) and Figure 50 (Sg2). The final aim is to analyse the total effect of alpha shape reconstruct algorithm changing alpha radius on different known shapes. For samples 1, the major error is given by cube. For Sample 2 reconstruction problem is confirmed in pyramidal shape. By this analysis is clear that the sphere is most problematic shape, in fact in Sample Group 2 the sphere never will be reconstructed in this investigation range, in fact the volume is zero. The Pyramid with side 50 and 500 mm is well reconstructed in both cases, with an outlier that correspond to alpha= 5 mm and has a high influence of alpha radius changing in Sample group 2. The Cube is well reconstructed by alpha shape algorithms in fact it is possible to reconstruct this shape from size equal to 30 mm.
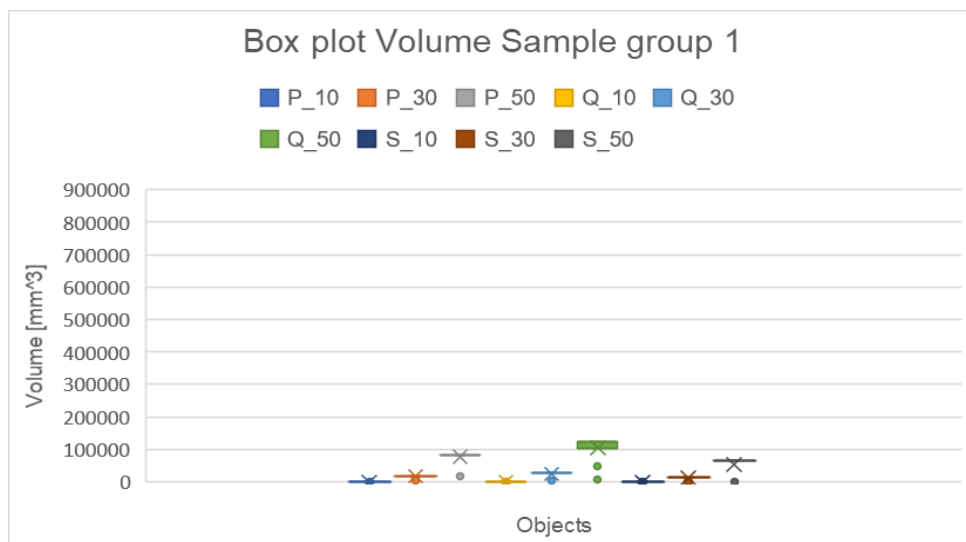
Figure 49 Box Plot of volume evaluated changing alpha radius for all geometries of Sample Group 1.
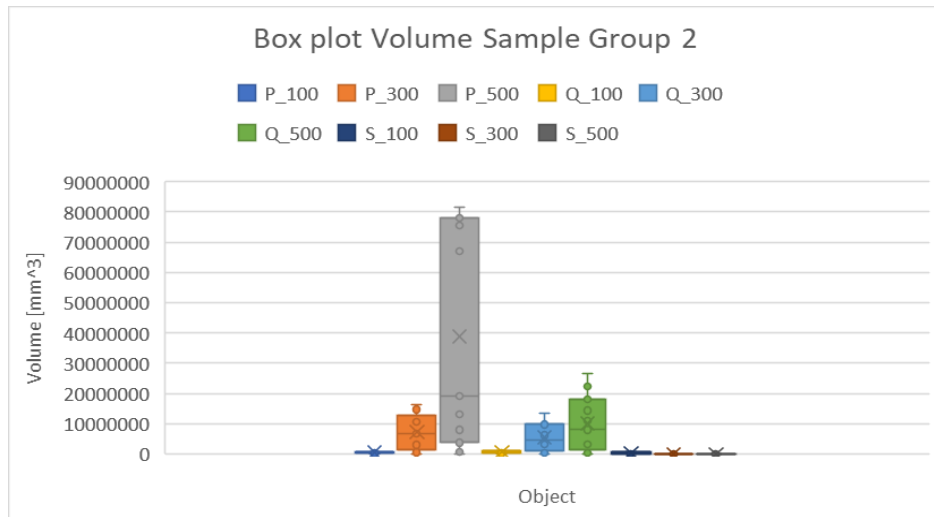
Figure 50 Box Plot of volume evaluated changing alpha radius for all geometries of Sample Group 2.

In general, the choose of alpha radius is influenced by the shape. Finally, the MAPE of all volume given changing alpha radius is shown in Figure 51. In Figure 52 the MAPE of different alpha radius reconstruction will be shown.
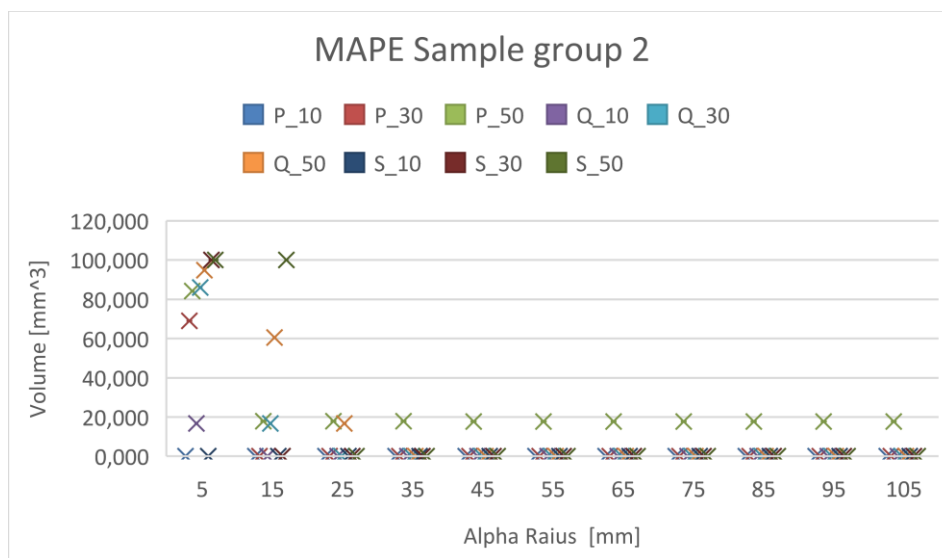
Figure 51 MAPE of volume reconstructed varying alpha radius Sample Group 1
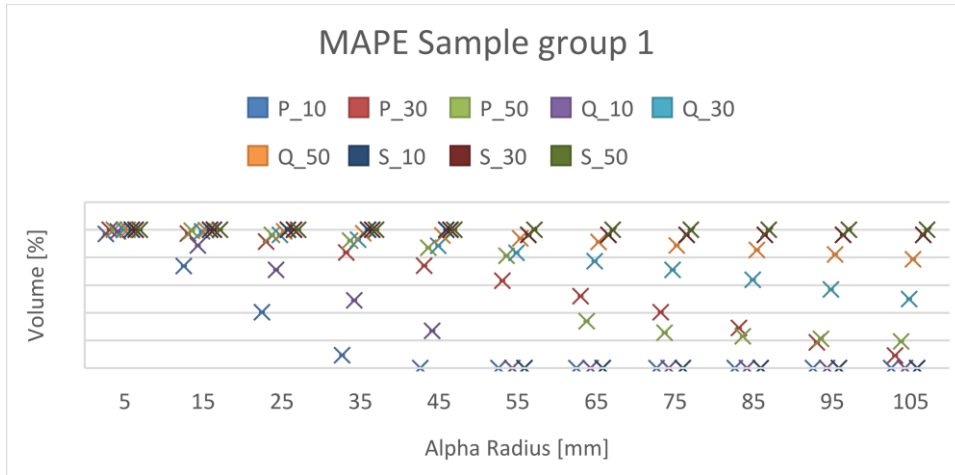
Figure 52 MAPE of volume reconstructed varying alpha radius Sample group 2

In Sample 1 MAPE start to be 20 % after alpha=15 mm. In this case the shape is reconstructed but not for sphere. In biggest sample, the sphere is never reconstructed in fact the MAPE is 100%. After alpha=35 mm the algorithms can reconstruct the other geometries with a MAPE inside the 20%. The distance with reference decrease since alpha increase. In Sample group 2 alpha radius > than 75 mm start to decrease the MAPE, in fact a lot of alpha value enter in a range of 20 %. By this analysis, this value can be selected and taken as reference for discard other value. Finally, the box plot of MAPE of different geometries and size is shown in Figure 53 an Figure 54 .
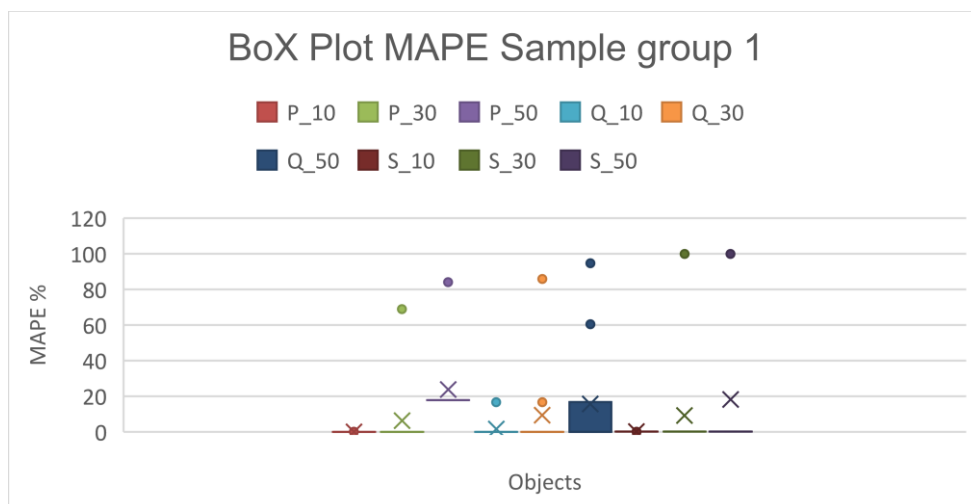
Figure 53 Box Plot of MAPE Sample Group 1
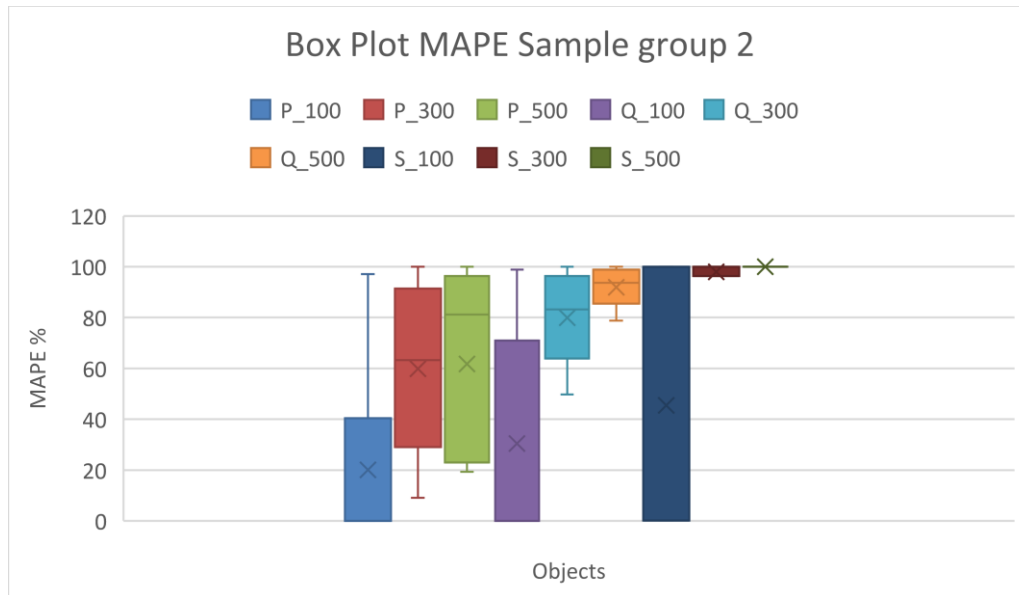
Figure 54 Box Plot of MAPE Sample Group 2

This plot shows the real influence of alpha radius changing compared with reference. The bed reconstruction is again confirmed by sphere.

Finally, the relationship between uncertainty of two different sample size and density is evaluated. Generally, smaller geometries allow better reconstruction, in fact for smaller geometries a minimum alpha radius of 15 mm is found. For bigger geometries a minimum alpha radius of 75 mm is found. The uncertainty ratio between the biggest and smallest geometry is found. The max uncertainty is located in less density, except for sample 2 with sphere diameter 500mm with point density of 0,015 np/mm^2.

3.3.2 Alpha Critical (AC), Alpha Optimal (AO) and Convex Hull (CH) Simple virtual objects

Analyzing the other algorithms applied to this simple geometry, since the Convex Hull has radius equal to infinite, will be compute the alpha radius given by Alpha Critical algorithm (A CR) and the alpha radius optimal (A Opt). In Table 14 the alpha radius of Sample group 1 (Sg1) and Sample group 2 (Sg2) are showed.

Table 14 alpha radius critical (A CR) and alpha radius optimal (A opt) of Sample group 1 (Sg1) and Sample group 2 (Sg2).

	S g 1		S g 2	
	A CR	A opt	A CR	A opt
P_1	3.53	18687529095.81	35.37	934969652998.52
P_3	10.52	94750358615.38	104.50	61138905461.3
P_5	10.40	13277388296.14	104.48	22141516909689600.
Q_1	4.79	130514.34	48.19	50631664.15
Q_3	14.32	30770.70	144.60	19442696.06
Q_5	23.89	300497.72	240.30	12723700.30
S_1	4.95	8231.75	49.67	28543.48
S_3	14.89	4759.09	148.68	143793.45
S_5	24.75	20303.56	249.17	188713.74

The previous Table shows the alpha radius evaluated by Alpha Critical that connects all points for each acquisition and the optimal alpha that returns the nearest volume to the reference one. As it is possible to notice, the Alpha Critical radius in both Sample groups is proportional. The Alpha Optimal algorithms, that search the best alpha radius that returns the nearest volume to the reference, has a high value of alpha radius. In Figure 55 and Figure 56 the value of volume evaluated by the three algorithms Alpha Optimal (V opt), Alpha Critical (V cr) and Convex Hull (VCH) are shown.
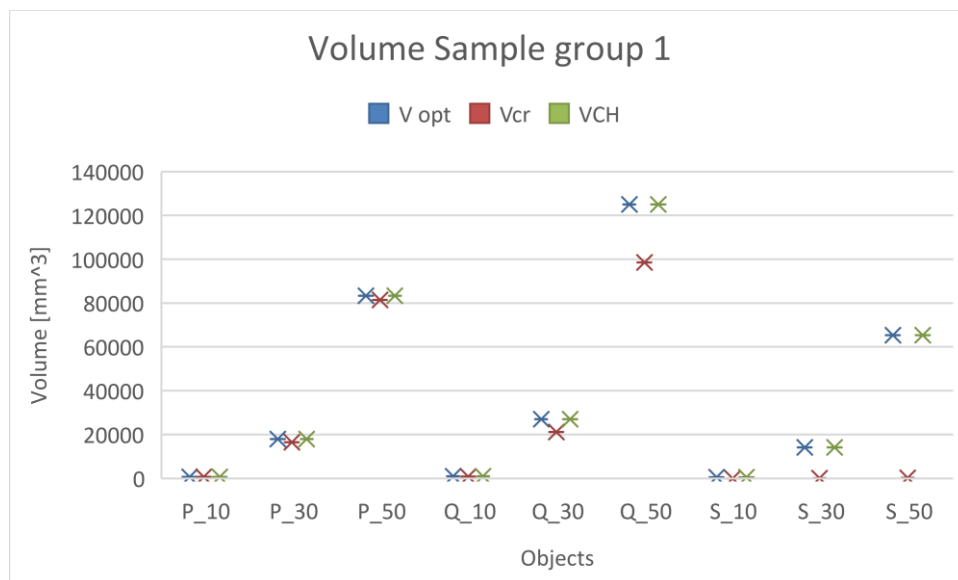
Figure 55 Volume evaluated by V opt, V cr and VCH algorithms for Sample group 1
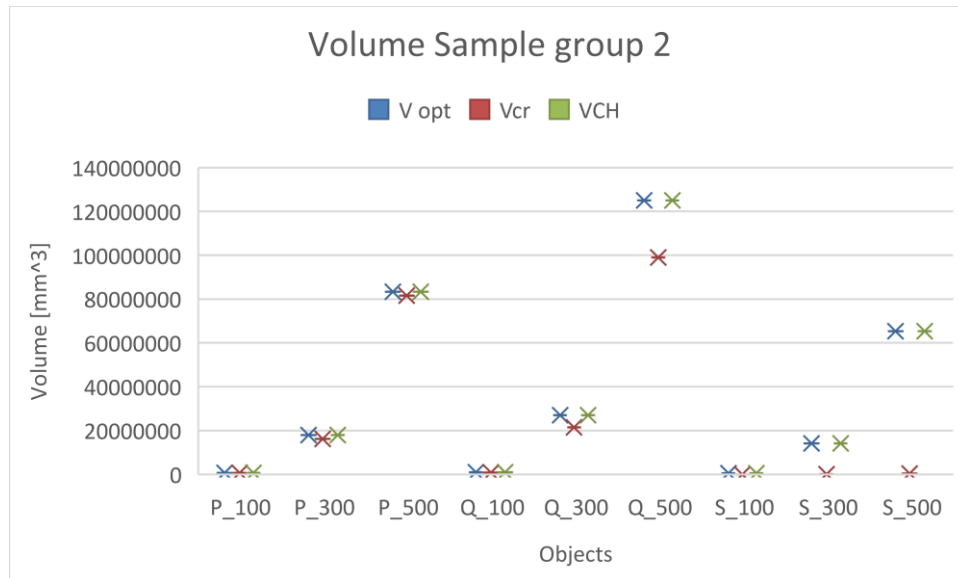
Figure 56 Volume evaluated by V opt, Vcr and VCH algorithms for Sample group 2

The volume gives by Alpha Optimal radius, for both Samples size is equal to Convex Hull this mean that the maximum value of volume is given by optimal radius. For both Samples group 1 and 2, the relationship between volume, shape and size of the nine simple objects are proportional for all algorithms. For biggest shape, in both cases Alpha Critical returns a lower value of volume and in sphere case. In Table 15 the value of Volume evaluated by different algorithms are showed.

Table 15 Volume evaluated by V opt, Vcr and VCH algorithms for Sample group 1 and 2.

S g 1	V opt	Vcr	VCH
P_10	666.62	612.32	666.62
P_30	17997.75	16401.26	17997.75
P_50	83320.63	81453.33	83320.63
Q_10	999.89	792.91	999.89
Q_30	26997.23	21085.60	26997.23
Q_50	124980.76	98480.71	124980.76
S_10	522.82	1.20	522.82
S_30	14116.17	43.93	14116.17
S_50	65353.54	160.64	65353.54

S g 2	V opt	Vcr	VCH
P_100	666585.10	614762.84	666585.10
P_300	17998720.56	16226319.98	17998720.56

P_500	83326720.21	81520196.40	83326720.21
Q_100	999880.20	801851.61	999880.20
Q_300	26995961.52	21504757.46	26995961.52
Q_500	124984595.05	98970287.90	124984595.05
S_100	522808.15	1727.16	522808.15
S_300	14116219.90	37178.34	14116219.90
S_500	65353085.87	326456.79	65353085.87

Since the reference volume is known, the MAPE of both Sample group is evaluated and showed in Figure 57 and Figure 58.
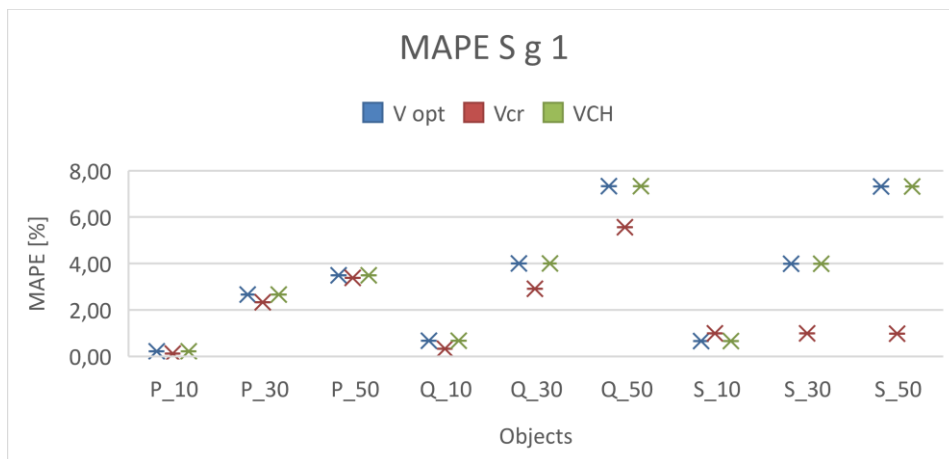
Figure 57 MAPE Sample group 1
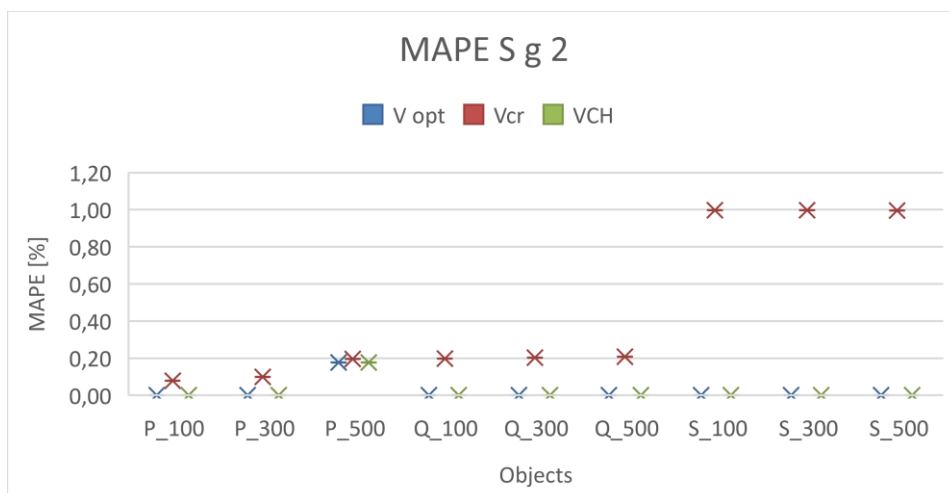
Figure 58 MAPE Sample group 2

These previous Figure are confirming that the MAPE is the same for both Alpha Optimal and Convex Hull algorithms. The maximum MAPE of Sample group 1 is near to 8% while for Sample group 2 is 1 %. This value of MAPE is also the same for all the spheres (S) in Sample group 1. This mean that for this shape, Alpha Critical in not influenced by size. For the other object Pyramid (P) and Cube (Q) Volume gives by Alpha Critical increase as for Alpha Optimal and Convex Hull. The minimum value of MAPE is by Pyramid (P). For as regard the objects of Sample group 2 with biggest size, the best representation of volume is given by Alpha optimal and Convex Hull algorithms. Alpha shape in both sphere diameter size is the same, equal to 1%. In this case for the Pyramid shape the three algorithms returns similar value.

The algorithm developed, in the case of simple and virtual geometries, therefore in ideal cases coincides with the Convex Hull. In this case it is also possible to evaluate the optimal alpha.

3.3.3 Alpha Shape (AS) on scanned complex object

The comparison of volume of complex geometry evaluated changing alpha radius from 5 mm to 105 mm with a step of 10 mm is showed in Figure 59.
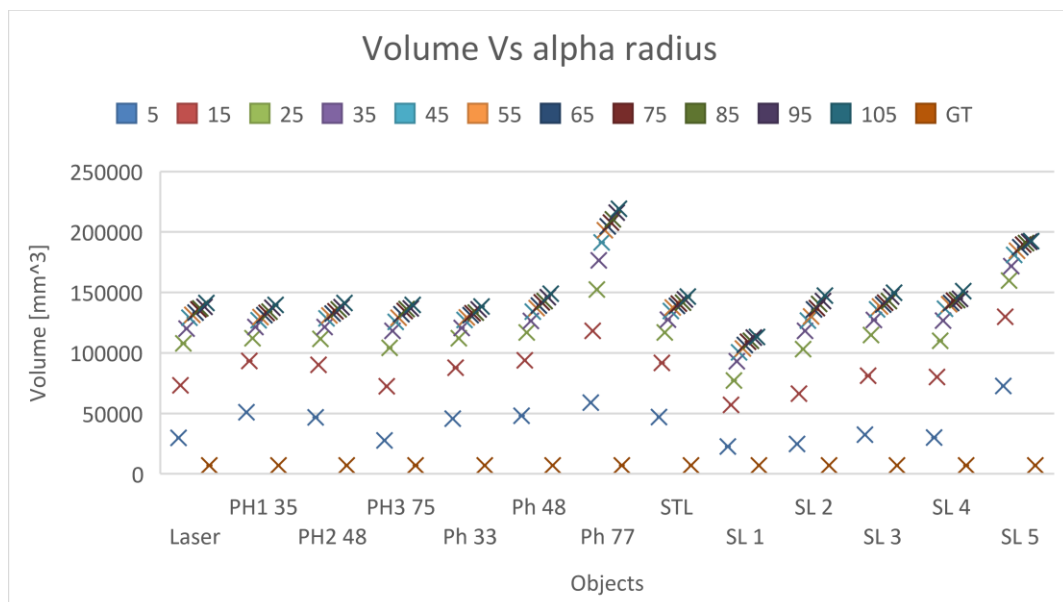
Figure 59 Box Plot show the effect of alpha radius changing on this shape.

The box Plot show the effect of alpha radius changing on this shape. The photogrammetric techniques bot high and low cost seems to have a same behavior except for webcam reconstruction by 77 pictures where the volume is exceeding the others. In this case the GT is equal to 7018.66 mm^3, this means that all alpha radius is overestimating the reference volume.

By this analysis it is possible to know the effect of alpha radius changing on this complex geometry (Figure 60).
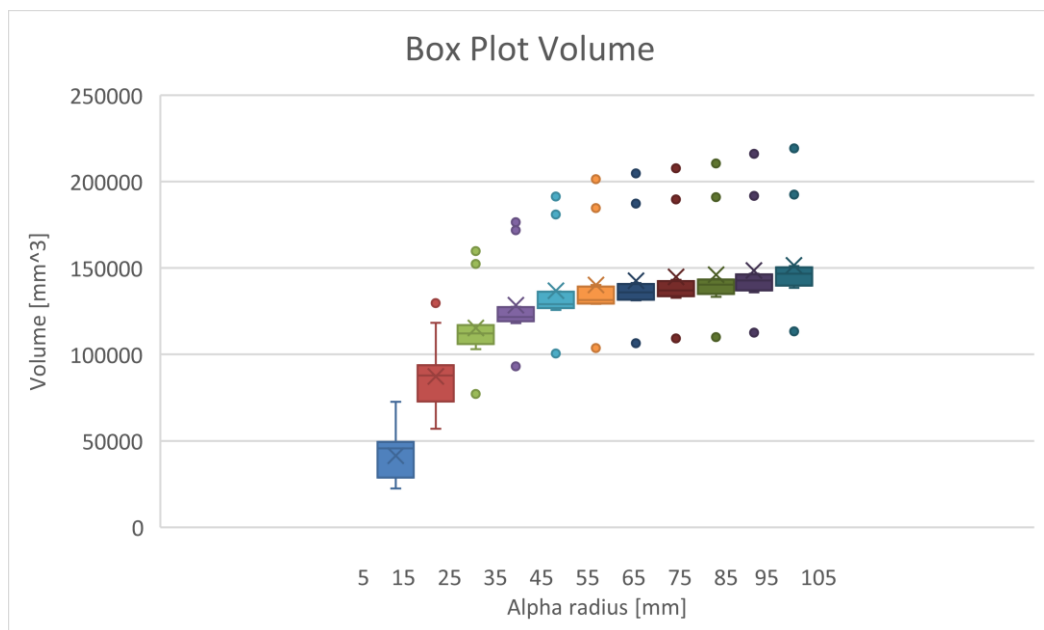
Figure 60 Effect of alpha radius on complex shape

From the Figure it can be seen how the volume increases as alpha increases. Here the effect can be seen as given the same number of points on different geometries, the effect of the scans has relatively little influence on the final evaluation of the volume. From the previous it is possible to see that the volume increase and the high error of value from alpha radius=5 mm and 15 mm. After this value there is a stabilization of value with the increase of outliers. In fact, for some alpha the geometry is not reconstructed. In Table 16 the uncertainty of reconstruction is showed as did for test A in Simple objects.

Table 16 the uncertainty of reconstruction.

	5	15	25	35	45	55	65	75	85	95	105
Max	72553.14	129751.1	159849.1	176563.1	191418.6	201306.1	204638.5	207717.4	210513.7	215963.6	219221.5
Min	22490.07	56922.86	77080.51	93172.98	100468.9	103723.3	106536.9	109184	110063.7	112578.4	113253.5
Mean	41287.01	87312.56	115342.4	128418.7	136797.9	140252.9	142639.9	144728.3	146081	148490.5	151465.4
Dev.std	14288.26	19118.37	20028.39	21294.65	22890.89	24287.68	24461.15	24662.55	25013.35	25475.82	25458.88
Unc	3962.85	5302.48	5554.88	5906.07	6348.79	6736.19	6784.3	6840.16	6937.46	7065.72	7061.02
Unc %	9.6	6.07	4.82	4.6	4.64	4.8	4.76	4.73	4.75	4.76	4.66

The peak in this case is in alpha equal to 35 mm as the Simple object group 1. After this value the uncertainty of reconstruction decrease with a low value of slope as the Sample group 2 with big dimensions. The alpha reconstruction of 3D printed lettuce of Webcam and Canon with 48 pictures are showed in Figure 61.
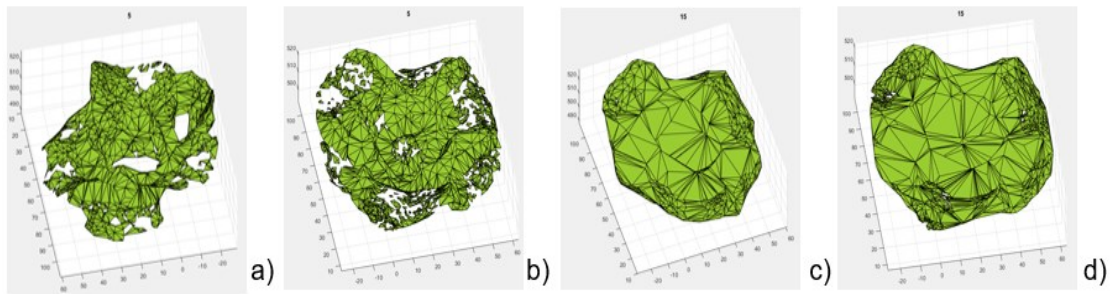
Figure 61 Example of alpha shape reconstruction with photogrammetric techniques using 48 pictures of a) Webcam and b) Canon with alpha radius = 5 mm; c) Webcam and d) Canon with alpha radius = 15 mm.

The Figure show that after a certain alpha located near to 20 mm, the alpha radius overestimates the shape. In Figure 62 the MAPE of each alpha radius was evaluated in order to analyze the differences of the reconstructed model compared with reference or GT.
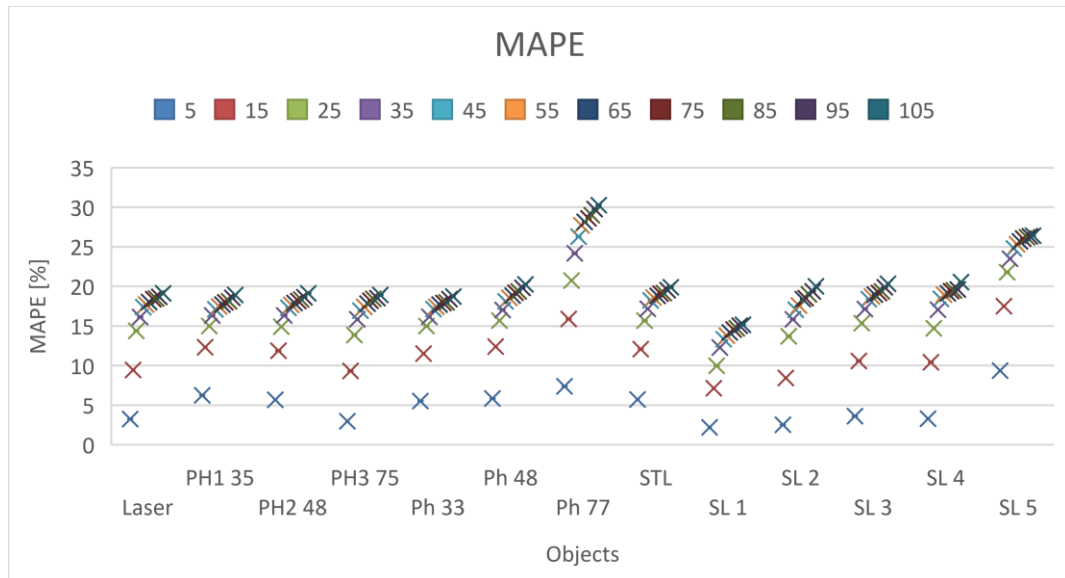
Figure 62 MAPE of different techniques.

As is possible to notice, changing the instrument and subsampling with the same number of point (resolutions), the behaviors is similar, in particular for photogrammetric both low (Ph) and high (PH) cost techniques. Finally, in Figure 63 the Box Plot of MAPE is showed.
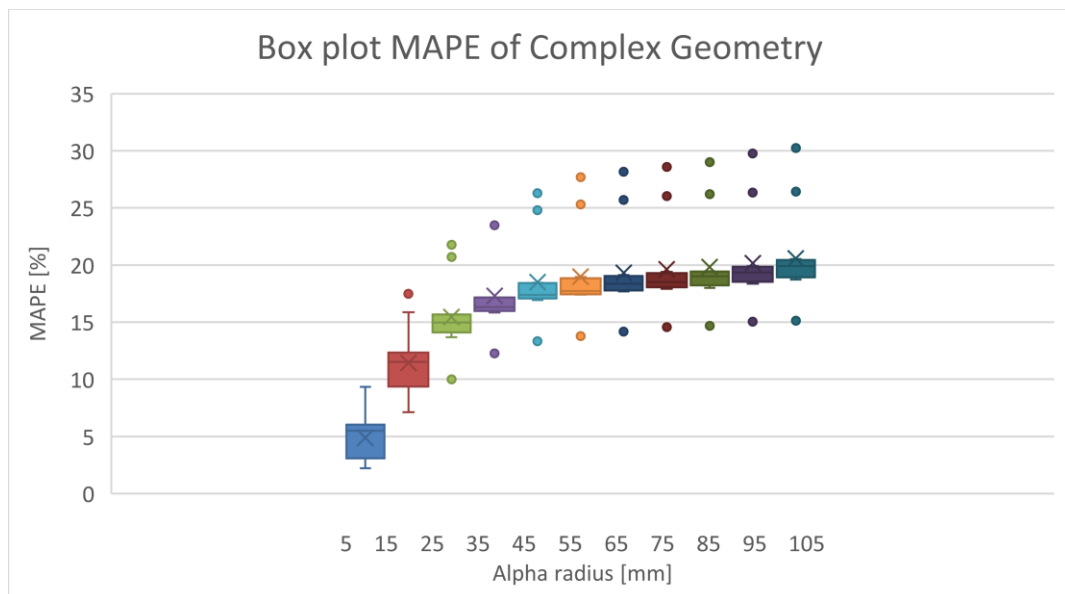
Figure 63 Box Plot of MAPE of 3D printed lettuce plant.

The previous Figure shows the outliers. The other alpha radius exceeds the volume for a 20 %. For some instrument the alpha is influencing too much the Volume evaluation, but with the same trend. After alpha = 25 mm the volume start to have the same shape except for some outliers. Furthermore, the MAPE has the same shape of the volume represented in previous Figure 64.

Finally, for each geometry the uncertainty of reconstruction varying alpha shape is evaluated. In Table 17 Analysis result. the result of analysis is showed.

Table 17 Analysis result.

	Min	**Max**	**Mean**	**Dev std**	**C.C.**	**Unc**	**Unc**	**Unc.corr**
	[mm^3]	**[mm^3]**	**[mm^3]**	**[mm^3]**	**[%]**	**[mm^3]**	**[%]**	**[%]**
Laser	141192.1	29746.52	116051.9	33040.24	0.06	9962.01	8.58	4.95
PH 35	139787.2	50868.59	119078.9	24983.02	0.06	7532.66	6.33	3.32
PH 48	141299.1	46773.22	119240	26796.75	0.06	8079.52	6.78	3.64
PH 75	139796.9	27679.81	114264.4	33161.85	0.06	9998.67	8.75	5.05
Ph 33	138418	45618.95	117657.9	26566.38	0.06	8010.06	6.81	3.63
Ph 48	148986	47913.79	125037.1	28646.31	0.06	8637.19	6.91	3.75
Ph 77	219221.5	58861.43	177901.6	47604.33	0.04	14353.25	8.07	5.09
STL	146638.6	47031.75	124303	28679.7	0.06	8647.26	6.96	3.77
SL 1	113253.5	22490.07	91406.82	27301.97	0.08	8231.86	9.01	5.55
SL 2	147289.9	24757.61	115704	36218.42	0.06	10920.27	9.44	5.85
SL 3	149758.8	32299.53	122804.2	34072.48	0.06	10273.24	8.37	4.65
SL 4	151036.7	30136.68	122464.8	35077.12	0.06	10576.15	8.64	4.9
SL 5	192371.7	72553.14	168323.2	35188.07	0.04	10609.6	6.3	3.34

The correcting factor in this case is near to zero, so this mean that the volume increases linearly. The highest uncertainty of reconstruction is in SL.

3.3.4 Alpha Critical (AC), Alpha Optimal (AO) and Convex Hull (CH) scanned complex object.

Again, the Volume given by Convex Hull, Alpha Critical and alpha optimal algorithms was evaluated. In this case alpha radius optimal give a different value of volume compared with Convex Hull in contrast to simple geometry. Alpha Optimal returns the lower volume. Alpha Critical again give a good representation of shape

but with an overestimation. In Figure 64 the Result of different algorithms are showed.
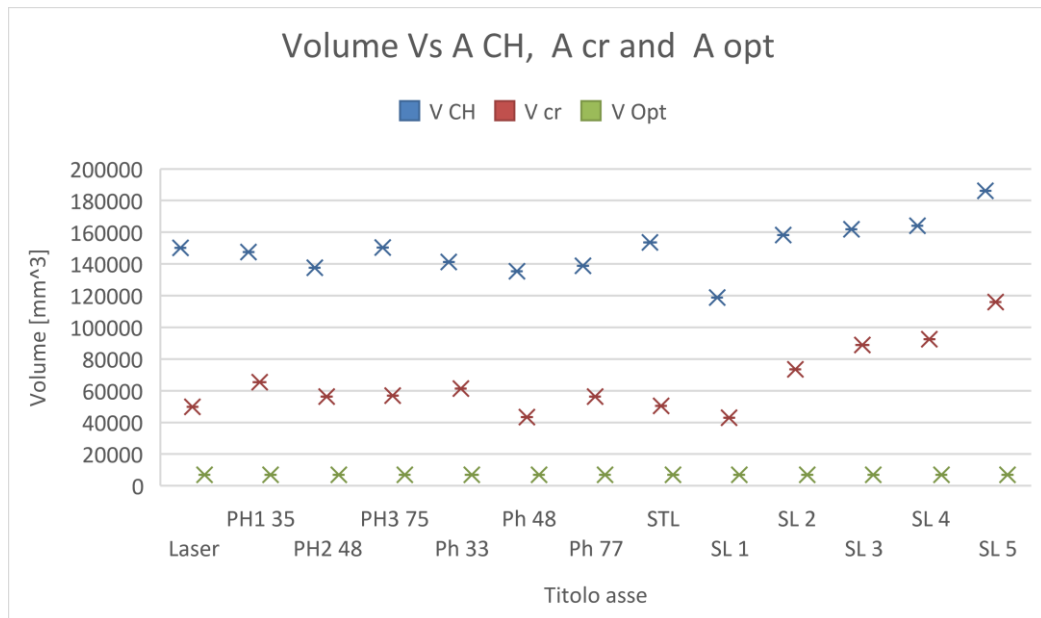
Figure 64 Volume by CH AC A opt of 3D printed lettuce.

Considering that the STL volume is 7018 mm^3 these algorithms are overestimating the reference. Alpha Optimal seems to give a good representation of volume. Alpha Critical and Convex Hull have the same shape but with different dimensions, in fact CH is overestimating the shape as sow in the precious analysis of simple object. In Table 18 the volume and radius given by AC and Opt. algorithms and Convex Hull are showed.

Table 18 Volume Convex Hull, Critical Volume, Optimal Volume, Alpha Critical and Optimal radius of the different acquisitions.

	V CH	V CR	V opt	A Cr	A opt
Laser	150218.53	49786.90	7012	10.90	2.84
PH1 35	147569.02	65348.34	7002.43	11.03	2.79
PH2 48	137591.36	56286.31	7018.26	11.29	2.68
PH3 75	150359.37	56989.98	7017.88	10.37	2.62
Ph 33	141200.60	61298.51	6938.15	10.77	2.81
Ph 48	135322.74	43431.15	6976.05	7.64	2.85
Ph 77	138777.58	56327.32	6924.46	10.57	2.71
STL	153502.77	50519.22	7018.68	9.80	1.90

SL 1	118871.46	42845.25	7022.56	13.70	3.28
SL 2	158286.18	73456.85	7018.30	16.87	2.54
SL 3	161961.66	88921.82	7018.71	16.94	1.91
SL 4	164059.31	92446.01	7013.08	17.24	1.61
SL 5	186174.40	115872.33	7017.63	13.90	2.53
Max	186174.40	115872.33	7022.56	17.24	3.28
Min	118871.46	42845.25	6924.46	7.64	1.61
Mean	149530.38	65656.15	6999.86	12.39	2.54
Dev.std	15872.66	20765.65	31.54	2.95	0.45
Unc	4402.28	5759.35	8.75	0.82	0.12
Unc %	2.94	8.77	0.12	6.60	4.87

In addition, alpha Optimal radius is too low for reconstruct the geometry, this means that the algorithm is failed in fact by the previous analysis changing alpha, the radius = 5mm was not reconstructed the shape. Looking at MAPE, in Figure 65 the distance of these algorithms and GT is showed.
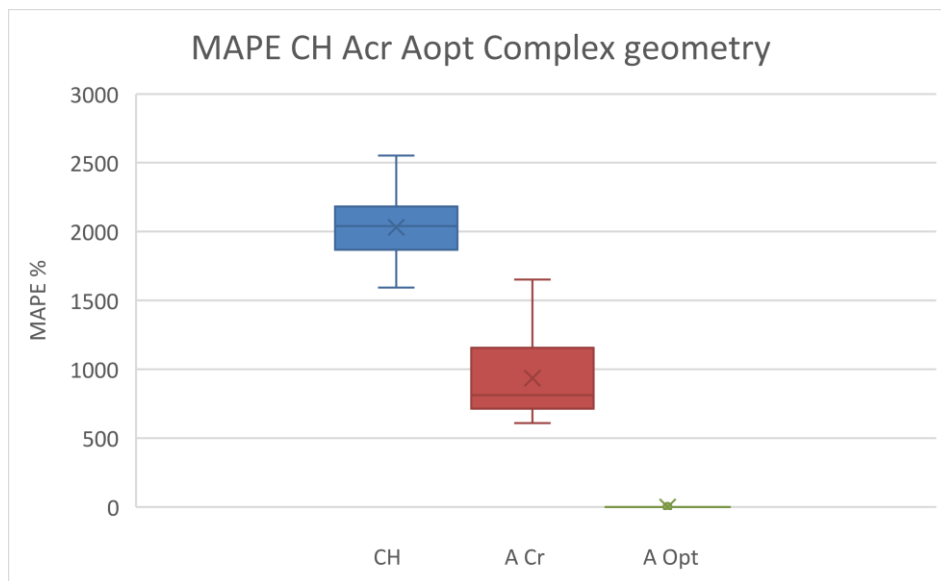
Figure 65 MAPE CH, A Cr, A Opt on Complex geometry 3D printed lettuce plant

The Convex Hull and Alpha Critical are overestimating the real volume of about 2000 % and 890 %. In this case the best representation is given by Alpha Optimal algorithms.

3.4 Conclusions

Alpha shape, Alpha Critical Alpha Optimal and Convex Hull algorithms was tested on simple object in order to evaluate the effect of size, density and shape on volume evaluation. In general, for these simple convex objects, too small alpha radii do not reconstruct the shape well and therefore the volume is not calculated. Up to alpha radius values of 105 mm some shapes, such as the sphere, are not reconstructed due to their large size and low density.

- Generally, smaller geometries allow better reconstruction.

- The spherical geometry is the hardest to reconstruct for alpha radius <105 mm, especially for bigger sizes.

- For smaller geometries a minimum alpha radius of 15 mm is found.

- For bigger geometries a minimum alpha radius of 75 mm is found.

- The uncertainty ratio between the biggest and smallest geometry is found.

Particularly for the sphere in Samples group 2, the alpha radius required to close the form is greater than 100 mm. The Convex Hull and the Optimal Alpha return the same volume value, the latter of which also calculates the radius required for the calculation. Finally, the critical alpha best approximates the actual volume. The maximum value for which the models deviate from the reference value is approximately 8 %.

In the case of more complex object:

- Varying the Alpha radius, a similar performance is obtained using different sensors.
- The distance of the CH and AC reconstructions from the reference model, ranges from 500% to 2000%
- A much better performance is obtained using the Alpha Optimal algorithms failed.
- Using the proposed algorithms, the reconstruction can be achieved even with cheaper scanning techniques.

In general, for simple convex object a high alpha radius is needed. For small radius the reconstruction failed and for high alpha the evaluation of volume starts to be constant. Convex Hull and Alpha Optimal are equal. Alpha Critical has a lower volume compared with reference. For complex Object, varying alpha radius the volume increases linearly. Alpha Optimal failed the reconstruction. Alpha Critical and Convex Hull has the same shape but with different value.

The selection of the optimal alpha value, extensively discussed in various articles [68], [88], [65], [66], [86], is influenced by the density and shape of the object being measured. The first question is how to choose this alpha value.

While the algorithm can reconstruct the entire shape of simple elements, it challenges more complex geometries, such as intricate leaves or thin objects (3D printed lettuce plant). In such cases, the alpha shape may not work well since is not reconstructing the shape. Despite the different tools used, a correspondence can still be seen in the calculation of the volume.

When analysing the sensitivity for simple geometries, the optimal alpha value is quite high, especially for concave shapes. Generally, smaller geometries are less influenced by variations in the alpha radius, while larger geometries exhibit the highest uncertainty, reaching up to 29.86%. Another study [67] assessed the uncertainty in volume measurement by directly immersing the object in water. The uncertainty is approximately 3%, slightly higher in our case due to the complexity of the geometries and the lack of an exact reference model. In [65] the volume overestimations range from 25% to 50%.

The volume increases with the radius alpha for both small and large geometries. Specific values have been identified, such as an alpha minimum of 15 mm necessary for shape reconstruction [61] and an alpha of 75 mm, beyond which the calculated volumes remain nearly constant [86].

Despite these challenges, our method fits well within the model and is computationally efficient, taking only 15 minutes for calculations, as opposed to the 30 minutes reported in another article [68].

Since the studies conducted up to now are limited to specific applications, the alpha shape algorithm will be evaluated in different fields in the next chapter.

Chapter 4

Advantage of Structured Light scanning system in different applications: Cultural Heritage, Biomedicine, Sport Training, Design

4.1 Introduction

The analysis and tests shown in the previous Chapter 2 will be applied to static objects that have never been scanned before, so there is no reference. The aim is to understand the potential of these algorithms combined with low-cost sensors. In this Chapter qualitative analysis are presented where a digitalization method was applied. Then a quantitative analysis will be performed using the previous algorithms presented in Chapter 2. This section will highlight examples of applications within the fields of four different applications are tested during experimental case studies, carried out in different field: Cultural Heritage (CH) [71] [72] [73], Medicine (M), Design (D) [74] and Sport Training (ST). Among all the possible applications, photogrammetry in general and SL in particular have been revealed in recent years as powerful methods to help protect and document cultural heritage, and especially to obtain details [75]of historical and archaeological object [8]. Factors contributing to accuracy and precision of Structured Light systems are investigated[76] [77] [39] [78] with a study of performance in the different applications [23]. The final high quality STL model in terms of meshes resolution and shape was taken as reference.

The objects are: the World Cup in Cultural Heritage application (CH), a 3D reconstructed human torso in Biomedicine application (B). In Sport Training application (ST), a test (stone) and a part of a boulder will be analysed. Finally, the last object is a pomegranate for Design application (D) [79]. For some of these

objects, like human for example, the measurements are almost difficult to repeat since they are changing their shape over the time. In the case of design applications, most fruits lost their organotypic characteristics very quickly. In the case of biomedical application, the object of study is a living organism. For the human body, the problem is that it changes in every moment (e.g., breathing and movement as presented in Chapter 6). For the qualitative approach, these different objects with different sizes were tested varying the number of points (1000, 3000, 6000, 9000 np) in order to analyse the effect of resolution in changed shape. This step is necessary because the number of points, and with it the resolution, will influence the computation time. In all cases the reference is given by the instrument with the maximum resolution and minimum uncertainty: the Structured Light scanner GO!Scan 50 that is a certified scanner. The scans were reconstructed, cleaned and modelled by an expert operator and high-quality software (GeomagicWrap). The volume given by this firs analysis was taken as reference. From STL files it is possible to transform the mesh into a point cloud maintain the resolution of final model, or to subsample the objects.

4.2 Materials and Methods

4.2.1 Cultural Heritage case

On the occasion of the 50th anniversary of its creation, the original plaster prototype of the World Cup made by Milanese artist Silvio Gazzaniga in 1971 was scanned at the University of Perugia, Italy. The solid gold original of the World Cup remains stored in a chest at FIFA's Zurich headquarters. The scanning of the original mould will make it possible to have an electronic graphic copy of the cup for possible future additive printing, so as to avoid damage if it is displayed in public at national and international exhibitions. Moreover, as the original cup is made of plaster, it is subject to deterioration even if kept in a museum. This project is part of a broader context, with the aim of assessing the feasibility of low-cost, non-contact measurement systems for the conservation of cultural heritage. There are no other 3D reproductions of this cup, all data in fact are subject to copyright.

The high-resolution scan performed with Go!SCAN 50 was used for the reconstruction of the final model. First the most complete scan was chosen as reference. A cleaning phase with noise reduction follow. A merge of missing part was performed taking the greater part of the other scans. The scans given by LiDAR were used for modeling since the texture were qualitatively greater. In the photogrammetric case, about one hundred pictures was taken ad a distance of 1 m

around the subject with an overlapping between images > 90%. The pictures were processed via 3DF Zephyr 6.0 by 3D FLOW and the 3D model was reconstructed. A smoothing phase than follow to sculpt the final model Figure 66.

a,b.c,d)

e)

Figure 66 Word Cup Scanned by a) LiDAR b) Photogrammetry c) Structured Light scanner with 1 mm of resolution d) Structured Light scanner with 0.5 mm of resolution and e) Final model.

The final model is now stored in Brescia Museum, Italy. Since the model was completed, it was also compared with the previous row scans in order to analyze the quality of reconstruction. In Figure 68 and Figure 68 Final model of Word Cup. Comparison with: c) Structured Light scanner with 1 mm of resolution d) Structured Light scanner with 0.5 mm of resolution.are showed the standard deviation between the reference model (by SL scan at maximum resolution of 0.5 mm and modelled) and

the other scans other measurement techniques (high and low cost) e.g., Photogrammetry with Canon, and LiDAR with I-Phone.
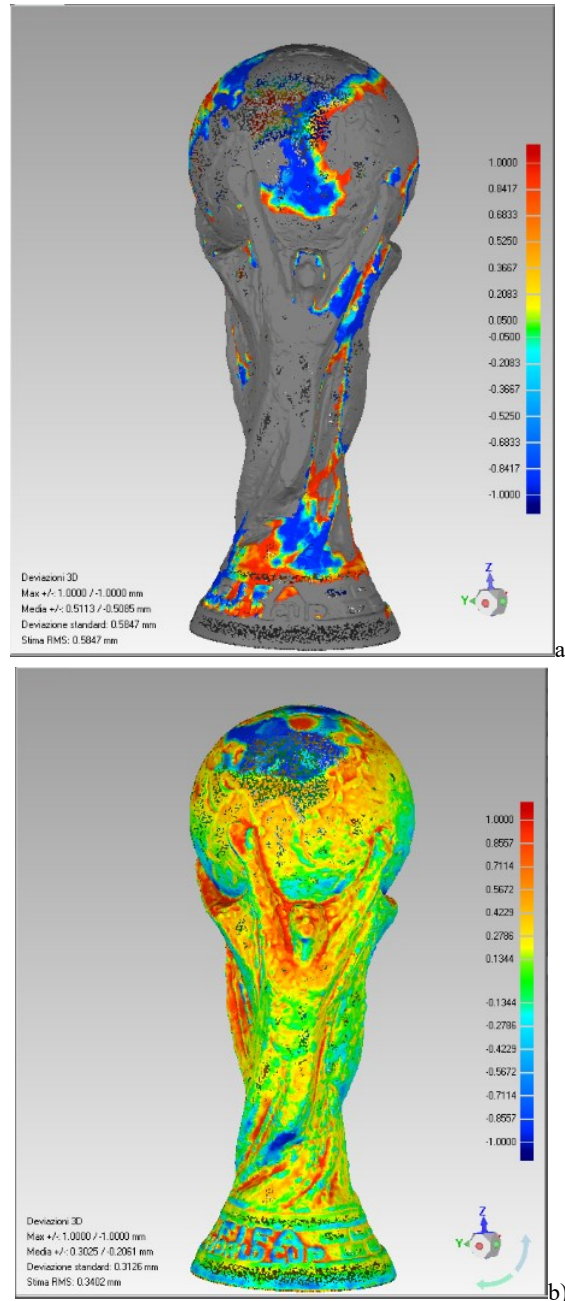
Figure 67 Final model of Word Cup. Comparison with: a) LiDAR b) Photogrammetry
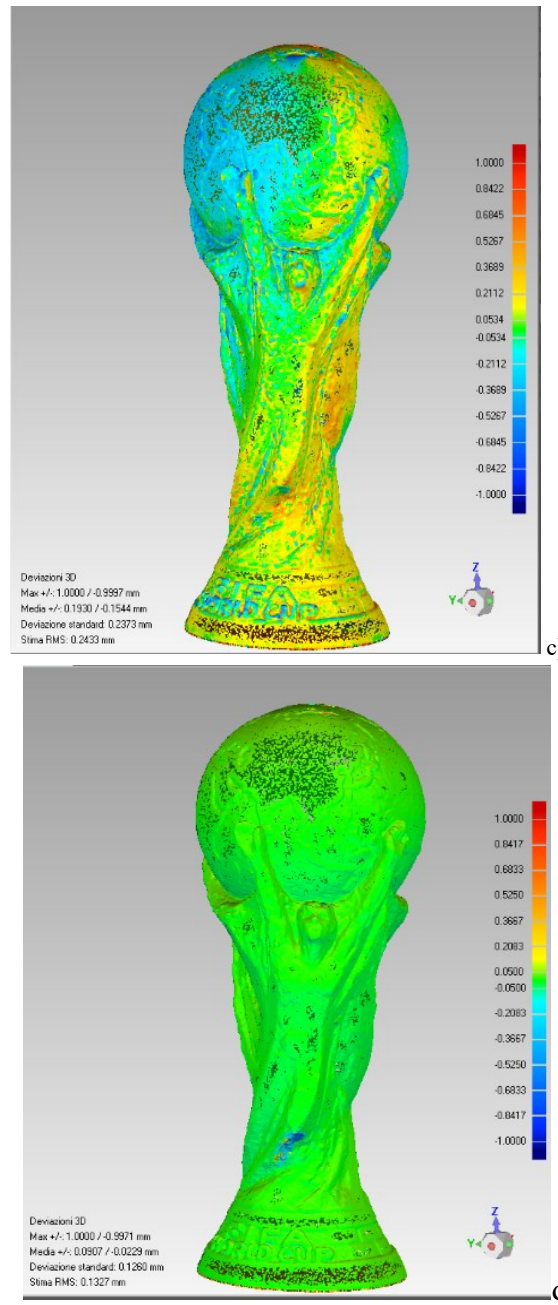
c)

d)

Figure 68 Final model of Word Cup. Comparison with: c) Structured Light scanner
with 1 mm of resolution d) Structured Light scanner with 0.5 mm of resolution.

A color-coded image of the computed distance of the points cloud is evaluated by
Geomagic Wrap the limit of distance to evaluate was set at 1 mm. Thanks this

analysis it is possible to know the quality of the final model and of the models given by the other instruments.

The LiDAR reconstruction in Figure 68 a is noisier than the others. This is confirmed by the higher Standard Deviation (St.Dev.) value of 0.58 mm. In addition, different error zones can be observed: in gray color are representing the scans parts more far than 1 mm (tacked as threshold) from the references. For as regard the photogrammetric reconstruction, with a St.Dev.=0.31 mm, has a failure of reconstruction in the top spherical part (coloured in blue) of the Cup where the deviation is -1 mm (the sign minus indicate that the shape is lower than reference). This mean that the shape of the World Cup scanned by photogrammetry it was not well reconstructed, in fact more pictures was needed in different heigh. The red colour indicate that the most concave part is not well detailed. The model scanned with SL resolution of 1 mm and 0.5 mm has respectively a Standard Deviation equal to 0.23 mm and 0.12 mm. From this Figure it is possible to see as LiDAR failed in reconstruction, but it was helpful for operator reconstruction of final model because his high quality of texture. The photogrammetry required 4 hours to process the pictures resulting time expensive but well detailed. The uncertainty increases with technique and instruments resolution decreasing.

4.2.2 Biomedicine case

For this application, two studies were performed: The first one is about a multi-scanning approach presented in Chapter 7 for the reconstruction of prothesis in a dynamic scenario. The second study is showed in this Chapter since the analysis are performed in a 3D printed mould, so in a static scenario. In general, a case study involving a child was considered, with the main aim of providing useful information on performances of scanning techniques for clinical applications, where boundary conditions are often challenging (i.e., non-collaborative patient). A full procedure for the 3D reconstruction of a human shape is proposed, in order to setup a helpful workflow for clinical applications in Chapter 7. This work was made in collaboration with an orthopedic laboratory (Officine Orthopedical Semidoro srl, Perugia, Italy).

In this Chapter the aim was to evaluate the volume of a 3D printed body shape in order to know how this shape affect the scans. By knowing the volume, one can know the amount of filament for what concerns 3D printing, it gives much more information to the doctor and one can also think of using these scanning methods

for monitoring other pathologies. The final reconstructed scan, was cleaned, filtered and analysed in order to print the modul for the prothesis. In Figure **69** The final the 3D printed mould is showed.

a)

b)
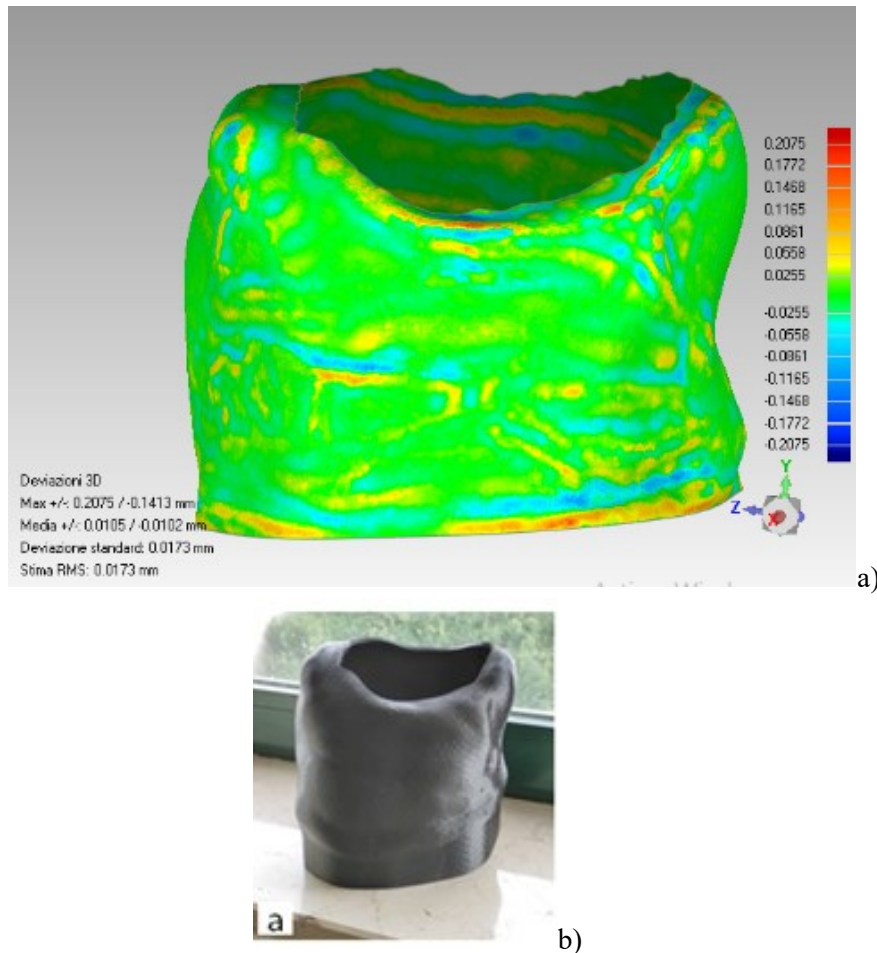
Figure 69 a) Comparison between row model scanned with the structured light scanner GO!Scan 50 and final model b) 3D printed torso

The Standard Deviation is low around 0.01 mm. The maximum standard deviation is located near the neck and is equal to 0.1 mm. Another point where the effect of modelling can be seen is at the creases created by the clothesline (since the child was scanned with the shirt), which have been removed. In general, the torso was well reconstructed.

4.2.3 Sport Training case

Structured Light scans have also been used for reproduction of natural rock for bouldering sport training. A bouldering rock of 4 meters heigh was scanned in Monte Cimino, a few kilometers from Soriano, Cimino (VT), Italy on 07/02/2020 in collaboration between Start-up Idea-Re (Perugia, Italy) and Carpentry Innocenzi Franco & Americo (Foligno, Italy). The aim of the work was to reproduce a 3D model indoor in the owner gym for Sport Training (S.T).

First a test was performed on a stone presented in Chapter 2 where smoothing algorithms was tested, then was aligned and modelled. This final model given by digitalization process was compared with row model in order to quantify the quality of the reconstructed object. This analysis allows also to know how the digitalization process affect the measurements and the operator skills is influencing the final shape.

Finally, the scans were performed in an outdoor condition by Structured Light scan GO!Scan 50 and Photogrammetric techniques By Canon EOS 7D. For the final analysis, only a part was selected in order to combine different scanning techniques for have more detail in a useful to have more detail in the parts needed for the athlete's climbing and less detail in the parts not needed for training, saving time in terms of time, money and amount of data to manage.

Stone (test case)

The aim is to test the resolution of the instrument compared to the operator experience. In this case, the problem is how to position the object for scanning, so two scans must be taken and then aligned. Once aligned, smoothing is carried out in order to best reproduce a natural shape. This test was used precisely to understand how best to reproduce natural shapes since the aim is to scan a rock and reproduce it indoors. Figure 70 show the final result of alignment and reconstruction. In Figure 70 b the comparison with row aligned point cloud is evaluated.
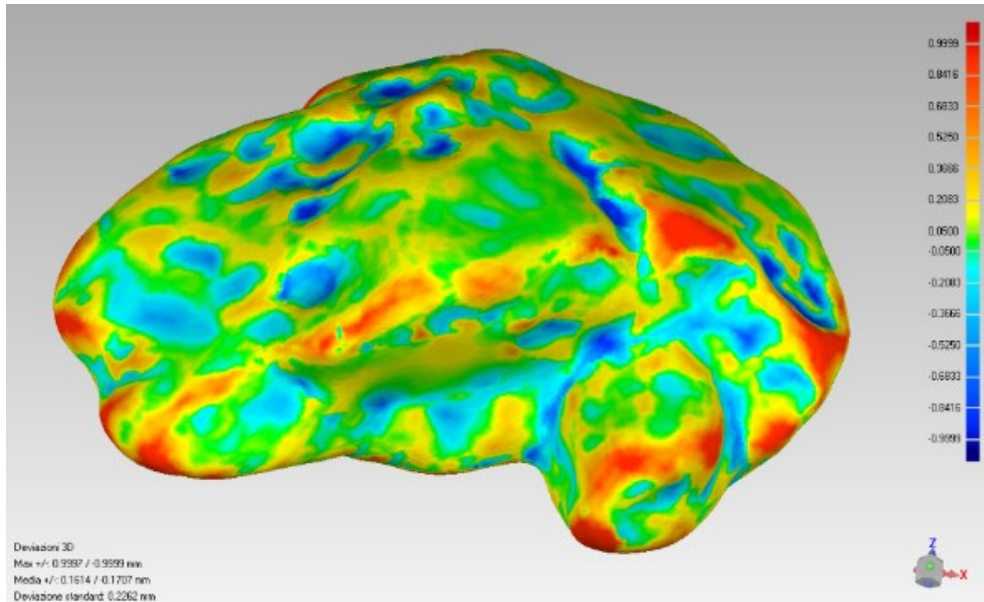
Figure 70 Final alignment result of digitalization process. Comparison with 1 mm of resolution of row model given by SL1 scan.

In the previous Figure the Standard deviation between digitalized point cloud and row model is 0.02 mm. Finally, the stone was reconstructed using stereolithography 3D printer Formals Form 2 with white resin V4. In Figure 71 the stone and the reconstruction are showed.
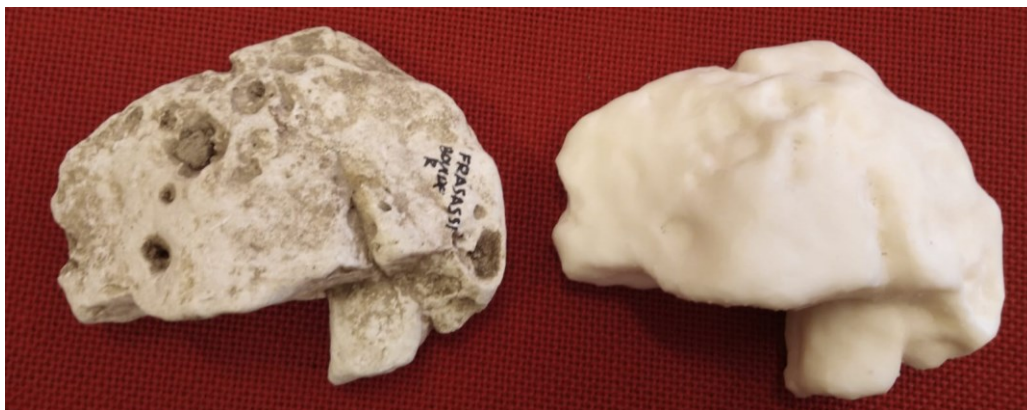
Figure 71 a) Lef, Stone; b) Right, 3D printed stone.

From the reconstruction, it can be seen that the holes are indeed not sufficiently hollowed out compared to the original object. All in all, the shape is well reconstructed and is clearly distinguishable. (In this figure, there are some inaccuracies due to the removal of the substrate in the print). In general, it can be

said that the scanner resolution at 1 mm can be used for subsequent analysis avoiding 0.5 mm of resolution that means heavy computational time.

Boulder (portion)

Since the object is big, a multi-scanning approach was used to get more detail in the holds that athletes use for climbing (scanned with SL1) and more approximation in other part of the boulder that is not needed for training scanned with high resolution photogrammetric techniques PH1 with a total of 266 pictures (Less resolution, means less Gigabytes of memory). The mesh resulting from the scan with Go! Scan 50 required higher manual processing times, due to the computational heaviness caused by the high resolution and the object dimension. The meshes were cleaned and reconstructed. The two scans were then compared by analyzing the deviations between the meshes in Gemoagic Wrap. In Figure 72 the result of the two scans is showed.

a)

b)
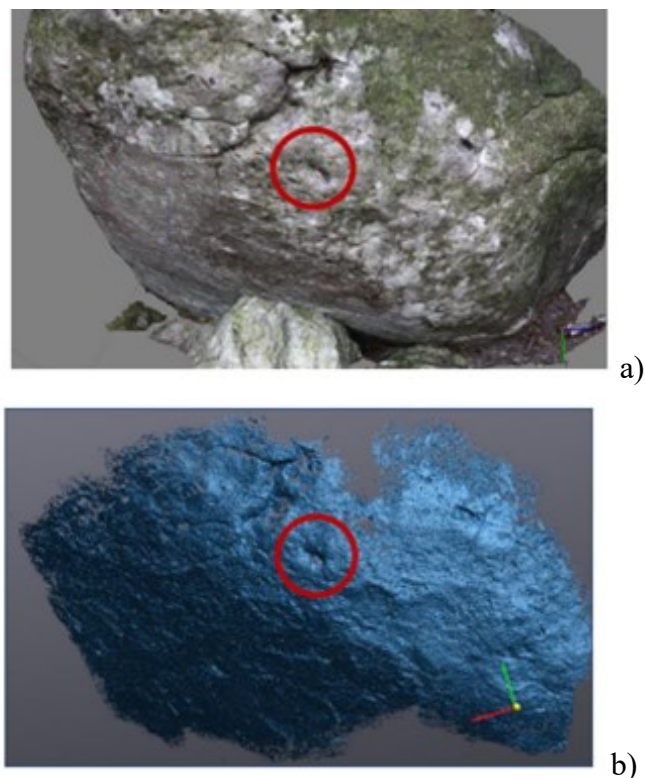
Figure 72 Reconstruction of boulder by a) Photogrammetric techniques b) Structured Light scanner c

Next, a part of the boulder was extrapolated for the volume analysis for both the SL1 and PH1 techniques. The holds were chosen based on maximum distances and geometric complexity. The two-hold given by the different techniques were then compared and analyzed, evaluating the standard deviation. The 3D model of the grip resulting from the scan using Go! Scan 50, cleaned, optimized and completed. Finally, the reconstructed volume was compared with row SL 0.5 mm accuracy acquisition. The result of the digitization process is shown in Figure 73.
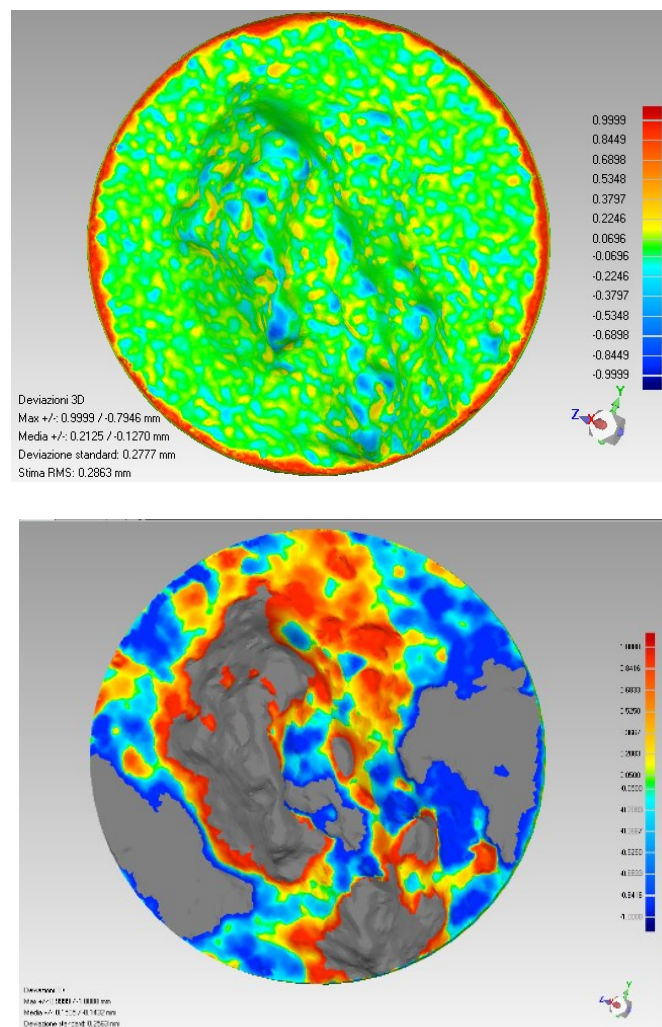
Figure 73 a) Comparison of final model to reconstruct in wood and the row
Structured Light scan b) Comparison final model with photogrammetry techniques.

The Reconstruction show a Standard deviation of 0.27 mm with a max of 1 mm (threshold) in the edges. The smoothing procedure delated some noise (yellow colour) given a good result. The reconstruction by photogrammetry is composed by 40 % of outliers point (gray color). In Figure 74 the 3D models of parts of the boulder (holds) given by the Photogrammetry and Structured Light Scanner, (printed using the Ultimaker 3 with TPU filament) are showed.
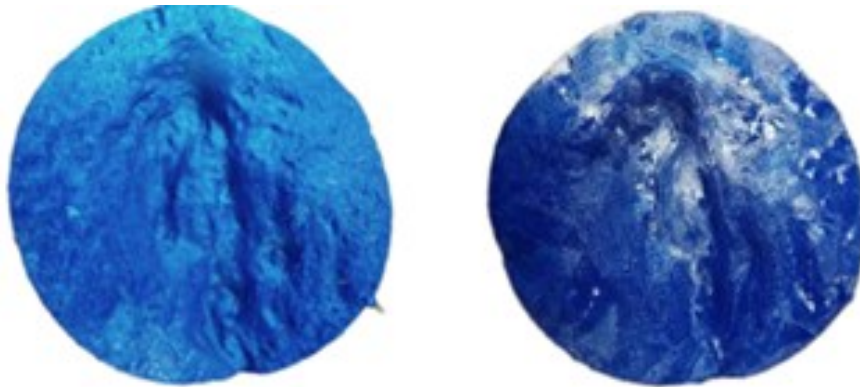
Figure 74 a) Boulder part scanned by SL1 b) Boulder part scanned by PH1

The two printed models showed a close shape match: more detailed in the case of the Go! Scan 50 compared to the photogrammetry. The latter, however, was faster, while the structured light scanner required more acquisition time (but was more accurate). Finally, was reconstructed in wood using a three-axis milling machine from the Innocenzi Franco & Americo joinery. The aim is to find the main points for boulder climbing. The boulder is to be reconstructed using the photogrammetric technique, which is much faster, and the holds, which are detailed, reconstructed using the GO!Scan 50.

4.2.4 Design case

SL scanning technologies were also used in industry and design fields. This work was performed in collaboration with 3DiFiC (a start-up in Perugia, Italy) and Pepe Jeans, London. The aim was to for scan a pomegranate and 3D print the objected in gold for make button for a new collection of clothes. Since every fruit is different and details are important to make the piece unique, a high-cost scanning system was used in order to detect its particularities Figure 75. Since there is a high reflectance of material, a spry opaque withe colour was used to avoid noise. In this

case two scan was performed up and down the object and then aligned, cleaned and smoothed. Moreover, they are delicate parts and can easily break. In Figure 76 the standard deviation between final model and row model are showed.

a)
b)
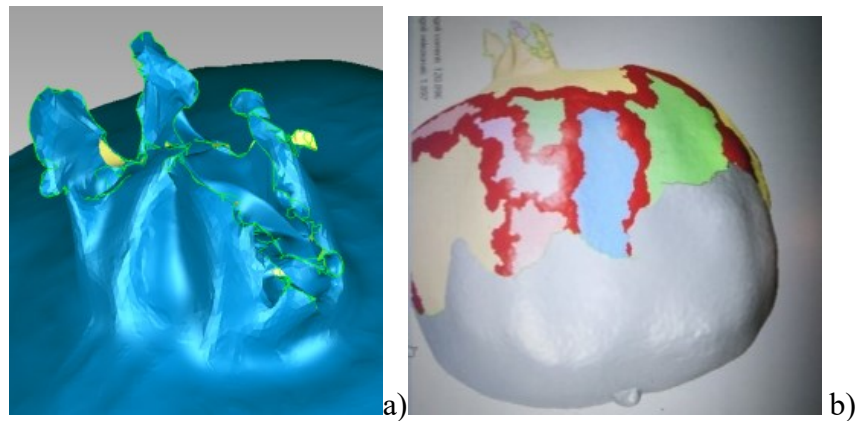
Figure 75 Pomegranate reconstruction a) particular crown b) alignment and analysis
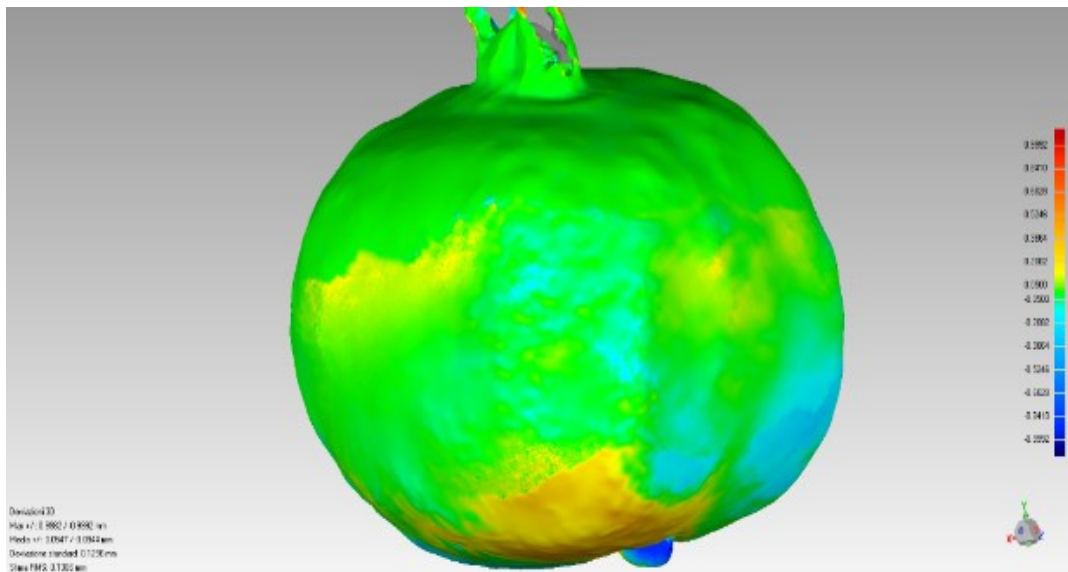
Figure 76 Final model comparison with row aligned scan.

Again, the methodologies presented in Chapter 2 digitalization process is applied. With a threshold of 1 mm, the standard deviation is about 0.12 mm. In Figure 77 the pomegranate and the 3D printed button are showed.
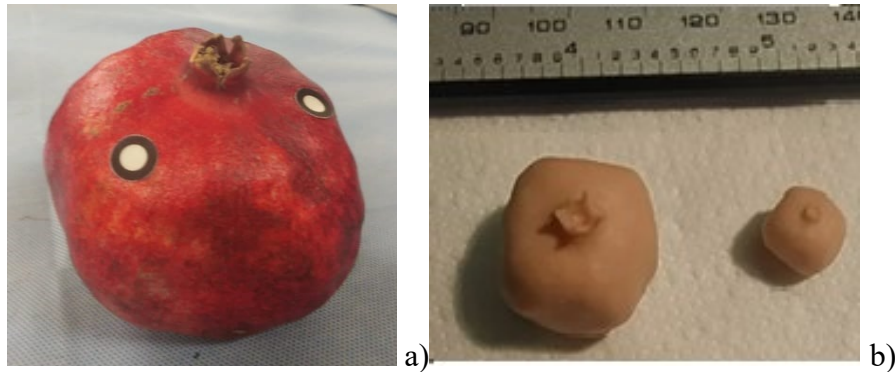
Figure 77 a) Pomerene b) 3D printed object with different size

In this case, it can see how, by reducing the shape, the details remain the same. Structured light proved its worth in terms of the quality of the final object, although it did present material issues with a consequence expensive time for the measurements. In general, the final product is acceptable as there is no alteration of the shape, and the digitising process did not exceed one millimetre, making this system suitable for use.

Before the introduction of the volume evaluation, the number of scans performed and analysed are shown. The CH was scanned with Structured Light scanner with high resolution and cost (SL1), with 0,5 mm and 2mm of resolution, with high-cost photogrammetry techniques (PH1) and low-cost LiDAR (L2). The choice depends on the length of the object, the resolution required (depending on the application and purpose) and data heaviness (e.g., scan of boulder). In total there are four scans: 1) CH SL1 0,5 mm; 2) CH SL1 2 mm; 3) CH ph1_High; 4) CH L2_low. The 3D printed torso of child (B) was scanned with SL1 with 1 mm of resolution 5) Biomedicine. For the ST, the first two scans were performed on a Test, scanned by SL1 with 0,5 mm and 1 mm of resolution: 6) ST test SL 0.5 digitalized and 7) ST Test SL 2. After, a boulder was scanned by SL1 with resolution of 1 mm and PH1. For the analysis, a little part of the boulder was extracted located in a complex place of the boulder. Those scans are called 8) ST SL 2 mm and 9) ST Ph1_high. The D was scanned with SL with 0.5 mm of resolution 10) Design (D). The total of object to analysed is ten. For all the object, a qualitative analysis is performed for the final reconstruction of the shape, going to study the texture, the mesh and comparing the different points cloud (so the row cloud point gives by instruments and the final reconstructed model). Additionally, for those ten measurements a quantitative analysis was performed as described in Chapter 2. Since the uncertainty of GO!

SCAN 50 (SL1) is known and is certified, Geomagic Wrap is a high-performance software for post processing, and the operator is specialized, for all acquisition presented, the highest resolution model derived by SL 1 is considered as reference [80]

Structured light proved to be excellent in various applications, being able to reconstruct important details of different shapes and sizes, demonstrating a wide versatility in applications. Photogrammetry as well as low-cost instruments have proven to give a lot of information albeit with uncertainty in shape reconstruction. They are promising, however, in large-scale use.

4.3 Results

Considering that the point cloud original is in too heavy to compute, it is necessary to reduce the number of points for the reconstruction. Resampling the acquisition, make possible to investigate the influence of resolution on the reconstructions. In this paragraph will be shown the considerations made in Chapter 2 applied to complex geometries in different applications (CH, ST, B, D). In the analysed geometries there are edges and concave parts, thin parts and holes, is difficult to have a reference. In Table 19 the volume and area evaluated by Geomagic Wrap is showed of the reference points cloud. Finally, the density is evaluated.

Table 19 Volume and density of final points cloud.

	Volume [mm^3]	Area [mm^2]	N points [adm]	Density np/[mm^2]
1_CH SL 0.5 mm	3299339.06	152197.39	1620374.00	10.65
2_CH SL 2 mm	3312267.49	165294.72	34236.00	0.21
3_CH Ph1_High	3133700.87	157195.16	33603.00	0.21
4_CH L2_Low	2934166.68	137706.91	4273.00	0.03
5_Biomedicine (B)	3472976.28	127480.56	33816.00	0.27
6_ST SL 2 mm	366927.51	41986.66	330254.00	7.87
7_ST Ph1_High	394650.11	41404.28	1000127.00	24.16
8_ST test SL 0.5 mm	203778.98	28028.55	98060.00	3.50
9_ST test SL 2 mm	206576.03	22696.45	5237.00	0.23
10_Design (D)	396066.94	27462.17	519457.00	18.92

For some objects, the density is high. As seen, it influences the reconstruction in 20 % depending on size, but changing scale and point density, the uncertainty CH and ACR and A opt doesn't change in simple shape. In some applications there is the necessity to reduce the number of points in order to reduce the processing time.

The number of point cloud was varied from 9000, 6000, 3000 and 1000 points since the final model given by high-cost scanner (SL1) was too heavy, for example, the word cup (CH SL 0.5 mm) is one million points. An example is shown in Figure 78.
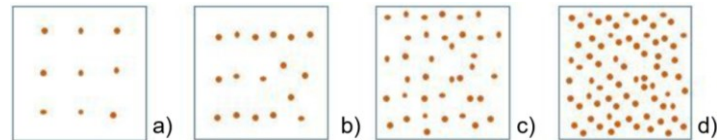
Figure 78 square exemple of oints number changing effect: a=1000 np, b=3000 np, c=6000 np, d=9000 np.

The previous Figure show an example of the different number of points effects on a same square. Dividing the Area of the object by the different points number, the density is lower than 0.4 np/mm^2 (located in 8_ST test SL 0.5 mm). Also, in this case alpha was varied from 5 mm to 105 mm, then the MAPE and box plot was analysed, and the uncertainty evaluated. Finally, the Alpha, Critical, The Alpha Optimal and the Convex Hull was evaluated.

3.3.1 Alpha Shape (AS) Test 1

As explained before, the alpha radius was changed form 5 mm to 105 mm with a step of 10 mm. The alpha rays are in fact concentrated in this range. Let us take as an example two geometries of different sizes, the world cup and the pomegranate, but with spherical elements that have been shown to be the most problematic. The spectrum of alpha values that fall within this range was therefore seen. In Figure 79 the spectrum of alpha shape is showed of big object (e.g., Word Cup). In Figure 80 the spectrum of alpha shape is showed of small object (e.g., Pomegranate).
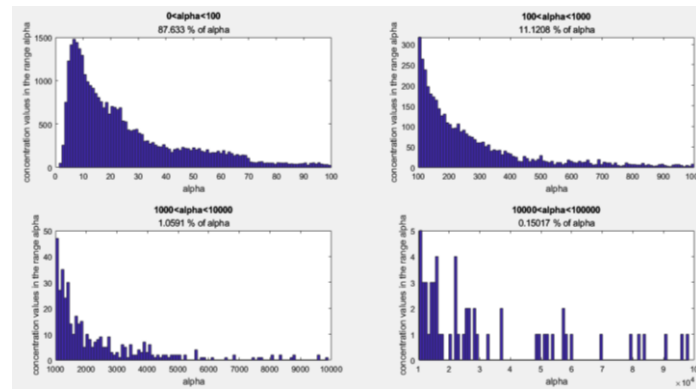
Figure 79 Alpha shape spectrum of Word Cup scanned with Structured Light scanner with resolution of 0.5 mm.
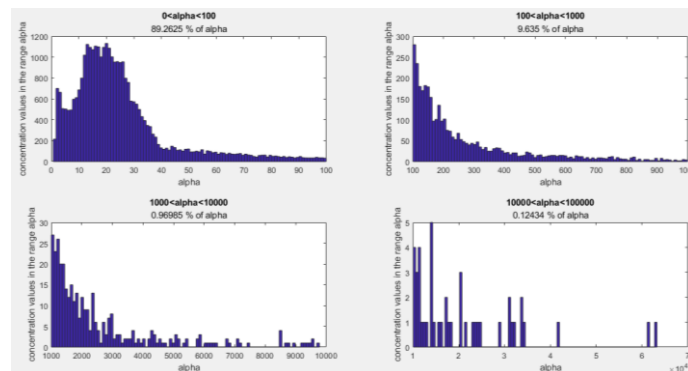
Figure 80 Alpha shape spectrum of Pomegranate scanned with Structured Light scanner with resolution of 0.5 mm.

Investigating the alpha spectrum of different objects, it is possible to notice that the maximum density is located in this range, in fact for all geometries, more than 80 % of alpha are located in this range.

As told, each of the ten acquisition was subsampled in 1000, 3000, 6000 and 9000 points for a total of 40 object. For each radius the volume of the different acquisition was evaluated. In Figure 81 and example of volume evaluation changing alpha radius of CH SL 0.5 mm (Word Cup of Cultural Heritage application, scanned with Structured Light techniques SL1with a resolution of 0.5 mm,) and a pomegranate (Design application scanned with SL1with a resolution of 0.5 mm) with different points number are shown.
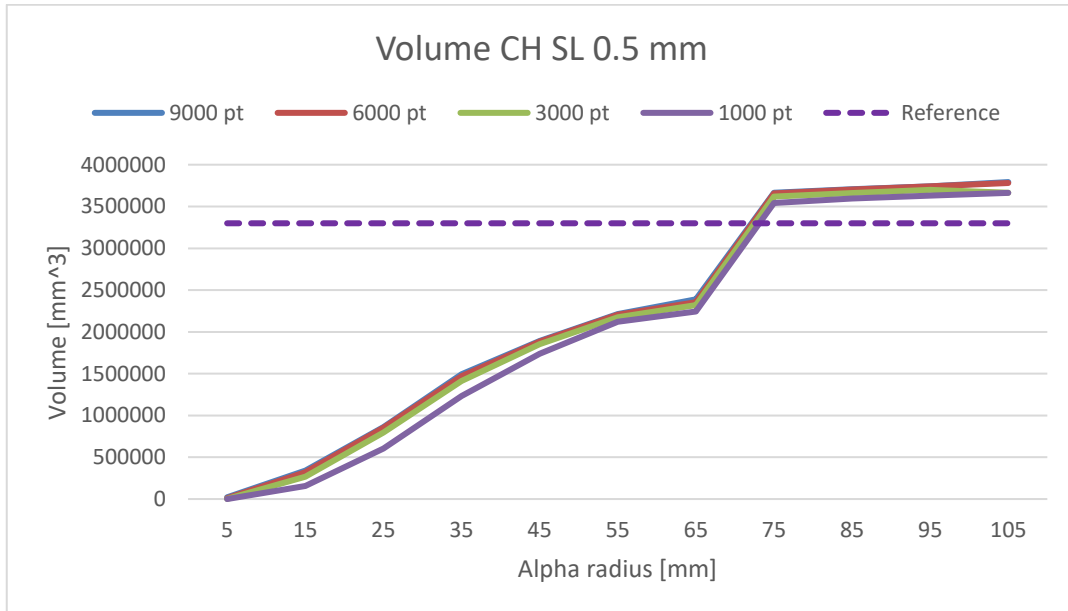
Figure 81 Volume of the Word Cup of Cultural Heritage application subsampled
with 1000, 3000, 6000 and 9000 points.

As is possible to notice, the volume starts to be correctly evaluated after alpha equal to 75 mm, for the same object with different point number. After this value the volume is overestimated. In Figure 82 an example of volume evaluation changing alpha radius a Pomegranate (Design application scanned with SL1with a resolution of 0.5 mm) with different points number is shown.
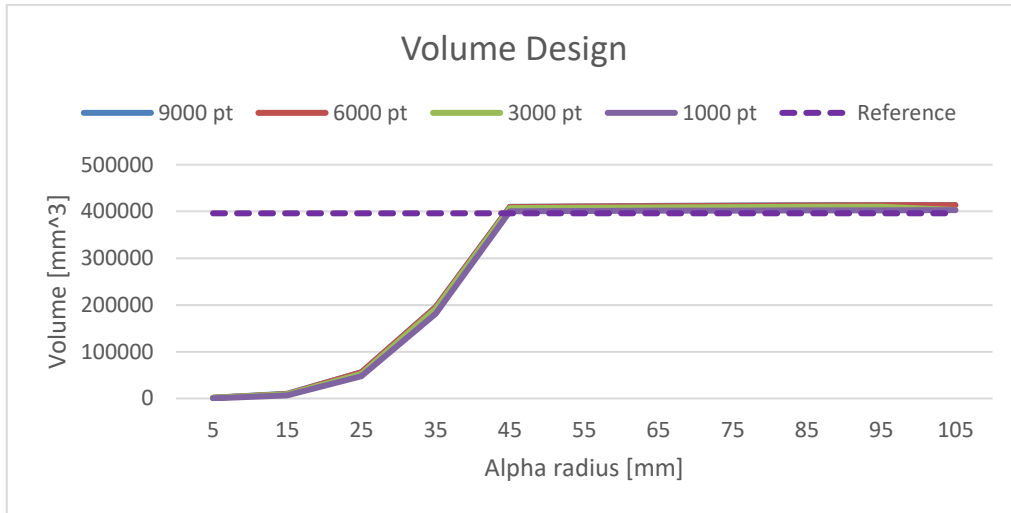
Figure 82 Volume of the Word Cup of Cultural Heritage application subsampled
with 1000, 3000, 6000 and 9000 points.

In this case the volume is correctly evaluated after alpha radius equal to 45 mm.
Decreasing the shape, decrease the alpha needed for the reconstruction. After this
value the volume star to be mor or less constant. For analyse the global effect of
changing of points number a Box Plot of the ten acquisition is showed, considering
all point number. In Figure 83 the box plot of the of the Word Cup of Cultural
Heritage (CH SL 0.5 mm) application with different of resolution is shown.
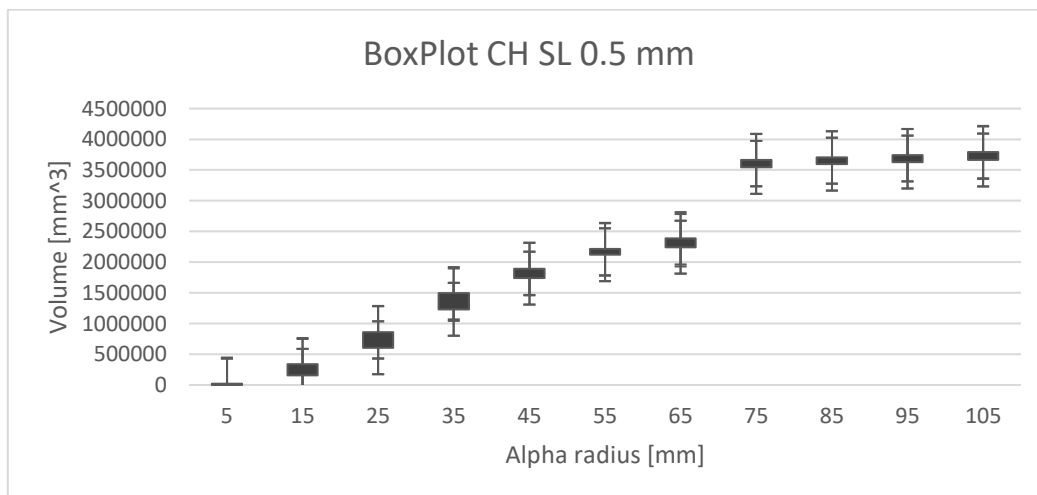
Figure 83 Box Plot of the Word Cup of Cultural Heritage application for all the four
subsampled 1000, 3000, 6000 and 9000 points clouds.

By this Figure is possible to notice that the resolution of the points clouds has a similar error bar for all the alpha radii. In Figure 84 the box plot of the Pomegranate (Design application scanned with SL1with a resolution of 0.5 mm) with different points number is shown.
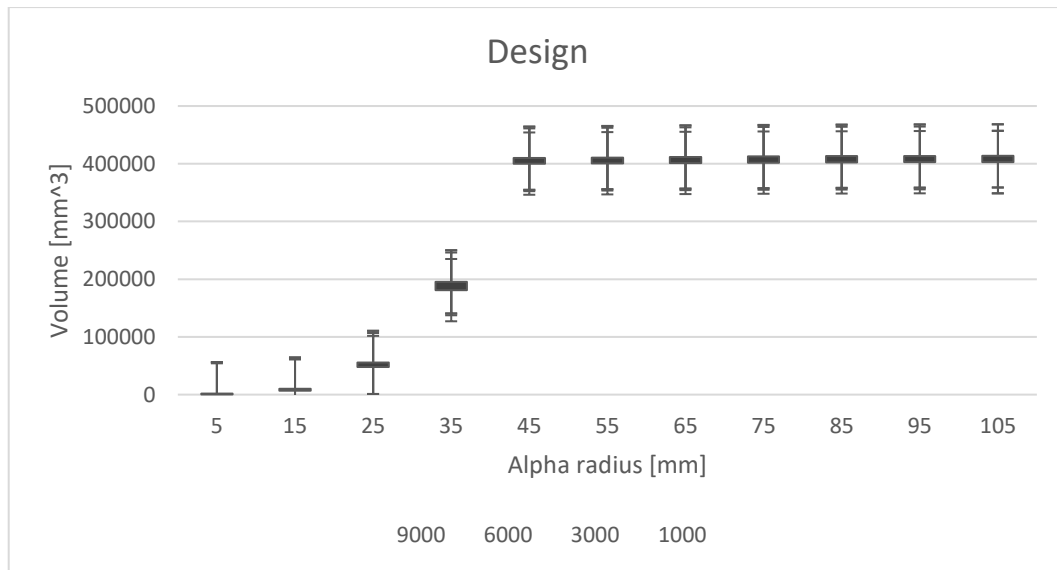
Figure 84 Box Plot of the Pomegranate of Design application subsampled with 1000, 3000, 6000 and 9000 points.

As it is possible to see in CH SL 0,5 mm, the volume increases with alpha radius. The standard deviation differs from the mean by 50 % for alpha = 5 mm and 17 % at alpha 15 mm. At alpha 5 mm the shape is not reconstructed. At alpha 25 mm the standard deviation is 8 %. The standard deviations start to decrease after alpha=35 mm (4 %), in fact at alpha 45 mm there is a % ratio between standard deviation and mean of 2 %. This ratio decreases linearly up to alpha 95 mm (0.7 %) and then grows again at alpha=150 mm where the values deviate by 0.9 %. The graph shows that even after alpha=75 mm, the volume values do not change too much. This shape of graph is near or above the reference volume equal to 3299339,063 mm3. This behaviour also occurs for CH SL 2 mm and CH PH1, while in CH L2_Low the volume stabilises around 65 mm of radius alpha. This means that by increasing alpha further, the volume grows very slowly. The R^2 value is CH SL 0,5 mm = 0.9556, CH SL=2 mm 0.9558, CH pH1=0.9574 and CH L2_Low=0.9083. The torso having a fairly large volume (larger than the previously presented objects with a side or diameter of 50 mm), the volume trend is exponential

in the first part of the curve up to alpha = 75 mm, and then follows the constant trend of the World Cup with higher resolution. Also in this case, the volume starts to become almost constant at the reference volume of 3472976.284 mm3. On the other hand, in the case of the pomegranate (with between 10 mm and 20 mm of simple object, e.g., sphere), the volume begins to become constant for alpha=45 mm, at the reference volume of 396066.943 mm^3. The objects in the ST including the test (i.e., the stone) and the socket (that have size near to 20 mm of simple object), has a volume increasing from alpha 5 mm to 15 mm, after which it begins to grow more slowly. In Table 20 Uncertainty of reconstruction changing alpha radius value. is shown. The minimum, maximum, standard deviation and uncertainty of effect of alpha radius reconstruction on the 40 points cloud (ten object subsampled with four different number of points).

Table 20 Uncertainty of reconstruction changing alpha radius value.

Np	Max [mm^3]	Min [mm^3]	Mean [mm^3]	Dev std [mm^3]	C Coeff [adm]	Unc [mm^3]	Unc [%]	Unc corr [%]
1_9000	3792422.92	21098.01	2192450.05	1347187.77	0.66	406192.39	18.53	15.95
1_6000	3781136.72	10616.57	2180369.51	1349616.89	0.66	406924.80	18.66	16.08
1_3000	3698994.64	118.61	1800636.34	1374129.07	0.49	414315.50	23.01	20.94
1_1000	3662962.23	118.61	2048259.63	1361431.38	0.62	410487.01	20.04	17.63
2_9000	3807668.25	18269.19	2200289.51	1355567.32	0.67	408718.92	18.58	16.00
2_6000	3795594.52	8746.01	2187066.58	1357275.96	0.66	409234.10	18.71	16.13
2_3000	3726243.14	1788.99	2150307.82	1347397.13	0.65	406255.52	18.89	16.32
2_1000	3667458.21	7.22	2047988.47	1365899.17	0.62	411834.09	20.11	17.71
3_9000	3606882.68	15284.89	2123015.62	1288810.79	0.64	388591.07	18.30	15.68
3_6000	3585886.54	7786.64	2105722.87	1289444.29	0.64	388782.08	18.46	15.84
3_3000	3528439.28	1593.91	2068691.58	1282321.80	0.63	386634.57	18.69	16.08
3_1000	3495409.04	64.14	2002735.59	1296520.70	0.61	390915.70	19.52	17.03
4_9000	3081401.30	10354.30	1841622.18	1226168.29	0.56	369703.65	20.07	17.70
4_6000	3073914.53	6577.40	1837043.84	1224592.10	0.56	369228.41	20.10	17.72
4_3000	3037019.93	2407.46	1816342.94	1220436.04	0.55	367975.31	20.26	17.88
4_1000	3019693.60	10.63	1777598.53	1218490.42	0.54	367388.68	20.67	18.34
5_9000	3530671.22	6953.05	1765437.34	1443838.65	0.51	435333.73	24.66	22.76
5_6000	3529972.19	4193.13	1762168.70	1444052.03	0.51	435398.07	24.71	22.81
5_3000	3513123.77	1393.96	1751227.49	1440188.04	0.50	434233.03	24.80	22.89
5_1000	3489391.20	149.92	1712433.38	1442047.10	0.49	434793.56	25.39	23.53
6_9000	470157.61	17153.72	388741.21	133272.52	1.06	40183.18	10.34	4.90
6_6000	468390.46	15558.95	388108.42	133930.34	1.06	40381.52	10.40	4.97

6_3000	465520.60	10728.89	384973.99	135249.59	1.05	40779.29	10.59	5.14
6_1000	463830.20	1698.46	378531.86	138997.40	1.03	41909.29	11.07	5.70
7_9000	478018.05	10674.59	393854.46	141697.26	1.07	42723.33	10.85	5.64
7_6000	478891.94	10233.68	393556.93	142252.70	1.07	42890.80	10.90	5.72
7_3000	477622.25	7522.76	390868.94	143167.25	1.07	43166.55	11.04	5.89
7_1000	467031.11	1039.78	383639.10	145088.43	1.05	43745.81	11.40	6.30
8_9000	242762.70	9771.52	204473.13	71961.55	1.00	21697.22	10.61	5.52
8_6000	242462.68	9019.93	203967.63	72192.29	1.00	21766.79	10.67	5.58
8_3000	240013.67	7100.91	201767.22	72133.06	0.99	21748.94	10.78	5.64
8_1000	234588.78	2662.93	196137.12	72578.58	0.96	21883.26	11.16	6.01
9_9000	246328.55	7667.05	207593.31	73975.72	1.02	22304.52	10.74	5.60
9_6000	246089.52	7327.35	207023.01	74132.83	1.02	22351.89	10.80	5.67
9_3000	244457.09	5898.73	205369.17	73985.29	1.01	22307.40	10.86	5.69
9_1000	240210.26	2086.88	200571.97	74835.99	0.98	22563.90	11.25	6.13
10_9000	413778.63	1575.17	286205.18	173173.95	0.72	52213.91	18.24	15.59
10_6000	413392.93	1474.41	285860.29	173038.50	0.72	52173.07	18.25	15.60
10_3000	410023.53	1419.10	282692.06	171982.79	0.71	51854.76	18.34	15.71
10_1000	402902.27	289.20	277130.84	170608.29	0.70	51440.34	18.56	15.93

Alpha changing confirm what said before about relationship between size and point cloud. The resolution is influencing the volume with an uncertainty of about 20 % for biggest object (CH and Biomedicine), while is around 10 % in smallest object (the two stones and the part of the boulder). In pomegrane, that is a small object, the Uncertainty is about 18 % this becouse the spherical shape is hard to reconstruct, as presented in (Chapter 2).

An example of the effect of point number (a= 1000, b=3000, c=6000 and d=9000 pt) on alpha radius =25 mm for different point number of CH1 0.5 mm and Design is showed in Figure 85 and Figure 86.
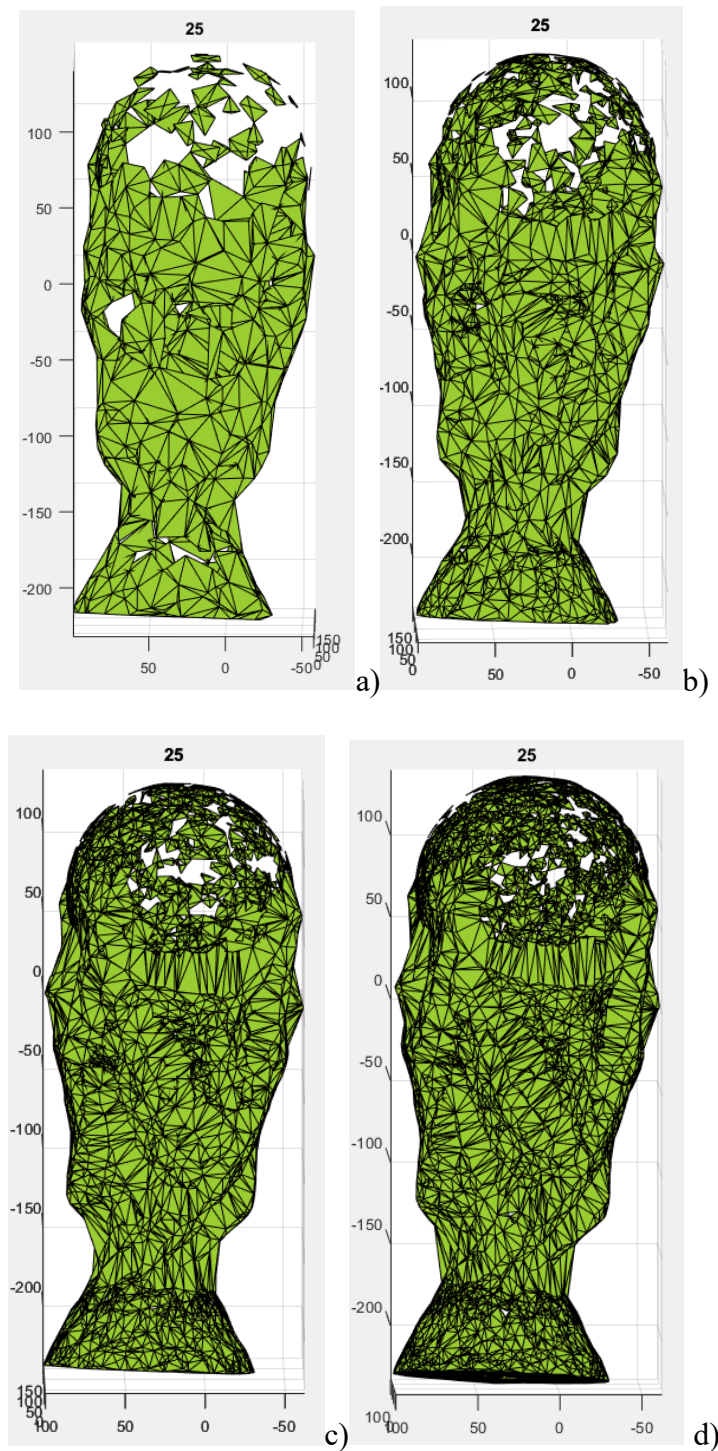
Figure 85 Effect of alpha radius on World Cup scanned with Structured Light techniques with 0.5 mm of resolution
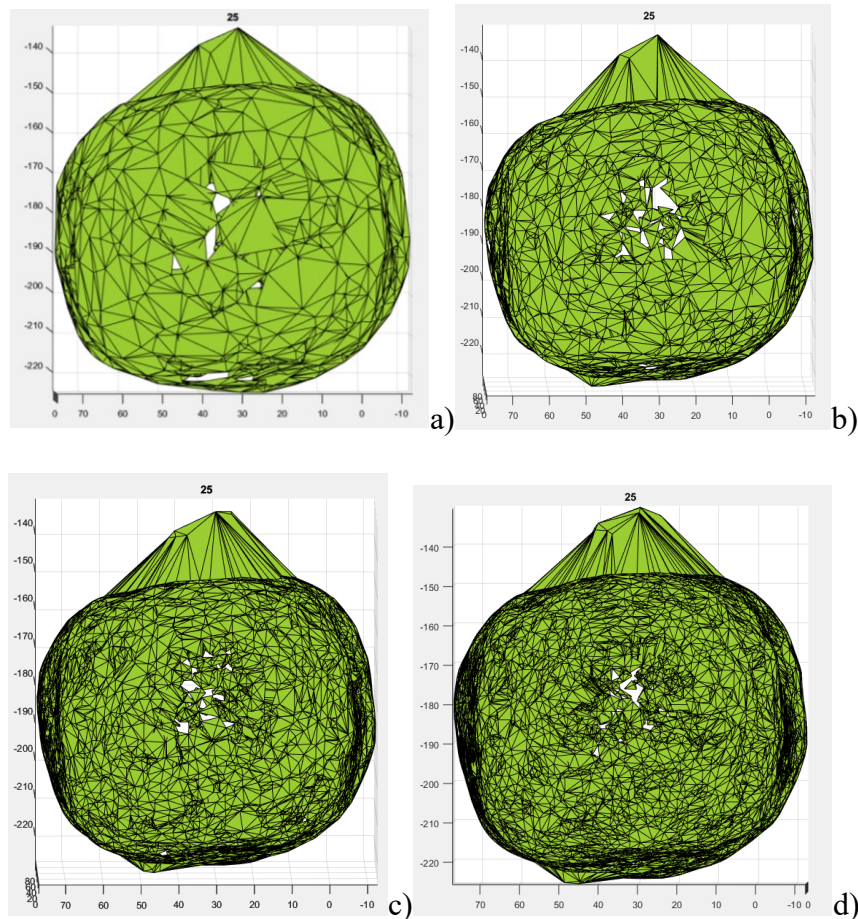
Figure 86 Effect of alpha radius on Design application scanned with
Structured Light techniques with 0.5 mm of resolution

As can be seen, for the same geometry scanned with two different tools and resampled with the same number of points, the alpha shape returns similar behaviour in terms of shape reconstruction. Let us now see what the overall effect is for the 10 scanned objects on the volume value. This example show that alpha shape radius = 25 mm cannot reconstruct the shape, in particular the problems of reconstruction are located with a spherical geometry and on the flat shape as presented in test examples (sphere, pyramid and cube). For both cases, with similar spheric shape on top of World Cup (CH) and pomegranate (D) 10.64 % and 18.91% of density. Then the ten objects were analysed considering all the four resolutions (different number of points) In Figure 87 the effect of alpha radius changing on different geometry is shown.
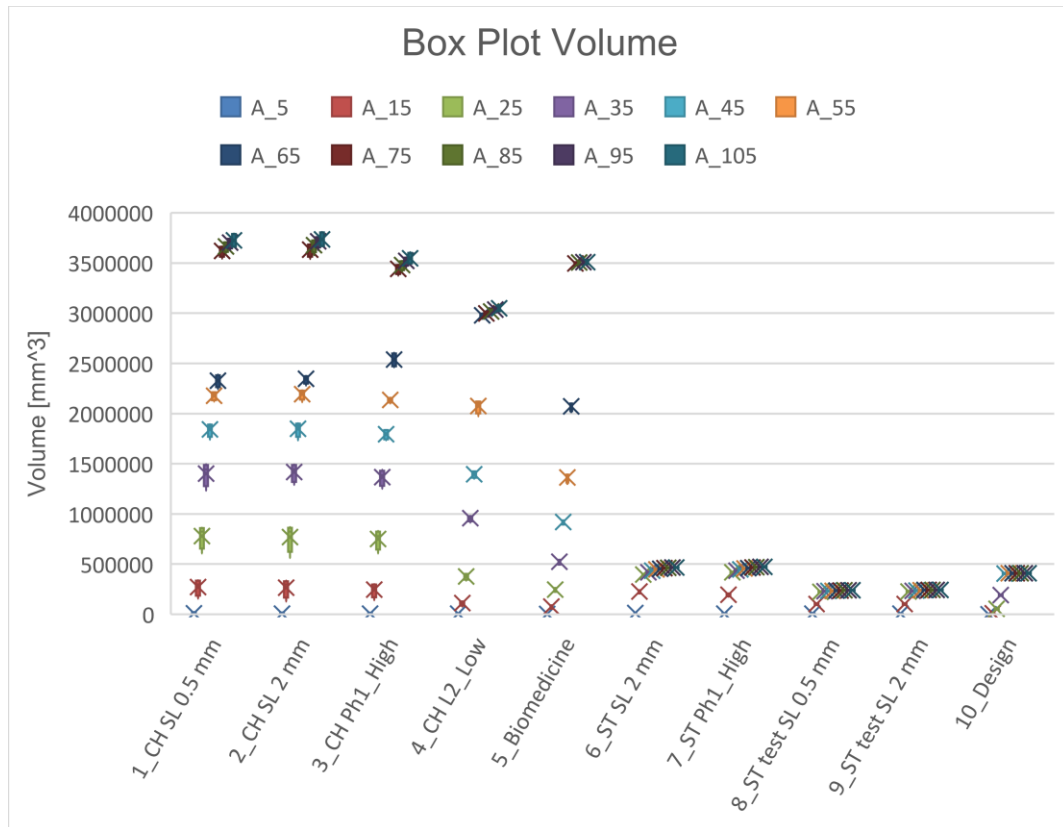
Figure 87 Box Plot of objects volume evaluated changing alpha radius.

This Figure show the highest dispersion of alpha for biggest object. In fact, the alpha < 75 mm rarely reconstruct the shape. rarely reconstruct the shape (in case of Biomedicine applications alpha radius equal to 75 mm can reconstruct the shape). For smallest object, regardless of resolution lower value of alpha radius can reconstruct the shape.

For all objects, the MAPE was evaluated considering the effect of different number of points. In Figure 88 and Figure 89 the Box Plot of MAPE of the four Point cloud of Word Cup (Cultural Heritage) and Pomegranate (Design) Scanned by SL1 with 0.5 mm of resolution are showed.
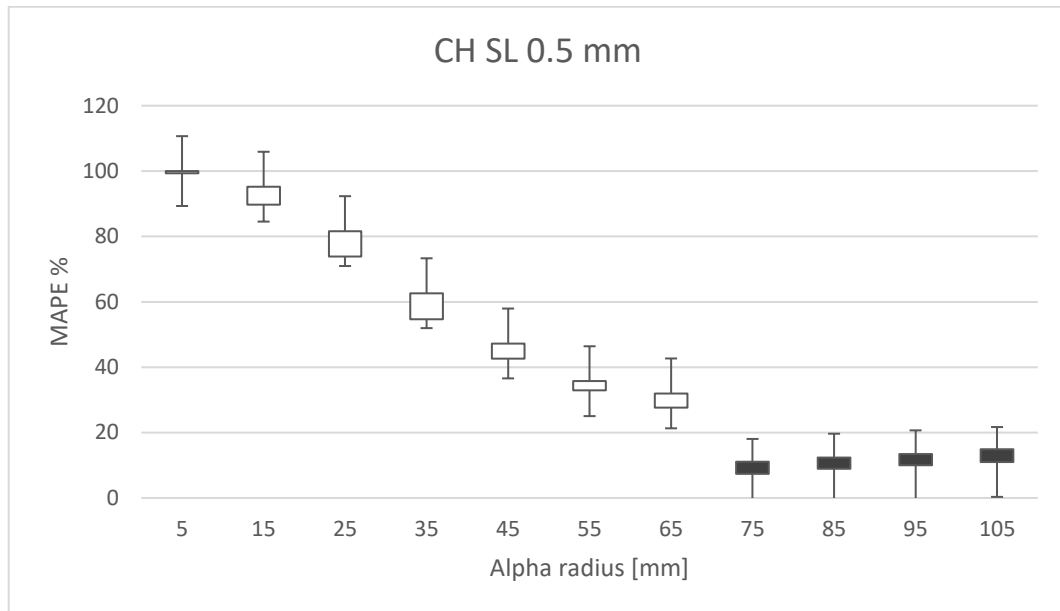
Figure 88 MAPE of Word Cup scanned with SL with 0.5 mm of resolution
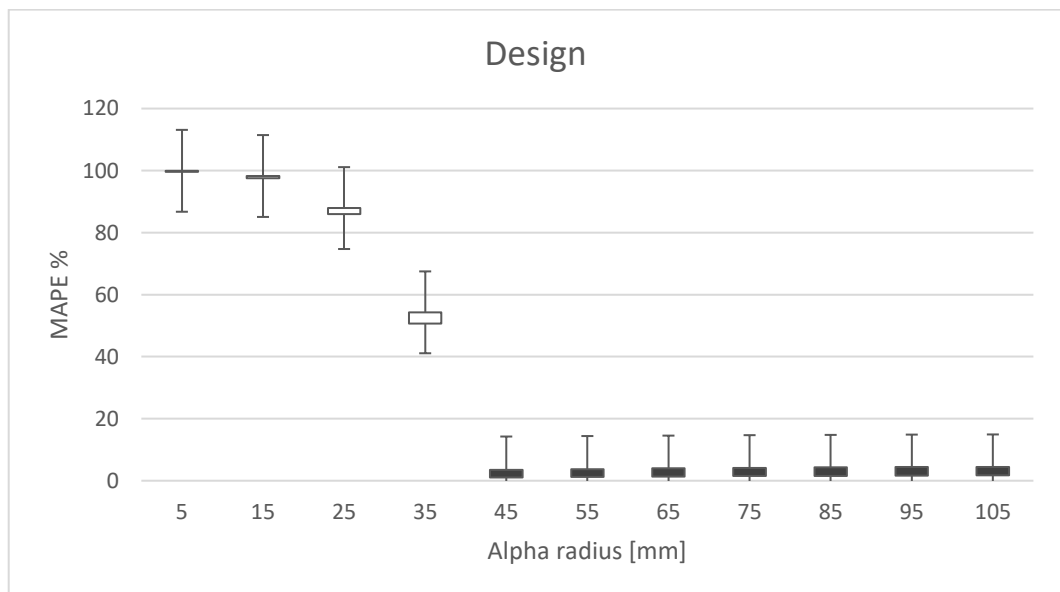
Figure 89 MAPE of Pomegranate scanned with SL with 0.5 mm of resolution.

In both cases, after a certain alpha radius, the uncertainty of reconstruction is inside 20 %. The MAPE of all objects are showed in Figure 90.
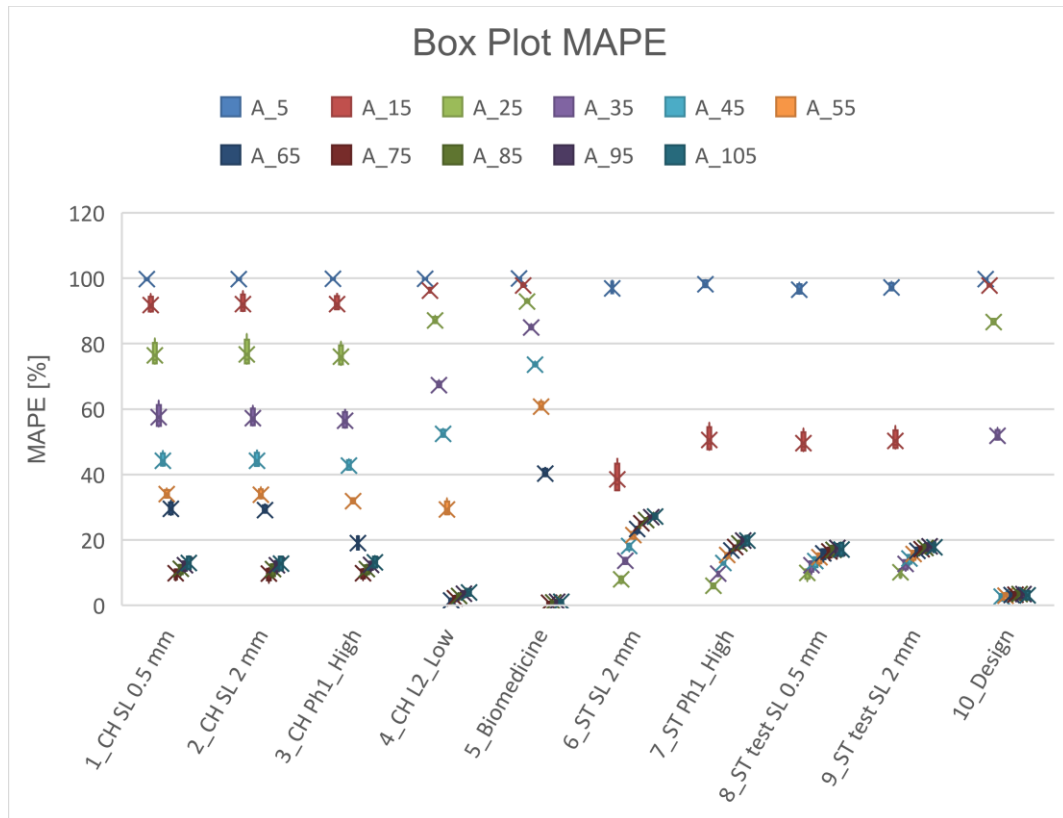
Figure 90 MAPE of different objects

From here it can be seen how, one moves away from the reference models for values of the alpha radius that are too small, while increasing the radius brings the volume value closer to the reference one. The acceptable threshold is around 20 %, (where, incidentally, the alpha values are concentrated) within which shape reconstruction and thus volume calculation takes place. In Table 21 the MAPE for each Alpha radius is shown.

Table 21 MAPE varying Alpha radius

		5	15	25	35	45	55	65	75	85	95	105
9000	**1_CH SL 0.5 mm**	99.4	89.7	73.9	54.7	42.6	32.9	27.6	11.1	12.4	13.4	14.9
6000	**1_CH SL 0.5 mm**	99.7	90.2	74.1	55.4	42.9	33.2	28.6	10.9	12.2	13.4	14.6
3000	**1_CH SL 0.5 mm**	99.9	91.9	75.9	57.2	43.8	34.1	29.7	9.7	11.0	12.1	11.0
1000	**1_CH SL 0.5 mm**	100.0	95.2	81.6	62.6	47.3	35.7	32.0	7.4	9.0	10.0	11.0
9000	**2_CH SL 2 mm**	99.4	89.9	73.7	54.8	42.3	32.4	28.1	11.8	13.0	14.0	15.4
6000	**2_CH SL 2 mm**	99.7	90.5	74.4	55.3	42.8	32.7	28.0	11.2	12.7	13.7	15.0

3000	2_CH SL 2 mm	99.9	91.6	75.7	57.2	43.4	33.0	28.4	10.2	11.8	12.9	11.2
1000	2_CH SL 2 mm	100.0	96.1	82.9	60.9	47.4	35.9	30.9	7.3	8.5	10.1	11.2
9000	3_CH Ph1_High	99.5	90.9	74.8	56.3	44.4	34.6	21.1	5.6	6.8	7.8	9.3
6000	3_CH Ph1_High	99.8	91.4	75.6	57.6	44.4	34.9	21.7	5.1	6.2	7.4	8.7
3000	3_CH Ph1_High	100.0	92.2	77.1	58.4	46.2	35.3	24.0	4.3	5.6	6.9	5.9
1000	3_CH Ph1_High	100.0	95.7	81.6	62.1	47.5	36.4	25.4	2.2	3.4	4.8	5.9
9000	4_CH L2_Low	99.7	96.1	87.8	70.3	56.9	35.8	9.2	8.5	7.9	7.2	6.6
6000	4_CH L2_Low	99.8	96.1	87.9	70.6	56.9	35.8	9.4	8.7	8.0	7.4	6.8
3000	4_CH L2_Low	99.9	96.6	88.7	70.7	58.0	36.8	9.7	9.1	8.5	8.0	8.5
1000	4_CH L2_Low	100.0	97.7	89.8	72.3	59.0	40.2	10.8	10.3	9.7	9.2	8.5
9000	5_Biomedicine	99.8	97.4	92.5	84.4	73.0	59.8	39.5	1.1	1.3	1.5	1.7
6000	5_Biomedicine	99.9	97.4	92.6	84.3	73.2	60.2	39.5	1.0	1.2	1.4	1.6
3000	5_Biomedicine	100.0	97.6	92.9	85.0	73.4	60.0	39.9	0.8	1.0	1.2	0.5
1000	5_Biomedicine	100.0	98.7	93.8	86.0	74.6	62.8	42.3	0.2	0.0	0.2	0.5
9000	6_ST SL 2 mm	95.3	34.9	8.9	14.5	19.0	22.0	23.9	25.1	26.7	27.5	28.1
6000	6_ST SL 2 mm	95.8	35.7	8.6	14.3	18.5	22.6	23.8	25.7	26.5	27.4	27.7
3000	6_ST SL 2 mm	97.1	38.1	7.9	13.3	18.4	21.4	24.0	25.2	25.8	26.9	26.4
1000	6_ST SL 2 mm	99.5	45.1	6.6	12.4	16.5	20.0	21.6	24.3	25.5	26.1	26.4
9000	7_ST Ph1_High	97.1	43.6	14.6	18.6	21.8	24.8	25.8	27.2	28.6	29.6	30.3
6000	7_ST Ph1_High	97.2	44.5	14.7	18.4	21.8	24.5	26.1	27.2	28.8	29.5	30.5
3000	7_ST Ph1_High	97.9	46.8	13.8	18.1	21.4	24.6	25.8	27.1	28.2	30.2	27.3
1000	7_ST Ph1_High	99.7	52.5	13.0	16.8	20.8	22.8	24.4	25.4	25.7	26.2	27.3
9000	8_ST test SL 0.5	95.2	47.2	11.0	13.5	14.7	15.8	17.2	17.7	18.4	18.7	19.1
6000	8_ST test SL 0.5	95.6	47.9	10.9	13.2	14.6	15.9	17.0	17.4	17.8	18.7	19.0
3000	8_ST test SL 0.5	96.5	49.1	10.4	12.7	13.8	14.9	16.2	16.7	17.2	17.8	15.1
1000	8_ST test SL 0.5	98.7	54.1	7.3	9.5	10.9	12.2	13.4	13.9	14.4	14.8	15.1
9000	9_ST test SL 1 mm	96.2	47.2	12.7	15.4	17.0	18.1	19.3	19.7	20.3	20.6	20.9
6000	9_ST test SL 1 mm	96.4	48.1	12.3	15.1	16.7	18.3	19.0	19.4	19.9	20.4	20.8
3000	9_ST test SL 1 mm	97.1	48.7	11.9	14.4	16.1	17.6	18.3	18.9	19.3	20.0	17.9
1000	9_ST test SL 1 mm	99.0	54.3	9.5	11.8	13.6	14.8	16.3	17.0	17.3	17.6	17.9
9000	10_Design	99.6	97.5	85.9	50.6	3.5	3.7	4.0	4.2	4.3	4.4	4.5
6000	10_Design	99.6	97.6	85.9	50.7	3.4	3.6	3.9	4.1	4.2	4.3	4.4
3000	10_Design	99.6	97.8	86.8	51.6	2.7	3.0	3.2	3.3	3.4	3.5	1.7
1000	10_Design	99.9	98.2	87.9	54.3	1.1	1.2	1.3	1.5	1.6	1.7	1.7

3.3.2 Alpha Critical (AC), Alpha Optimal (AO) and Convex Hull (CH) Test 2

Also, in this case was evaluated the Alpha Critical, Alpha Optimal and Convex Hull algorithms. In Table 22, the alpha radius Critical and optimal are showed for each acquisition and resolutions.

Table 22 Alpha Critical and Alpha Optimal radius for each point clouds.

		A Cr	A opt
9000	1_CH SL 0.5 mm	59.80	69.98
6000	1_CH SL 0.5 mm	59.99	70.10
3000	1_CH SL 0.5 mm	59.76	70.23
1000	1_CH SL 0.5 mm	61.98	70.35
9000	2_CH SL 2 mm	52.11	70.08
6000	2_CH SL 2 mm	57.66	69.91
3000	2_CH SL 2 mm	60.26	70.09
1000	2_CH SL 2 mm	59.39	70.26
9000	3_CH Ph1_High	45.28	66.95
6000	3_CH Ph1_High	55.41	67.14
3000	3_CH Ph1_High	53.47	67.38
1000	3_CH Ph1_High	54.15	67.57
9000	4_CH L2_Low	54.11	61.03
6000	4_CH L2_Low	57.18	61.08
3000	4_CH L2_Low	57.47	61.26
1000	4_CH L2_Low	52.99	61.99
9000	5_Biomedicine	71.74	72.94
6000	5_Biomedicine	70.78	72.95
3000	5_Biomedicine	70.68	72.93
1000	5_Biomedicine	66.72	83.09
9000	6_ST SL 2 mm	21.30	20.32
6000	6_ST SL 2 mm	21.19	20.41
3000	6_ST SL 2 mm	20.50	20.64
1000	6_ST SL 2 mm	19.28	21.25
9000	7_ST Ph1_High	21.68	19.48
6000	7_ST Ph1_High	21.69	19.51
3000	7_ST Ph1_High	21.10	19.49

1000	7_ST Ph1_High	20.62	20.13
9000	8_ST test SL 0.5 mm	15.27	20.76
6000	8_ST test SL 0.5 mm	12.77	20.77
3000	8_ST test SL 0.5 mm	15.56	21.12
1000	8_ST test SL 0.5 mm	14.26	22.17
9000	9_ST test SL 2 mm	17.80	21.02
6000	9_ST test SL 2 mm	19.84	21.03
3000	9_ST test SL 2 mm	19.60	21.35
1000	9_ST test SL 2 mm	18.03	21.88
9000	10_Design	34.54	38.75
6000	10_Design	33.91	38.83
3000	10_Design	34.78	38.90
1000	10_Design	36.25	39.04

As it possible to see, the alpha Critical radius is lower than Optimal one. Both, for some subject has holes. In Figure 91 Pomerene with 6000 points and Alpha Critical = 33.91 mm is showed.

a)   b)
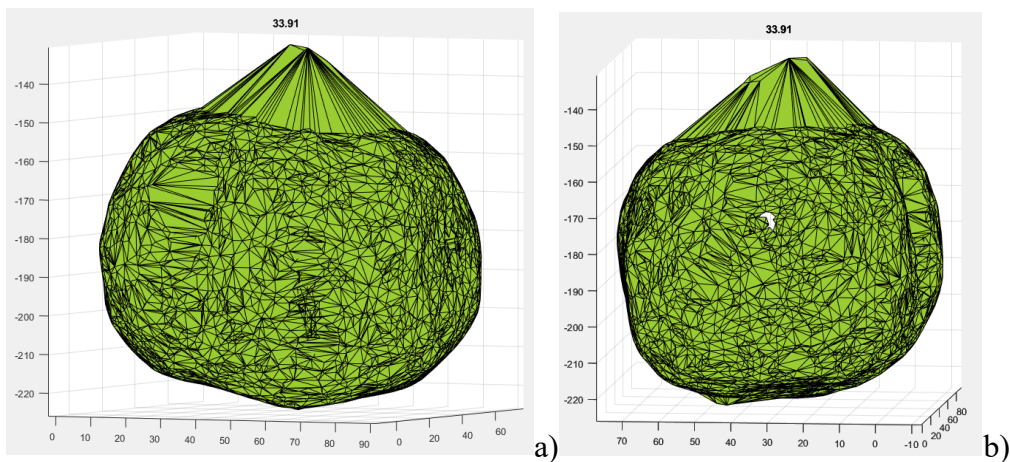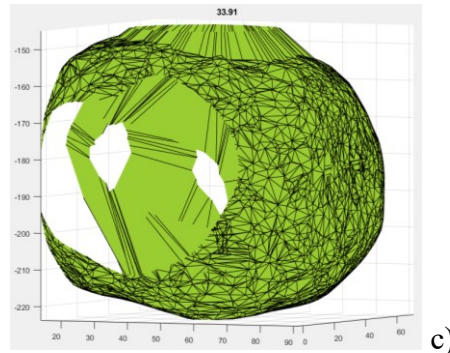
Figure 91 Pomegranate (Design application) a) Reconstruction by Alpha Critical radius =33.91mm b) Hole detail c) Zoom inside the shape.

The algorithms Alpha Critical in fact has to contain all points and if the shape is complex, for certain value of alpha radius, with complex shape some triangles are connected but non well closed. The same happen for Alpha Optimal algorithms but with less reconstruction error, since is finding the volume nearest to the reference and alpha is higher. In this case is useful to fill holes. These errors were also found in the top spherical part of the cup.

In Figure 92 an example of Box Plot of World Cup scanned with SL1 with resolution of 0.5 mm where the volume reference is = 3299339,06 mm3.
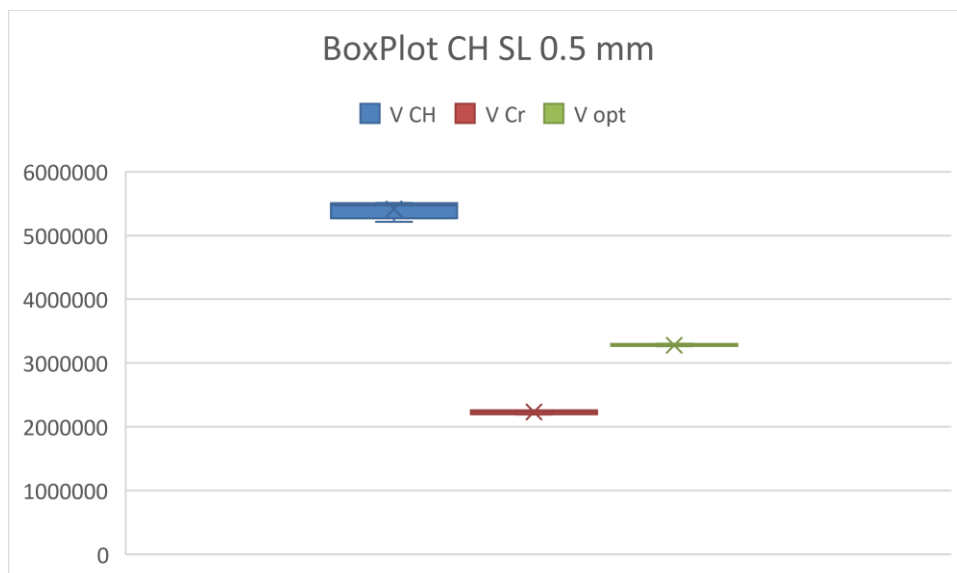
Figure 92 Example Boxplot of Word Cup

In Figure 93 an example of Box Plot of Pomegranate scanned with SL1 with resolution of 0.5 mm where the volume reference is = 396066,94 mm^3.
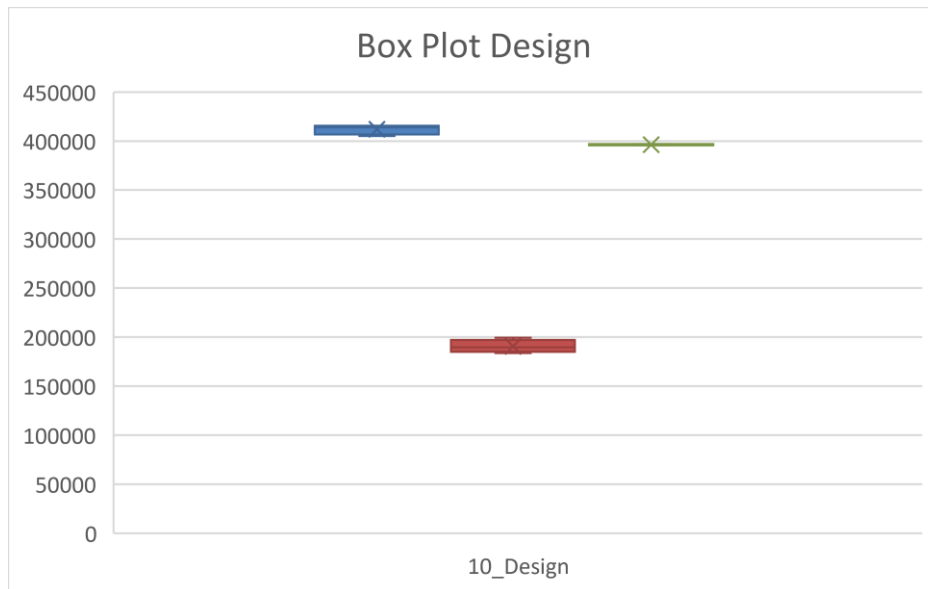
Figure 93 Example Boxplot of Pomegranate

In Table 23 the uncertainty of the four number of points for each application is showed.

Table 23 Uncertainty of the four resolution (1000,300,6000 and 9000 points) value of voulm evaluation by ACR A opt and CH.

	Unc %	Unc%	Unc %
	CH	V cr	V opt
1_CH SL 0.5 mm	1.11	0.61	0.77
2_CH SL 2 mm	1.11	0.94	2.76
3_CH Ph1_High	0.76	3.04	3.83
4_CH L2_Low	0.75	4.66	1.74
5_Biomedicine (B)	0.31	8.12	1.38
6_ST SL 2 mm	0.35	2.29	1.95
7_ST Ph1_High	0.42	1.66	1.05
8_ST test SL 0.5 mm	0.66	6.52	3.78
9_ST test SL 2 mm	0.59	5.39	2.42
10_Design (D)	0.52	1.48	1.23

The maximum uncertainty of reconstruction by the three algorithms on different object with different resolution is equal to 8,12%. This means that the resolution is irrelevant.

In Figure 94 the Box Plot of ten objects volume is showed.
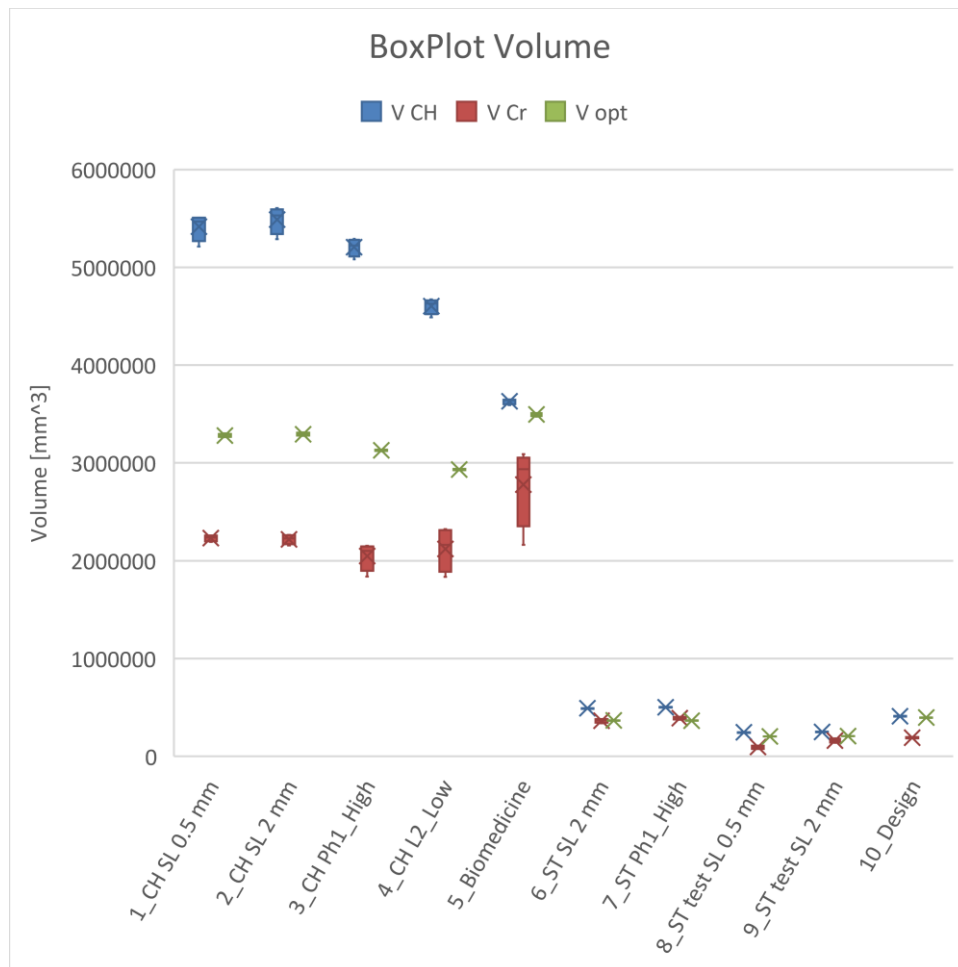
Figure 94 Box Plot of Volume given by CH, AC and A opt algorithms.

The resolution is influencing a little more the reconstruction of Biomedicine object with Alpha Critical algorithms since the deviation is higher.

In Figure 95 the Box plot of the volume (given by the three algorithms) for all the acquisition, and different number of points, is showed.
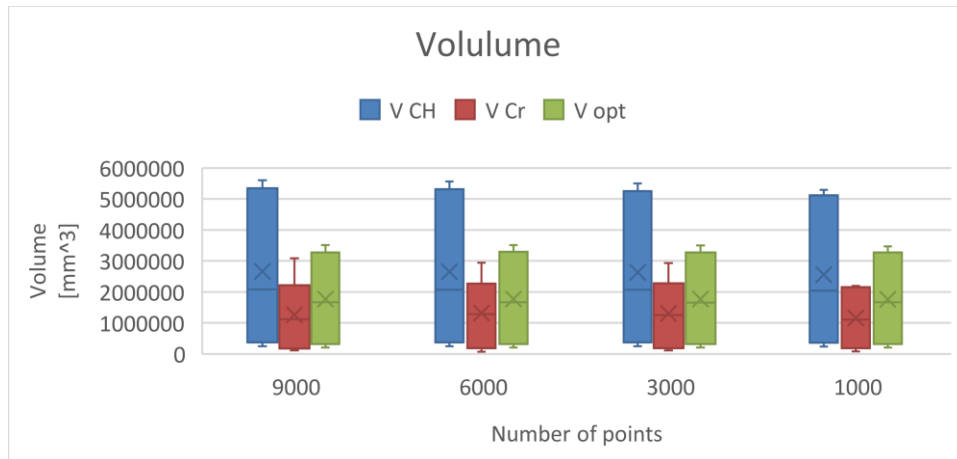
Figure 95 Box Plot CH V Cr V opt changing number of points

This Figure show that in this case the resolution is not highly influencing the final volume evaluation, in fact Convex Hull, Alpha Critical and Alpha optimal have the same shape. Furthermore, Alpha Critical give the lower volume. Unlike the simple objects, here the Convex Hull and the alpha Optimal have two different trends.

Finally, for each object, Box Plot of MAPE of the three algorithms was evaluated (Figure 96).
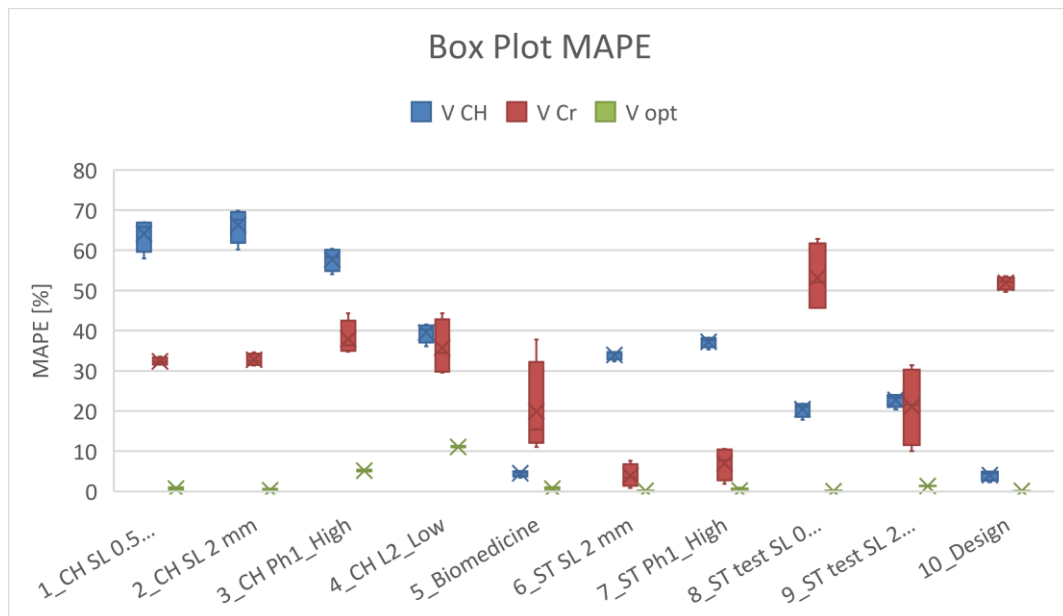
Figure 96 Box Plot MAPE of the ten objects.

The volume calculated with the Alpha Critical algorithm is more influenced by the size of the object, and the resolution, as mentioned, as well as the complexity of the shape. The volume is calculated but is not always reliable. In fact, MAPE is only within 20 % for a few objects. The best reconstruction would appear to be the optimal alpha, which, although it reconstructs the shape well, also has reconstruction errors. The alpha radii for the world cup, for example, are < 75 mm and have reconstruction errors that are compensated for by the algorithm. The MAPE of the Convex Hull decreases as the size of the object decreases, in particular it overestimates large objects by more than 60 %, while smaller objects are overestimated by 40-50 %.

4.4 Conclusions

As told in the introduction, both qualitative and qualitative analysis were performed in order to reconstruct a high-quality final product and compare it with the different instruments and resolution for analyse the differences of models. A quantitative analysis was than performed in order to study the effect of volume evaluation algorithms parameters on resolution.

Qualitative analysis

In all the applications and objects shown so far, Structured Light enabled the best reconstruction of the shape, in terms of detail, mesh quality and texture. The comparison shows that as the resolution of the tool used is lowered, the problems in reconstruction increase.

The LiDAR system used in the World Cup, although low resolution, returned an excellent texture that was useful for modelling. The photogrammetric system, although heavy in terms of Gigabyte processing, showed excellent versatility, and good mesh quality was also important for modelling. As far as the reconstructed torso is concerned, a separate chapter has been dedicated to this as mentioned above. The smoothing algorithms of the final reconstruction of static objects with concave and convex and complex parts (e.g., crown of the pomegranate) were analysed here. In general, the analysed meddles, set at a threshold of 1 mm result in acceptable smoothing values. The part of the rock scan is the most distant from the structured light value with a percentage of points out of calculation of 40 %. The photogrammetry in fact higly approximated the concave details.

Quantitative analysis

By the spectrum it is possible to know the best investigation range for Alpha Shape Analysis (Test 1). The reconstruction uncertainty analysis was carried out by varying the alpha radius in this range. Through this analysis, it was possible to select the most suitable alpha range for the reconstruction of the shape and thus in the calculation of the volume, for large objects (alpha radius < 75 mm) and small objects (Alpha radius > 35mm/45 mm). In this range, by changing the resolution of the point cloud, for each object the maximum uncertainty of the reconstruction between the various subsampled models is 25.39 % (Biomedicine). In general, in the survey range (5 mm to 105 mm), the alpha radius of 5 mm does not reconstruct to shape. After selecting the appropriate alpha radii for larger and smaller objects, MAPE was assessed, i.e., the distance between the reference volume and the reconstruction.

With regard to the other algorithms tested, namely alpha Critical, alpha optimal and Convex Hull, the uncertainty of the shape reconstruction is relatively low, around 8% for the different resolutions of each object. This means that the resolution does not have much influence on these algorithms for these types of shapes and sizes. Looking at MAPE, it can be seen that the Convex Hull overestimate large objects by up to 70 %. The Alpha Critical and Alpha Optimal algorithms tend to create errors in the reconstruction of the model and the final calculation of the volume with a critical radius overestimates the volume by up to 40 %, while the Alpha Optimal is closer to the reference volume.

Low-cost systems such as the LiDAR used in this study, although not reliable in terms of mesh quality, returned not only good texture quality, as mentioned, but also a good level of shape reconstruction for volume calculation. For the purpose of volume calculation, the performance of the tools is comparable. In conclusion, through these analyses, one could consider using low-cost, non-contact monitoring systems using these uncertainty values to calibrate the systems.

The qualitative analysis of the comparison between the raw point cloud, (given by the Structured Light scan with the maximum resolution), and the reconstructed models showed a maximum reconstruction uncertainty of 0.31mm (World Cup scanned with the photogrammetric technique). This value is under the resolution of

Structured Light scanner GO!SCAN 50 (0.5 mm) in agreement with [61], [62] and [63].

The quantitative analysis confirmed what was said in the previous chapter: it was possible to identify a range of alpha values (15-75mm) within which to conduct the analyses, thus making the calculation faster. The impact of the point cloud density on the reconstruction was also evaluated. Also, in correspondence with the world cup scanned with photogrammetry, greater uncertainty is noted (22.76% for 9000 points, still 23.53% for 1000 points). Increasing the density of the points, the uncertainty of the reconstruction decreases, according to [68], [88], [65], [66] and [86].

Chapter 5

Methodology for 3D reconstruction and volume estimation of fruit trees by using low-cost RGB-D cameras and LiDAR based scanner.

5.1 Introduction

In this Chapter, the analysis of algorithms will be performed on a calibrated sphere and an artificial tree without reference. In this case, first Alpha Critical, Alpha Optimal and Convex Hull will used to evaluate the volume. After the algorithms Alpha Shape changing radius will be used in order to analyze the best alpha radius to select for tree volume evaluation. The aim of this chapter is to study the ability of RGB-D cameras to generate 3D reconstructions of fruit trees and estimate their canopy volume and leaf area under controlled lighting condition [47]. Knowledge of these geometric parameters is essential so that farmers can adjust the inputs applied to the crops (pesticides, fertilizers, irrigation, etc.) to their variability, following the Precision Agriculture paradigm [81]. The ultimate goal is to improve the efficiency of these applications, with the consequent economic savings and less environmental impact. The work presented in this chapter was carried out within the framework of a research stay carried out with the Research Group on AgroICT & Precision Agriculture (GRAP) at the University of Lleida (Spain).

Many studies demonstrate various methods for estimating canopy volume and characterising orchards using 3D measurement techniques and point cloud processing techniques.

[104] presented a convex hull algorithm for estimating tree volume from 3D laser measurements. The algorithm minimises error and returns the convex hull points and associated volume.

[105] evaluated four methodologies for orchard characterisation, including the convex hull approach, segmented convex hull approach, cylinder-based approach, and occupancy grid approach. The convex hull and cylinder-based methods correspond better, while the occupancy grid approach yields the best results.

[106] A Mobile Terrestrial Laser Scanner (MTLS) characterised an olive plantation. They classified points into vertical and horizontal prisms to obtain width, centroid coordinates, and average width for each section.

[107] developed a method for estimating canopy volume and height in an orange plantation using the convex hull and alpha-shape reconstruction algorithms. Both methods yield similar results, with the alpha-shape offering concavities based on the α index. The optimal α value of 0.75 was determined in the study, striking a balance between capturing concavities and maintaining a solid canopy object.

[108] employed a 3D LiDAR and IMU for tree mapping in fruit orchards. They used the voxel grid method, dividing the 3D space into voxels, and the convex hull method for volume estimation.

[109] introduced the partition-hull method, which segments trees vertically and partitions them into clusters, excluding holes within the canopy. The convex hull is computed for each partition, and the sub-volumes are summed to estimate the tree's final volume, showing high accuracy.

The alpha-shape algorithm stands out as the best option for estimating canopy volume due to its ability to capture concavities in shape. By adjusting the α index, the level of concavity can be controlled. Lower α values better represent the outer profile of the canopy. However, disconnected structures and holes can appear with higher α values. This makes the alpha shape algorithm suitable for individual trees and provides a more accurate canopy volume and shape estimation than other methods.

In reference [110], the authors utilised lidar for reconstruction and volume calculation but highlighted that lidar data is noisy and unable to overcome

occlusions. On the other hand, RGB-D sensors can mitigate these issues. Therefore, using RGB-D sensors in field conditions for tasks like volume estimation and phenotyping can provide valuable depth information to address challenges such as occlusion [64].

As expected, the cylinder-based approach and the convex hull approach provide upper bounds of the volume estimation. The convex hull approach also affects the computational cost since it underestimates non-convex regions of the point cloud, resulting in lower computational costs than the segmented convex hull approach and the 3D grid approach. Additionally, it can be observed that the convex hull and cylinder-based approaches reach their steady-state estimation faster than the other approaches [111]. Furthermore, this article highlights the close relationship between the increase in volume and the number of points, which follows a logarithmic pattern.

Studies analyse a relationship between leaf area and volume, and they have specifically evaluated this relationship [17], [112], [113], [114]. This relationship is crucial for understanding plant growth and development, as well as for crop yield prediction and optimization [61].

A study by [62] examined the relationship between volume and leaf area in a pear tree canopy using various volume estimation methods. The researchers specifically employed the Linear Fitting-Based method, which utilises linear fitting techniques to establish a connection between the estimated volume and the surface area of the foliage. The findings from this research offer significant insights into estimating volume in agricultural applications by highlighting the linear correlation between foliage surface area and volume.

In [115], the researchers examined the growth factor of trees by measuring height, volume, and fruit yield (which is associated with volume). They discovered a clear growth trend and employed linear interpolation to analyse this growth. They specifically stated that there is no universal model for predicting growth, as the growth pattern depends on factors such as the type of plant and the season. Furthermore, the researchers developed growth prediction models by fitting crop growth and growth rate curves to time series data. These models utilised the first derivative to estimate the maximum growth rate, specific event days, and the duration of the growth period. The article also emphasises that the correlation

between within-season attributes and growth is stronger for annual fruit crops compared to perennial ones. Therefore, it is recommended to use customised models specific to individual orchards and seasons for accurate growth predictions. While the growth curves of certain fruit trees, such as apples and pears, tend to remain relatively consistent across various locations, following a linear trend, the growth patterns of other plants, like grapes, can exhibit significant variations.

The study [63] investigates tree volume growth, considering the limitations of linear relationships in natural settings and favouring a logarithmic model as a more suitable approach. Specifically, the researchers focus on hedgerow fruit tree crops (such as apple and pear trees) and hedgerow vineyards (vines) to examine the association between Total Registered Leaf Volume (TRLV) and Leaf Area Density (LAD). The results reveal a significant correlation between TRLV and LAD in the crops, indicating a shared pattern of leaf competition for light and utilisation of volume or space across all three crop types. A logarithmic relationship is observed at an individual plant level between TRLV and LAD, with an R^2 value of 0.87. This finding substantiates the hypothesis that a nonlinear connection exists between TRLV and LAD.

5.2 Materials and Methods

A defoliated apple tree (*Malus domestica* Bork) fixed on a wood pallet (Fig. 1a) was geometrically characterized by using an RGB-D camera (Azure Kinect) and a backpack LiDAR mobile scanner (Viametris BMS3D) as described in Chapter 2. To study how the presence of leaves affects the volume estimates, artificial leaves held by clamps were placed on the tree. 15 tests were performed with each sensor by varying the number of leaves from 700 to 0 with a step of 50. All the tests required the sensors to be moved around the target (tree) following different paths. In case of the RGB-D camera, 8 acquisitions per test were performed taking captures on fixed points (every 45º) on a circle pattern with a radius of 1.40 m. In case of the backpack LiDAR scanner, only a single capture was carried out, with the operator walking a square pattern with side of 4.80 m. Each test required 15 min and 8 min for the RGB-D and for the LiDAR, respectively. Throughout the experiment, a black towel was mounted around the tree to avoid the presence of external light. The different paths are shown in Figure 97.
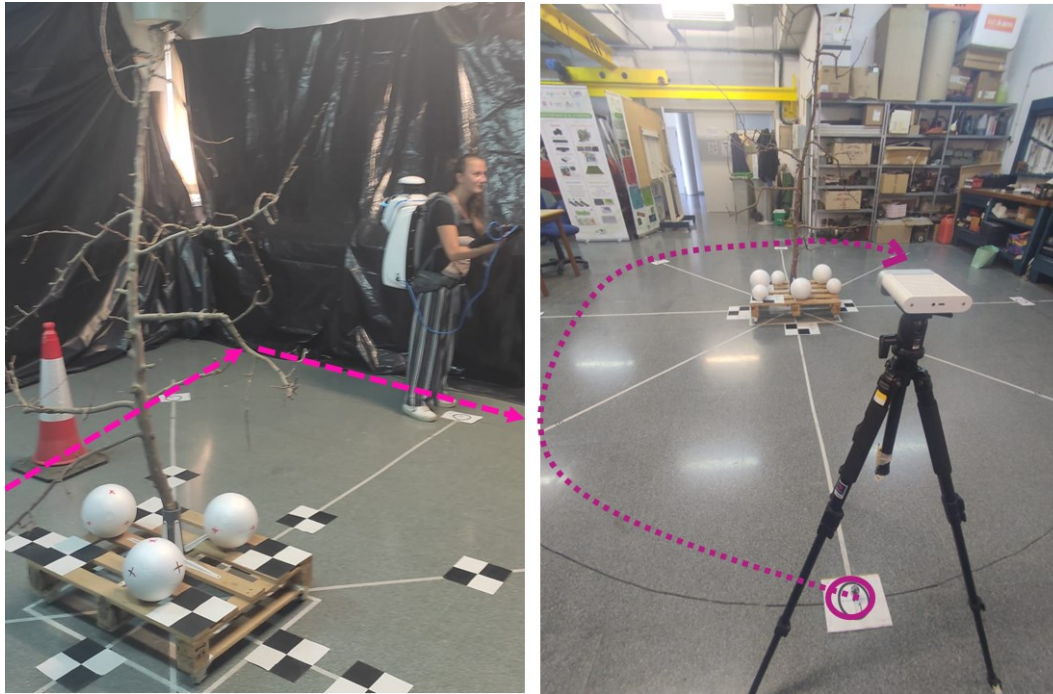
Figure 97 Measuring paths followed with: a) backpack LiDAR scanner; b) RGB-D camera.

As shown in Figure 98, four different reference targets types have been used in order to facilitate the alignment and matching between scans on the post-processing phase:

- Three 19-cm diameter sphere targets were located on the wood pallet.
- Seventeen black and white 40×40 cm square targets were also used: four located on the wood pallet (80×60×12 cm) and thirteen located on the floor.
- Eight 10-mm diameter circle targets for the RGB-D camera coordinate position numbered from 1 (starting point) to 8 (ending point).
- Four cones with a height of 71 cm and a square base of 36.5×36.5 cm were used for LiDAR point clouds alignment.
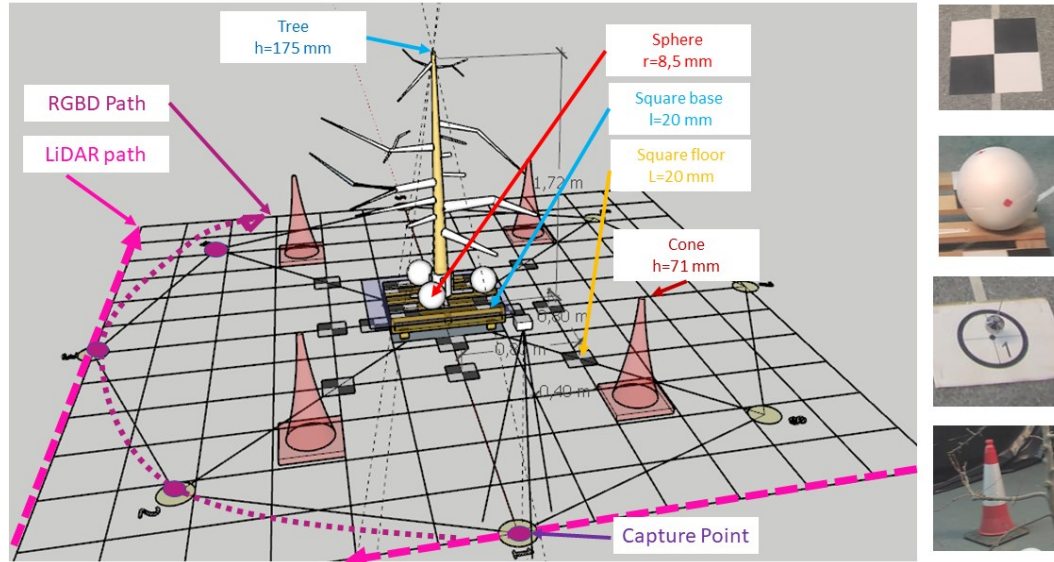
Figure 98 Reference targets used for alignment and positioning.

The Azure Kinect RGB-D camera was configured to save colour, infrared and depth data, with the following parameters: 30 frames per second (FPS), 1920×1080 color resolution, NFOV depth mode without binning, BGRA color format, and Matroska (MKV) format for video storage (https://www.matroska.org/). The Azure Kinect camera also includes an Inertial Measurement Unit (IMU) that was disabled for this experiment. The AK_SM_RECORDER software application (https://pypi.org/project/ak-sm-recorder/) developed by the GRAP was used to record the videos of the scene. A total of 120 videos were captured (8 videos per test) with a duration of 3 seconds each, in the time interval of 14:30 – 18:30 (UTC +2) Spanish summer time, on July 21, 2022.

For as regard the LiDAR scanner, since the scan was carried out inside, it was not possible to use the GPS receiver, so measurements were affected by noise. In fact, it was not possible to close the path through the proprietary software (Viametris). In this case, 4 frames per test were extracted corresponding to the four sides of the square path, resulting in a total of 60-point clouds.

5.2.1 Data processing

Data extraction. Video data captured by the RGB-D camera were extracted using the AK_FRAEX software developed by the GRAP (Miranda et al., 2022)

[82]. After 1 s from the beginning of each video, one frame (one point cloud) was extracted, resulting in a total of 120-point clouds (one per video).

In case of LiDAR data, frames were extracted using Cloud Compare (Cloud Compare GPL software v2.10 alpha and filtering the acquisitions (that depends on operator time to scan the path and close the loop) by time value of LiDAR sensors scans speed, in the Scalar Field (SF) that is represented by a colour spectrum [83]. Figure 99 show an example of the LiDAR scan of tree with 700 leaves and color spectrum of filtering procedure by time of LiDAR acquisitions. The colour represents the four sides: blue is the start of the scan while red represents the end of the scan acquisition time. As showed in the previous Figure 98, the path of the mobile LiDAR scanner (worn by the operator) is square, so it has four linear sides and four corners. The operator walked along four straight sides of the square at a constant speed. At the four corners, the operator had to stop to rotate 90 degrees to continue scanning along the sides. This rotation took place at a slow pace in order to prevent noise from the movement. In Figure 99 a, the SF colour spectrum shows in the Y-axis the times of the operator's movements and in the X-axis the LiDAR acquisition speed. In particular, the peaks (blue, green, yellow, orange and red) represent the four sides of square path, traveling at a constant speed (fast movement). In this case, there are five peaks, not four, since the operator has retraced part of the initial side to close the loop. The fifth peak (in red) will not be considered as it is only needed by the scanner software to close the path, optimize it and perform the reconstruction. In the colour spectrum of the SF, it is possible to distinguish values close to zero that correspond to the rotation of the operator (slow movement) at the corners. Only the time intervals corresponding to the path on each side of the square (fast movement) were selected (Figure 99 b in blue color). This selection was then filtered again in a shorter time interval as showed in Figure 99 c (green colour) thus avoiding overlapping the scanning of the side with noises due to rotation, close to the colours blue and red in the colororbar (Figure 99 d). Finally, after the various steps of filtering the acquisitions over time, the time window of about half a minute per side was selected (Figure 99 e).
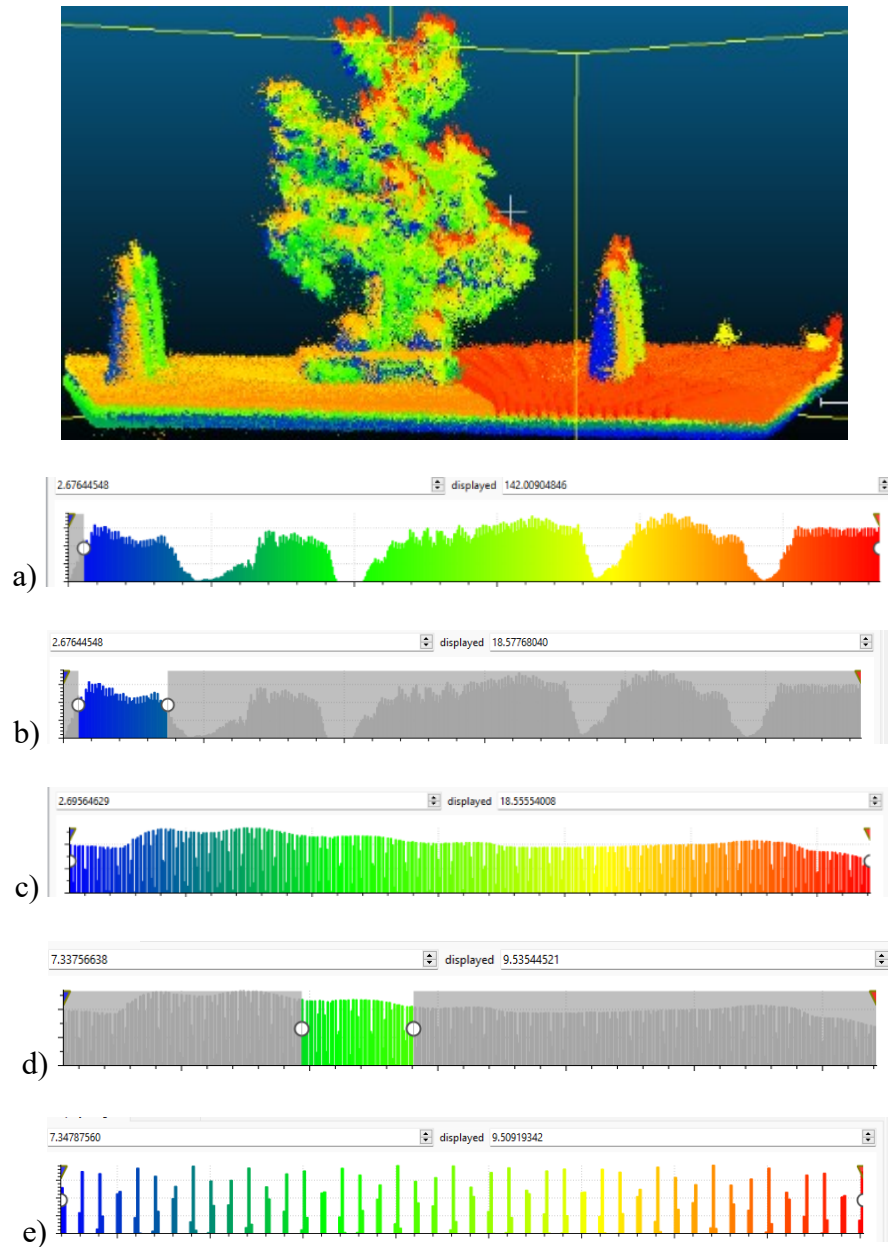
Figure 99 LiDAR path reconstruction Example corresponding to the test with 700 leaves. Steps followed for frame extraction on LiDAR data; a) Colored peaks (From blue to red) represent the sides of square traveling at a constant speed (fast movement). The interval between peaks corresponds to the slow rotation of the operator at the corners (slow movement). Note that red peack was not considered; b) Selection of first side of square; c) Zoom of the time interval selected; d) Filtering from noise due to rotation; e) shows in the Y-axis the times of the operator's movements and in the X-axis the LiDAR acquisition speed of first side of square selected.

By this procedure it is possible to select the time interval with less noise given by movement and rotation. Since the path is a square, four frames were extracted in order to reconstruct the shape, with a total of 60 points clouds (15 tests with 4 frames per test).

In conclusion, 15 tests were performed with the RGB-D camera with 8 points clouds to be aligned per test. 15 tests were performed with LiDAR with 4 points clouds to be aligned per test.

Point cloud alignment. Those point clouds (frames) were aligned by using the Cloud Compare software. The procedure followed was based on pairwise point cloud alignment. The first frame was taken as the initial reference for both scanners. The second frame was aligned and then taken as reference for the third frame and so on. The alignment was performed manually selecting about 14 key points in each pairwise point cloud captured by the RGB-D camera. These key points were selected on the square targets positioned on the floor (about 9 points per acquisition), on the spheres (2 or 3 points depending on the camera position and occlusions), on the wood pallet and on the top of tree.

Concerning the LiDAR scanner, since point cloud captures were filtered (procedure of Fig. 3), they lack much detail at the RGB colour level. In this case, a key point located on the top of the tree (at least 1), on the target on the floor (at least 1), on the wood pallet (at least 1) and at the top of the cones (about 2) were used. The number of key points in each pairwise of aligned frames varied from 4 to 8.

Depending on the number of points selected in the parawais of acquisition to align, CloudCompare give the total Root Mean Square (RMS) of all points selected, in order to check the effect of the alignment on the reconstruction of model. Examples of points selected for alignment in RGB-D camera and LiDAR scanner are showed in Figure 100.

(a)   (b)   (c)

(d)   (e)   (f)
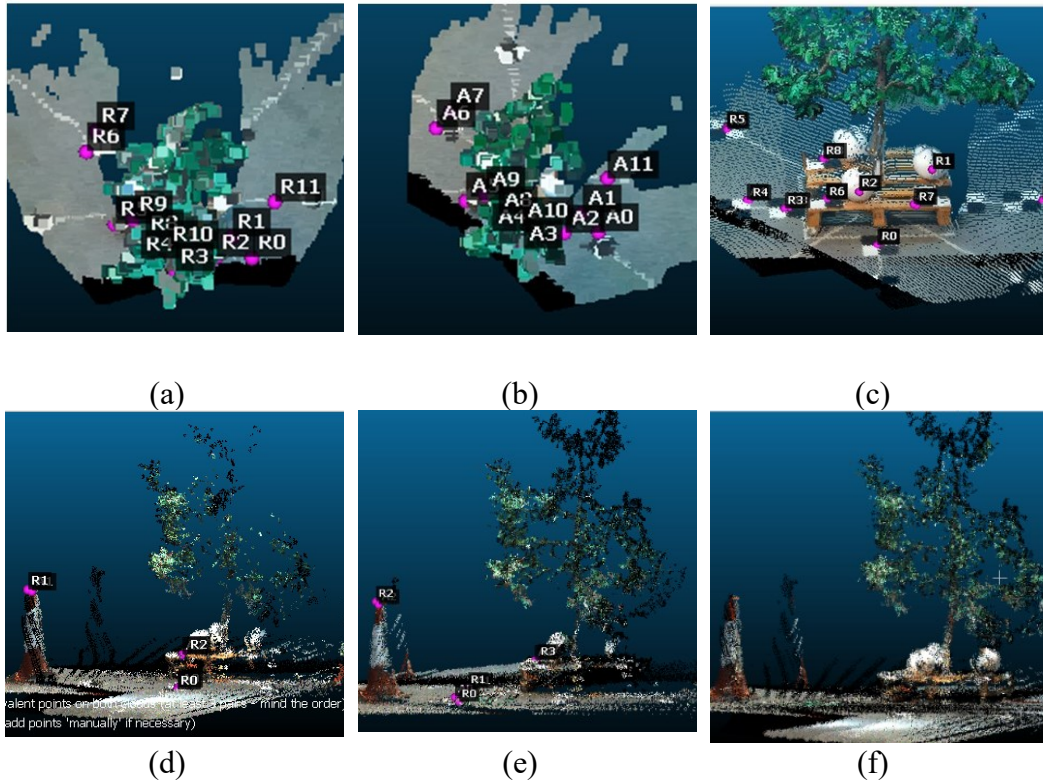
Figure 100 Example of pairwise frame alignment (tree with 700 leaves) for the RGB-D camera (upper row) and for the LiDAR scanner (lower row). The process followed is: (a,d): frame 1 (reference point cloud); (b,e) frame 2 (aligned point cloud); (c,f) result of aligning frames 1 and 2.

Some of the selected point in the previous Figure were used to compare linear manual measurements in other to verify the accuracy of the reconstructed model. Figure 101 presents an example of key point selection and point cloud alignment corresponding to RGB-D camera captures. Figure 101 (left) shows main points picked for alignment located respectively: on the sphere(s), in the wood pallet (b), on the floor (f) and at the top height of the tree (h). In the 3D point cloud, the tree height was evaluated as the the average difference between the Z axis coordinates on the wood pallet (b1, b2 and b3) and the Z coordinate on the top of the tree (h). The tree height was manually measured positioning the tape on the top of the tree and intersecting the wood pallet with 90° angle by gravity (checked by level). Other measurements on the floor plane (distances between p1-p2= Y and p2-p3= X) were checked and compared with manual measurements. The last two measurements were taken on the centre of square targets. Figure 101 (right) shows an example of

the resulting alignment of all the eight RGB-D camera acquisitions (tree with 400 leaves) and the points selected for comparison with linear manual measurements.
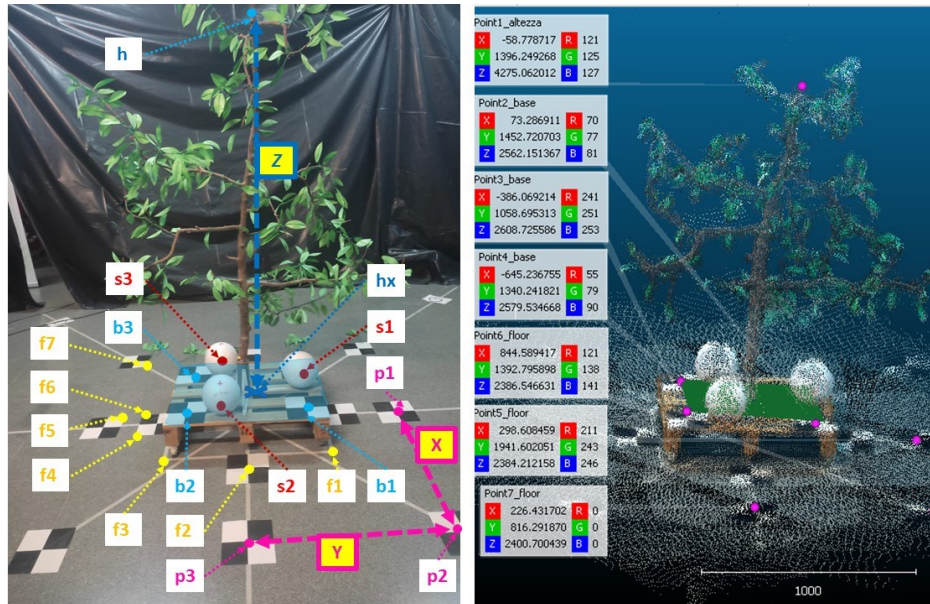
Figure 101 (left) Key points selected to perform the point cloud alignment. (right) Example of alignment of point clouds captured by the RGB-D camera for the test with 400 leaves.

Finally, to achieve the final geometry, a first segmentation is carried out to identify sphere and tree points.

Segmentation. Taking as reference the surface of the wood pallet (green plane in Figure 4b), the points corresponding to the spheres and the tree were segmented from the rest of the scenario. For both the RGB-D camera and the LiDAR scanner, there were a total of 45 sphere point cloud and 15 tree point clouds. After segmentation, the resulting point clouds were cleaned and filtered. In addition, since CloudCompare allows to fit a point cloud with simple geometry (e.g., plane or sphere), it was used this function to check the final reconstruction of the spheres. In Figure 102 the result of segmentation is shown.
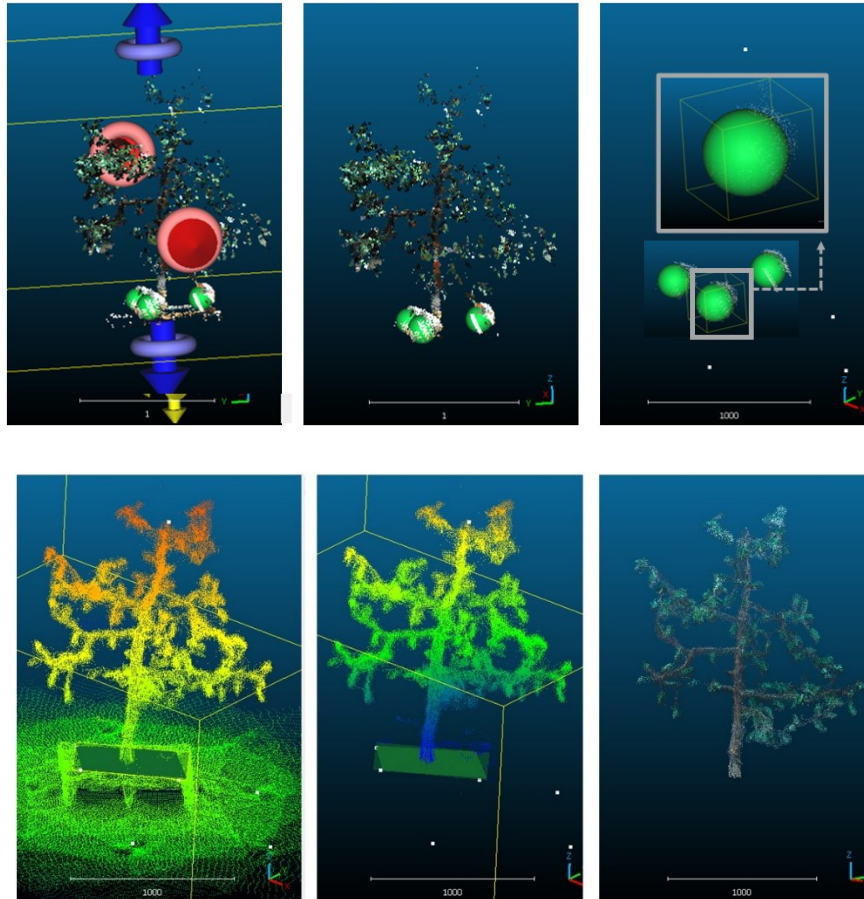
Figure 102 Acquisition with 300 leaves. Steps of sphere and tree segmentation and CloudCompare reconstruction of sphere by fitting points.

The final RMS of point picked in each pairwise of frames aligned by CC will be shown. After segmentation and cleaning phase, the linear measurement uncertainty will be presented in other to analyze the differences between RGB-D camera and LiDAR models.

Furthermore, for as regard the sphere in which the reference was determinate (by repeated measurements by caliper) it is possible to evaluate the uncertainty of the volume given by adjustment of fitting sphere of point in CC and the volume, by Alpha Shape and Voxelization algorithms reconstruction. For as regard the tree, it is difficult to use the CC function for volume evaluation (unlike lettuce plant as presented in Chapter 4) or to find a shape to fit (e.g., sphere).

5.2.2 Sphere measurements: uncertainty evaluation

The goal is to measure the tree, but first three spheres were measured. The aim is to measure the uncertainty of the volume reconstruction so that an initial comparison can be made between the two instruments. Subsequently, the tree will be studied. Note that these spheres were used as targets to perform the alignment, so for each sphere there are 15 measurements. This analysis also helps to better understand the goodness of the final reconstruction. The three sphere's diameters were measured ten times in different planes by a caliper Mantax Blue 500 mm 0402-MID-SC0986 (Haglöf, Långsele, Sweden), with a total of 30 measurements with a resolution of centimeter (Figure 103) [84].
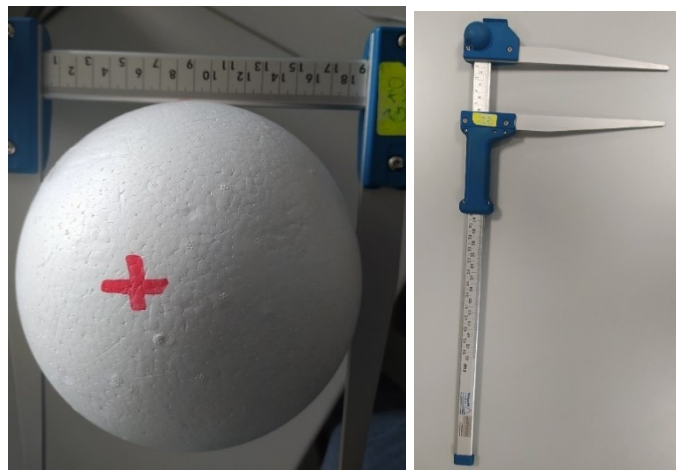
Figure 103 Sphere 1 and caliper.

For each sphere, the mean diameter, the standard deviation of the diameter, the uncertainty of the diameter, and the sphere volume were computed in order to verify the volumetric uncertainty. For cubic propagation that is known, the volumetric uncertainty has to be three times the linear (diameter) uncertainty [58]. The uncertainty of diameter (direct measure), of radius and volume (indirect measures) was evaluated. Since the uncertainty of diameter was equal to the uncertainty of radius, this last will be considerate. In Table 24, the relationship between volume and radius uncertainty of manual measurements are shown.

Table 24 Manual measurements uncertainty of the three spheres (S1, S2 and S3).

	Mean [r, V]	Dev.std [r, V]	Unc [r, V]	Unc [%]	Vol/Radius [adm]
S1_V mm³	3689675.72	106033.28	33530.67	0.91	2.94
S1_r mm	95.85	0.94	0.3	0.31	
S2_V mm³	3694509.7	34645.77	10955.95	0.3	3
S2_r mm	95.9	0.3	0.09	0.1	
S3_V mm³	3694630.06	50261.53	15894.09	0.43	2.99
S3_r mm	95.9	0.45	0.14	0.14	

The results are coherent with Taylor formula because the volume uncertainty is tree time the linear uncertainty as show the relationship Volume/Radius uncertainty percentage (with a minimum value in sphere 1 equal to 2.94). The maximum uncertainty of manual measurements is about 0.3 % for as regards linear measurements (radius) and 0.4 % in volumetric formula. Those value of measurements are acceptable and they near to instrument resolution of Azure Kinect RGB-D camera and backpack mobile LiDAR [42] [34]. Those geometries were taken as reference for Alpha Shape and Voxelization algorithms reconstruction uncertainty evaluation applied on sphere. Since the tree is a complex geometry, it is difficult to have a mathematical equation of model. In this case, the error propagation by determination coefficient R^2 was evaluated in order to select the best reconstruction (the nearest to $R^2=1$).

5.3 Results

5.3.1. RGB-D and LiDAR alignment comparison

Result of RMS alignment: In this section, seven combinations for the RGB-D and three for the LiDAR RMS given by CC are showed. For each point cloud derived from the processing of scans, the total RMS of the key points selected to align the reference cloud and the subsequent was evaluated. Firstly, it was evaluated the RMSE of each scans point cloud picked distances, respectively called d1-2, d2-3, d3-4, d4-5, d5-6, d6-7, d7-8 for the RGB-D and d1-2, d2-3, d3-4 for the LiDAR.

Table 26 and 26, the RMSE of the pairwise alignment for the 7 combinations for RGB-D and 3 combinations for LiDAR of the final alignment is showed.

Table 25 RMSE of RGB-D alignment of distances between selected point (on reference and aligned point cloud) for the alignment (d)

RMSE [mm]	d1-2	d2-3	d3-4	d4-5	d5-6	d6-7	d7-8	Mean.d [mm]
Max	35.17	33.96	36.32	35.41	34.98	31.81	35.79	34.78
Min	19.47	21.76	22.68	15.75	21.19	12.07	16.30	18.46
Mean	26.60	27.37	27.26	24.5	28.33	23.86	24.73	26.09
Dev. Std.	3.71	3.23	3.65	5.71	4.60	4.78	5.55	4.46

Table 26 RMSE of LiDAR alignment of distances between selected point (on reference and aligned point cloud) for the alignment (d)

RMSE [mm]	d1-2	d2-3	d3-4	Mean.d [mm]
Max	63.10	79.39	70.98	71.16
Min	3.38	7.12	7.43	5.98
Mean	35.66	32.78	33.89	34.11
Dev. Std.	16.45	18.55	17.76	17.59

It is possible to notice that the RMS of alignment of LiDAR is higher than RGB-D. LiDAR technology from a cloud of points allows to reconstruct the detail of a tree and, therefore, measure its elements. However, the reconstruction of all the vegetative elements of the plant due to their complexity cannot be addressed with complete accuracy.

RGB-D: The final RMS resulting from alignment was max for alignment d5-6 with 28.33 mm and min for alignment d6-7 with 23.86 mm. The total standard deviation has a maximum in d4-5 with 5.71 mm and a minimum in d2-3 with 3.23 mm.

LiDAR: The max Mean resulting RMS is in pairwise d1.2 with 35.66 mm. The minimum RMS is in d2-3 with 32.78 mm. The max standard deviation is in d2-3 resulting 18.53 and the min is in d1-2 16.45 mm.

Finally, the mean value of RMS and standard deviation of all the acquisitions aligned resulting to have an RMS of 26.09 mm and standard deviation of 4.46 for RGB-D and RMS equal to 34.11 mm and standard deviation of 17.59 mm for LiDAR. In conclusion, the RGB-D camera gives better reconstructions considering also the possibility to pick more points. In addition, LiDAR was limited for making the reconstructions since there was no GPS signal, it was difficult to reconstruct the path by the software. The path in fact was resulting not closed.

Comparison with manual measurements: It was evaluated the uncertainty of the reconstruction for both the RGB-D camera (ToF=T) and the LiDAR scanner (L). The following measurements have been considered:

- Height error Z. Given by the difference between mean height of 3 points (b1, b2, b3) and height coordinate h).
- Target distances error X and Y (of centre point coordinates on floor f1 f2 and f3).
- Sphere's diameter error. Corresponds to the error between manual measurements and fitted sphere by CC algorithms.

The following manual measurements (references) have been used to compute the previous errors:

- Height of the tree (H.Tr) =1730 mm.
- Target distances X and Y (T.d.) =800 mm.
- Sphere radius (R.S) = 93.52 mm ± 0.31 %.
- Sphere volume (V.S) = 3460777 mm^3 ± 0.91 %.

The target was distributed with the same distance in floor (X=Y=T.d). The reference sphere radius and volumes were taken the same for all spheres and for all target since the uncertainty of manual measurement was evaluated. It has to notice that the perfect sphere is represented by 95 mm of radius and 3591364 mm3 of volume. Finally, the mean of MAE, MAPE and RMSE of the measures are showed in Table 27.

    Table 27 Height of tree H.Tr, measurement on floor target T.d radius and Volume sphere's V.S by CloudCompare.

	Linear measurements	Height [mm]	MAE [mm]	MAPE [%]	RMSE [mm]
H.Tr mm					
	Mean T	1746.28	29.98	1.73	38.23
	Dev.std T	34.59	23.71	1.37	
	Mean L	1766.64	36.64	2.12	41.28
	Dev.std L	19.03	19.03	1.1	
T.d	**Mean T**				

	Sphere CC measurements	Radius, Volume [R, V]	MAE [R, V]	MAPE [%]	RMSE [R, V]
mm		820.68	24.45	3.06	29.1
	Dev.std T	20.47	15.79	1.97	
	Mean L	865.12	65.12	8.14	111.74
	Dev.std L	90.81	90.81	**11.35**	
R.S					
mm	Mean T	93.52	3.53	3.72	5.78
	Dev.std T	5.58	4.57	4.81	
	Mean L	84.89	11.15	**11.71**	2.06
	Dev.std L	9.461	8.25	8.69	
V.S mm³	Mean T	3460777	373494.6	10.4	544830
	Dev.std T	528945.5	396658.5	11.05	
	Mean L	2656707	1055948.55	**29.41**	1256940
	Dev.std L	840424.3	681813.91	18.98	

As it possible to see, RGB-D camera gives the best result in terms of MAPE. How it is possible to see, augmenting the dimensions of measurements Frome line height Htr, Tr to V.S, increase the uncertainty. It can be seen from the table that LiDAR deviates the most from the reference measurement in terms of both linear and volume measurements.

In the Figure 104, the volume evaluated by fitting the sphere with CloudCompare is represented against the point number.
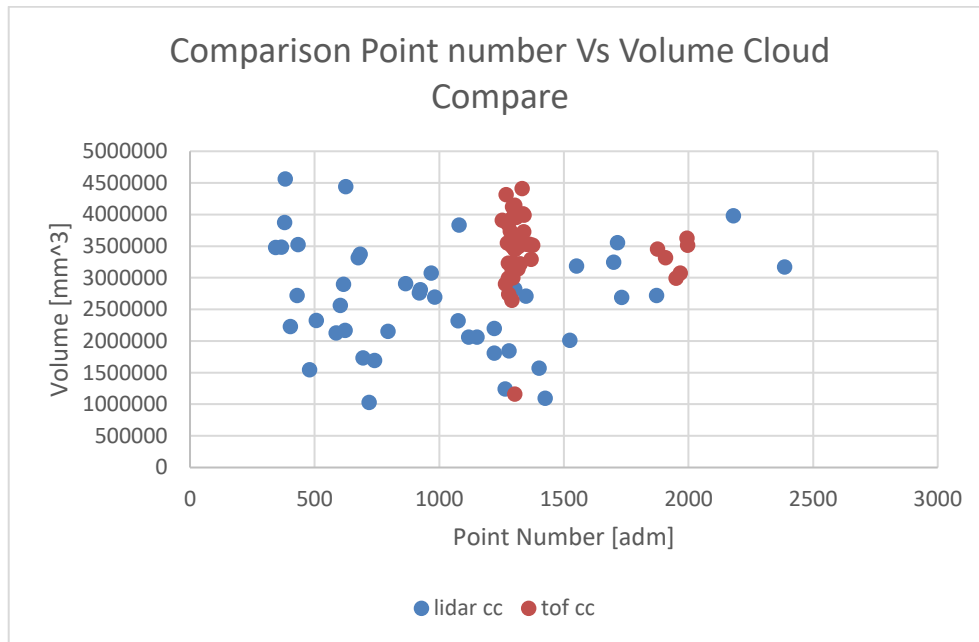
Figure 104 Comparison between LiDAR and RGB-D sphere volume reconstruction
by CloudCompare versus point number

As is possible to see, in LiDAR spheres there is more data dispersion in terms
of point cloud number. Figure 105 represents the volume of each sphere for each
acquisition (3 spheres, 15 acquisitions).
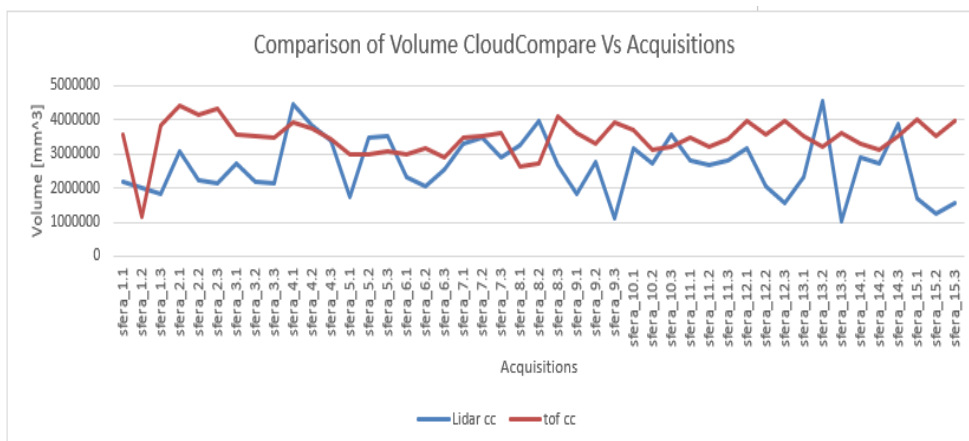
Figure 105 Comparison between LiDAR and RGB-D sphere volume reconstruction
by CloudCompare for each acquisition

Since the LiDAR values have a high dispersion, they were not used to evaluate the quality of the reconstruction given by the alpha shape algorithms and for uncertainty evaluation. By contrast, the scans made using Azure-Kinect allow a more stable volume reconstruction. Hence, the following results are based only on the acquisition using this technology, neglecting the LiDAR scans. For each sphere measured with the RGB-D camera, the total uncertainty and MAPE is represented in Table 28.

Table 28 Radius and volume evaluation of sphere by CloudCompare: Uncertainty of reconstruction and MAPE.

S1	CC rad [mm]	CC vol [mm^3]	CC_MAPE [%]
Max	101.72	4408020.64	28.39
Min	85.76	2642255.62	0.91
Mean	94.43	3545812.30	**9.65**
Dv.st	3.93	434590.77	
Unc	1.01	112210.85	
Unc%	**1.07**	**3.16**	
S2			
Max	99.65	4145423.39	68.63
Min	65.16	1158937.00	1.12
Mean	90.89	3204425.47	**15.04**
Dv.st	7.48	635070.00	
Unc	1.93	163974.37	
Unc%	**2.13**	**5.12**	
S3			
Max	100.99	4314561.13	21.55
Min	88.45	2898588.33	1.70
Mean	95.24	3632094.38	**8.76**
Dv.st	3.37	380618.29	
Unc	0.87	98275.22	
Unc%	**0.91**	**2.71**	

The reconstruction of sphere 2 by CC is more problematic since the MAPE of the volume between the reconstruction and the reference is about 15 %.

5.3.2 Alpha shape and Convex Hull uncertainty evaluation on sphere

This section evaluates the volume given by the Alpha Shape (considering both Alpha Critical (V AC) and Alpha optimal (V OPT) values) and by the Convex Hull (V CH) algorithms. An example of alpha optimal values for the three reference spheres used in this experiment is shown in Figure 106.
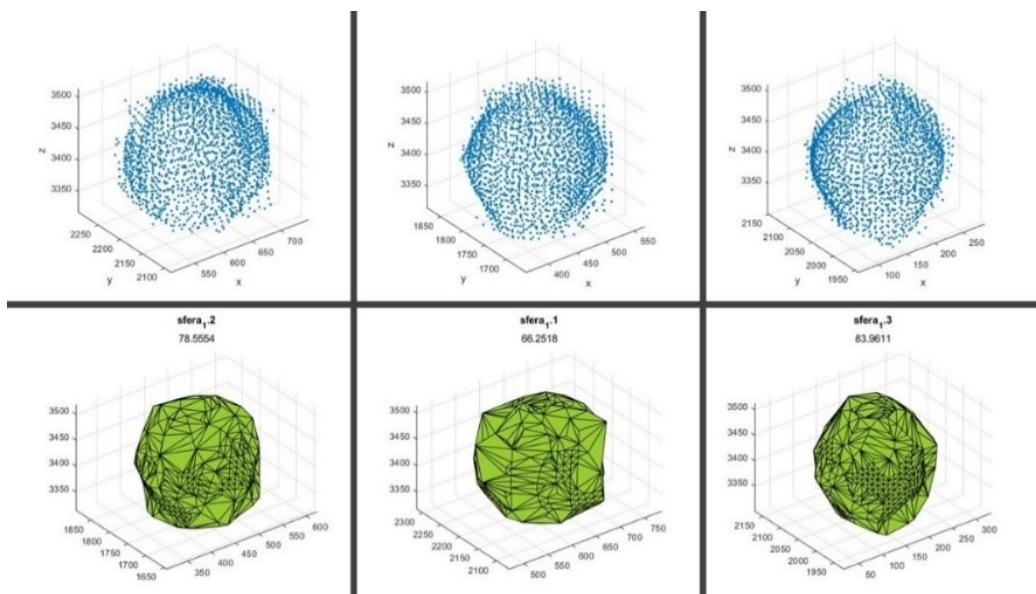
Figure 106 Point cloud and Alpha optimal reconstruction of spheres 1, 2, and 3 (tree with 0 leaves).

This figure shows the influence of the acquired point cloud on the final reconstruction.

Furthermore, by using the Alpha Spectrum function it is possible to know where the density of alpha radius is located for each point cloud as showed in Chapter 2 (Figure 107).
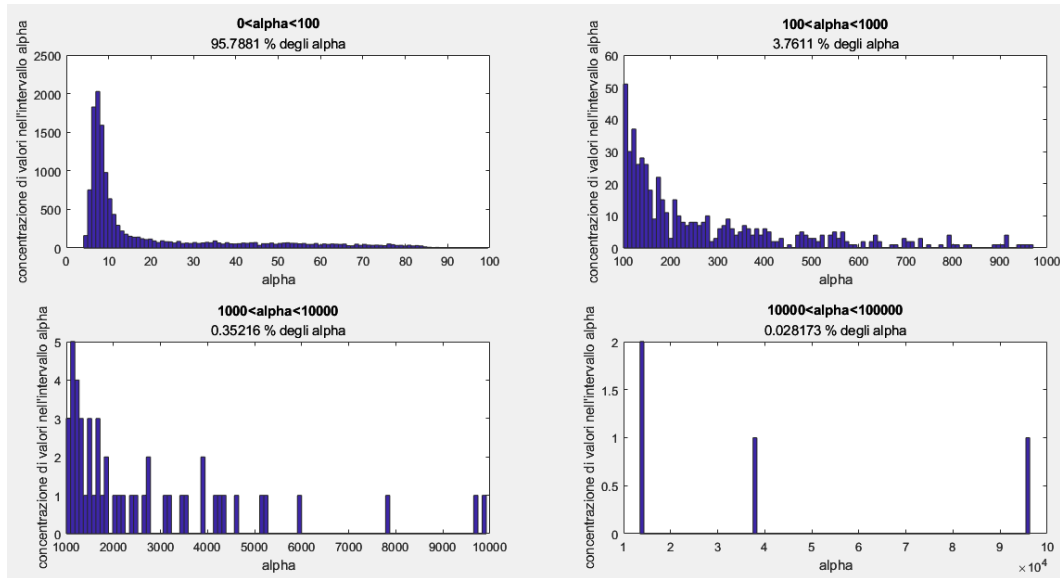
Figure 107 Point cloud and Alpha optimal reconstruction of spheres 1, 2, and 3 (tree with 0 leaves).

For all spheres, 96 % of alpha values are located between 4 and 100 mm and the density are distributed near alpha=10 mm. This means that this value of alpha is sufficient to reconstruct the shape. By this consideration, the effect on the reconstruction when changing alpha radius will be evaluated in section 5.4.3.

Alpha Critical, Alpha Optimal and Convex Hull Analysis

In this section, a comparison between the reconstructions when using Alpha critical (Cr), Alpha Optimal (A Opt) and Convex Hull (CH) algorithms will be shown and discussed.

Point number versus alpha radius: Figure 108 shows for each of the 45-point clouds of the spheres (3 spheres, 15 acquisitions) the point number, the alpha critical (Cr) and the alpha Optimal (A Opt). CH is not represented in this graph since alpha radius is infinite.
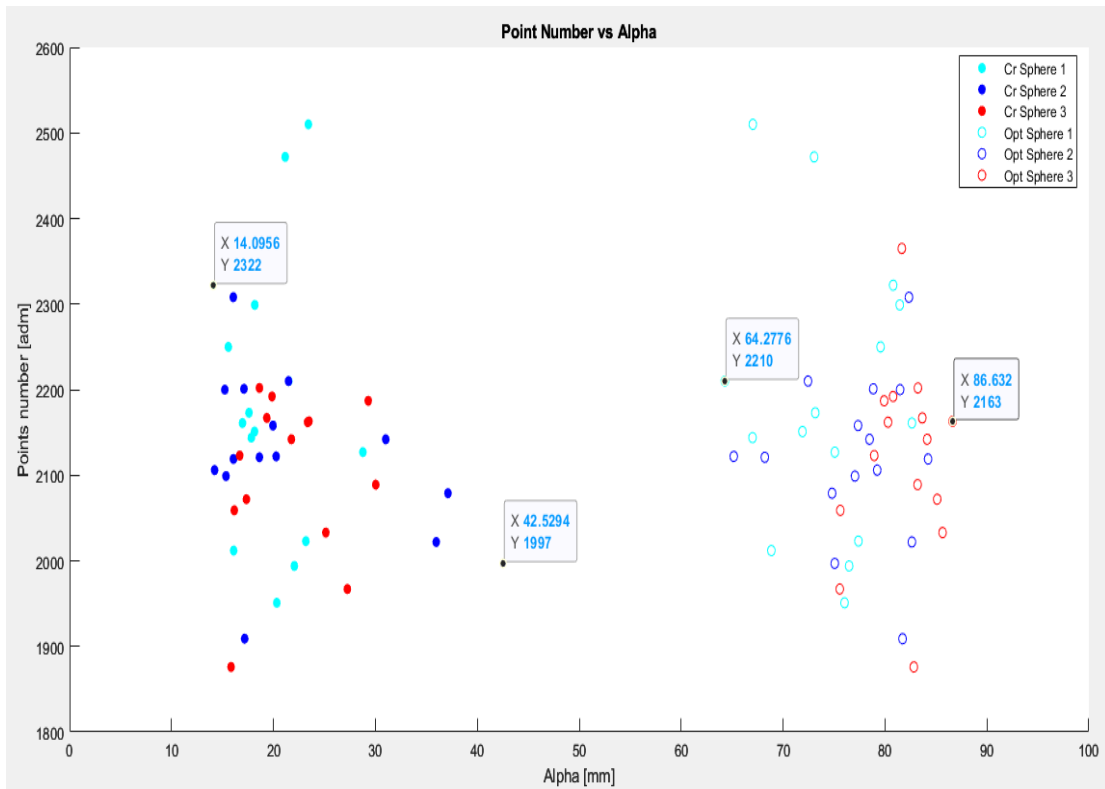
Figure 108 Alpha critical and alpha optimal Vs Number of points of the three spheres.

It is possible to notice that the number of points is varying from about 1900 to 2500. For all the different point clouds, the alpha optimal value shifts between 60 and 87 mm. The critical alpha is located between 14 and 42 mm, near the alpha spectrum range. The convex hull is not represented since the radius is equal to infinite.

Volume versus alpha radius: Moving on volume, in Figure 109 the volumes given by alpha values showed before are represented.
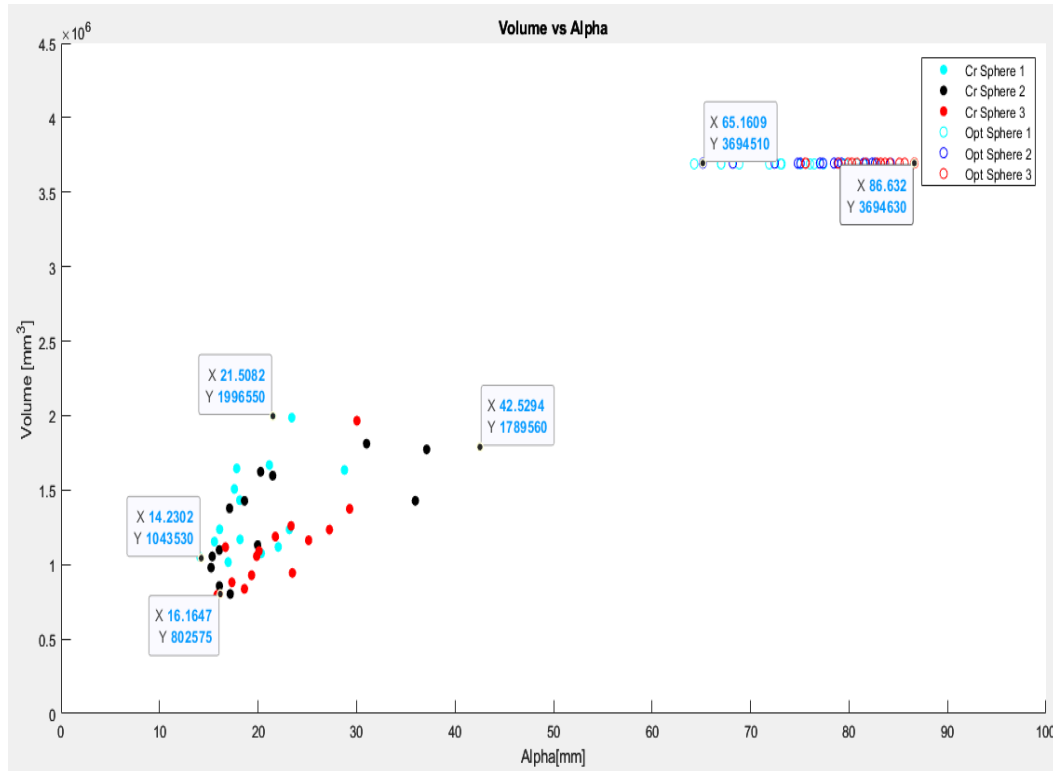
Figure 109 Spheres Volume versus alpha radius

The Figure show that the volume changes sensibly. In fact, for alpha critical the volume is changing from $80 \times 10^4 \, mm^3$ to $199.6 \times 10^4 \, mm^3$ showing a high dispersion (filled points on the left of graph). All these volumes are much lower than the reference ($360 \times 10^4 \, mm^3$). In case of optimal alpha, the volume results to be the reference as expected. This is obvious in fact the optimal value has been determined by adjusting alpha until the volume equals the reference (Chapter 3). Again, the convex hull will not be examined because the alpha radius is equal to infinite.

Volume versus acquisition number: The final volume versus acquisition number (where the leaves of the tree changed from 0 to 700 with a step of 50 leaves) is shown in Figure 110.
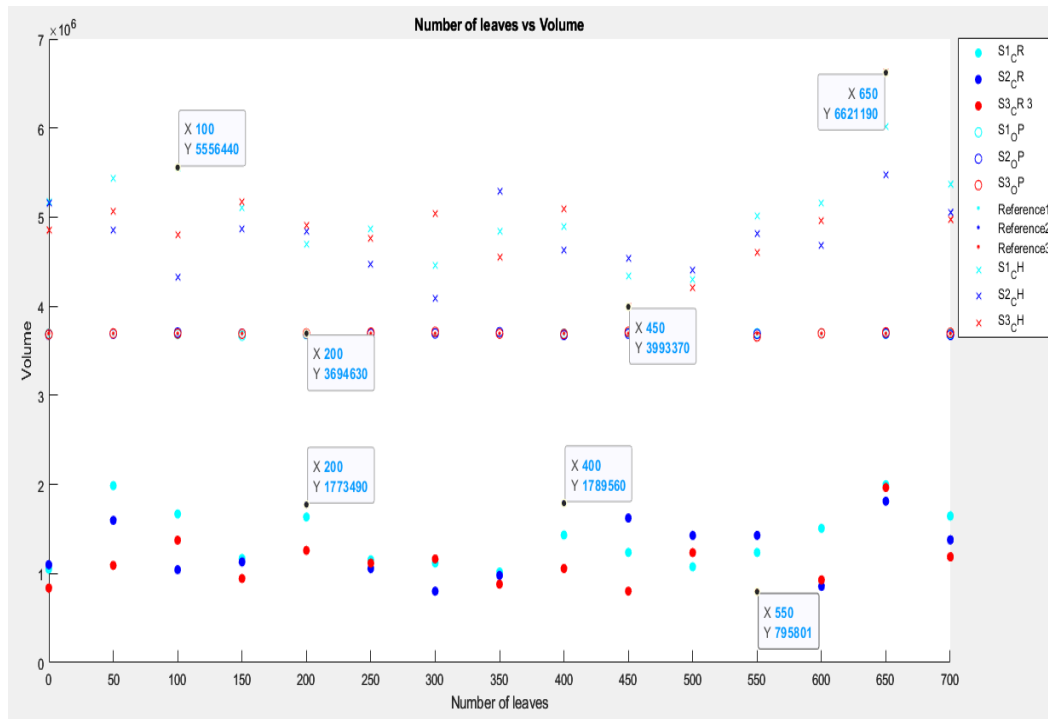
Figure 110 Sphere Volume versus leaves number (acquisitions)

This Figure represents, for each sphere, the estimates of the volume using the Alpha Critical indicated with filled circles, the Alpha Optimal indicated with empty circles (that correspond to the reference indicated with dots) and the Convex Hull, indicated with cross. As can be seen, the volume given by the Alpha Critical that includes all-point (that in this case is equal to one region) and permits the closing of the shape, is lower than the reference, since we do not have a prefect sphere and the model is affected by noise. In x axis, the Number of Leaves corresponds to the 15 acquisitions. The value of volume by Convex Hull is higher than reference and the shape is more dispersive than Alpha Critical.

Finally, for each sphere, the mean of manual measurements (r S and V s) was taken as reference and the uncertainty of reconstruction was evaluated. It was also computed the Mean Absolute Percentage Error (MAPE), that is the error between reference and reconstruction of shape by algorithms, as follows in Table 29. The aim is to know how far the reconstructed model by the three algorithms is from the reference.

Table 29 Sphere Uncertainty analysis of reconstruction

S1	Volume CR [mm³]	MAPE [%]	Volume OPT [mm³]	MAPE [%]	Volume CH [mm³]	MAPE [%]
Max	1996554.13	72.45	3696344.10	0.54	6017599.45	63.09
Min	1016581.25	45.89	3669570.27	0.00	4299723.31	16.53
Mean	1395231.40	62.19	3689746.83	0.12	5015930.04	**35.95**
Dv	318275.16		6482.31		454871.55	
Unc	82178.29		1673.73		117447.33	
Unc%	**5.89**		**0.05**		**2.34**	
S2						
Max	1811754.89	78.28	3709831.53	0.49	5470072.54	48.06
Min	802309.79	50.96	3676547.07	0.00	4094174.02	10.82
Mean	1319541.87	64.28	3692000.76	0.17	4766120.35	**29.01**
Dv	336063.61		8465.89		361258.41	
Unc	86771.25		2185.88		93276.52	
Unc%	**6.58**		**0.06**		**1.96**	
S3						
Max	1965561.05	78.46	3713133.43	0.96	2926562.85	79.21
Min	795800.98	46.80	3659296.90	0.02	298740.28	8.09
Mean	1109277.82	69.98	3695444.35	0.23	1211413.95	**32.79**
Dv	286664.02		12517.04		557984.67	
Unc	74016.33		3231.88		144071.02	
Unc%	**6.67**		**0.09**		**11.89**	

This Table shows that the critical alpha gives a large uncertainty. In particular, for all the algorithms the best reconstruction is given by alpha optimal reconstruction that represent the reference. In Figure 111 an example of MAPE for the four algorithms is shown.
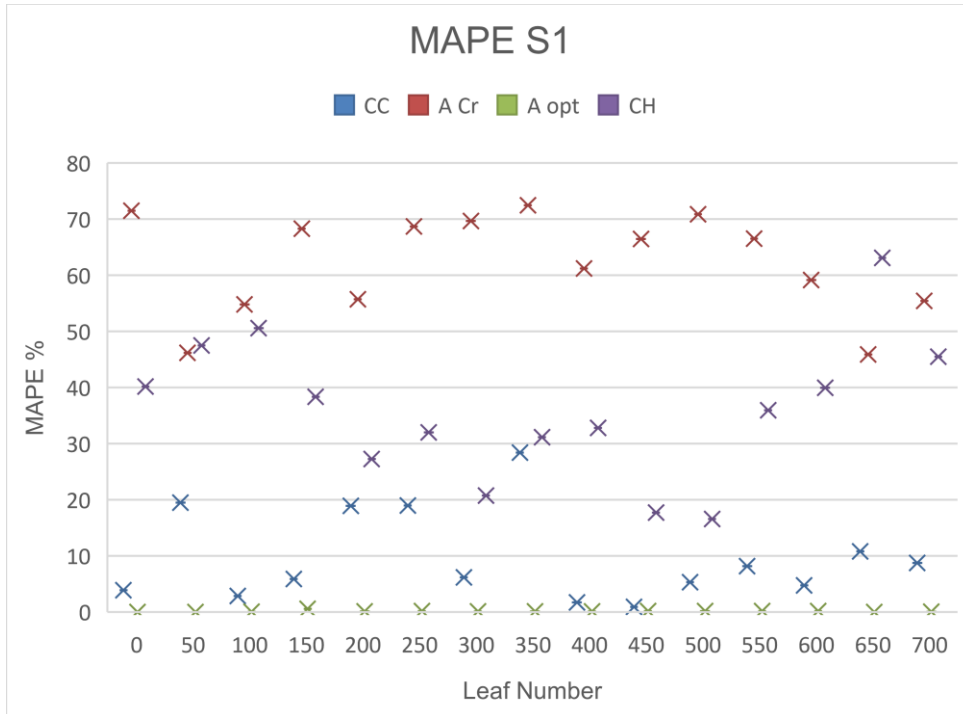
Figure 111 MAPE sphere 1

The Sphere 3 gives the worst reconstruction in all cases, Convex Hull return the worst results. In sphere 1 and 2 Convex Hull Give more accurate results compared with Alpha Critical. In general, Alpha critical gives the highest MAPE (69.98 %), Alpha optimal is well representing the reference and Convex Hull have an error of about 35.95 %.

Effect of alpha radius on sphere reconstruction

Since the alpha is not known, the alpha was changed from 5 to 105 mm with a step of 15 mm. As can be seen in Figure 112, the sphere volume increases with the alpha value. This range was chosen because those targets are not a perfect sphere. Also, the spectrum in fact shows the concentration of alpha radius in that range.
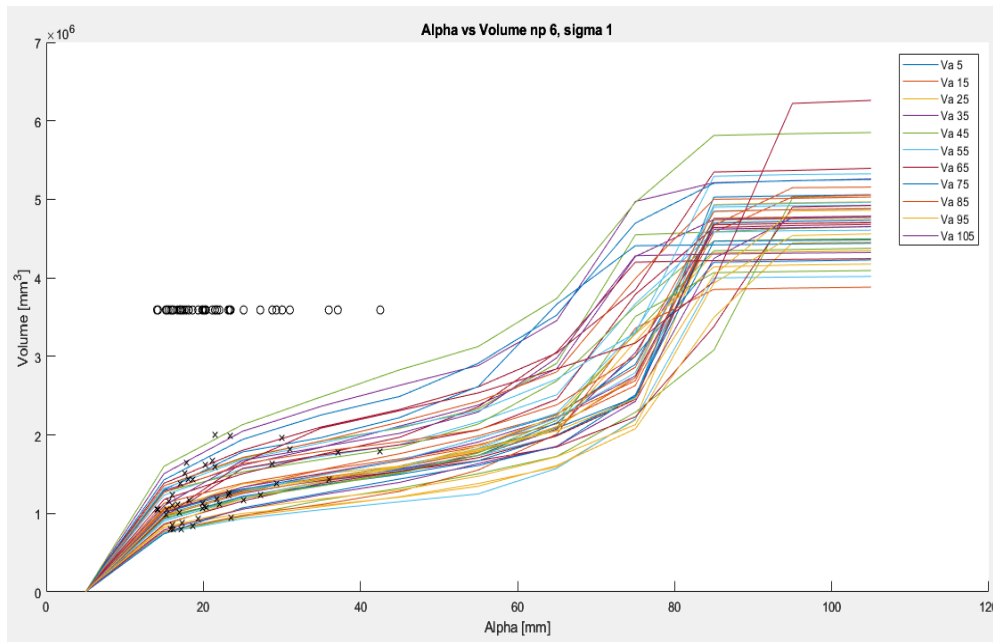
Figure 112 Volume versus alpha (repeatability) of the three spheres changing alpha value.

In the previous Figure, the critical alpha is located in a range from above 5 mm up to a maximum of 50 mm and is represented by cross. The Alpha Optimal (represented by circle) is in the same range of alpha critical radius values. For alpha values greater than 90 mm the volume estimate of each sphere has not more variation, so it has not sense to increase more the alpha. Figure 113 shows an example of alpha radius variation.
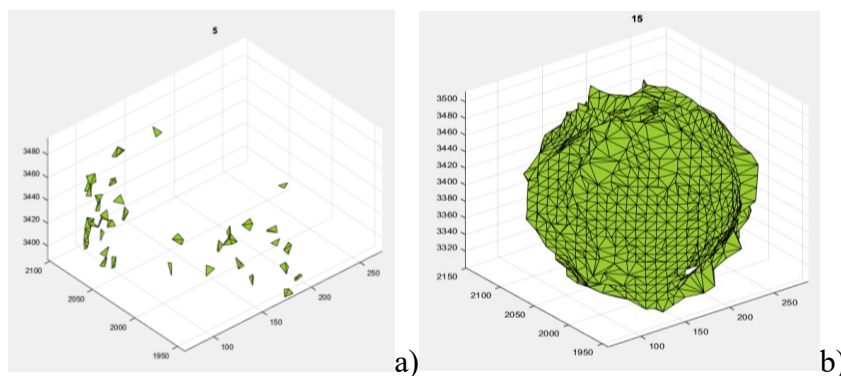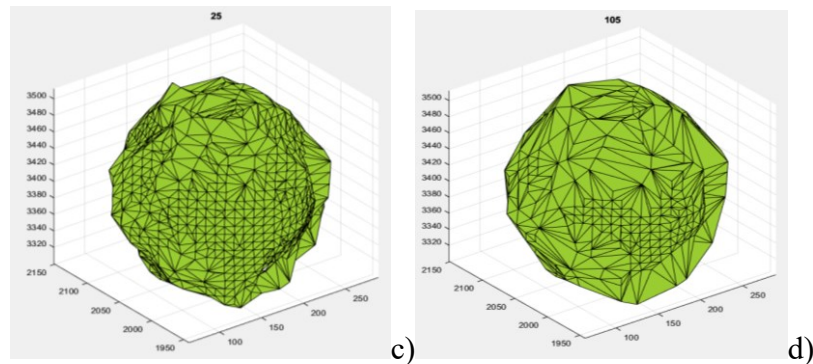
Figure 113 Reconstructions of the sphere 1 (acquisition with 300 leaves). Alpha values (left to right and up to down): (a) 5 mm, (b). 15 mm (c) 25mm and (d) 105 mm.

As it is possible to see, for alpha=5 mm the volume was not reconstructed, in alpha=15 mm there are holes, and from alpha =20 to 105 mm the shape evident variation is not. In this figure it is also possible to note the scanners noise located in the big triangles.

For alpha=5 mm the uncertainty is near to 100% so it is clear that it failed the reconstruction (in fact the volume is zero). Figure 114 shows the effect of changing the alpha radius size on sphere 1.
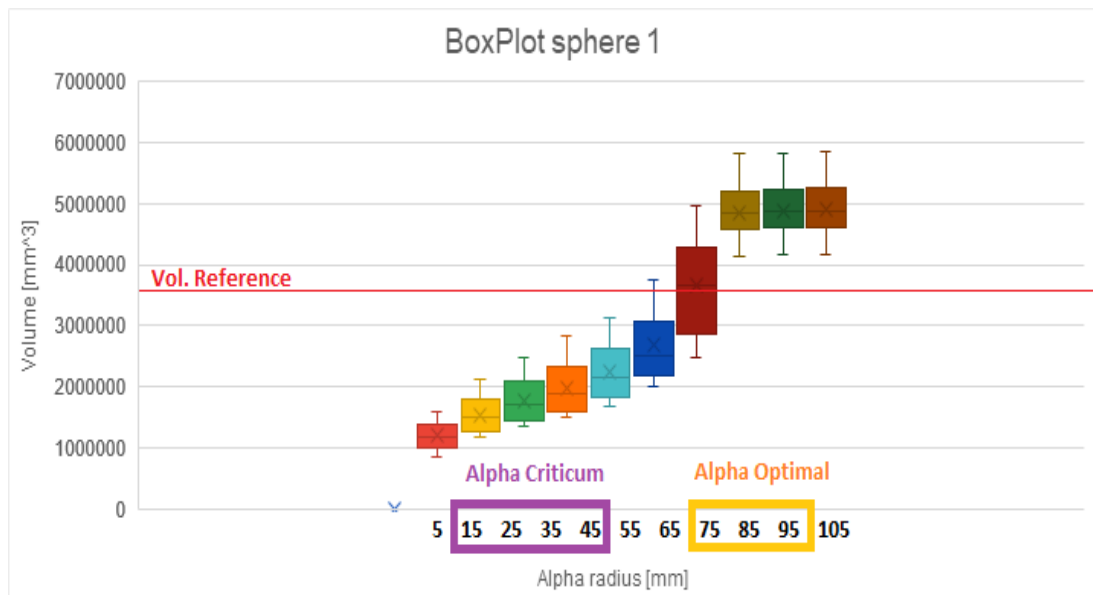
Figure 114 Example box plot of sphere 1

This box plot shows the variation of the volume of sphere 1 when changing the value of alpha radius for all the 15 acquisitions. This confirms what showed before. For spheres 1 and 2 the maximum error is given by alpha=85 mm, for sphere 3 is located at alpha=95 mm. Those results are comparable with what showed in Chapter 2 for simple geometry (Sphere). For alpha values greater than 75 mm the volume does not change. The same happened for the spheres 2 and 3. In Figure 115 an example of the effect of alpha radius changing in Sphere 1 is shown.
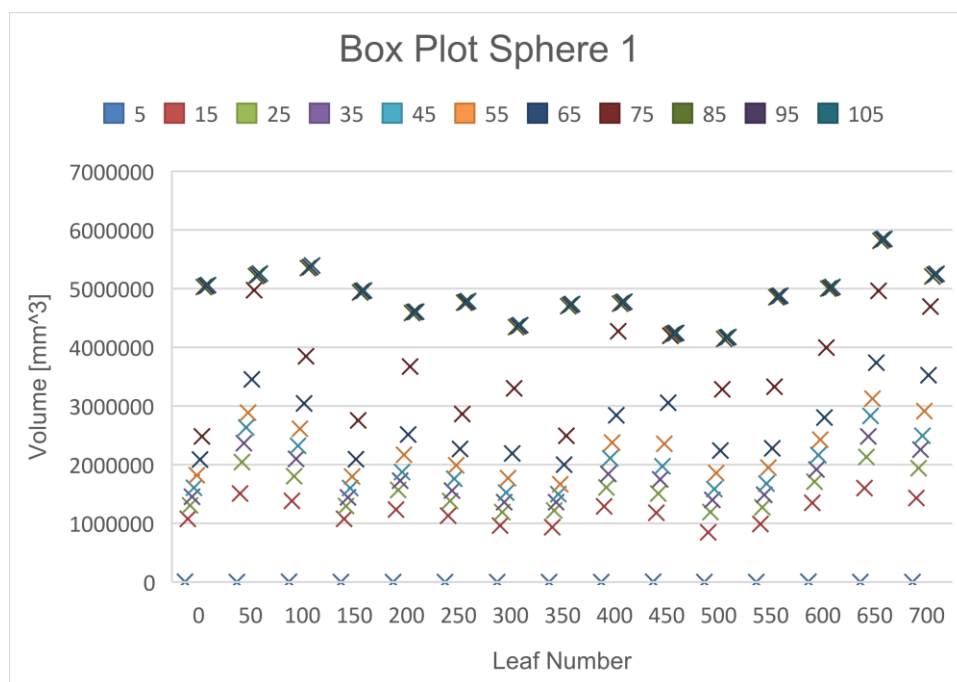
Figure 115 Box Plot of Volume evaluation changing alpha radius.

For alpha lower (e.g., 5 mm) The volume is not reconstructed. This Figure is showing what told before, after alpha radius = 75 mm the value of volume are concentrated in the similar value of volume. In Figure 116 a MAPE for each alpha radius (from 5 to 105 mm) of sphere 1 is shown as example.
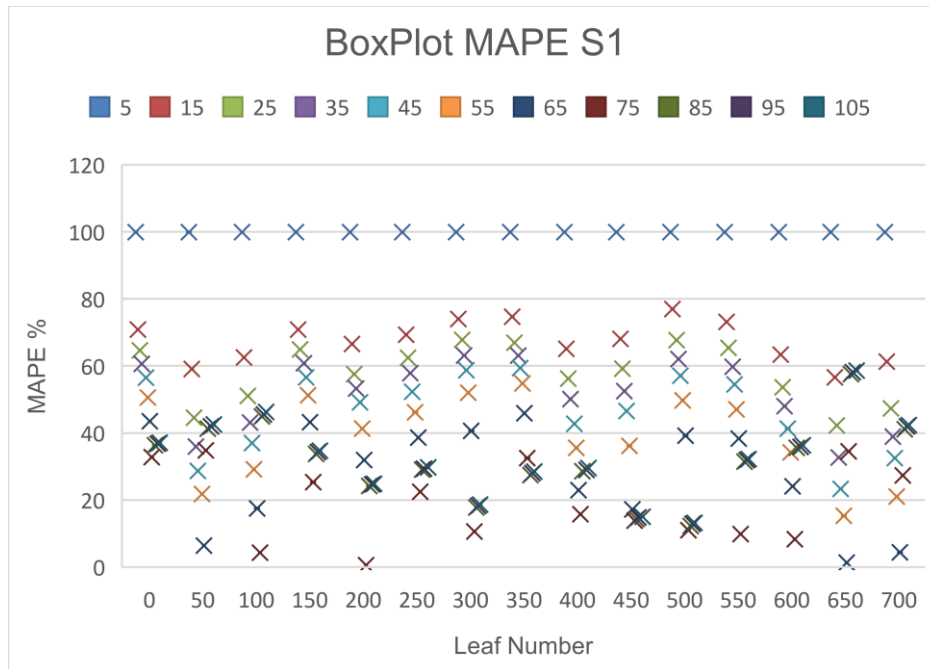
Figure 116 Box Plot MAPE Sphere 1

The previous Figure show that the alpha radius has a high dispersion, in particular for lower radius The MAPE is near to 80%. The MAPE for higher alpha radius than 75 mm the MAPE of sphere is lower than 40%. The uncertainty of reconstruction for each sphere, for each alpha radius on the 15 acquisitions [60] is shown in Table 30.

Table 30 Uncertainty of reconstruction of sphere changing alpha parameter

	Sphere 1	Sphere 2	Sphere 3
N Leaves	Unc %	Unc %	Unc %
0	20.85	19.98	23.83
50	15.70	16.49	21.27
100	17.03	18.33	19.84
150	20.47	19.87	22.96
200	17.26	18.04	19.50
250	18.97	18.52	19.19
300	19.24	21.94	21.04
350	20.87	20.56	22.05
400	16.89	16.98	20.84

450	16.30	15.51	19.88
500	18.62	16.32	18.72
550	19.71	20.48	21.24
600	17.00	21.77	21.73
650	16.04	18.10	19.38
700	15.97	17.96	20.02

Changing the alpha parameter shows an uncertainty around 20 % for all the spheres.

Finally, for all alpha radius from 5 mm to 105 mm, for each sphere it was computed the MAPE of volume reconstruction changing alpha. The results of MAPE are shown in Table 31.

Table 31 MAPE of alpha radius reconstruction

S1	5	15	25	35	45	55	65	75	85	95	105
Max	99.98	77.01	67.76	63.09	59.40	54.78	45.85	34.80	57.58	58.18	58.57
Min	99.91	56.62	42.25	32.68	23.33	15.30	1.35	0.51	12.22	12.85	13.18
Mean	99.94	67.50	58.11	52.11	46.42	39.07	27.66	18.91	31.70	32.23	32.63
S2											
Max	99.99	79.53	74.69	71.62	68.82	66.16	57.33	42.27	43.46	44.06	44.32
Min	99.94	63.39	51.65	46.73	39.79	29.08	0.66	1.41	6.59	8.68	8.91
Mean	99.97	70.72	61.37	56.77	52.79	47.14	35.46	20.91	22.06	25.27	25.65
S3											
Max	99.98	79.91	74.05	70.56	67.28	63.52	56.82	43.66	33.47	68.62	69.67
Min	99.91	71.73	55.34	43.44	37.40	31.27	22.99	4.91	4.42	4.88	5.21
Mean	99.95	76.00	68.19	63.01	58.68	53.01	45.30	27.95	18.19	28.92	29.32

The result of the analysis shows that distances from reference increase since alpha radius, and the volume, increase too. Between alpha equal to 75 and 85 mm the reconstruction has a minimum increase that confirm what shown before: has not sense to augment the alpha value. Alpha 5 mm failed the reconstruction.

5.3.3 Alpha shape and Convex Hull uncertainty evaluation on Tree

In conclusion, the search for the optimal alpha is not easy when there are no references as in the case of the tree. Through the alpha spectrum, it has been seen that it is possible to investigate where alpha values are most concentrated. The alpha spectrum Figure 117 and Figure 118 shows the density where the radius values needed to reconstruct the shape are most concentrated of tree with 0 and 300 leaves.
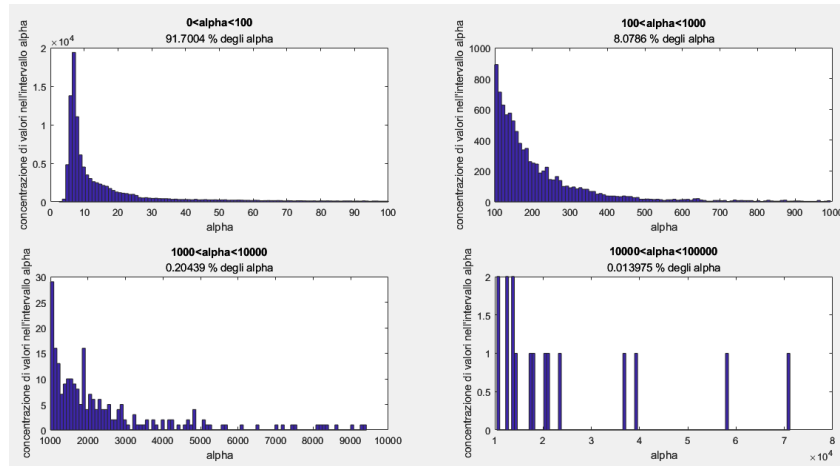
Figure 117 Alpha spectrum tree with 0 leaves
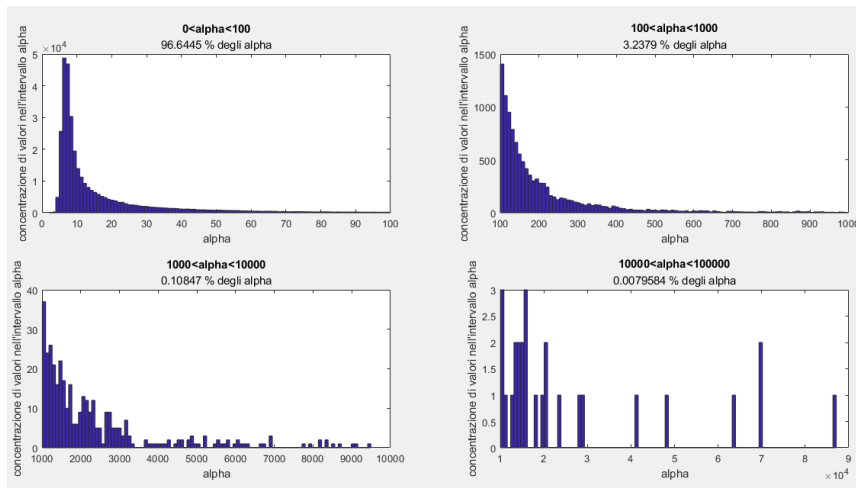
Figure 118 Alpha spectrum for the tree with 700 leaves.

Augmenting alpha spectrum, the concentration of alpha radius density tends to be at left of graph, near 10 mm. If we increase the interval of spectrum, the alpha has less density, also located in the same part of the graph. These figures confirm that the optimal alpha for reconstruction is around 10-15 mm, which is within the Kinect uncertainty [42]. The R^2 also gave good values for this survey range, where uncertainty is lower.

Filtering: We eliminated repeating points with the PCL library's S.O.R. (Statistical Outlier Removal) filter. It first calculates the average distance of each

point from its neighbours (considering k neighbours for each - k being the first parameter). It then discards points that are further than the average distance plus a number of times the standard deviation (second parameter).

The tree volumes were computed for different number of leaves (from 0 to 700 leaves). To perform these volume estimates, the alpha shape algorithm was used and the critical alpha value was considered in all the computations. In addition, the point clouds were filtered by applying the SOR filter and considering four different cases in correspondence with four different number of neighbours to be considered in the filter (4, 10, 20 and 30) as showed in Figure 119.
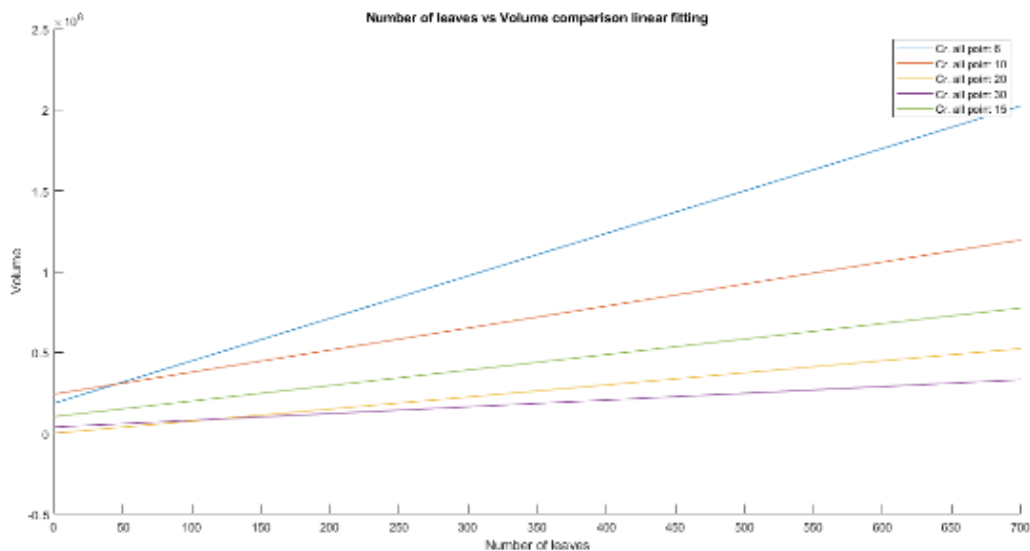
Figure 119 Fitting of volume variation of SOR filter with four different number of neighbours (4, 10, 20 and 30)

As we can see in the previous Figure, the volume is increasing with number of leaves and the filtering is influencing the slope of volume. Increasing the value of filter, the volume decrease. The filtering is influencing the slope

From here it can be seen that the acquisition with 6 nearest neighbours (default) has many outliers (high deviation between points), while the others have a more uniform pattern (low deviation between points).

Finally, it was analysed the potential correlation between these volumes and the number of leaves for the four evaluated cases. It was evaluated the maximum

R^2. We will now quantify the best line that best interpolates (fitting) the segmented point clouds from linear and exponential fitting (the logarithmic fitting failed because the dispersion of data). Based on the best R^2 with the highest value, the representation on which to calculate the uncertainty will be chosen. In Figure 120 and example of linear fit of volume evaluated with SOR filter 10 is shown.
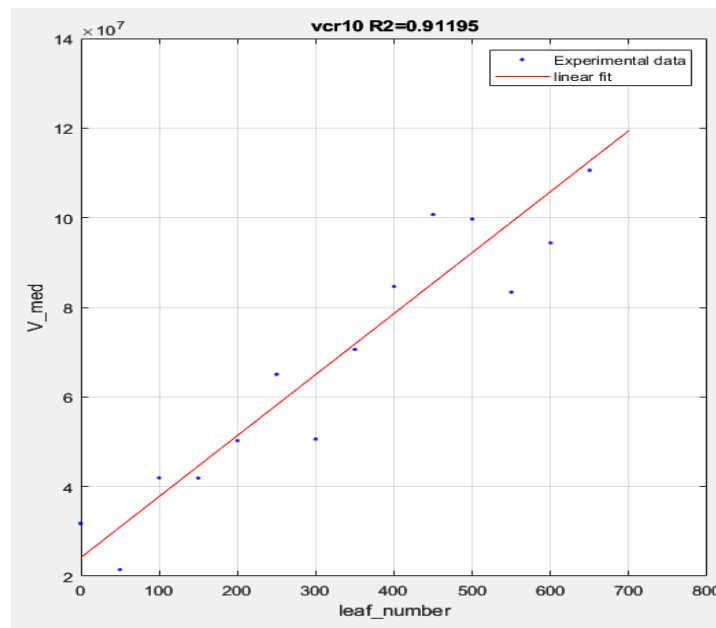
Figure 120 Example of linear fitting of tree Volume with SOR filter=10

In the previous Figure, a linear fitting is shown. In Table 32 the linear and exponential Fitting are given.

Table 32 linear and exponential Fitting.

SOR Filter	R^2 Linear	R^2 Exponential
6	0.47	0.43
10	0.91	0.84
20	0.71	0.8
30	0.52	0.52

In this case the linear fitting showed a best R^2 of 0.91 in volume critical given by SOR filter when considering 10 neighbour points. SOR Filter 10 was chosen. The exponential fitting has also been tested, providing an R^2 value of 0.8. Logarithm

fitting was also evaluated but it presented problems because of outliers, it works with SOR filter 10 and was equal to 0.89.

Alpha Critical "all point" and "one region" and CH Analysis

Since the alpha optimal was not possible to be evaluated and the shape is complex, the Alpha Critical (using both "all point" and "one region" options) and the Convex Hull were analyzed.

Point number versus alpha Critical all point one region radius: Figure 121 shows the points number versus the alpha critical given by the "all point" and "one region" algorithms.
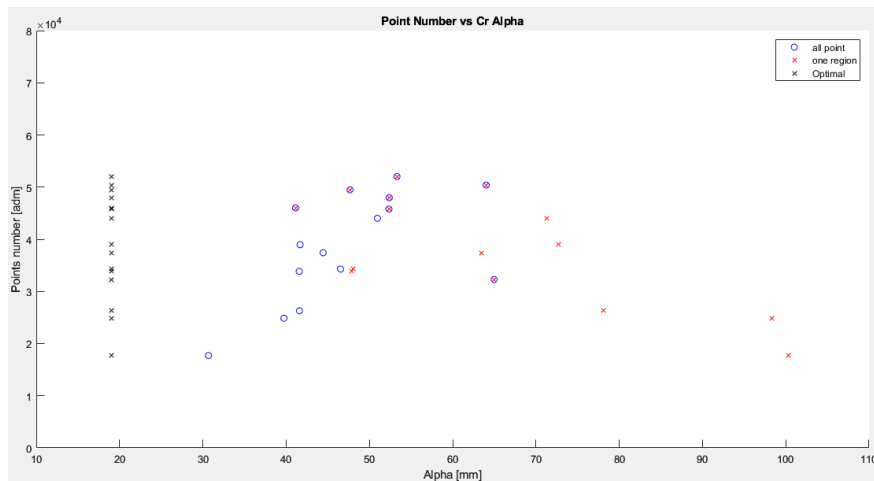
Figure 121 Alpha Critical all points and one region versus number of points of tree on all the 15 acquisitions (from 0 to 700 leaves)

Alpha critical values for "all point" and "one region" change from 30 to 100 mm. Half of the values coincide, half not. In particular, the range of union is between 30 and 70 mm. In Figure 122 The Critical Alpha Vs Critical Volume of tree are showed.
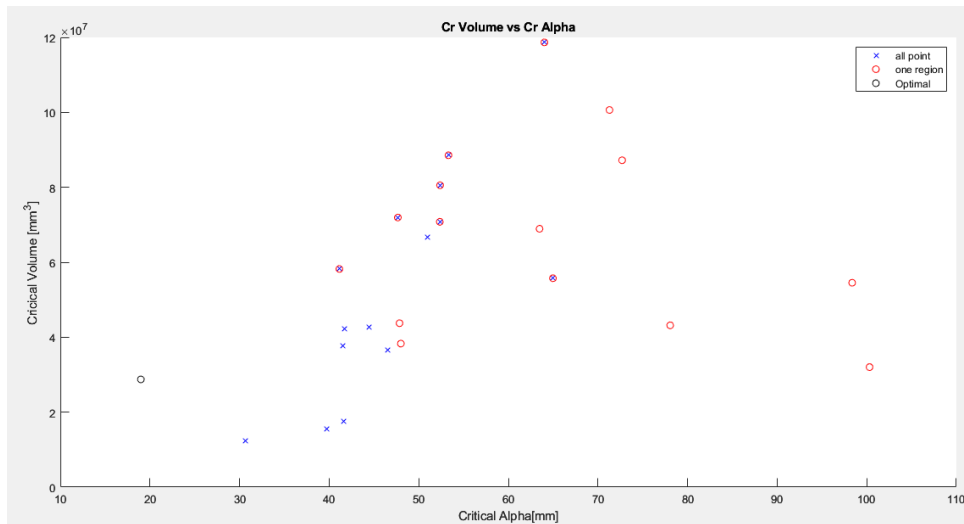
Figure 122 Alpha critical ("all points" and "one region") versus volume of tree on all the 15 acquisitions (from 0 to 700 leaves).

It is possible to see that changing number of points, the alpha value has the same range, what is changing is the volume.

In the Figure 123, Volume given by alpha Critical all-point, one region and Convex Hull algorithms, versus acquisitions will be showed.
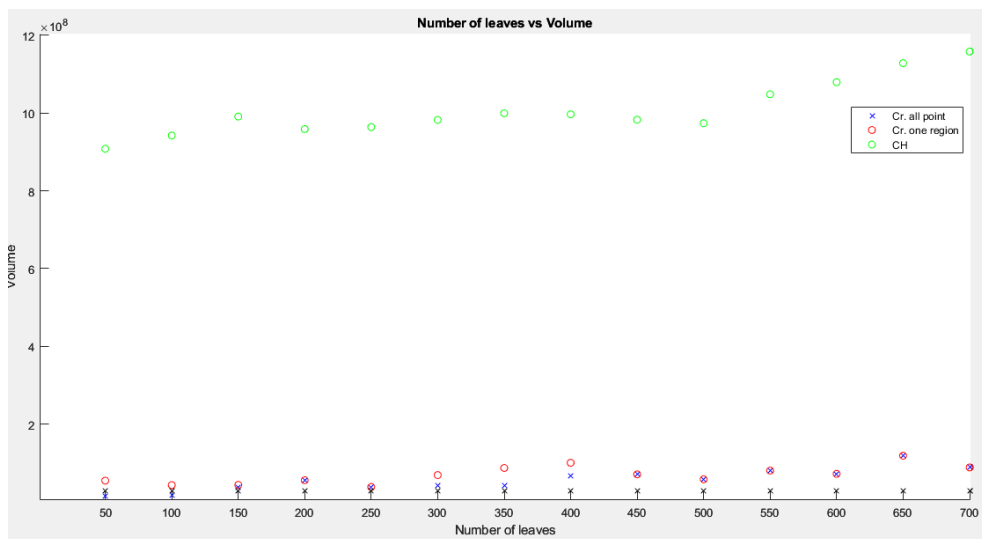
Figure 123 Alpha Critical all points and one region differences on all the 15 acquisitions (from 0 to 700 leaves)

As it possible to see, the Convex Hull is overestimating the AC algorithms of about 900 %. In Table 10 the result of the algorithms uncertainty reconstruction is shown.

Alpha Critical "all point" and "one region" and CH Comparison

The uncertainty evaluation of the algorithms Alpha Critical "all point" and "one region" and CH Comparison are showed in Table 33 Uncertainty evaluation of Alpha Critical "all point" and "one region" and CH.

Table 33 Uncertainty evaluation of Alpha Critical "all point" and "one region" and CH.

	V_CR-One region [mm^3]	V_CR-All-point [mm^3]	V_CH [mm^3]	A CR-One region [mm]	A CR-all-point [mm]
Max	130182578.86	130182578.86	1177198777.78	131.40	131.40
Min	31771870.16	21462807.94	754387635.29	38.27	33.30
Mean	79321397.26	71804527.37	1015929408.91	58.55	51.49
Devstd	31438582.18	30788488.46	96084036.79	21.51	22.27
Unc	8117407.02	7949553.54	24808791.62	5.55	5.75
Unc %	**10.23 %**	**11.07 %**	**2.44 %**	**9.48 %**	**11.17 %**

This Table shows the difference between convex hull and critical alpha "all-point" and "one region". CH shows a lower uncertainty reconstruction. The comparison between all point and one region shows that last algorithms reconstruction has lower uncertainty. For these reasons, volume by one region was tacked as reference for other analysis: It was decided to use alpha critical all points and one region as the former alone is not sufficient to enclose the whole object due to its complexity. For the three algorithms (A Cr all-point, A Cr one region and Convex Hull), the r2 value will be evaluated. Looking at fitting algorithms, Table 34 shows the results of linear (Lin) or logarithms (Log) fitting of data of the volume given by Alpha critical, Alpha Optimal and Convex Hull versus number of leaves.

Table 34 Fitting result.

	Fitting	R^2
V_Cr-point	Log	0.88
	Lin	0.91
V_Cr-region	Log	0.76
	Lin	0.82
V_CH	Log	0.81
	Lin	0.74

As it is possible to see, the volume given by CH is so far from volume evaluated by alpha all point and one region. The best value of R^2 is given by Volume critical all-point in both cases of linear (R^2=0.82) and log (R^2=0.91) fitting. In the other case the best fitting is logarithmic.

Effect of alpha radius on Tree reconstruction

TREE: as told, in case of tree, alpha optimal doesn't work. is not possible to have reference, so alpha optimal was first evaluated going to search the spectrum around alpha critical. If we take the first six value decreasing of alpha spectrum and we evaluate the mean, it is possible to have an optimal value of alpha that have a big standard deviation between mean. In Figure 124 an example is shown.
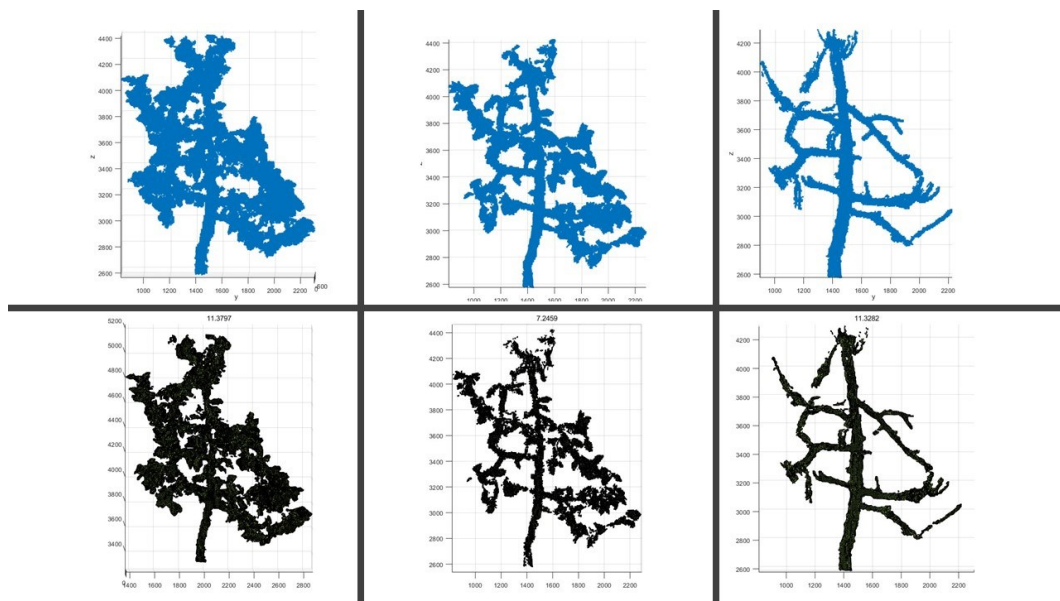
Figure 124 alpha variation of acquisition 9 (300 leaves). Figure alpha variation of acquisition 15 (0 leaves)

Finally, the analysis was performed varying alpha radius from 5 to 150 mm as for the sphere. In this case the SOR filter with number of neighbours 10 will be considerate. Since the fitting of Alpha Critical all-point has best R2, one region will be not considered in the following study. In Figure Figure 125 the volume gives by Critical Alpha all-point and alpha value variation are compared.
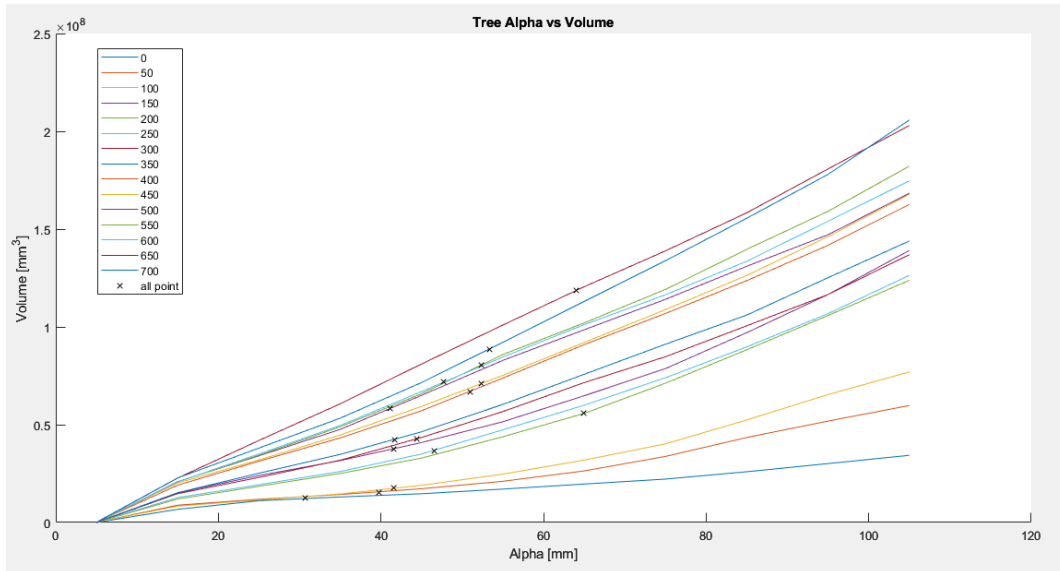
Figure 125 alpha radius versus volume

The volume increases linearly with alpha. If we look at volume given by alpha critical all-point (represented by cross) of each acquisition, it is possible to notice that the value is located between alpha=20mm and alpha=80mm. This mean that have not sense to investigate the volume for alpha>80mm, in fact the volume will be overestimated.

In Figure 126 the plot of volume reconstruction for the 15 acquisitions is shown. In alpha radius = 5 mm the volume is zero. In 15 mm has a linear shape, after increases the nose given by reconstructions.
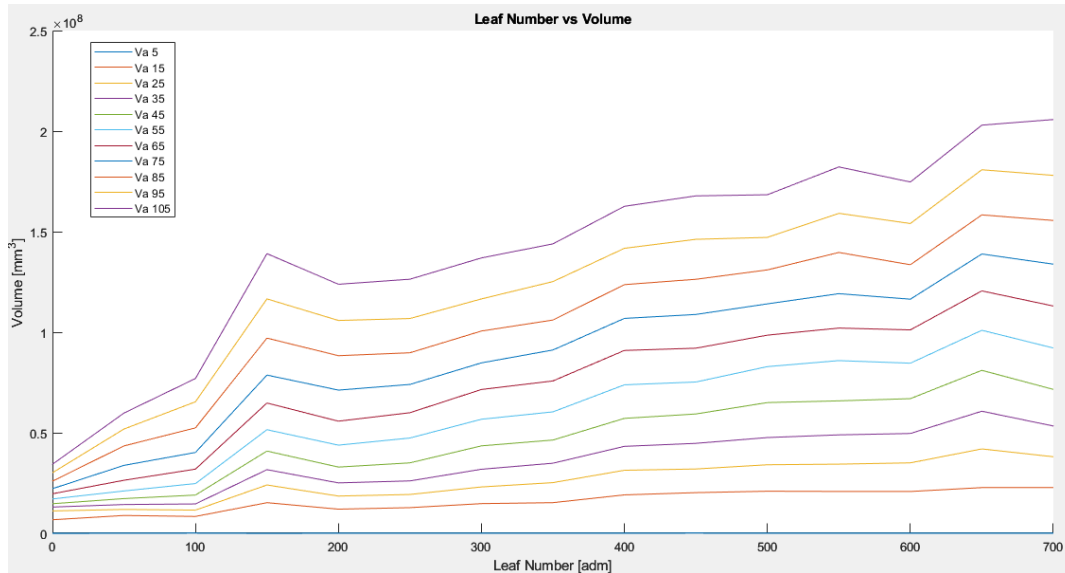
Figure 126 Volume evaluation of 15 acquisition (with different leaves number) of tree varying alpha radius

For each alpha radius, Linear and Logarithmic fitting are evaluated. In Table 35 the results are shown.

Table 35 Linear and Logarithmic fitting and R^2

	5	15	25	35	45	55	65	75	85	95	105
R^2 Lin	0,13	0,92	0,93	0,94	0,94	0,95	0,94	0,94	0,92	0,90	0,89
R^2 log	0,22	0,88	0,84	0,85	0,87	0,90	0,92	0,93	0,94	0,95	0,94

The best fitting values is given by alpha equal to 75 mm. By this analysis it is possible to see how also alpha=15 mm can well approximate the shape. In particular, the box plot presents a minimum deviation in this range, an after increase the reconstructed model uncertainty. In Figure 127 the analysis of alpha shape reconstruction effect is shown.
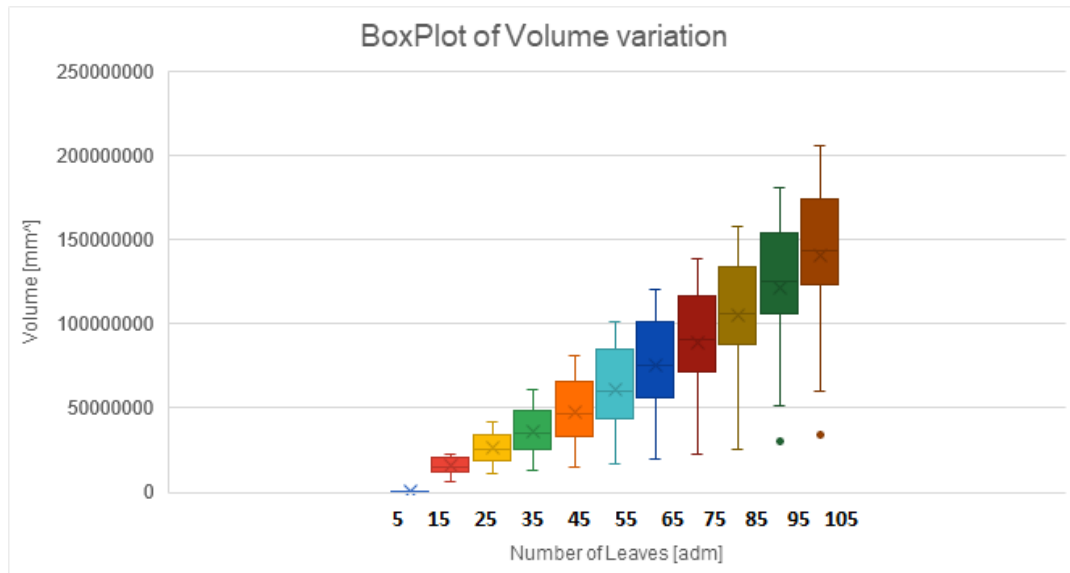
Figure 127 Box plot of tree's volume changing alpha shape radius value

The deviation from the mean, in this case is increasing with alpha radius. For lower alpha values (5 mm), the reconstruction fails. In Figure 128 an example of alpha Radius equal to 5 mm and 15 mm for the tree acquisition with 0 and 300 leaves is shown.

a)   b)

c)   d)
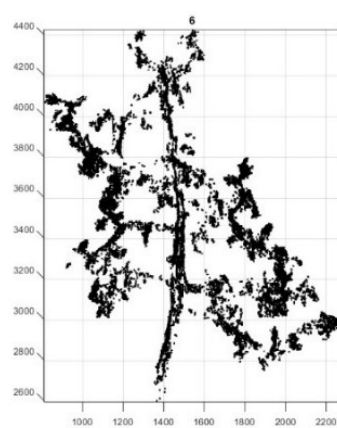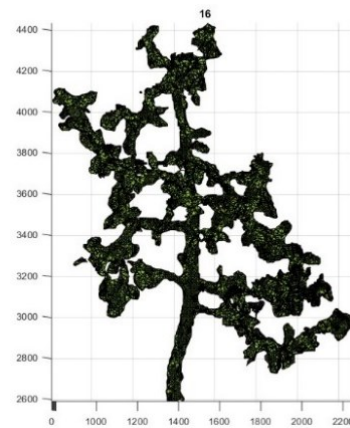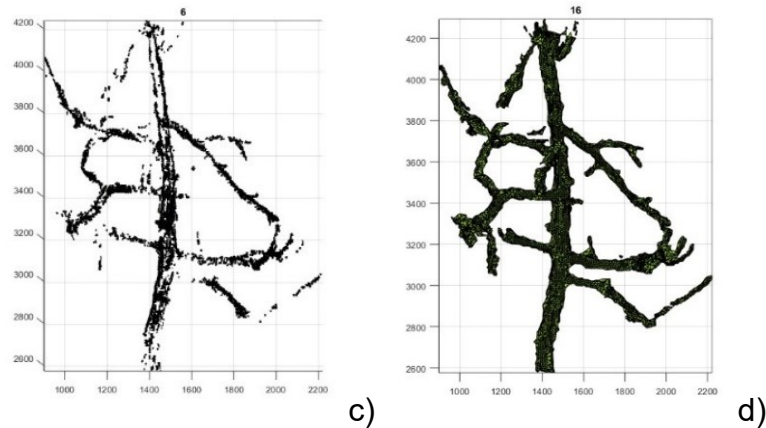
Figure 128 a) Alpha radius=6 mm of acquisition 9 (300 leaves) b) Alpha radius=6 mm of acquisition 9 (300 leaves). c) Alpha radius=6 mm of acquisition 15 (0 leaves) d) Alpha radius=6 mm of acquisition 15 (0 leaves)

As can be seen from the table, increasing alpha also increases uncertainty until alpha between 75 and 85 mm where it peaks and begins to decrease. Up to these alpha values, the best R^2 is given by fitting with the straight line, while as alpha increases up to CH, the best fitting begins to coincide with the logarithm. As far as the Convex Hull is concerned, it overestimates the volumes given by varying alpha by an ordain of magnitude.

5.4 Conclusions

One of the cornerstones in agriculture is to understand how plants grow, on what basis and by what law [26]. Furthermore, the correlation between volume and leaf area is the goal of this research [85]. Based on the assumption that leaves are artificial and all the same, the study analysed the trend in volume as the alpha radius increases.

For test the quality of reconstruction, linear measurements on tree and on target was evaluated. The height given by LiDAR had a MAPE of 1.1 % while RGB-D camera of 1.37 %. The target distances of LiDAR result a MAPE of 11.35% and RGB-D of 1.97 %. The uncertainty of sphere diameter was evaluated by repeatability and was taken as reference. The volume of spheres was also evaluated first by adjusting the shape by fitting the points cloud by CloudCompare. The volume of fitted sphere was evaluated and compared with references. The LiDAR's

MAPE is 18.98% and RGB-D of 11.05%. LiDAR is resulting in more dispersive value, in fact the reconstruction failed because the path was not closed.

Alpha Critical, Alpha Optimal and Convex Hull Analysis were performed on RGB-D camera. The uncertainty of shape reconstruction and volume evaluation was evaluated for each sphere. The highest value of Uncertainty is given by CH algorithm in sphere 3 with an uncertainty of 11.89%. For the other sphere the highest uncertainty is given by alpha critical reconstruction (5.89 for sphere 1 and 6.58% for sphere2). Looking at MAPE, in general Alpha critical gives the highest error (69.98 %). The lower is alpha optimal (0.23%) while CH the maximum MAPE is 35.95 %. Those algorithms are overestimating the sphere size. The analysis changing alpha parameter show that for lower alpha radius (e.g., 5 mm) the shape is not reconstructed (in fact the MAPE is 100%). Between alpha equal to 75 and 85 mm the reconstruction has a minimum increase that confirm what showed before: has not sense to augment the alpha value. In general, the effect of changing alpha radius for the spheres is 23 % and is located in sphere 3. This is confirming the analysis made on simple geometry.

For the analysis of tree and volume adjustments, first 4 SOR filter were applied changing the nearest neighbour (nn) parameters to change (6, 10, 20, 30 nn). The volumes given by these filters were compared by R^2 fitting. The best fitting is gives by 10 nn with $R^2 = 0.91$. Since the filter was selected, Alpha Critical "all point" and "one region" and CH Analysis were performed. Convex Hull give the minimum uncertainty of reconstruction equal to 2.44%, While the uncertainty of reconstruction of alpha critical one region and all point is respectively 10.23% and 11.07%. The best value of R2 is given by Volume critical all-point in both cases of linear ($R^2=0.82$) and log ($R^2=0.91$) fitting. Finally, the effect of alpha radius changing on tree was evaluated. For each alpha radius, Linear and Logarithmic fitting of volumes are evaluated. The best fitting values is given by alpha equal to 75 mm. By this analysis it is possible to see how also alpha=15 mm can well approximate the shape. For about the second analysis on the tree, the relation between Leaves Area and reconstructed volume was found and the uncertainty was evaluated. In conclusion, for alpha radius lower than 75 mm, the relation between the leaves area and the reconstructed volume is linear. If an alpha radius over 75 mm is selected, this relation becomes logarithmic.

- Alpha R<75 mm $R^2 lin = 0.95$ $R^2 log = 0.86$

- Alpha R>75 mm R^2lin= 0.82 R^2log=0.96

Using Convex Hull (Alpha R=∞), the relation becomes even more logarithmic, with R^2log=0.97. The linear variance reaches a value of 0.73.

From this analysis, in fact, it was possible to find a law that combines leaf area with volume.

The LiDAR has exhibited noisy results, consistent with the literature [110], [62]. On the other hand, the RGB-D sensor has shown better results [64].

In the case of the artificial tree, there is no reference volume as it is also a complex geometry. Therefore, in this case, a definition of volume was provided: the volume of the tree was calculated using the alpha shape algorithm. The alpha value is chosen in order to connect all parts of the tree in a single region, ensuring that leaves on thin branches, not detected by the sensors, will not be eliminated.

The relationship between volume and leaf area is linear, as confirmed by references [62] and [111] for certain alpha values. However, the relationship becomes logarithmic for other alpha values, as mentioned in references [115] and [63] specifically for alpha values greater than 75 mm in radius [120], [91]. It should be noted that the authors utilised other methods to assess volumes, such as Convex Hull or Voxelization, to select the optimal voxel, but this resulted in an overestimation of the volume.

In [62] the linear relationship between volume (obtained by interpreting the raw data provided by the LiDAR) and leaf area the correlation coefficient is R^2lin=0.80, while in [63] the logarithmic relationship between leaf area and volume (evaluated by TRLV) it is R^2log=0.87.

In this work, for Alpha R<75 mm, the linear relationship returns a R^2lin= 0.95while the logarithmic relation a R^2log=0.86; for Alpha R>75 mm, the coefficient result is R^2lin= 0.82 and R^2log=0.96. In Convex Hull case the coefficient result is R^2log=0.97.

Our observations indicate that the optimal alpha radius values tend to be around 15 mm for accurately reconstructing the tree's shape. The algorithm varies the alpha radius within this range to assess how well the straight line and logarithm function

fits the data for each alpha value, and the one with the lowest R² provides the most reliable reconstruction to evaluate the tree's volume. Moreover, the filtering system is also crucial for this purpose because it significantly reduces the error by effectively filtering the points with a certain filter threshold [121].

In this thesis is an artificial apple tree was analysed [122] in order to create a reference model. In this regard, the thesis fits into a broader context, aiming to simplify calculations by predicting tree growth through simple equations, such as linear, effective, and accurate linear models.

Finally, thanks to the determination of the R^2 factor, it becomes possible to effectively select the optimal alpha radius, which minimises the error distribution. Using the algorithm developed in this thesis, it is possible to evaluate a range of alpha radius values to identify the best alpha that accurately reconstructs the tree's volume and selects the appropriate spectrum. This approach allows an understanding of the probable range of alpha values for the reconstruction. Ultimately, with the R² analysis, the best alpha can be selected around that radius value.

Chapter 6

Deep Learning algorithms for detecting anomalies in lettuce plant growing, 2D and 3D data comparison.

6.1 Introduction

In this Chapter, the volume evaluation of real lettuce plant scanned in field will be performed using CloudCompare software, as described in Chapter 2 as the application of other algorithms was problematic since the shape has a slow modification of geometry [86]. So, the final shape was not well reconstructed. Furthermore, different 3D measurement techniques were analyzed in order to select the suitable one. The work was carried out in collaboration with R&D team Idea-Re, a start-up in Perugia, Italy. The study was presented in 2021 IEEE international workshop on metrology for agriculture and forestry and was awarded for "The best paper presented by a woman".

This Chapter presents a comparison of different methodologies for monitoring the plants growth in a greenhouse. A 2D measurement based on Computer Vision algorithms and 3D shape measurements techniques (Structured Light, LIDAR and Photogrammetry) are compared. From the joined 2D and 3D data, an analysis was performed considering health plant indicators. The methodologies are compared among each other. The acquired data are then fed into Deep Learning algorithms in order to detect anomalies in plant growth. The final aim is to give an assessment on the image acquisition methodologies, selecting the most suitable to be used to create the Deep Learning model inputs saving time and resources. With technology advancement, low-cost and contactless monitoring systems are emerging as powerful tools able to provide real-time information due to small computation time. These kinds of methodologies gain relevance in the agricultural sector, being able

to provide a great amount of information with time and cost reduction[87] [88], [89]. The crop growth, as an example, is a good indicator of the farming performances and can be monitored through contactless shape and colour detection at various time and spatial scales [90], [26]. The data extracted from different measurement techniques can be then processed through Machine Learning algorithms, such as classifiers, Deep Learning models or Autoencoders [91], in order to detect anomalies in the plant growth or in the greenhouse equipment or operational parameters. Such an approach in monitoring the efficiency of crop growth and operations acquires further relevance considering the increasing care for sustainable agricultural practices. In particular, the need of avoiding soil overexploitation led to leverage on the height direction, and consequently to the spread of vertical farming, a sector which can greatly benefit from the use of the aforementioned techniques in a "smart agriculture" context [6]. Keeping in mind the above considerations, this paper presents the application and comparison of 2D and 3D measurement techniques to monitor the plant growth in a greenhouse. The final aim of this study is therefore to assess the suitability of the investigated methodologies to reproduce the plant shape and volume, using the acquired images as inputs for Machine Learning models, and to compare the performances of the various image acquisition methods.

6.2 Materials and Methods

The case study deals with monitoring the growth of several Cichorium endivia plants in a controlled environment. Nine endivia plants were planted at the same time but fed with different amount of water and fertilizer. This was intended to make available different growing stages during the two weeks measurements with the scanning techniques (Figure 130).

A fixed camera is used a reference and its performance is compared with those of three scanning techniques, namely structured light scanner (SL), LIDAR (L), photogrammetry with high resolution camera (Pc), and an autonomous, low-cost photogrammetry system (Pl). The performances in reproducing the plant shape are assessed with the purpose of developing and standardizing a low-cost procedure to monitor the crop growth, saving time and resources [38]. Indeed, while 2D measurement performed by a fixed camera allows for a real-time monitoring thanks to sub-hourly image acquisition, on the other hand it would probably not be a feasible solution in a greenhouse, especially in vertical farms. A 3D scanning, performed once a day and possibly automated, could be a proper alternative.

All these measurements were performed once a day from 17:00 to 19:00 to reach the best enlightenment condition, for a total time scan off about two weeks.

Figure 129 Nine endivia plants. t1 represent the day 1, tn id the day 7

2D and 3D measurements with different techniques was performed.

2D measurements were performed with a home-made system (G), installed within the greenhouse. The device hosts a fixed camera and environmental sensors to constantly monitor the plants growth. Specifically, the Full-HD camera is equipped with a Sony IMX219 8-megapixel sensor. An Arduino-based shield can acquire temperature, relative humidity, pressure, light intensity and UVA. The camera and the sensors are connected to a Raspberry PI that acts as edge computational unit [91].

The 3D measurements were performed with:
(SL): Creaform Go! Scan 50.
(L): The embedded i-Pad 20 pro LIDAR, presented as L2_Low in Chapter 2.
(Pc): The Canon Eos 7D presented as Ph1_High in Chapter 2
(Pl): The automated 3D-printed scanner presented as Ph2_High in Chapter 2.
Figure 130 shows the setup of the 2D acquisition and the 3D acquisition made with the 3D printed scanner. The setup is shown in Figure 131.
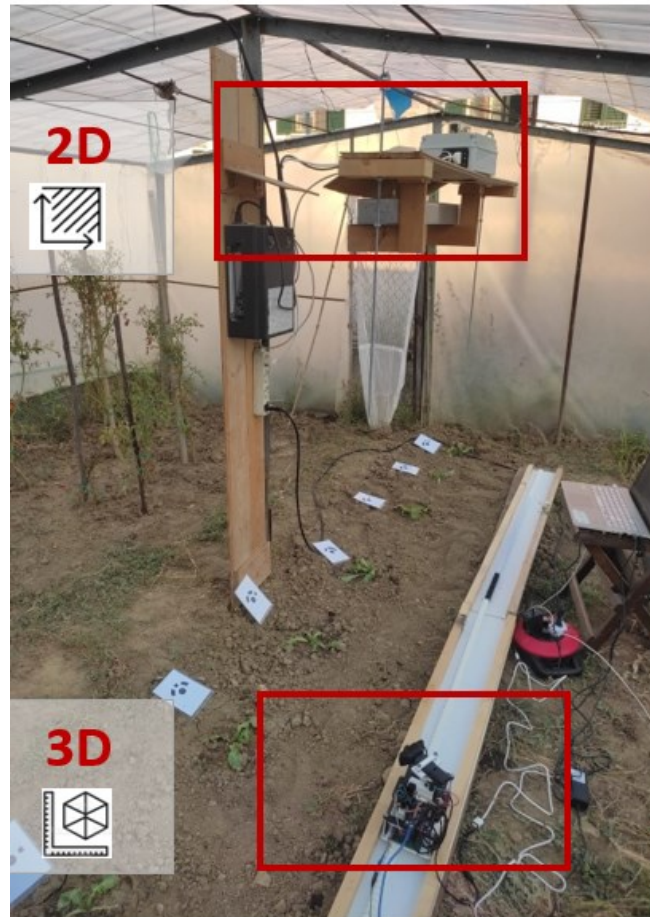
Figure 130 2D acquisition wikth fixed camera and the 3D acquisition made with the 3D printed scanner

The 2D measurement of area was made with own convolutional neural network CNN algorithms. 3D measurement was performed with SL, Pc, Pl, L and the volume evaluation was performed by CloudCompare. Figure 130 shows the output of acquisitions made by Photogrammetric techniques with Canon Eos 7D, 3D printed scanner, LiDAR acquisition made by i-Pad and Structured Light acquisition made by GO!SCAN 50.
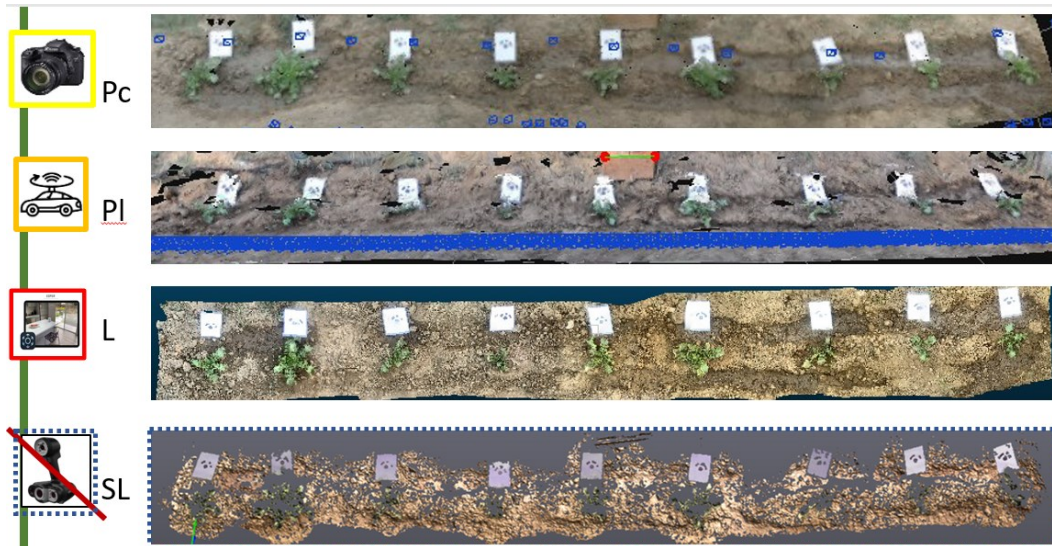
Figure 130 Acquisition was carried out by: Canon Eos 7D, 3D printed scanner, i-Pad and GO!SCAN 50.

6.2.1 2D Area evaluation

2D images are processed by a segmentation algorithm, written in python, to detect the leaf area [91]. First, a bilateral filter (i.e., a nonlinear digital filter). that reduces image noise while preserving edges is applied. It assigns weights to the pixels depending both on their proximity in terms of geometric distance (domain) and photometric similarity (codomain). Then the image is converted from RGB to HSV, and a mask is generated. Only pixel lying in a range of RGB values are maintained, the other pixels are rejected. The pixels within the threshold are used for the leaf area and RGB indices calculation. An additional filter is then applied to remove weeds from the area calculation. First, a topological analysis is performed: the edges of the pixel patches are determined, approximating the shapes with spheres. Next, spheres of smaller diameter are discarded. The coded targets with known size of 10x14 mm, gives a calibration value of 0.3 mm/px (target height and length/ camera resolution). The image is then converted back to RGB and the average values of the three parameters R/n°pixel, G/n°pixel and B/n°pixel are calculated over the masked image. Measurements of the major heights of each plant are then taken on field. Finally, the full volume intended as the "footprint" is evaluated. This resulting solid represents the maximum limit of each plant volume. In Figure 131 the main steps of leaf area segmentation are reported.

Figure 131 leaf area recognition process. Left panel: original image. Central panel: filtered image after the application of RGB threshold and weed removal routine. Right panel: Final result of the segmentation algorithm.

6.2.2 3D Volume evaluation

3D point clouds are obtained from different techniques and calibrated using reference distance [9,10]. The complex plant geometry led to sudden changes in curvature, making it difficult to reconstruct the scene, resulting in missing parts and loss of details, due to the resolution of the instrument and environmental conditions. Moreover, the influence of external factors such as wind and light make the structured light model reconstruction not available for volume evaluation of the plants. While the data obtained from LIDAR are automatically translated into a 3D point cloud by 3D Capture application, images from photogrammetric techniques, given by Canon and low-cost system, have been processed via 3DF Zephyr software by 3DFLOW. Different instruments led to different point clouds, in terms of point density. That means different meshes with various triangles size, depending on instrument resolution. As different resolutions led to different volume values for the same specimen, a common point density involving all the techniques is necessary. Each triangle was divided in points, with the density of points set on 1000 points/cm2, as the increase of this value returns a minimum volume variation of about 0.3%, across the techniques. From this consideration, it is possible to notice that increasing more than 1000 points per cm does not make sense.

The alignment process is carried out by choosing appropriate points distinguishable in each cloud in correspondence with targets. Even though scans from structured light are not used to obtain final data, they are very useful to verify and optimize the scales of the other models in order to have the same reference X, Y and Z. Taking as reference the dense point cloud given by SL scan, the alignment was performed on 10 points located on target. The maximum deviation reached in

this operation is 0.49 cm over all 3D data. The segmentation phase is necessary to obtain the plant volume (V) is shown in Chapter 2. This consists of 2 further steps:

1. Each cloud is analyzed individually; each plant has been cropped including a portion of soil (Figure 132 a).

2. Each single plant has been further isolated from the corresponding portion of soil, identifying the color gradient from brown (soil) to green (plant) (Figure 132 3b). In this way, two clouds are created: one relative to the empty land of the plant (used as a basis to originate the interpolating plane, Figure 132 c), the other related to the plant itself (used subsequently for determining the heights and values of the RGB indices).
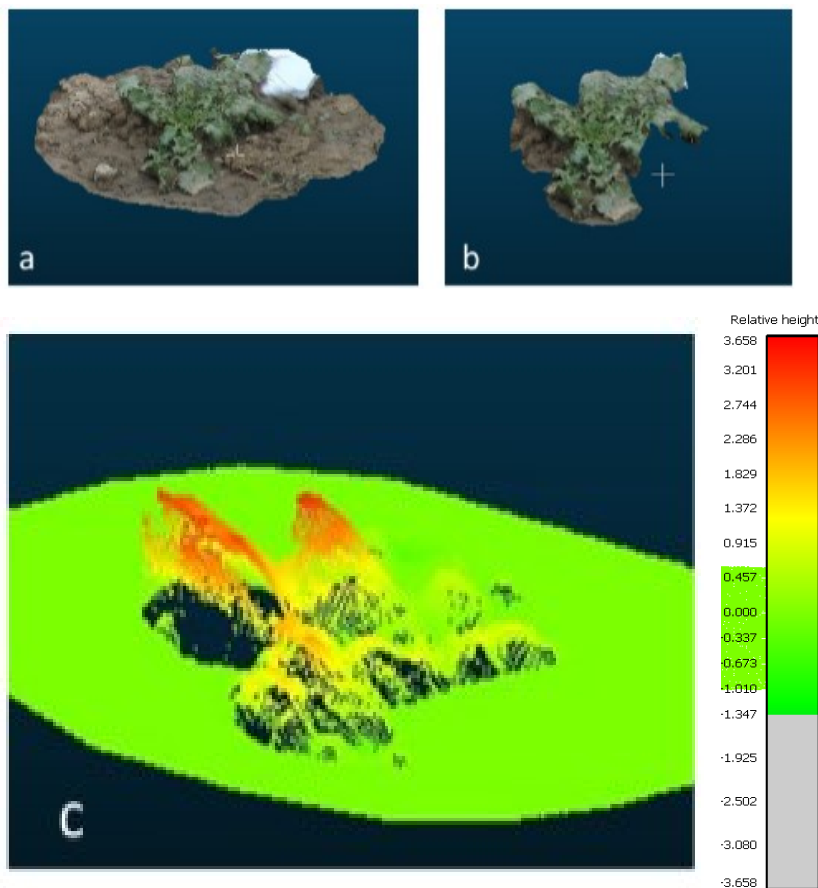
Figure 132 Panel a: isolating each plant from the total mesh, with a portion of soil. Panel b: isolating the plant from the soil. Panel c: generation of the reference plane, used for the 2.5D raster for the plant volume evaluation.

After volume calculation and colour extraction for the various experimental techniques, the resulting data are furnished as inputs to a Deep Learning algorithm, specifically an Encoder-Decoder based on Long Short-Term Memory artificial neural networks [11], aimed at detecting anomalies.

6.2.3 LSTM encoder-decoder for anomaly detection

The proposed approach for anomaly detection adopts a Long Short-Term Memory to encode the input sequence into a vector of a fixed dimensionality. Then, another deep LSTM decodes the target sequence from the vector. The input sequence is a time series having the following data structure:

1) Plant height (plant area for 2D images)

2) Plant volume

3) Mean Red, Green and Blue values of the plant surface.

Every sequence is composed of three-time steps, each one corresponding to 24 hours. Two different datasets were used as an input to the Autoencoder: one with data corresponding to normality and the other corresponding to anomalies. As all plants were grown quite well and no one died during the experimental session, we prepared an anomaly dataset to simulate the death of a plant, i.e., a marked volume reduction in the last days of measurements and a consequent reduction of the red and blue hue. Data pre-processing was completed by first normalizing them to a range between 0 and 1; then they were reshaped into a format suiting an LSTM input. Indeed, LSTM inputs are characterized by a 3-dimensional form, specifically samples×time and steps×features. Thus, in the present case, the input tensor has a 126×3×5 shape per plant. The implemented Encoder and Decoder are composed of two LSTM layers. We tested the model with a number of 32 LSTM. The ReLU activation function is used in all configurations. The state returned from the first LSTM Encoder layer is set as the initial state of the LSTM Decoder first layer. Analogously, the returned state of the LSTM Encoder second layer is set as the initial state of the LSTM Decoder second layer. The Encoder output – also called context vector – is reversed before being passed to the Decoder: the motivation behind this choice should be found in better performances that it is able to assure [92]. The context vector is copied n times in a repeat vector layer, with n being the number of timesteps of the Encoder input. The repeat vector layer is used as

Decoder input. The Decoder output is fed to a Time Distributed Layer, that applies the same dense layer to each time slice. The described model was applied for the whole set of endivia plants, since they represent the same cultivar, in order to obtain a more robust model and avoid overfitting on a specific plant. A model has been trained for each experimental technique, namely photogrammetry with Canon, photogrammetry with robot, LIDAR and 2D images from the fixed camera. The training was performed by minimizing the Huber loss function by means of ADAM optimization [130]. The learning rate is updated at every training epoch, with exponentially decreasing learning rate as the epoch number grows. The detection of anomalies is based on the loss value distribution under "normal conditions". A simple way to define a boundary between "normality" and the occurrence of anomalies, in fact, is to analyze the system response on "normal conditions" data, with the hypothesis that anomalies will produce reconstruction error values located at right of the "normality" distribution tail. Thus, the available time series was analyzed to detect where most of the anomalies are located. The Mean Absolute Error (MAE) was used as reconstruction error. The performance of the implemented models was evaluated according to the F1 score [131],defined as:

$$F1 = \frac{P \cdot R_c}{P + Rc}$$

Where P is precision and Rc is recall. These measurements are expressed as percentage [%].

The Autoencoder was developed using the TensorFlow framework and Keras wrapper.

6.3 Results

The following indicators of health status to identify possible anomalies was assumed and evaluated:

1. α, σ: assuming as a hypothesis that the growth trend is linear, this has been defined as the angular coefficient α of the regression line of data (surface, volume and height values) of each plant in time. The growth trend index evaluates the deviation of the measured points from the average value and quantifies them. The distances of these points were determined as difference (Δy) between the value assumed by the regression line and the value of the experimental data, reported in

terms of percentage deviation (e.g., the ratio between the distance of the points and the average value). This percentage deviation has made it possible to identify a threshold beyond which the points have an excessive deviation. These values, defined as outliers, could influence the trend, going to modify the value of α, which could indicate an anomaly in the plants or in the acquisition (Figure 133).
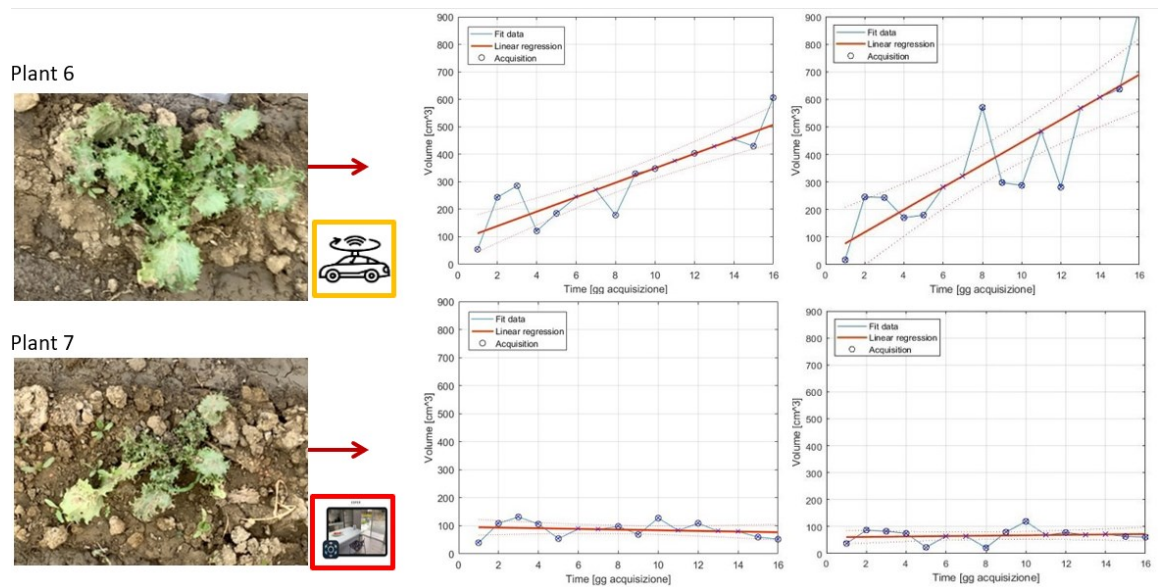
Figure 133 Example of growth trend of two different plants (6 and 7) estimation given by low-cost photogrammetry and LiDAR 3D shape measurement techniques.

2. Growth factor: it is represented by the ratio between the values of initial data of plants, deriving from 2D and 3D measurement systems, and the final value of the data. It is used to evaluate the variation of plant dimension in the various moments of growth, also giving indications about the initial plant dimension.

3. RGB factor: it was evaluated the trend of the variation of colours R, G and B of each plant for each temporal moment t. The hypothesis is that green is the predominant colour (Figure 134).
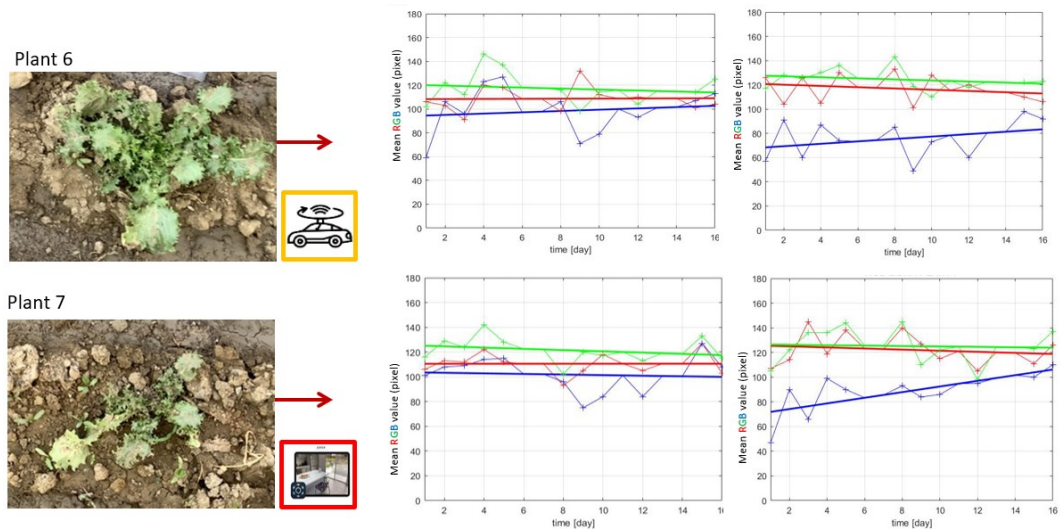
Figure 134 RGB value of Plant 6

These values indicate the state of growth of the plant which is linked to factors such as: age, lack of water, light, or minerals in the soil etc. The trend of the data (V, h, RGB) from the 3D measure (Pl, Pc, L) and the area (A) from the 2D measurement (G), was evaluated as a function of time t (Figure 135).
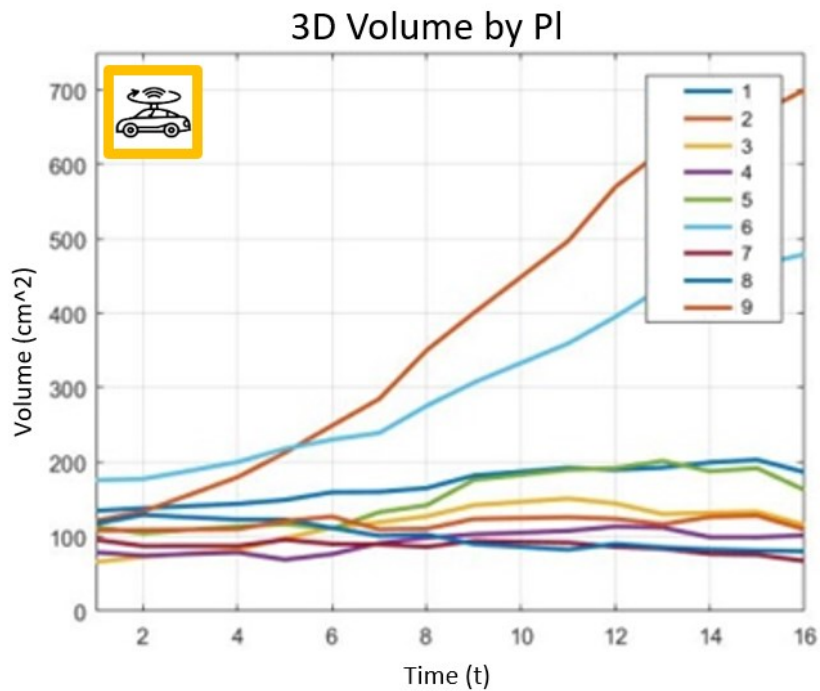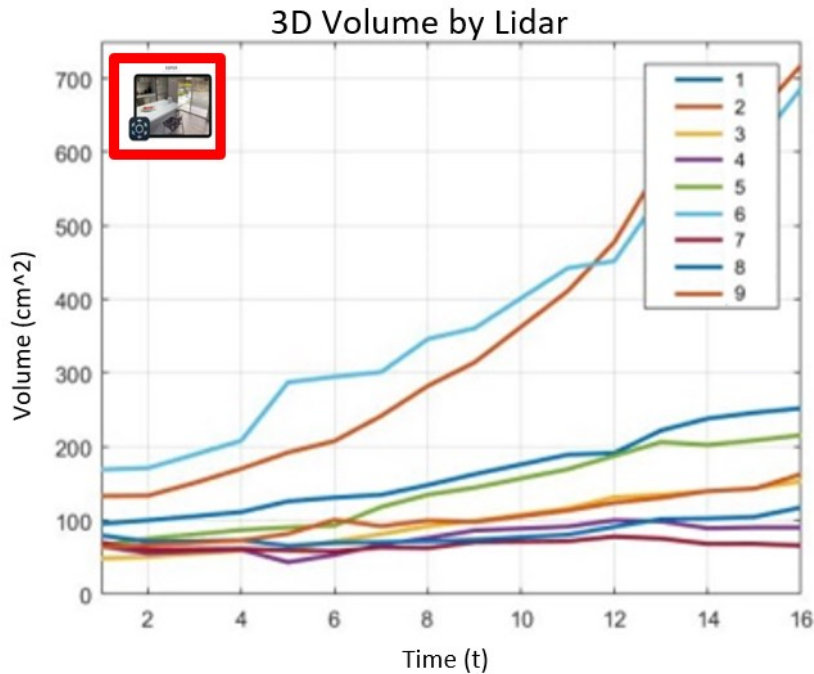
Figure 135 Example of Volume Vs acquisitions during the time using LiDAR of the nine plants.

On plants with larger dimensions the three chromatic levels are distinguished very clearly, while in smaller plants tend to get confused. In photogrammetric acquisitions, a correlation in trends can be seen of some alpha values, in volumes and heights, in particular: in acquisitions canon, the trend of the α index turns out to be negative on some plants (44% of negative of VPL and hPl value on total measure), which would suggest a decrease in volume. Going to consult the RGB indices, a constant trend of the values is denoted, where the average of the green colour remains predominant, thus providing indications on the age of the plant, even if the red and green indices remain very close between them; this is due to the few overlaps of photos and the sensitivity of the sensor with respect to the brightness of the scene. The values of the growth factor agree with this hypothesis. In low-cost acquisitions the negative trends are smaller and the number a of negative values of α are smaller (22%). As for the results LiDAR, these are all in agreement with the growth trend and they all turn out positive (100%). There are some RGB values of plants that seem to decrease without exceed 2% of the total trend of colour variation. The photographs show a trend of growth, in fact most of the values of the areas agree with the growth trend of the volume of 3D tools. However, with the sole

evaluation of parameters, such as height or leaf area, information useful for estimating growth is lost.

The trend of the 3D measurements techniques shows comparable data, while the trend given by area evaluation shows discording values for some plants (e.g., plant 4). Results, given by 2D and 3D measurement techniques, are shown in Figure 137 and 139.
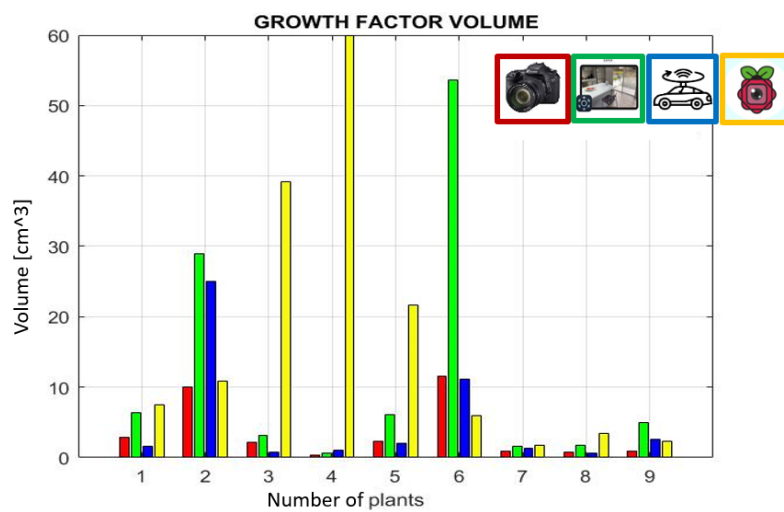
Figure 136 a) Data 2Dmeasure (A, Pl, Pc, L).
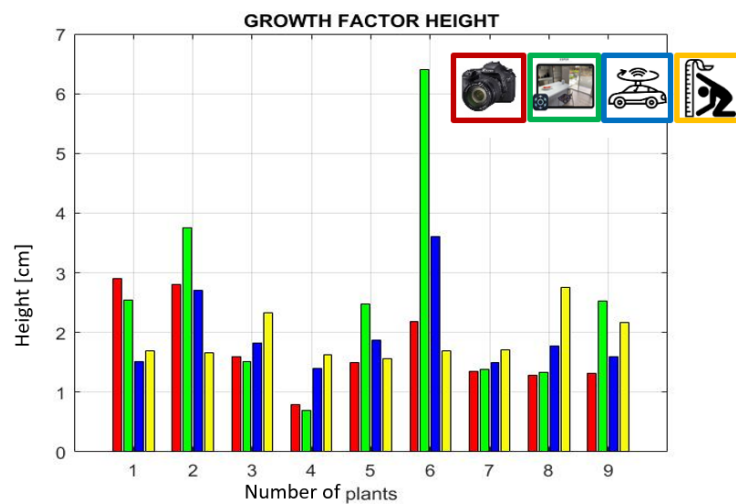
Figure 137 b) Data (h, V, RGB) of 3D measures.

A model for each experimental technique has been trained and tested for the simulated anomalous datasets. The reconstruction error for the four models is reported in Figure 140 where the reconstruction error is shown.

Pc		Pred	
		N	A
Meas	N	1,00	0,00
	A	0,64	0,36

L		Pred	
		N	A
Meas	N	0,99	0,01
	A	0,07	0,93

Pl		Pred	
		N	A
Meas	N	0,95	0,05
	A	0,36	0,64

G		Pred	
		N	A
Meas	N	0,97	0,03
	A	0,50	0,50

Figure 138 Confusion Matrix for LSTM per each model.

The Confusion Matrix for each LSTM model confirms the order of input data accuracy, with LiDAR showing the highest accuracy, followed by low-cost photogrammetry, 2D measurements, and finally high-cost photogrammetry. The final results are shin in Figure 141.
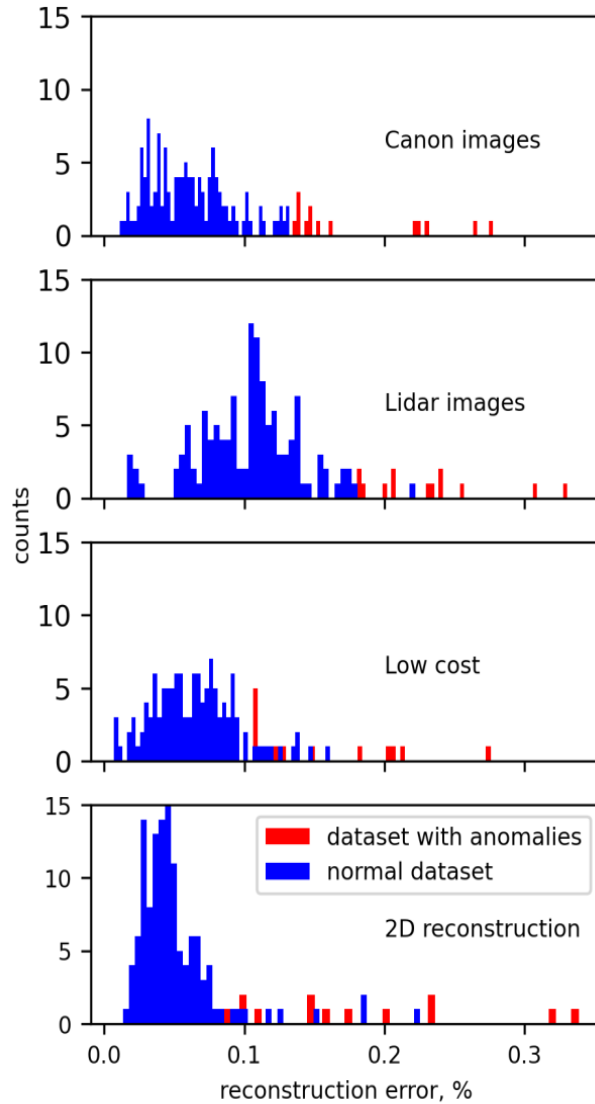
Figure 139 These histograms represent the reconstruction error distribution of the trained model on the normal and anomalous dataset, for each experimental technique.

From the image it is possible to derive that the anomalies we simulated are well detected, as the MAE is greater for the anomalous dataset, with respect to the normal dataset, for all the models. The training dataset has a very low MAE for the 2D measurements, but the anomaly detection is not necessarily more accurate, as the performance parameters in Table 36 reports. Analyzing the parameters in table 2, the best result is obtained with the LiDAR system, even though the starting point

cloud had less resolution. The low-cost system did not perform well, with a F1 score of 0.56. Nevertheless, one can look back at the point cloud and analyze the possible improvements on the experimental set-up.

Table 36 Performance for LSTM for each model

Model [%]	Pc	L	Pl	2D
Precision	0.5	10.5	0.44	0.42
Recall	0.5	0.86	0.79	0.71
F1 score	0.5	0.63	0.56	0.52

The anomalous dataset has a greater MAE, with respect to the normal dataset. The results obtained with LSTM network are in good accord with the 2D and 3D indicators shown in the previous section.

6.4 Conclusions

This paper presents the application of different 3D scanning methodologies for image acquisition in a greenhouse, thought to be used as inputs for Deep Learning algorithms aimed at detecting anomalies in plant growth. The performances of a fixed camera used as a baseline are compared to three 3D scanning techniques. The objective is to identify a suitable scanning technique to perform non contact 3D shape measuremets with comparable performance of the fixed camera. In [132] is emphasised that 3D evaluations will be added as inputs for Deep Learning algorithms to better characterise the health conditions of the plants. This article uses a fixed camera as a baseline to evaluate the leaf area (LA). The leaf area was calculated by using a computer vision procedure that employs the Easy Leaf Area (ELA) code of Easlon and Bloom (2014). This approach consists of several steps that make the process relatively long. In addition, there are limitations related to the calibration, the subjective elimination of poorly identified leaves, and the required time to adjust the parameters. In this thesis' work, this process has been simplified through topological analysis and has also made it possible to assess leaf details, together with eliminating noise (e.g., weeds). In this case, the calibration is done only once. Moreover, high and low-cost 3D scanners were used to evaluate area, height, volume and colour. These parameters were entered into the encoder-decoder

algorithem. The output is the comparison of these parameters given by the different sensors and the precision.

When comparing parameters such as area, volume and height (especially the height that was compared to manual measurements), the 3D instruments follow the same trend, except for 2D acquisitions, which show an anomalous value and the lowest accuracy compared to 3D scanning techniques (0.42 %). The accuracy of the 3D scanning systems based on high-cost and low-cost photogrammetry is almost comparable, with the accuracy being 0.5 % for the high-cost photogrammetry and 0.44 % for the low-cost scanner. In addition, the high-cost system required a long time of processing [133], in agreement with the literature, and is therefore not cost-effective for real-time applications, whereas the low-cost scanner required much less processing time. Photogrammetry with the Canon Eos 7D required 15 minutes of acquisition and 2 hours of processing, while photogrammetry with the 3D-printed scanner required 30 minutes of acquisition and 15 minutes of processing.

The high-resolution Structured Light scanner failed the reconstruction because the light conditions affected it. It was, however, useful for calibrating the points clouds. The low-cost LiDAR, on the other hand, resulted in 10.5 % better accuracy compared to the other instruments, making it suitable for agricultural applications [133]–[135].[134].

The first analysis performed with Deep Learning returns promising results, and the proposed approach could be convenient in large greenhouse settings or vertical farms.

Chapter 7

3D shape measurement techniques for human body reconstruction

7.1 Introduction

In this Chapter, from the digitization process, a methodology for shape reconstruction applied to complex and moving geometries will be shown[11] [136]. In Chapter 4.1 the final 3D printed model was analyzed. In this work the workflow of reconstruction is presented. First, the performances of three different techniques for 3D scanning have been investigated. In particular two commercial tools (smartphone camera and iPad Pro LiDAR) and a structured light scanner (Go!SCAN 50) have been used for the analysis. First of all, two different subjects have been scanned with the three different techniques and the obtained 3D model were analyzed in order to evaluate the respective reconstruction accuracy. A case study involving a child was then considered, with the main aim of providing useful information on performances of scanning techniques for clinical applications, where boundary conditions are often challenging (i.e., non-collaborative patient). Finally, a full procedure for the 3D reconstruction of a human shape is proposed, in order to setup a helpful workflow for clinical applications.

Biomedical applications often required device customization: as well known, no patient is identical to another one, and this is even truer referring to pathologic conditions. In the past, customization has often been sacrificed in favour of manufacturability, however, with the advent of 3D printing [137] [138], this shortcoming is being overcom, and more emphasis is being given to the necessity of providing fast and accurate systems to obtain the geometry of the whole body [139] [140] [141] of specific body segments [142]. Traditional techniques are based on plaster moulds and are affected by some major limitations such as: the invasiveness, the need to keep the patient still for the curing time [143], a limited

accuracy (over 15 mm, according to [77], [144]), and the impossibility of acquiring undercut geometries. More recently, and as a viable alternative, various non-contact instruments have been developed in order to perform digital scanning [145] [146] [147] and the respective performances have been extensively reported in literature [148] [149]. However, the application introduced in this work was somehow peculiar due to the young age of the patient [25] which led to add some requirements to the scanning methodology that are a time limit to perform the whole acquisition, and the possibility to compensate motions since the patient was not collaborative due to his young age [150] [110]. The final aim was obtaining the 3D geometry of his trunk in order to gather input data for brace design [111]. Prior attempts had been made with traditional moulding techniques and they failed due to frequent patient movements [112] [113] [114]. A specific methodology has been here developed, tested and discussed, which is based on a multimodal approach [23] where the benefits of different scanning technique are merged in order to optimize the result.

In the following three common scanning techniques are briefly described, reporting their specifications, and highlighting the respective advantages and disadvantages in relation to their application to human body scanning. These technologies are photogrammetry, light detection and ranging (LiDAR) and structured light scan. The performances of these shape measurement techniques have been assessed reconstructing the torso of two adults (one male and one female); the main objective of this first analysis was to evaluate the performances of two low-cost tools [68] [115] (smartphone camera and iPad Pro LiDAR), in relation to the accurate reconstruction obtainable with the structured light scanner, used as reference measurement system [26]. Once the performances of these tools have been defined under 'ideal' scanning conditions (collaborative subject able to maintain a position throughout the scan process), the same techniques have been used to obtain a set of 3D scans of a 4-year-old boy's torso, at an orthopaedic laboratory (Officina Ortopedica Semidoro srl, Perugia, ITALY). For both these analyses, the process of 3D reconstruction and structure extraction is described in detail in the 'Results' section. The accuracy and correlation among the geometries reconstructed with different visual devices, are evaluated and discussed, and the bias given by a non-collaborative patient is illustrated, leading to introduce a new methodology based on a multimodal approach, whose benefit are outlined and quantified.

In the 'Discussion' section it is demonstrated how this methodology can be applied in orthopaedics [104], and on least collaborative patients, making it possible to obtain body scans where the alternative based on plaster of Paris moulds would fail or would result in lower accuracy and longer execution times.

7.2 Materials and Methods

Techniques used to perform body scans include different technologies: photogrammetry, structured light and LiDAR. These measurement techniques have some specific advantages over contact measuring techniques, such as fast acquisition, high accuracy, and minimal invasiveness.

Depending on the application, some specifications may become more relevant than others. With reference to clinical applications, in some cases, high resolution and accuracy must be prioritised, while in other cases, a good representation of the colour and structure is mandatory.

The acquision where perfomed by the instument's presented in Capter 2. In particular, for photogrammetry a low cost (Ph3_Low) smartphone Redmi Note 10 where used. The Structerd Light scanner (SL) used was the high performance Go!SCAN 50, finally the LiDAR scanner was the low-cost sensor mounted on the iPad Pro 11 (L2_Low).

1. METHODOLOGY

(Figure 140). In the first part of this work, the reconstruction accuracy of the scanning techniques here considered was investigated through the trunk reconstruction of a male and a female human subject. It must be taken into account that for privacy reasons, all subjects were scanned with their dresses on in the case of both adults and the child. At most, close-fitting clothing was requested in other to limitate the error. Scanning results coming from this analysis have been used as reference for techniques comparison, since the subjects can be considered in a stable configuration, except for the intrinsic deformability of the trunk (micro movements due to breathing). In the following step, the same analysis has been repeated on a 4-year-old trunk, adding one more bias given by the subject's macro-movements.

PH is characterised by a timing video acquisition of about 50 s for each subject. Using Zephyr software, the geometry of the torso was reconstructed, taking a total

of 7 h with high software settings: up to 15000 keypoints per image and Pairwise image matching setting on at least 10 images. Keypoints are specific points in a picture that Zephyr can understand and recognise in different pictures. Matching stage depth (Pairwise image matching) controls how many pairwise image matching to perform. Usually, the more is the better, however, this comes at a computational cost.

The mesh given by this scan technique can result in shape's topological errors due to shadow areas and object's movement. The shape complexity and the macro movements led to sudden curvature changes, making the reconstruction difficult and resulting in missing parts and loss of details.

The mesh obtained from the scan performed with Go!SCAN 50 required higher manual processing times, given the computational heaviness due to the high resolution. The scan parameters were set directly in the VX Elements software according to the manufacturer, with a resolution of 2 mm. Targets, semi-rigid positioning, and natural features were used for placement parameters.

The acquisition and processing of data required an average time of 15 min under ideal conditions (collaborative subject).

Scanning with the iPad is the fastest technique. Accurate colour information (texture) can be obtained from the two rear cameras, whose images are managed by proprietary algorithms. Output meshes are of low quality due to the limited number of triangles used for surface discretisation.

For both adults and child scanning analyses, the procedure consists of four main steps:

1) Scanning:

Trunk acquisition required the scanners to rotate around the subject; adhesive circular reference targets with a diameter of 10 mm have been used in order to facilitate the alignment and matching between scans on the post-processing phase (Figure 142 b); these targets have been positioned over the trunk considering that, as well known, at least three tie-points must be present in two neighbouring scans in order to allow the respective alignment.
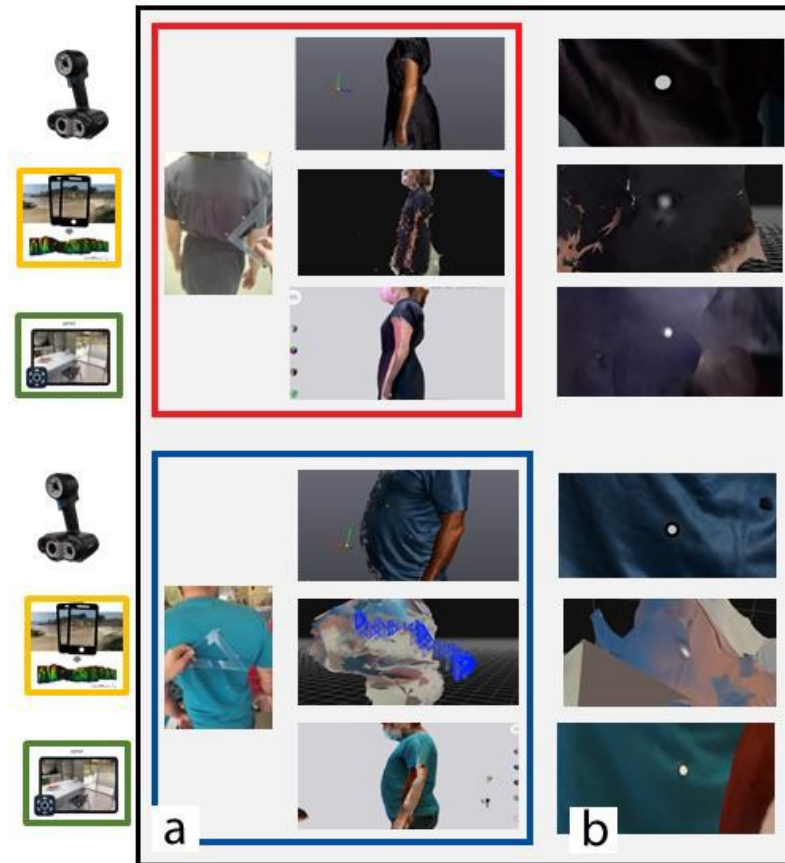
Figure 140 Data obtained by acquisition with the three instruments; a) Body reconstruction with clothe of a female and a male (red and blue); b) Marker details.

2) Geometry reconstruction (post-processing):

Post-processing was performed using Geomagic Studio Software (3D System, v. 12) [34]. Sometimes, data acquisition results in more than one point cloud, so these point clouds must be registered and merged to obtain one single cloud. A cleaning phase follows, where spurious points are eliminated; these points are generated by environment noise and by subject motion or by the camera resolution being close to the size of geometric details. A triangulated mesh is then generated and smoothed to obtain a more regular geometry. The smoothing phase must be performed carefully in order to avoid losing relevant information. Finally, obtaining a manifold geometry, the mesh is edited to avoid double vertices, discontinuities of the face's normal, holes, and internal faces. At the end of editing, the mesh is optimised to reduce the number of triangles.

3) Comparison among measurement techniques:

First of all, the scanners' performances were evaluated in terms of the times required to obtain the final geometry (Figure 143). The geometries were compared through a fully automated operation performed by dedicated Geomagic Studio software. It should be reminded that mesh coming from different scanning are not iso-topological [25], and this can make this operation more critical in addition to the 288389, 431000, and 158000 triangles being processed for male, female and child torso respectively.
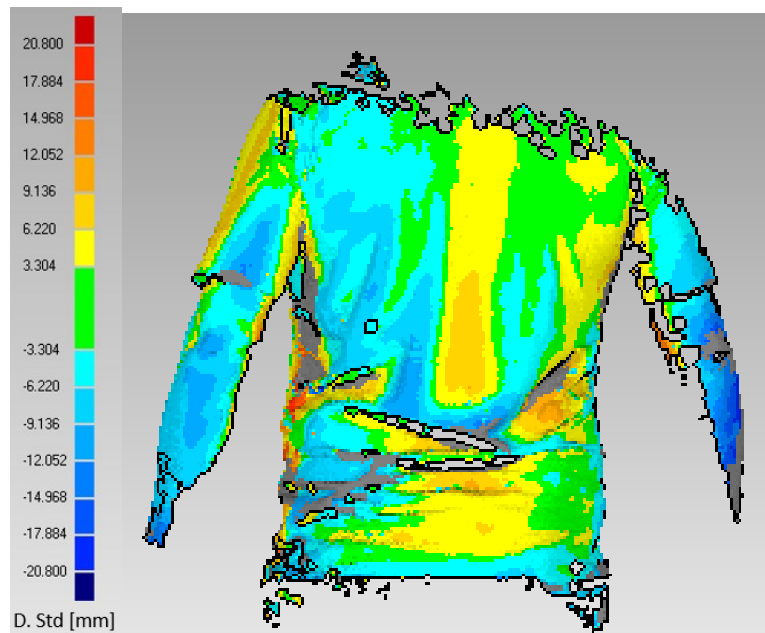
Figure 141 Example of distances' distributions between the outputs obtained with SL and LiDAR instruments: male torso.

More in detail, for the adults' scans case, the reference geometry obtained from Go!SCAN 50 was compared to output geometries from PH and LiDAR, analysing the distribution of distances before and after mesh filtering. A software-coded mapping analysis between pairwise scans was performed: results of this analysis are represented by the standard deviation of the statistical distribution of the shortest distance between two scans, along with the mean value of this distance. This analysis is a signed type of analysis; for this reason, in the following positive and negative values of the mean distance will be provided, representing deviations towards the outer or inner scanned volume, respectively.

For the child torso, this deviation analysis was performed twice. In the first instance, LiDAR scans were compared, analysing the deviation distribution at different threshold levels (10, 20, 80, 120 and 180 mm), where the threshold parameter represents the distance value (in mm) beyond which the mesh points are considered as outliers (Figure 142 a) Young child torso and detail of scan's output given by b) PH, c) LiDAR and d) SL techniques.).

Figure 142 a) Young child torso and detail of scan's output given by b) PH, c) LiDAR and d) SL techniques.

This analysis was performed because three LiDAR scans were obtained: a full body scan (longer acquisition time) and two partial body scans (shorter acquisition time). Over the acquisition time of the two partial scans, the subject's torso could be reasonably considered still, while the full body scan, due to the longer acquisition time, was more biased by macro movements. The multimodal approach used for the child torso consists in the reconstruction of the 3D geometry using the two partial SL scans after their alignment with the LiDAR scan, which was used as a reference for the global alignment, since it was the only technique which allowed obtaining a full body scan. The deviation analysis among LiDAR models has allowed quantifying full scan's macro movements and the respective reconstruction uncertainty for the final torso 3D model, if this scan was used as reference for the Go!SCAN 50 model positioning.

4) Measurement:

Prior to subjects' trunk scanning, some main measurements were taken with a seamstress meter in order to have a reference when checking the scanned geometry scale.

7.3 Results

7.3.1 Adult subject's scan

Scans from SL scanner are the most accurate and are certified; therefore, as aforementioned, they were used as a reference. For PH, it was possible to reconstruct only a portion of the surface for the female subject, while meshes related to the male test has resulted without detail: 94% of points were too far from SL points to be used for the calculation of geometric deviation Figure 141.

With reference to the female subject, 57% of points resulted to be far from the SL model. This is due to male subject movement, colour and reflection of clothes. The best matching points were located at the torso back. LiDAR scans were more complete: only 17% of points had to be discarded for the female subject and 38% for the male one (Table 37).

Table 37 Comparison of distances' distributions between LiDAR and SL scans, for the adult case.

	Reference Scan	Max (mm)	Mean +/- (mm)	Dev. Std. (mm)	Distant point (%)
SL_LiDAR (Female subject)	SL	20	7.61/5.42	8.63	17
SL_PH (Female subject)	SL	20	12.52/11.06	13.14	57
SL_LiDAR (Male subject)	SL	20	6.00/7.00	9.00	38
SL_PH (Male subject)	SL	20	15.00/14.00	16.00	94

In terms of triangles number, which is closely related to the geometry accuracy, SL scan has given a total of 350614 triangles, PH has resulted in 14430 triangles, and LiDAR has provided 37792 triangles for the male subject and 46811 triangles for the female subject. Two reference points have been tracked through apposite markers. The respective distance was equal to 100 mm with reference to the male subject, and 90 mm for the female subject. In the male subject this same distance was evaluated equal to 98.6 mm with SL (1.49% uncertainty); 109 mm with LiDAR (9% uncertainty). With reference to the female subject, the respective

distance was evaluated equal to 89.9 mm with SL (1.11% uncertainty), and 104 mm with LiDAR (15.5% uncertainty).

7.3.2 Young body's scan.

The following information has been obtained: a) 1 PH scan, with partial covering of the subject's trunk, obtained in 18 s with 110244 triangles (referred as 'PH' in the following); b) 3 LiDAR scans: one full-body scan (biased by the movement of the subject) with 8420 triangles and two partial scans of the left (4310 triangles) and right side (4303 triangles), minimally affected by child's movements. These scans required 4 s and 10 s for the left and the right side, and 20 s for the full trunk. In the following, these scans are referred to as LiDAR '1', '2' and '3' (left, right and full-body respectively), according to the respective position in the scanning sequence (Figure 143); c) 2 partial SL scans from Go!SCAN 50: these are much more accurate (47294 triangles) and required about 5 min for the back side and 4 min for front side.
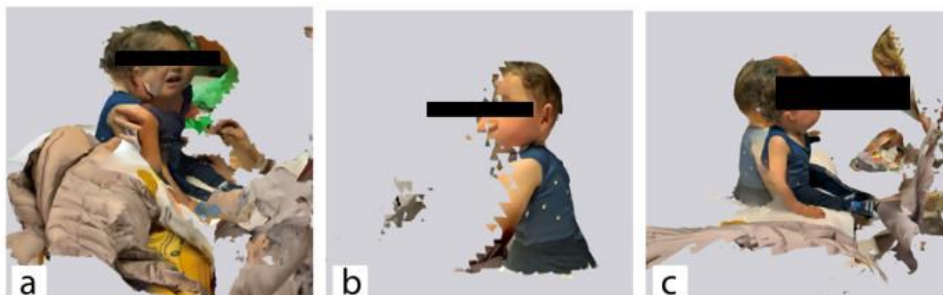
Figure 143 LiDAR acquisition: a) right side scan detail of three LiDAR scan acquisitions referred to as 'LiDAR 1'; b) left side scan without movement, referred to as 'LiDAR 2'; c) total body scan movement, referred to as 'LiDAR 3'.

PH failed to reconstruct the trunk because the legs were the only still part of the child's body.

7.3.1 Analysis of LiDAR's results

In Figure 144 a detail of LiDAR scans alignment is shown.

Figure 144 Example of LiDAR scans alignment: a) point selection for alignment; b) alignment; c) top view of alignment.

The three scans were compared through three pairwise combinations, varying the threshold distance: the distribution of distances between two scans has been obtained on a limited set of points, whose distance laid below this given threshold value. This threshold has been varied in order to assess its influence on final results. According to literature analysis, 10 mm or 20 mm threshold values have to be chosen in order to keep the standard deviation below 60 mm. However, 10 mm threshold would produce a too high percentage of outliers, as shown in Figure 145.
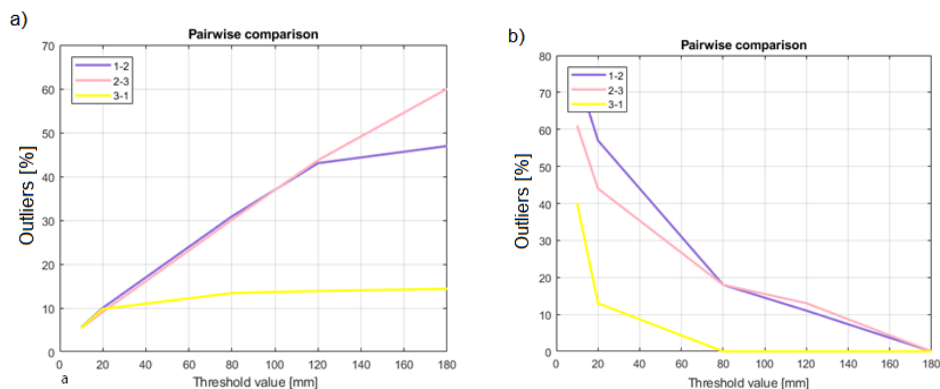
Figure 145 Trend of a) standard deviation and b) percentage of outliers versus threshold values for different pairwise comparisons.

Therefore, a threshold value equal to 20 mm has been chosen: it represents the trade-off between the standard deviation and the percentage of retained points. Having chosen the 20 mm threshold as reference, the mean values for the standard deviation of distances among LiDAR scans have been analyzed. These values are reported in Table 39: they show that the minimum value of the deviation is associated to LiDAR 2 (which is the fastest scan) versus LiDAR 3 comparison and LiDAR 3 (which is the only full body scan available) versus LiDAR 1 comparison

(bolded values in Table 39). For this reason, LiDAR 3 has been chosen as a reference for the following alignment procedure in multimodal scans.

Table 38 Comparison of distances' distributions between LiDAR scans for the child case

	Reference Scan	Max (mm)	Mean +/- (mm)	Dev. Std. (mm)	Distant point (%)
LiDAR 1 (Young boy)	LiDAR 2	20	7.60/9.54	10.00	57
LiDAR 2 (Young boy)	**LiDAR 3**	**20**	**8.27/7.52**	**9.16**	**44**
LiDAR 3 (Young boy)	**LiDAR 1**	**20**	**6.05/5.97**	**7.90**	**13**

7.3.2 LiDAR versus Structured Light

Scans from SL have been considered as a reference since the respective scanner has been certified and this technique is known to be the most accurate [63]. An optimized geometric alignment was performed by Geomagic Studio software, which is based on Iterative Closest Point algorithms. Figure 146 a and b show the displacement between scans after alignment. The sections are evaluated by a level curves measurement tool that returns the circumferences of trunk. Three combinations have been studied: three scans form LiDAR were compared to both SL scans (Figure 146 c).
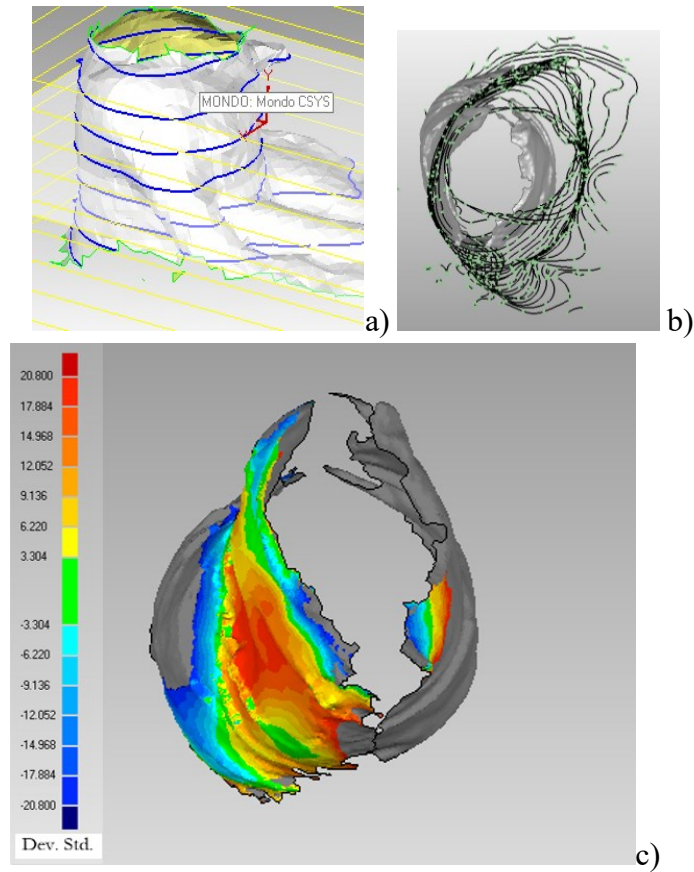
Figure 146 a) Level curves (blue curves) for distance evaluation between LiDAR and SL scans: b) Example of LiDAR 3 to SL scan alignment c) Example of distances distribution between SL and LiDAR 3 scan

The maximum standard deviation has resulted to be equal to 6.93 mm with mean values equal to +6.32 mm and -6.36 mm (where positive and negative values represent deviations towards the outer or inner scanned volume, respectively) obtained from SL-LiDAR 3 combination, corresponding to the overlap between the full LiDAR and the SL scans (reference). On the other hand, the minimum standard deviation is represented by overlapping the fastest LiDAR scan (LiDAR 2) and both partial SL scans (references). The value of standard deviation in this case is 6.65 mm with mean values equal to +5.71 mm and -5.49 mm (Table 39).

Table 39 Comparisons between Structured Light and LiDAR scans for the child.

	Reference Scan	Max (mm)	Mean +/- (mm)	Dev. Std. (mm)	Distant point (%)
SL_LiDAR 1	SL	20	6.73/5.83	6.68	55
SL_LiDAR 2	SL	20	5.71/5.49	6.65	75
SL_LiDAR 3	SL	20	6.32/6.93	6.93	62

As noted, the full body LiDAR scan (LiDAR 3) has the closest values to both SL scans and it is the best suited to replicate the actual back shape and to be used as reference for SL scans alignment.

7.3.2 Multimodal procedure

The full body scan obtained from LiDAR 3 was used as reference for both SL scans positioning, since PH provided an incomplete result which could not be merged to obtain a full trunk scan. However, since PH technique reconstructed the lower part of the body, (the only one that did not show movement), this acquisition was used to align and adapt the LiDAR 3 full scan (which does show movement) and the LiDAR 1 and LiDAR 2 side scans (much shorter in therms of acquisition time and without movement). At this point, thanks to the textures of the three LiDAR scans it was possible to assess the movement of the child and cut the mesh, so as to have a global reconstruction that did not overestimate the initial shape. Thanks to these steps, it was possible to correctly place the two SL scans (chest and back). The integration of several scanning techniques made possible to reconstruct the torso by eliminating movement. Looking at LiDAR results, the lines of movement can be outlined in texture scans (Figure 147).
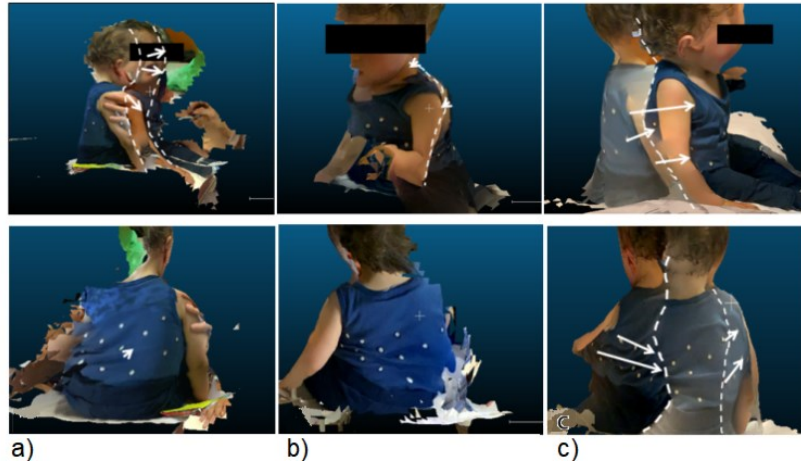
Figure 147 LiDAR movement texture detail. Upper Row: side view. Lower Row: back view. a) Column: LiDAR 1; b) Column: LiDAR 2 scan; c) Column: LiDAR 3

The two SL scans were overlapped on the 3D LiDAR full scan and in the next step a topological optimization of the trunk was performed with 3-Matic (Materialise, v. 12) [35], a software used for clinical application (Figure 148).
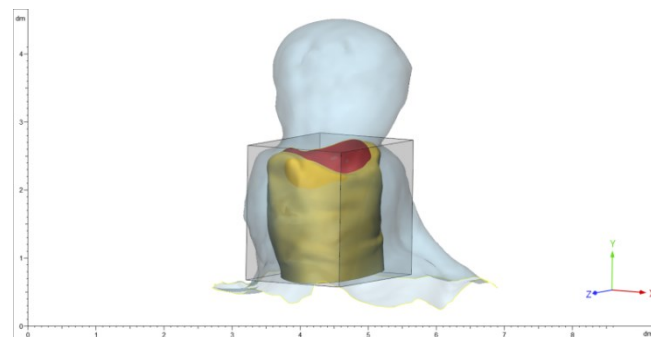
Figure 148 Reconstruction of torso in 3-Matic Materialise, using the full LiDAR scan as a reference.

Finally, a comparison between the actual trunk measurements (circumferences at chest and waist levels) and the corresponding measurements taken on the reconstructed geometry was performed, resulting in a difference of 5.9 mm (1.25%) at the waist level, and an uncertainty of 8.2 mm (1.64%) at the chest level (Figure 51).
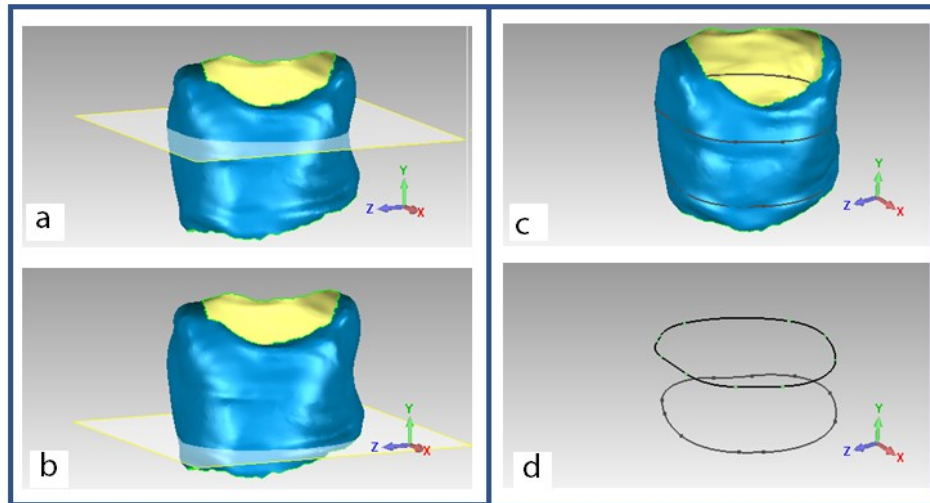
Figure 149 Reconstruction of torso and measurement of a) circumferences at chest and b) waist levels c) Intersection between a horizontal plane and model. d) Level curves to be measured.

The plaster mould accuracy, acceptable for medical applications is above 15 mm [9], [10]. The uncertainty of the reconstruction for this multimodal non-contact measurement methodology is within this limit in fact the maximum uncertainty is 8.2 mm.

7.4 Conclusions

All instruments, photogrammetry, structured light scanner and LiDAR have been proved to be able to capture trunk geometry in a still patient; when results coming from all three instruments were compared to those coming from traditional techniques based on plaster moulding, they proved to be more accurate with the advantage of producing a digital editable model. Structured light scanner produced the most accurate results. When a non-collaborative patient is considered, new specifications must be considered such as the time required for scanning the whole geometry and the robustness of reconstruction algorithms. As a result, LiDAR technique was proved to be the only technique able to provide a full scan, thanks to the lowest acquisition time. However, the respective accuracy was quite low and LiDAR could not be used alone; however, it could be used as reference for structured light scans registration, so removing the major source of noise in SL, that is non-collaborative patient's movement. From this, it can be pointed out that a

multimodal methodology was needed in order to overcome the limited accuracy of LiDAR, recovering information from partial scans obtained from SL. The whole methodology has been set up and tested with encouraging results: the final outcome has an acceptable accuracy (8.2 mm), where the only alternative would be taking a limited number of measurements on the non-collaborative patient body. Compared to plaster moulding, the accuracy is greatly improved (8.2 mm against 15 mm according to [77], [144]), and the bias given by dermal tissue compressibility [36], [37] is totally absent. Once the scans were cleaned, simplified and merged, the Standard Triangulation Language (STL) model was exported and 3D printed, to evaluate the viability of this workflow to produce a customized brace. Finally, the brace was manufactured with traditional method on the 3D printed volume, without any contact with the subject (Figure 150), after having been virtually tested through mock up techniques [38].

Figure 150 a) 3D printed trunk, b) Plaster mould built on printed model, c) Plaster realization d) Final model.

In this work a multimodal scanning approach was proposed. The uncertainty given by movement was analyzed and compensated. A full procedure for the reconstruction of the 3D external shape was developed by integration of different 3D measurement techniques. The shape of the human torso of a child was finally measured, 3D printed and used for the creation of a patient-specific brace. Future developments will focus on combining fast and low-cost techniques and algorithms with low-cost measurement systems for orthopaedical applications, in order to improve the measurement technique without the need for high-performance tools.

Chapter 8

Conclusions

This thesis contributes significantly to the understanding and application of 3D scanning technology by comprehensively analysing different 3D scanners with varying performances and costs across various applications. The focus on complex geometries, subject movement, and uncertainties associated with shape reconstruction and volume measurement provides valuable insights for users of these instruments. Multiple applications, including Cultural Heritage, Sports Training, Design, Biomedicine, and Agriculture, are analysed in order to give a usage and performance of these techniques in different scenarios. Moreover, developing algorithms to address the challenges of reconstructing complex geometries and evaluating volumes adds to the advancement of 3D scanning technology.

Chapter 1 recognises the extensive applications of 3D scanning and its potential role in various domains, including history preservation, design, reverse engineering, and accurate measurements before production. It also highlights the importance of considering specific requirements, such as execution speed, accuracy, repeatability, and integration costs, while selecting suitable scanners for different applications. Standardised guidelines governing the use of 3D scanning technology are identified as a challenge, and the thesis serves as a foundation for future research to establish comprehensive frameworks for applying these scanners in different fields.

Further work in this area could focus on refining the algorithms for complex geometries, exploring more efficient methods for volume evaluation, and extending the multi-modal scanning approach to different scenarios. Additionally, investigations into integrating 3D scanning technology with other emerging technologies, such as AI and automation, could be explored to enhance its capabilities and potential applications.

In conclusion, this thesis contributes to advancing 3D scanning technology by providing valuable insights, addressing challenges, and laying the groundwork for future developments and applications in diverse fields. As 3D scanning continues to evolve, its widespread adoption is anticipated to revolutionise various industries, streamline manufacturing processes, and enable precise measurements and reconstructions of complex objects.

In Chapter 2, the study and evaluation of uncertainty in different measurement techniques, focusing on 3D scanning technologies like Structured Light scanners, Photogrammetry, RGB-D, and LiDAR ([12], [13], [1], [14], [15], [16], [17]). presents the evaluation of smoothing processes and the development of an algorithm to find the optimal alpha value for volume calculation close to the reference volume. The relative percentage error obtained in the study is less than 0.5×10^{-3}, which is an improvement compared with scanner uncertainty [9] [2],

The study compares scanning approaches, such as active and passive sensors, data acquisition methods, and processing algorithms, offering insights into their advantages and limitations, particularly in digitisation, by exploring the repeatability and accuracy of Structured-Light 3D scanners [12], [13].

Exploring new active and passive sensors, improving data acquisition approaches, refining processing algorithms, and enhancing computational systems. For this reason, a new strategy was proposed for scanning that can be further investigated and optimised to achieve higher automation, accuracy, and processing times.

This contributes address uncertainties in different measurement techniques, presents a developed alpha-shape algorithm, and explores the potential of emerging technologies in different applications. The results and methodologies presented in this chapter provide a foundation for further advancements in 3D scanning technology and its application in diverse fields, contributing to giving an overview of the functioning of 3D measuring instruments [3].

Chapter 3 aims to Address Geometrical Complexity with Alpha Shape Algorithm. The study of contributions of utilising the alpha shape algorithm for 3D reconstruction and volume evaluation of various geometries emphasises the significance of selecting the optimal alpha value, which is influenced by the density and the shape of the object being measured ([1], [6], [10], [11], [12]). The research

identifies specific alpha values for shape reconstruction and volume calculation, providing valuable insights into the sensitivity of simple and complex geometries to variations in the alpha radius.

Developing an efficient and computationally feasible method for reconstructing the entire shape of simple elements using the alpha shape algorithm acknowledges the challenges faced when dealing with more complex geometries, where the alpha shape algorithm may need to perform optimally in reconstructing the shape. The literature demonstrates that correspondence can still be observed in the volume calculation when comparing results obtained from different tools.

The study further investigates the uncertainty in volume measurement for simple geometries and highlights those optimal alpha values are relatively high, especially for concave shapes. It also identifies that those larger geometries tend to exhibit higher uncertainty in volume measurement, reaching up to 29.86%, than directly immersed objects in water for volume measurement, demonstrating the potential accuracy achievable with the alpha shape algorithm even without an exact reference model [10], [9].

It was shown that the proposed method outperforms a similar algorithm in computation time, taking only 15 minutes [5] for calculations compared to the reported 30 minutes in [12].

The findings provide valuable insights into selecting the optimal alpha value and its influence on different geometries. Moreover, the efficient computational method developed in the study enhances the applicability of the alpha shape algorithm for various practical applications.

The research calls for further evaluation and optimisation of the algorithm for applications in diverse domains, potentially expanding its applicability and impact in various scientific and engineering disciplines.

In Chapter 4, Analysing Uncertainty and Resolution in Static Objects is performed. Surface reconstruction methods were tested on a comprehensive rockfall database, and the implications of 3D volume estimation were analysed through various visualisation and statistical techniques.

The findings reveal that the uncertainty of shape reconstruction is relatively low for certain shapes and sizes, namely Alpha Critical, Alpha Optimal, and Convex Hull, with variations around 8% for different object resolutions. This suggests that the resolution does not significantly influence these algorithms' performance for these particular shapes and sizes. However, it is observed that the Convex Hull tends to overestimate the volume of large objects by up to 70%. At the same time, the Alpha Critical and Alpha Optimal algorithms introduce errors in the reconstruction and final volume calculation. The Alpha Critical, in particular, results in a volume overestimation of up to 40%. Nevertheless, the Alpha Optimal algorithm shows closer proximity to the reference volume.

The research highlights the potential of low-cost LiDAR systems for shape reconstruction and volume calculation. Despite potential imperfections in mesh quality, the LiDAR system used in the study demonstrated good texture quality and shape reconstruction capabilities. The performance of the tools for volume calculation was found to be comparable. As a result, low-cost, non-contact monitoring systems utilising the uncertainty values obtained from the study could be considered for calibration purposes.

Furthermore, the quantitative analysis identified a range of alpha values (15-75mm) suitable for conducting the analyses, thereby optimising the calculation process. The impact of point cloud density on reconstruction was also evaluated, and higher point cloud densities were found to reduce uncertainty in reconstruction. The study also reports a maximum reconstruction uncertainty of 0.31mm for the World Cup scanned with the photogrammetric technique, which aligns with previous studies ([61], [62] and [63]).

In conclusion, the research comprehensively evaluates surface reconstruction algorithms for volume estimation, specifically in the context of complex points clouds models and provides a foundation for further advancements in 3D reconstruction and volume estimation techniques, which can find applications in various fields, including hazard assessments, crop phenotyping, and other areas involving shape analysis and volume measurement ([9], [6], [10], [11] and [12]).

In **Chapter 5**, tree growth and volume-area relationship were analysed. The alpha shape algorithm was used for volume calculation and shape reconstruction of an artificial tree using high-cost LiDAR and RGB-D low cost-based scanner [97],

[103]. The research explores the tree volume and leaf area relationship, examining the linear and logarithmic correlations with different alpha values. The contribution of this thesis lies in developing and validating an algorithm for selecting the optimal alpha radius that minimises error distribution in tree volume reconstruction.

The research reveals that the relationship between tree volume and leaf area can be linear and logarithmic, depending on the chosen alpha value [99].

To effectively select the optimal alpha radius, which minimises error distribution, the algorithm evaluates various alpha values within a specified range (e.g., around 15 mm) to determine the best fit for the data. The coefficient of determination (R^2 factor) is crucial in this selection process, as it allows the identification of the most reliable reconstruction for tree volume evaluation. Additionally, the filtering system significantly reduces errors by effectively filtering points with a certain threshold [103], [105], [111].

The research demonstrates the significance of selecting the optimal alpha radius for improved accuracy and provides insights into the relationship between tree volume and leaf area. This knowledge can benefit various applications, such as forest inventory, ecological studies, and tree management. Moreover, the proposed approach opens avenues for further research in refining tree attribute estimation methods and enhancing the understanding of tree growth dynamics.

In **Chapter 6**, the Deep Learning algorithm was used to investigate the performance of various high-cost and low-cost 3D scanning instruments on complex geometries, such as plants, by introducing the concept of calculating the integral of the volume enclosed by the points, which helps to reduce processing times. Through an in-depth analysis utilising deep learning techniques, we identified that the low-cost scanner effectively demonstrated superior performance in reconstructing volumes. The comparison of parameters like area, volume, and height (particularly height compared to manual measurements) showed that the 3D instruments exhibited consistent trends, except for 2D acquisitions, and the lowest accuracy (0.42%) compared to the 3D scanning techniques. Notably, the accuracy of the 3D scanning systems, whether based on high-cost or low-cost photogrammetry, was nearly comparable, with 0.5% accuracy for the high-cost photogrammetry and 0.44% for the low-cost scanner. It's important to mention that the high-cost system required a substantial amount of processing time in line with

---

prior research findings, making it less cost-effective for real-time applications. On the other hand, the low-cost scanner necessitated significantly less processing time [123].

Moreover, the research encountered a limitation in the high-resolution Structured Light scanner, which failed to reconstruct due to light condition sensitivity. However, it proved to be useful for calibrating the point clouds. In contrast, the low-cost LiDAR demonstrated superior accuracy, having 10.5% better outcomes than the other instruments, making it highly suitable for agricultural applications [123], [125], [124].

The initial application of Deep Learning produced promising results, and its potential it's foreseen in large greenhouse settings or vertical farms. Future studies focus on automating the multi-scanning approach for larger, more complex objects and the low-cost scanning system for tree volume estimation. Additionally, it is interesting to explore how plant volume overestimations can be effectively utilised to correct measurements and further optimise the scanning process.

Chapter 7 presents a Multi-Modal procedure for reconstructing Moving Objects. Photogrammetry, structured light scanner (SL), and LiDAR were used for capturing trunk geometry in still patients to be compared to traditional plaster moulding techniques, and the process demonstrated superior accuracy, providing digital, editable models. Among them, the structured light scanner produced the most accurate results. However, new considerations such as scanning time and reconstruction algorithm robustness were essential when dealing with non-collaborative patients. LiDAR was identified as the only technique capable of providing a full scan due to its quick acquisition time . Although the accuracy of LiDAR alone was relatively low, it served as a reference for registering structured light scans, effectively reducing noise caused by non-collaborative patient movement [38].

To overcome the limited accuracy of LiDAR, a multimodal scanning approach was proposed, integrating partial scans from structured light into a comprehensive methodology. This methodology was tested and produced promising results, achieving an acceptable accuracy of 8.2 mm compared to limited measurements on the non-collaborative patient body to ([67], [134]). Importantly, this approach greatly improved accuracy compared to plaster moulding, which typically results

in 15 mm accuracy. Furthermore, dermal tissue compressibility, a bias observed in plaster moulding, was eliminated.

The final step involved exporting the Standard Triangulation Language (STL) model of the 3D external shape and 3D printing the patient-specific brace without direct contact with the subject. The workflow proved viable for producing customised braces, demonstrating the potential for improved orthopaedic applications.

The thesis's contribution lies in proposing and implementing a multimodal scanning approach that compensates for movement uncertainties, resulting in an accurate 3D external shape reconstruction. This methodology allows for combining fast, low-cost techniques and algorithms with affordable measurement systems for orthopaedic applications, aiming to enhance measurement techniques without needing high-performance tools. By focusing on such future developments, the field of orthopaedics can further benefit from patient-specific manufacturing and 3D technology to optimise surgical procedures and improve patient outcomes.

The thesis's findings focus on evaluating 3D scanning algorithms, particularly the alpha shape algorithm, in various applications. The alpha shape algorithm demonstrated consistent performance across high and low-cost scanners, making it a valuable tool for complex geometries.

The research explored different applications of 3D scanning, including volume growth and volume-to-leaf area ratio analysis in trees, biomedical applications for reconstructing non-collaborative patient busts, and its potential in Cultural Heritage, Sports Training, Design, Biomedicine, and Agriculture.

The alpha shape method was used to quantify shape complexity without the need for clear homologous landmarks, providing valuable insights into morphological structures. The research also proposed a dedicated algorithm for estimating optimal volume in challenging scenarios and demonstrated the utilisation of statistical analysis to estimate volume when reference measurements are unavailable.

The thesis suggests future research directions, such as utilising volume overestimation for improved measurements, automating multi-scanning approaches for larger objects, and applying the analysis to real plants of different species.

Overall, this research significantly contributes to 3D scanning by developing innovative methodologies for volume estimation in complex geometries and exploring the performance of high and low-cost scanning systems across various applications. It opens new possibilities for more accurate and efficient measurements in diverse fields, advancing the understanding and utilisation of non-contact scanning technologies.

Reference

[1]   J. R. Rosell and R. Sanz, "A review of methods and applications of the geometric characterization of tree crops in agricultural activities," *Computers and Electronics in Agriculture*, vol. 81. pp. 124–141, Feb. 2012. doi: 10.1016/j.compag.2011.09.007.

[2]   A. Haleem., "Exploring the potential of 3D scanning in Industry 4.0: An overview," *International Journal of Cognitive Computing in Engineering*, vol. 3, pp. 161–171, Jun. 2022, doi: 10.1016/j.ijcce.2022.08.003.

[3]   M. Javaid, A. Haleem, R. P. Singh, and R. Suman, "Industrial perspectives of 3D scanning: Features, roles and it's analytical applications," 2021, doi: 10.1016/j.sintl.2021.100114.

[4]   M. Vázquez-Arellano, H. W. Griepentrog, D. Reiser, and D. S. Paraforos, "3-D imaging systems for agricultural applications—a review," *Sensors (Switzerland)*, vol. 16, no. 5. MDPI AG, May 01, 2016. doi: 10.3390/s16050618.

[5]   C. Buzi., "Measuring the shape: Performance evaluation of a photogrammetry improvement applied to the Neanderthal skull Saccopastore 1," *Acta IMEKO*, vol. 7, no. 3, pp. 79–85, 2018, doi: 10.21014/acta_imeko.v7i3.597.

[6]   J. Wang, Y. Zhang, and R. Gu, "Research status and prospects on plant canopy structure measurement using visual sensors based on three-dimensional reconstruction," *Agriculture (Switzerland)*, vol. 10, no. 10, pp. 1–26, 2020, doi: 10.3390/agriculture10100462.

[7]   G. Zhang, S. Yang, P. Hu, and H. Deng, "Advances and Prospects of Vision-Based 3D Shape Measurement Methods," *Machines*, vol. 10, no. 2. MDPI, Feb. 01, 2022. doi: 10.3390/machines10020124.

[8]   Manferdini, A.M., Remondino, "Image-based 3D Modelling: A Review". September 2006, The Photogrammetric Record 21(115):269 – 291, doi:10.1111/j.1477-9730.2006.00383.x.

[9]   T. K. Sarkar, M. Salazar-Palma and D. L. Sengupta, "James Clerk Maxwell: The Founder of Electrical Engineering," 2010 Second Region 8 IEEE Conference on the History of Communications, Madrid, Spain, 2010, pp. 1-7, doi: 10.1109/HISTELCON.2010.5735323.

[10]   Potapov, P., Hansen, M.C., Kommareddy, I., Kommareddy, A., Turubanova, S., Pickens, A., Adusei, B., Tyukavina A., and Ying, Q., 2020. Landsat analysis ready data for global land cover and land cover change mapping. Remote Sens. 2020, 12, 426; doi:10.3390/rs12030426 https://www.mdpi.com/2072-4292/12/3/426.

[11]   X. Su and Q. Zhang, "Dynamic 3-D shape measurement method: A review," *Opt Lasers Eng*, vol. 48, no. 2, pp. 191–204, Feb. 2010, doi: 10.1016/j.optlaseng.2009.03.012.

[12]   E. K. Stathopoulou, M. Welponer, and F. Remondino, "Open-source image-based 3D reconstruction pipelines: Review, comparison and evaluation," in *International Archives of the Photogrammetry, Remote Sensing and Spatial Information Sciences - ISPRS Archives*, International Society for Photogrammetry and Remote Sensing, 2019, pp. 331–338. doi: 10.5194/isprs-archives-XLII-2-W17-331-2019.

[13]   J. Lumme., "Terrestrial laser scanning of agricultural crops," *International Archives of the Photogrammetry, Remote Sensing and Spatial Information Sciences - ISPRS Archives*, vol. 37, no. June 2014, pp. 1–5, 2008.

[14]   Fang Chen, Gordon M. Brown, and Mumin Song "Overview of 3-D shape measurement using optical methods," Optical Engineering 39(1), (1 January 2000). https://doi.org/10.1117/1.602438.

[15]   S. F. El-Hakim, J. A. Beraldin, and F. Blais, "Comparative evaluation of the performance of passive and active 3D vision systems," *https://doi.org/10.1117/12.227862*, vol. 2646, pp. 14–25, Dec. 1995, doi: 10.1117/12.227862.

[16] Chatzifoti, Olga. "On the popularization of digital close-range photogrammetry: a handbook for new users." (2016).

[17] T. Liu, A. W. Burner, T. W. Jones, and D. A. Barrows, "Photogrammetric techniques for aerospace applications," *Progress in Aerospace Sciences*, vol. 54. Elsevier Ltd, pp. 1–58, 2012. doi: 10.1016/j.paerosci.2012.03.002.

[18] Luhmann, T., Robson, S., Kyle, S., & Boehm, J. (2013). "Close-range photogrammetry and 3D imaging". Walter de Gruyter. Book.

[19] F. Remondino, A. Guarnieri, and A. Vettore, "3D modeling of close-range objects: photogrammetry or laser scanning?" in *Videometrics VIII*, J.-A. Beraldin, S. F. El-Hakim, A. Gruen, and J. S. Walton, Eds., SPIE, Jan. 2005, p. 216. doi: 10.1117/12.586294.

[20] A. Probst, D. Gatziolis, and N. Strigul, "Intercomparison of photogrammetry software for three-dimensional vegetation modelling," *R Soc Open Sci*, vol. 5, no. 7, Jul. 2018, doi: 10.1098/rsos.172192.

[21] Freeman, M., & Sargent, I. (2008, September). Quantifying and visualising the uncertainty in 3D building model walls using terrestrial lidar data. In Proc. of the Remote Sensing and Photogrammetry Society Conference (pp. 15-17).

[22] A. Probst, D. Gatziolis, and N. Strigul, "Intercomparison of photogrammetry software for three-dimensional vegetation modelling," *R Soc Open Sci*, vol. 5, no. 7, Jul. 2018, doi: 10.1098/rsos.172192.

[23] A. Stumpf, J. P. Malet, P. Allemand, M. Pierrot-Deseilligny, and G. Skupinski, "Ground-based multi-view photogrammetry for the monitoring of landslide deformation and erosion," *Geomorphology*, vol. 231, pp. 130–145, Feb. 2015, doi: 10.1016/j.geomorph.2014.10.039.

[24] M. A. Isa, D. Sims-Waterhouse, S. Piano, and R. Leach, "Volumetric error modelling of a stereo vision system for error correction in photogrammetric three-dimensional coordinate metrology," *Precis Eng*, vol. 64, pp. 188–199, Jul. 2020, doi: 10.1016/j.precisioneng.2020.04.010.

[25] C. Pérez *et al.*, "Data-driven three-dimensional reconstruction of human bodies using a mobile phone app," *International Journal of the Digital Human*, vol. 1, no. 4, p. 361, 2016, doi: 10.1504/ijdh.2016.10005376.

[26] A. F. Colaço, R. G. Trevisan, J. P. Molin, J. R. Rosell-Polo, and A. Escolà, "A method to obtain orange crop geometry information using a mobile terrestrial laser scanner and 3D modeling," *Remote Sens (Basel)*, vol. 9, no. 8, Aug. 2017, doi: 10.3390/rs9080763.

[27] G. Pérez *et al.*, "3D characterization of a Boston Ivy double-skin green building facade using a LiDAR system," *Build Environ*, vol. 206, Dec. 2021, doi: 10.1016/j.buildenv.2021.108320.

[28] J. Guevara, F. A. Auat Cheein, J. Gené-Mola, J. R. Rosell-Polo, and E. Gregorio, "Analyzing and overcoming the effects of GNSS error on LiDAR based orchard parameters estimation," *Comput Electron Agric*, vol. 170, Mar. 2020, doi: 10.1016/j.compag.2020.105255.

[29] T. Palleja, M. Tresanchez, M. Teixido, R. Sanz, J. R. Rosell, and J. Palacin, "Sensitivity of tree volume measurement to trajectory errors from a terrestrial LIDAR scanner," *Agric For Meteorol*, vol. 150, no. 11, pp. 1420–1427, Oct. 2010, doi: 10.1016/j.agrformet.2010.07.005.

[30] F. A. Auat Cheein and J. Guivant, "SLAM-based incremental convex hull processing approach for treetop volume estimation," *Comput Electron Agric*, vol. 102, pp. 19–30, 2014, doi: 10.1016/j.compag.2014.01.002.

[31] B. Chao, L. Yong, F. Jian-Guo, G. Xia, L. Lai-Peng, and D. Pu, "Calibration of laser beam direction for optical coordinate measuring system," *Measurement (Lond)*, vol. 73, pp. 191–199, Jun. 2015, doi: 10.1016/j.measurement.2015.05.022.

[32] J. Wei and M. Salyani, "DEVELOPMENT OF A LASER SCANNER FOR MEASURING TREE CANOPY CHARACTERISTICS: PHASE 2. FOLIAGE DENSITY MEASUREMENT," *Transactions of the ASAE*, vol. 48, no. 4, pp. 1595–1601.

[33] H. F. Murcia, S. Tilaguy, and S. Ouazaa, "Development of a low-cost system for 3d orchard mapping integrating ugv and lidar," *Plants*, vol. 10, no. 12, Dec. 2021, doi: 10.3390/plants10122804.

[34] M. Elhashash, H. Albanwan, and R. Qin, "A Review of Mobile Mapping Systems: From Sensors to Applications," *Sensors*, vol. 22, no. 11. MDPI, Jun. 01, 2022. doi: 10.3390/s22114262.

[35] Mettenleiter, M., Härtl, F., Neumann, B., Hildebrandt, A., Abmayr, T., & Fröhlich, C. (2004). Terrestrial laser scanning–new perspectives in 3d surveying. In International Conference Laser-Scanners for Forest and Landscape Assessment-Instruments, Processing Methods and Applications, Freiburg im Breisgau, Germany.

[36] Boehler, W., Vicent, M. B., & Marbs, A. (2003). Investigating laser scanner accuracy. The international archives of photogrammetry, remote sensing and spatial information sciences, 34(Part 5), 696-701.

[37] T. P. Kersten, K. Mechelke, M. Lindstaedt, and H. Sternberg, "Methods for geometric accuracy investigations of terrestrial laser scanning systems," *Photogrammetrie, Fernerkundung, Geoinformation*, vol. 2009, no. 4, pp. 301–316, Oct. 2009, doi: 10.1127/1432-8364/2009/0023.

[38] I. Xhimitiku, G. Rossi, L. Baldoni, R. Marsili, and M. Coricelli, "Critical analysis of instruments and measurement techniques of the shape of trees: Terresrial Laser scanner and Structured Light scanner," *2019 IEEE International Workshop on Metrology for Agriculture and Forestry, MetroAgriFor 2019 - Proceedings*, pp. 339–343, 2019, doi: 10.1109/MetroAgriFor.2019.8909215.

[39] Mechelke, K., Kersten, T. P., & Lindstaedt, M. (2007). Comparative investigations into the accuracy behaviour of the new generation of terrestrial laser scanning systems. Proc. in the Optical, 3, 19-327. Optical 3-D Measurement Techniques VIII, Gruen/Kahmen (Eds.), Zurich, July 9-12, 2007, Vol. I, pp. 319-327.

[40] S. Zhang, "High-speed 3D shape measurement with structured light methods: A review," *Optics and Lasers in Engineering*, vol. 106. Elsevier Ltd, pp. 119–131, Jul. 01, 2018. doi: 10.1016/j.optlaseng.2018.02.017.

[41] M. Tölgyessy, M. Dekan, Ľ. Chovanec, and P. Hubinský, "Evaluation of the azure kinect and its comparison to kinect v1 and kinect v2," *Sensors (Switzerland)*, vol. 21, no. 2, pp. 1–25, Jan. 2021, doi: 10.3390/s21020413.

[42] C. Neupane, A. Koirala, Z. Wang, and K. B. Walsh, "Evaluation of depth cameras for use in fruit localization and sizing: Finding a successor to kinect v2," *Agronomy*, vol. 11, no. 9, Sep. 2021, doi: 10.3390/agronomy11091780.

[43] S. Pasinetti, C. Nuzzi, A. Luchetti, M. Zanetti, M. Lancini, and M. de Cecco, "Experimental Procedure for the Metrological Characterization of Time-of-Flight Cameras for Human Body 3D Measurements," *Sensors*, vol. 23, no. 1, p. 538, Jan. 2023, doi: 10.3390/s23010538.

[44] A. Vit and G. Shani, "Comparing RGB-D sensors for close range outdoor agricultural phenotyping," *Sensors (Switzerland)*, vol. 18, no. 12, Dec. 2018, doi: 10.3390/s18124413.

[45] D. Borrmann., "A mobile robot based system for fully automated thermal 3D mapping," in *Advanced Engineering Informatics*, Elsevier Ltd, Oct. 2014, pp. 425–440. doi: 10.1016/j.aei.2014.06.002.

[46] A. F. Colaço, J. P. Molin, J. R. Rosell-Polo, and A. Escolà, "Spatial variability in commercial orange groves. Part 1: canopy volume and height," *Precis Agric*, vol. 20, no. 4, pp. 788–804, Aug. 2019, doi: 10.1007/s11119-018-9612-3.

[47] W. -C. Chang, C. -H. Wu, Y. -H. Tsai and W. -Y. Chiu, "Object volume estimation based on 3D point cloud," 2017 International Automatic Control Conference (CACS), Pingtung, Taiwan, 2017, pp. 1-5, doi: 10.1109/CACS.2017.8284244.

[48] Windreich, G., Kiryati, N., & Lohmann, G. (2003). Voxel-based surface area estimation: from theory to practice. Pattern Recognition, 36(11), 2531-2541. https://doi.org/10.1016/S0031-3203(03)00173-0

[49] Z. Yan, R. Liu, L. Cheng, X. Zhou, X. Ruan, and Y. Xiao, "A Concave Hull Methodology for Calculating the Crown Volume of Individual Trees Based on Vehicle-Borne LiDAR Data," *Remote Sens (Basel)*, vol. 11, no. 6, p. 623, Mar. 2019, doi: 10.3390/rs11060623.

[50] Akkiraju, N. (1998). Approximating spheres and sphere patches. Computer aided geometric design, 15(7), 739-756. https://doi.org/10.1016/S0167-8396(98)00017-X.

[51] Gruson, H. (2020). Estimation of colour volumes as concave hypervolumes using α-shapes. Methods in Ecology and Evolution, 11(8), 955-963. https://doi.org/10.1111/2041-210X.13398.

[52] J. D. Gardiner, J. Behnsen, and C. A. Brassey, "Alpha shapes: Determining 3D shape complexity across morphologically diverse structures," *BMC Evol Biol*, vol. 18, no. 1, Dec. 2018, doi: 10.1186/s12862-018-1305-z.

[53] Mandelbrot, B. (1967). How long is the coast of Britain? Statistical self-similarity and fractional dimension. science, 156(3775), 636-638. Vol 156, Issue 3775. pp. 636-638. doi: 10.1126/science.156.3775.63

[54] Edelsbrunner, Herbert; Mücke, Ernst P. Three-dimensional alpha shapes. ACM Transactions On Graphics (TOG), 1994, 13.1: 43-72. Volume 13Issue 1pp 43-72. https://doi.org/10.1145/174462.156635.

[55] "H. Edelsbrunner, D. Kirkpatrick and R. Seidel, 'On the shape of a set of points in the plane,' in IEEE Transactions on Information Theory, vol. 29, no. 4, pp. 551-559, July 1983, doi: 10.1109/TIT.1983.1056714.".

[56] TAYLOR, John Robert. Book: Introduzione all'analisi degli errori: lo studio delle incertezze nelle misure fisiche. Zanichelli, 1986. ISBN 808032922, 9788808032928. 223 pagine.

[57] N. T. Anderson, K. B. Walsh, and D. Wulfsohn, "Technologies for forecasting tree fruit load and harvest timing—from ground, sky and time," *Agronomy*, vol. 11, no. 7. MDPI AG, Jul. 01, 2021. doi: 10.3390/agronomy11071409.

[58] "GUM-Guide to the Expression of Uncertainty in Measurement-and its possible use in geodata quality assessment.". Available: www.iso.org/sites/JCGM/JCGM

[59] M. Bolognesi, A. Furini, V. Russo, A. Pellegrinelli, and P. Russo, "Accuracy of cultural heritage 3D models by RPAS and terrestrial photogrammetry," in

International Archives of the Photogrammetry, Remote Sensing and Spatial Information Sciences - ISPRS Archives, International Society for Photogrammetry and Remote Sensing, 2014, pp. 113–119. doi: 10.5194/isprsarchives-XL-5-113-2014.

[60]   J. P. Underwood, C. Hung, B. Whelan, and S. Sukkarieh, "Mapping almond orchard canopy volume, flowers, fruit and yield using lidar and vision sensors," *Comput Electron Agric*, vol. 130, pp. 83–96, Nov. 2016, doi: 10.1016/j.compag.2016.09.014.

[61]   M. Boukhana, J. Ravaglia, F. Hétroy-Wheeler, and B. De Solan, "Geometric models for plant leaf area estimation from 3D point clouds: A comparative study," *Graphics and Visual Computing*, vol. 7, p. 200057, Dec. 2022, doi: 10.1016/j.gvc.2022.200057.

[62]   T. Palleja, M. Tresanchez, M. Teixido, R. Sanz, J. R. Rosell, and J. Palacin, "Sensitivity of tree volume measurement to trajectory errors from a terrestrial LIDAR scanner," *Agric For Meteorol*, vol. 150, no. 11, pp. 1420–1427, Oct. 2010, doi: 10.1016/j.agrformet.2010.07.005.

[63]   R. Sanz, J. R. Rosell, J. Llorens, E. Gil, and S. Planas, "Relationship between tree row LIDAR-volume and leaf area density for fruit orchards and vineyards obtained with a LIDAR 3D Dynamic Measurement System," *Agric For Meteorol*, vol. 171–172, pp. 153–162, 2013, doi: 10.1016/j.agrformet.2012.11.013.

[64]   A. Vit and G. Shani, "Comparing RGB-D sensors for close range outdoor agricultural phenotyping," *Sensors (Switzerland)*, vol. 18, no. 12, Dec. 2018, doi: 10.3390/s18124413.

[65]   "Iyer, N., Jayanti, S., Lou, K., Kalyanaraman, Y., & Ramani, K. (2005). Three-dimensional shape searching: state-of-the-art review and future trends. Computer-Aided Design, 37(5), 509-530. https://doi.org/10.1016/j.cad.2004.07.002

[66]   J. D. Gardiner, J. Behnsen, and C. A. Brassey, "Alpha shapes: Determining 3D shape complexity across morphologically diverse structures," *BMC Evol Biol*, vol. 18, no. 1, Dec. 2018, doi: 10.1186/s12862-018-1305-z.

[67]   M. S. Hamoud Al-Tamimi, G. Sulong, and I. L. Shuaib, "Alpha shape theory for 3D visualization and volumetric measurement of brain tumor progression using magnetic resonance images," *Magn Reson Imaging*, vol. 33, no. 6, pp. 787–803, Jul. 2015, doi: 10.1016/j.mri.2015.03.008.

[68]   J. D. Gardiner, J. Behnsen, and C. A. Brassey, "Alpha shapes: Determining 3D shape complexity across morphologically diverse structures," *BMC Evol Biol*, vol. 18, no. 1, Dec. 2018, doi: 10.1186/s12862-018-1305-z.

[69]   Xhimitiku, I., Pascoletti, G., Zanetti, E. M., & Rossi, G. (2022). 3D shape measurement techniques for human body reconstruction. ACTA IMEKO, 11(2), 1-8. vol. 11, no. 2, article 33, June 2022, identifier: IMEKO-ACTA-11 (2022)-02-33.

[70]   L. Ma, T. Xu, and J. Lin, "Validation of a three-dimensional facial scanning system based on structured light techniques," *Comput Methods Programs Biomed*, vol. 94, no. 3, pp. 290–298, 2009, doi: 10.1016/j.cmpb.2009.01.010.

[71]   Polo, M. E., Cuartero, A., & Felicísimo, Á. M. (2019). Study of uncertainty and repeatability in structured-light 3D scanners. Doi: arXiv preprint arXiv:1910.13199...

[72]   C. S. Bamji *et al.*, "IMpixel 65nm BSI 320MHz demodulated TOF Image sensor with 3μm global shutter pixels and analog binning," in *Digest of Technical Papers - IEEE International Solid-State Circuits Conference*, Institute of Electrical and Electronics Engineers Inc., Mar. 2018, pp. 94–96. doi: 10.1109/ISSCC.2018.8310200.

[73]   R. Hänsch, T. Weber, and O. Hellwich, "Comparison of 3D interest point detectors and descriptors for point cloud fusion," *ISPRS Annals of Photogrammetry, Remote Sensing and Spatial Information Sciences*, vol. II–3, no. January 2015, pp. 57–64, 2014, doi: 10.5194/isprsannals-ii-3-57-2014.

[74]   Glover, J. B., Moss, J., & Rissolo, D. (2020). Digital Archaeologies, Material Worlds (Past and Present). Proceedings of the 45rd Annual Conference on Computer Applications and Quantitative Methods in Archaeology. Universität Tübingen. ISBN: 978-3-947251-15-5.

[75]   S. Pagano, M. Moretti, R. Marsili, A. Ricci, G. Barraco, and S. Cianetti, "Evaluation of the accuracy of four digital methods by linear and volumetric analysis of dental impressions," *Materials*, vol. 12, no. 12, 2019, doi: 10.3390/ma12121958.

[76]   L. Barazzetti, L. Binda, M. Scaioni, and P. Taranto, "Photogrammetric survey of complex geometries with low-cost software: Application to the 'G1′ temple in Myson, Vietnam," *J Cult Herit*, vol. 12, no. 3, pp. 253–262, 2011, doi: 10.1016/j.culher.2010.12.004.

[77]   M. Farhan, J. Z. Wang, P. Bray, J. Burns, and T. L. Cheng, "Comparison of 3D scanning versus traditional methods of capturing foot and ankle morphology for the fabrication of orthoses: a systematic review," *J Foot Ankle Res*, vol. 14, no. 1, pp. 1–11, 2021, doi: 10.1186/s13047-020-00442-8.

[78]   J. R. Rosell-Polo *et al.*, "Advances in Structured Light Sensors Applications in Precision Agriculture and Livestock Farming," *Advances in Agronomy*, vol. 133, pp. 71–112, 2015, doi: 10.1016/bs.agron.2015.05.002.

[79]   Polo, M. E., Cuartero, A., & Felicísimo, Á. M. (2019). Study of uncertainty and repeatability in structured-light 3D scanners. arXiv preprint arXiv:1910.13199.

[80]   A. Vit and G. Shani, "Comparing RGB-D Sensors for Close Range Outdoor Agricultural Phenotyping," *Sensors 2018, Vol. 18, Page 4413*, vol. 18, no. 12, p. 4413, Dec. 2018, doi: 10.3390/S18124413.

[81]   M. Tölgyessy, M. Dekan, Ľ. Chovanec, and P. Hubinský, "Evaluation of the azure kinect and its comparison to kinect v1 and kinect v2," *Sensors (Switzerland)*, vol. 21, no. 2, pp. 1–25, Jan. 2021, doi: 10.3390/s21020413.

[82]   T. Palleja, M. Tresanchez, M. Teixido, R. Sanz, J. R. Rosell, and J. Palacin, "Sensitivity of tree volume measurement to trajectory errors from a terrestrial LIDAR scanner," *Agric For Meteorol*, vol. 150, no. 11, pp. 1420–1427, Oct. 2010, doi: 10.1016/j.agrformet.2010.07.005.

[83]   T. Palleja, M. Tresanchez, M. Teixido, R. Sanz, J. R. Rosell, and J. Palacin, "Sensitivity of tree volume measurement to trajectory errors from a

terrestrial LIDAR scanner," *Agric For Meteorol*, vol. 150, no. 11, pp. 1420–1427, Oct. 2010, doi: 10.1016/j.agrformet.2010.07.005.

[84] H. Edelsbrunner, "Alpha shapes - a survey," in Tessellations in the Sciences: Virtues, Techniques and Applications of Geometric Tilings, R. van de Weygaert, G. Vegter, J. Ritzerveld, and V. Icke, Eds. Springer.

[85] L. Mu and R. Liu, "A heuristic alpha-shape based clustering method for ranked radial pattern data," *Applied Geography*, vol. 31, no. 2, pp. 621–630, Apr. 2011, doi: 10.1016/j.apgeog.2010.11.012.

[86] Fischer, K. (2000). Introduction to alpha shapes. Department of Information and Computing Sciences, Faculty of Science, Utrecht University, 17.

[87] X. Xu and K. Harada, "Automatic surface reconstruction with alpha-shape method," *Visual Computer*, vol. 19, no. 7–8, pp. 431–443, 2003, doi: 10.1007/s00371-003-0207-1.

[88] Guo, B., Menon, J., & Willette, B. (1997, October). Surface reconstruction using alpha shapes. In Computer graphics forum (Vol. 16, No. 4, pp. 177-190). Oxford, UK and Boston, USA: Blackwell Publishers. https://doi.org/10.1111/1467-8659.00178.

[89] F. Cazals, J. Giesen, M. Pauly, and A. Zomorodian, "The conformal alpha shape filtration," *Visual Computer*, vol. 22, no. 8, pp. 531–540, Aug. 2006, doi: 10.1007/s00371-006-0027-1.

[90] Maillot, Y., Adam, B., Melkemi, M. (2010). Shape Reconstruction from Unorganized Set of Points. In: Campilho, A., Kamel, M. (eds) Image Analysis and Recognition. ICIAR 2010. Lecture Notes in Computer Science, vol 6111. Springer, Berlin, Heidelberg. https://doi.org/10.1007/978-3-642-13772-3_28.

[91] M. Teichmann and M. Capps, "Surface reconstruction with anisotropic density-scaled alpha shapes," Proceedings Visualization '98 (Cat. No.98CB36276), Research Triangle Park, NC, USA, 1998, pp. 67-72, doi: 10.1109/VISUAL.1998.745286.

[92] "Dispositivo di misurazione di profili in linea ad alta velocità Serie LJ-V7000 Serie LJ-V7000."

[93] H. Rahaman and E. Champion, "To 3D or not 3D: Choosing a photogrammetry workflow for cultural heritage groups," *Heritage*, vol. 2, no. 3, Sep. 2019, doi: 10.3390/heritage2030112.

[94] Alshawabkeh, Y. (2006). Integration of laser scanning and photogrammetry for heritage documentation. http://dx.doi.org/10.18419/opus-3730.

[95] A. Grande, "Virtual Archaeology Review VIRTUAL ARCHAEOLOGY REVIEW EQUIPO EDITORIAL EDITORIAL TEAM Directores / Directors Secretarios / Secretaries Consejo de Redacción / Editorial Board Robert Vernieux," 2014.

[96] A. Kus, E. Unver, and A. Taylor, "A comparative study of 3D scanning in engineering, product and transport design and fashion design education," *Computer Applications in Engineering Education*, vol. 17, no. 3, pp. 263–271, Sep. 2009, doi: 10.1002/cae.20213.

[97] F. Buchón-Moragues, J. M. Bravo, M. Ferri, J. Redondo, and J. V. Sánchez-Pérez, "Application of structured light system technique for authentication of wooden panel paintings," *Sensors (Switzerland)*, vol. 16, no. 6, Jun. 2016, doi: 10.3390/s16060881.

[98] R. Wang, A. C. Law, D. Garcia, S. Yang, and Z. Kong, "Development of structured light 3D-scanner with high spatial resolution and its applications for additive manufacturing quality assurance", doi: 10.1007/s00170-021-07780-2/Published.

[99] T. Bell, B. Li, and S. Zhang, "Structured Light Techniques and Applications," in *Wiley Encyclopedia of Electrical and Electronics Engineering*, John Wiley & Sons, Inc., 2016, pp. 1–24. doi: 10.1002/047134608x.w8298.

[100] J. R. Rosell-Polo *et al.*, "Advances in Structured Light Sensors Applications in Precision Agriculture and Livestock Farming," *Advances in Agronomy*, vol. 133, pp. 71–112, 2015, doi: 10.1016/bs.agron.2015.05.002.

[101] B. Yilmaz *et al.*, "Influence of 3D analysis software on measured deviations of CAD-CAM resin crowns from virtual design file: An in-vitro study," *J Dent*, vol. 118, Mar. 2022, doi: 10.1016/j.jdent.2021.103933.

[102] Polo, M. E., Cuartero, A., & Felicísimo, Á. M. (2019). Study of uncertainty and repeatability in structured-light 3D scanners. doi: arXiv preprint arXiv:1910.13199.

[103] Gregorio, E., & Llorens, J. (2021). Sensing crop geometry and structure. Sensing approaches for precision agriculture, 59-92.

[104] F. A. Auat Cheein and J. Guivant, "SLAM-based incremental convex hull processing approach for treetop volume estimation," *Comput Electron Agric*, vol. 102, pp. 19–30, 2014, doi: 10.1016/j.compag.2014.01.002.

[105] F. A. Auat Cheein *et al.*, "Real-time approaches for characterization of fully and partially scanned canopies in groves," *Comput Electron Agric*, vol. 118, pp. 361–371, Oct. 2015, doi: 10.1016/j.compag.2015.09.017.

[106] A. Escolà *et al.*, "Mobile terrestrial laser scanner applications in precision fruticulture/horticulture and tools to extract information from canopy point clouds," *Precis Agric*, vol. 18, no. 1, pp. 111–132, Feb. 2017, doi: 10.1007/s11119-016-9474-5.

[107] A. F. Colaço, R. G. Trevisan, J. P. Molin, J. R. Rosell-Polo, and A. Escolà, "A method to obtain orange crop geometry information using a mobile terrestrial laser scanner and 3D modeling," *Remote Sens (Basel)*, vol. 9, no. 8, Aug. 2017, doi: 10.3390/rs9080763.

[108] M. Chakraborty, L. R. Khot, S. Sankaran, and P. W. Jacoby, "Evaluation of mobile 3D light detection and ranging based canopy mapping system for tree fruit crops," *Comput Electron Agric*, vol. 158, pp. 284–293, Mar. 2019, doi: 10.1016/j.compag.2019.02.012.

[109] F. Westling, K. Mahmud, J. Underwood, and I. Bally, "Replacing traditional light measurement with LiDAR based methods in orchards," *Comput Electron Agric*, vol. 179, Dec. 2020, doi: 10.1016/j.compag.2020.105798.

[110] M. Béland, D. D. Baldocchi, J. L. Widlowski, R. A. Fournier, and M. M. Verstraete, "On seeing the wood from the leaves and the role of voxel size in determining leaf area distribution of forests with terrestrial LiDAR," *Agric For Meteorol*, vol. 184, pp. 82–97, Jan. 2014, doi: 10.1016/j.agrformet.2013.09.005.

[111] F. A. Auat Cheein *et al.*, "Real-time approaches for characterization of fully and partially scanned canopies in groves," *Comput Electron Agric*, vol. 118, pp. 361–371, Oct. 2015, doi: 10.1016/j.compag.2015.09.017.

[112] M. Chakraborty, L. R. Khot, S. Sankaran, and P. W. Jacoby, "Evaluation of mobile 3D light detection and ranging based canopy mapping system for tree fruit crops," *Comput Electron Agric*, vol. 158, pp. 284–293, Mar. 2019, doi: 10.1016/j.compag.2019.02.012.

[113] Waring, R. H. (1983). Estimating forest growth and efficiency in relation to canopy leaf area. In Advances in ecological research (Vol. 13, pp. 327-354). Academic Press. https://doi.org/10.1016/S0065-2504(08)60111-7.

[114] J. Ma, K. J. Niklas, L. Liu, Z. Fang, Y. Li, and P. Shi, "Tree Size Influences Leaf Shape but Does Not Affect the Proportional Relationship Between Leaf Area and the Product of Length and Width," *Front Plant Sci*, vol. 13, Jun. 2022, doi: 10.3389/fpls.2022.850203.

[115] N. T. Anderson, K. B. Walsh, and D. Wulfsohn, "Technologies for forecasting tree fruit load and harvest timing—from ground, sky and time," *Agronomy*, vol. 11, no. 7. MDPI AG, Jul. 01, 2021. doi: 10.3390/agronomy11071409.

[116] J. C. Miranda, J. Gené-Mola, J. Arnó, and E. Gregorio, "AKFruitData: A dual software application for Azure Kinect cameras to acquire and extract informative data in yield tests performed in fruit orchard environments," *SoftwareX*, vol. 20, Dec. 2022, doi: 10.1016/j.softx.2022.101231.

[117] J. P. Underwood, C. Hung, B. Whelan, and S. Sukkarieh, "Mapping almond orchard canopy volume, flowers, fruit and yield using lidar and vision sensors," *Comput Electron Agric*, vol. 130, pp. 83–96, Nov. 2016, doi: 10.1016/j.compag.2016.09.014.

[118] "Mantax Precision Blue Calipers." [Online]. Available: www.haglofsweden.com

[119] M. Béland, D. D. Baldocchi, J. L. Widlowski, R. A. Fournier, and M. M. Verstraete, "On seeing the wood from the leaves and the role of voxel size in determining leaf area distribution of forests with terrestrial LiDAR," *Agric For Meteorol*, vol. 184, pp. 82–97, Jan. 2014, doi: 10.1016/j.agrformet.2013.09.005.

[120] A. F. Colaço, R. G. Trevisan, J. P. Molin, J. R. Rosell-Polo, and A. Escolà, "A method to obtain orange crop geometry information using a mobile terrestrial laser scanner and 3D modeling," *Remote Sens (Basel)*, vol. 9, no. 8, Aug. 2017, doi: 10.3390/rs9080763.

[121] A. F. Colaço, J. P. Molin, J. R. Rosell-Polo, and A. Escolà, "Spatial variability in commercial orange groves. Part 1: canopy volume and height," *Precis Agric*, vol. 20, no. 4, pp. 788–804, Aug. 2019, doi: 10.1007/s11119-018-9612-3.

[122] Haghshenas, A., Emam, Y. Accelerating leaf area measurement using a volumetric approach. Plant Methods 18, 61 (2022). https://doi.org/10.1186/s13007-022-00896-w.

[123] A. Escolà *et al.*, "Mobile terrestrial laser scanner applications in precision fruiticulture/horticulture and tools to extract information from canopy point clouds," *Precis Agric*, vol. 18, no. 1, pp. 111–132, Feb. 2017, doi: 10.1007/s11119-016-9474-5.

[124] F. A. Auat Cheein *et al.*, "Real-time approaches for characterization of fully and partially scanned canopies in groves," *Comput Electron Agric*, vol. 118, pp. 361–371, Oct. 2015, doi: 10.1016/j.compag.2015.09.017.

[125] T. Lin, "An automatic vision based plant growth measurement system for leafy vegetables," *Biosyst Eng*, vol. 117, pp. 43–50, 2014. https://doi.org/10.1016/j.biosystemseng.2013.08.011.

[126] S. Paulus, "Measuring crops in 3D: Using geometry for plant phenotyping," *Plant Methods*, vol. 15, no. 1, pp. 1–13, 2019, doi: 10.1186/s13007-019-0490-0.

[127] A. S. Barrett and L. R. Brown, "A novel method for estimating tree dimensions and calculating canopy volume using digital photography," *Afr J Range Forage Sci*, vol. 29, no. 3, pp. 153–156, 2012, doi: 10.2989/10220119.2012.727471.

[128] M. Proietti, "Edge Intelligence with Deep Learning in Greenhouse Management," in *International Conference on Smart Cities and Green ICT Systems, SMARTGREENS - Proceedings*, Science and Technology Publications, Lda, 2021, pp. 180–187. doi: 10.5220/0010451701800187.

[129] Sutskever, I., Vinyals, O., & Le, Q. V. (2014). Sequence to sequence learning with neural networks. Advances in neural information processing systems, 27. Part of Advances in Neural Information Processing Systems 27 (NIPS 2014).

[130] D. P. Kingma and J. Ba, "Adam: A Method for Stochastic Optimization," Dec. 2014, [Online]. Available: http://arxiv.org/abs/1412.6980

[131] Powers, D. M. (2020). Evaluation: from precision, recall and F-measure to ROC, informedness, markedness and correlation. doi: arXiv preprint arXiv:2010.16061.

[132] M. Proietti., "Edge Intelligence with Deep Learning in Greenhouse Management", doi: 10.5220/0010451701800187.

[133] L. Shaw, D. Preece, and H. Rubinsztein-Dunlop, "IOP Conference Series: Earth and Environmental Science A comparison of low-cost techniques for three-dimensional animal body measurement in livestock buildings", doi: 10.1088/1755-1315/275/1/012015.

[134] J. R. Rosell and R. Sanz, "A review of methods and applications of the geometric characterization of tree crops in agricultural activities," *Computers and Electronics in Agriculture*, vol. 81. pp. 124–141, Feb. 2012. doi: 10.1016/j.compag.2011.09.007.

[135] M. Vázquez-Arellano, H. W. Griepentrog, D. Reiser, and D. S. Paraforos, "3-D Imaging Systems for Agricultural Applications—A Review," *Sensors 2016, Vol. 16, Page 618*, vol. 16, no. 5, p. 618, Apr. 2016, doi: 10.3390/S16050618.

[136] K. Bartol, D. Bojanic, T. Petkovic, and T. Pribanic, "A Review of Body Measurement Using 3D Scanning," *IEEE Access*, vol. 9. Institute of Electrical and Electronics Engineers Inc., pp. 67281–67301, 2021. doi: 10.1109/ACCESS.2021.3076595.

[137] D. F. Redaelli *et al.*, "3D printing orthopedic scoliosis braces: a test comparing FDM with thermoforming," *International Journal of Advanced Manufacturing Technology*, vol. 111, no. 5–6, pp. 1707–1720, 2020, doi: 10.1007/s00170-020-06181-1.

[138] K. P. Simmons and C. L. Istook, "Body measurement techniques: Comparing 3D body-scanning and anthropometric methods for apparel applications," *Journal of Fashion Marketing and Management*, vol. 7, no. 3, pp. 306–332, 2003, doi: 10.1108/13612020310484852.

[139] S. Grazioso, M. Selvaggio, and G. di Gironimo, "Design and development of a novel body scanning system for healthcare applications," *International Journal on Interactive Design and Manufacturing*, vol. 12, no. 2, pp. 611–620, 2018, doi: 10.1007/s12008-017-0425-9.

[140] F. Remondino, "3-D reconstruction of static human body shape from image sequence," *Computer Vision and Image Understanding*, vol. 93, no. 1, pp. 65–85, 2004.

[141] J. Tong, J. Zhou, L. Liu, Z. Pan, and H. Yan, "Scanning 3D full human bodies using kinects," *IEEE Trans Vis Comput Graph*, vol. 18, no. 4, pp. 643–650, 2012, doi: 10.1109/TVCG.2012.56.

[142] N. Tokkari *et al.*, "Comparison and use of 3D scanners to improve the quantification of medical images (surface structures and volumes) during follow up of clinical (surgical) procedures," *Advanced Biomedical and Clinical Diagnostic and Surgical Guidance Systems XV*, vol. 10054, p. 100540Z, 2017, doi: 10.1117/12.2253241.

[143] P. Andrés-Cano, J. A. Calvo-Haro, F. Fillat-Gomà, I. Andrés-Cano, and R. Perez-Mañanes, "Role of the orthopaedic surgeon in 3D printing: current applications and legal issues for a personalized medicine," *Rev Esp Cir Ortop Traumatol*, vol. 65, no. 2, pp. 138–151, 2021, doi: 10.1016/j.recot.2020.06.014.

[144] W. Clifton, M. Pichelmann, A. Vlasak, A. Damon, K. ReFaey, and E. Nottmeier, "Investigation and Feasibility of Combined 3D Printed Thermoplastic Filament and Polymeric Foam to Simulate the Cortiocancellous Interface of Human Vertebrae," *Sci Rep*, vol. 10, no. 1, pp. 1–9, 2020, doi: 10.1038/s41598-020-59993-2.

[145] J. C. Rodríguez-Quiñonez *et al.*, "Optical monitoring of scoliosis by 3D medical laser scanner," *Opt Lasers Eng*, vol. 54, pp. 175–186, 2014, doi: 10.1016/j.optlaseng.2013.07.026.

[146] D. G. Chaudhary, R. D. Gore, and B. W. Gawali, "Inspection of 3D Modeling Techniques for Digitization," *International Journal of Computer Science and Information Security (IJCSIS),* vol. 16, no. 2, pp. 8–20, 2018. ISSN 1947-5500.

[147] P. Dondi, L. Lombardi, M. Malagodi, and M. Licchelli, "3D modelling and measurements of historical violins," *Acta IMEKO*, vol. 6, no. 3, pp. 29–34, 2017, doi: 10.21014/acta_imeko.v6i3.455.

[148] C. Boehnen and P. Flynn, "Accuracy of 3D scanning technologies in a face scanning scenario," *Proceedings of International Conference on 3-D Digital Imaging and Modeling, 3DIM*, pp. 310–317, 2005, doi: 10.1109/3DIM.2005.13.

[149] P. Treleaven and J. Wells, "3D body scanning and healthcare applications," *Computer (Long Beach Calif)*, vol. 40, no. 7, pp. 28–34, 2007, doi: 10.1109/MC.2007.225.

[150] M. Pesce, L. M. Galantucci, G. Percoco, and F. Lavecchia, "A low-cost multi camera 3D scanning system for quality measurement of non-static subjects," *Procedia CIRP*, vol. 28, pp. 88–93, 2015, doi: 10.1016/j.procir.2015.04.015.

[151] R. F. de Oliveira *et al.*, "Enhanced Reader.pdf," *Nature*, vol. 388. pp. 539–547, 2018.

[152] I. Molnár and L. Morovič, "Design and manufacture of orthopedic corset using 3D digitization and additive manufacturing," *IOP Conf Ser Mater Sci Eng*, vol. 448, no. 1, 2018, doi: 10.1088/1757-899X/448/1/012058.

[153] F. Remondino and A. Roditakis, "3D reconstruction of human skeleton from single images or monocular video sequences," *Lecture Notes in Computer Science (including subseries Lecture Notes in Artificial Intelligence and Lecture Notes in Bioinformatics)*, vol. 2781, pp. 100–107, 2003, doi: 10.1007/978-3-540-45243-0_14.

[154] J. A. Beraldin, "Basic theory on surface measurement uncertainty of 3D imaging systems," *Three-Dimensional Imaging Metrology*, vol. 7239, p. 723902, 2009, doi: 10.1117/12.804700.

[155] V. Rudat, P. Schraube, D. Oetzel, D. Zierhut, M. Flentje, and M. Wannenmacher, "Combined error of patient positioning variability and prostate motion uncertainty in 3D conformal radiotherapy of localized prostate cancer," *Int J Radiat Oncol Biol Phys*, vol. 35, no. 5, pp. 1027–1034, 1996, doi: 10.1016/0360-3016(96)00204-0.

[156] M. Vogt, A. Rips, and C. Emmelmann, "Comparison of iPad Pro®'s LiDAR and TrueDepth Capabilities with an Industrial 3D Scanning Solution," *Technologies (Basel)*, vol. 9, no. 2, p. 25, 2021, doi: 10.3390/technologies9020025.